Functional network macroscopes for probing past and present Earth system dynamics

Complex hierarchical interactions, tipping points, and beyond

D I S S E R T A T I O N

zur Erlangung des akademischen Grades

d o c t o r   r e r u m   n a t u r a l i u m
(Dr. rer. nat.)
im Fach Physik

eingereicht an der
Mathematisch-Naturwissenschaftlichen Fakultät I
Humboldt-Universität zu Berlin

von
Dipl.-Phys. Jonathan Friedemann Donges

Präsident der Humboldt-Universität zu Berlin:
Prof. Dr. Jan-Hendrik Olbertz

Dekan der Mathematisch-Naturwissenschaftlichen Fakultät I:
Prof. Stefan Hecht, Ph.D.

Gutachter:

1. Prof. Dr. Dr. h.c. mult. Jürgen Kurths

2. Prof. Dr. Shlomo Havlin

3. Prof. Dr. Michael Small

Tag der mündlichen Prüfung: 13. Dezember 2012

To Maja Manou and Larissa Diane

Abstract

The Earth, as viewed from a physicist's perspective, is a dynamical system of great complexity. The contemporary presence and ever-increasing magnitude of anthropogenic perturbations, such as greenhouse gas emissions and large-scale land-use changes, call for a detailed understanding of critical subsystems that can exhibit abrupt qualitative change induced by small shifts in some control parameter (tipping elements). In this context, the complex interdependency structure between tipping elements is of major interest. (i) Complimenting and (ii) connecting research techniques and results concerning the detailed processes at work in the Earth system's subdomains (*e.g.*, the atmosphere, hydrosphere, lithosphere, or anthroposphere), the theory of complex networks provides the concepts and methods needed for a holistic and data-driven approach to Earth system analysis. Functional complex networks serving as *macroscopes*, scientific instruments that condense instead of magnify information, are either inferred from observational data and model runs or constructed on the basis of theoretical considerations. Representing statistical interdependencies or causal interactions between objects (*e.g.*, Earth system subdomains, processes, or locations), functional complex networks are conceptually well-suited for naturally addressing some of the fundamental questions of Earth system analysis concerning, among others, major dynamical patterns, teleconnections, and feedback loops in the planetary machinery, as well as critical elements such as thresholds, bottlenecks, and switches.

The first part of this thesis offers an introduction to the basic concepts of choice: complex network theory and network-based analysis of time series data. Specifically, novel theoretical contributions to both fields are reported, which are applicable to the study of general complex network-structured systems found in nature, society, and technology. Regarding complex network theory, these include consistent frameworks for analyzing the topology of (i) general *networks of interacting networks* and (ii) *networks with vertices of heterogeneously distributed weights, size, or importance*, as well as (iii) an *analytical theory for describing the structure of spatial networks*. In the realm of time series analysis, (i) *recurrence network analysis* is put forward as a conceptually simple, but versatile, nonlinear technique for the study of single, but possibly multivariate time series, that is well-founded in classical mechanics, as well as in dynamical systems and graph theory. (ii) *Coupled climate networks* are introduced as an exploratory tool of data analysis for mapping and quantitatively characterizing the intricate statistical interdependency structure within and between several fields of time series.

The novel concepts and techniques developed in the first part are motivated by and designed for their application to real-world problems and data in the context of Earth system analysis. Consequently, the second part of this dissertation focusses on investigating tipping elements and their interactions, tipping points, and regional vulnerability. Recurrence network analysis is employed to robustly detect dynamical transitions or tipping points in synthetic and paleoclimate data. This reveals a possible influence of large-scale shifts in Plio-Pleistocene African climate variability on events in human evolution, *i.e.*, an interaction of climatic and biological tipping points. Finally, coupled climate networks yield insights

into the atmosphere's general circulation structure and allow to quantify regional centrality and vulnerability with respect to interactions between disparate parts of the Earth system.

Zusammenfassung

Vom Standpunkt des Physikers aus gesehen, ist die Erde als ein dynamisches System von großer Komplexität zu betrachten. Das gegenwärtig stets zunehmende Ausmaß anthropogener Einflüsse wie Treibhausgasemissionen und großskaliger Landnutzungsänderungen erfordert ein detailliertes Verständnis kritischer Subsysteme, die auf kleine Variationen von Kontrollparametern mit abrupten, qualitativen Veränderungen in Zustand und Dynamik reagieren können (Kippelemente). Insbesondere ist dabei die komplexe Wechselwirkungsstruktur zwischen einzelnen Kippelementen von großem Interesse. Die Theorie komplexer Netzwerke stellt die Konzepte und Methoden für solch einen holistischen und datengetriebenen Zugang zur Erdsystemanalyse zur Verfügung. Der auf Ideen aus der Graphentheorie und statistischen Physik basierende Netzwerkansatz kann so (i) zur Ergänzung und (ii) zur Zusammenführung von Forschungsergebnissen zu detaillierten Vorgängen in den verschiedenen Sphären des Erdsystems, z. B. der Atmosphäre, Hydrosphäre, Lithosphäre und Anthroposphäre, beitragen. Funktionale, komplexe Netzwerke können als Makroskope aufgefasst werden, die Information kondensieren anstatt immer weitere Details zu liefern. Sie werden aus Beobachtungs-, Reanalyse- und Modelldaten abgeleitet oder aufgrund theoretischer Überlegungen konstruiert. Indem sie statistische Zusammenhänge oder kausale Wirkbeziehungen zwischen der Dynamik gewisser Objekte, z. B. verschiedenen Sphären des Erdsystems, Prozessen oder geographischen Orten darstellen, bieten funktionale komplexe Netzwerke einen natürlichen Ansatz zur Bearbeitung fundamentaler Probleme der Erdsystemanalyse. Dazu gehören Fragen nach dominanten, dynamischen Mustern, Telekonnektionen und Rückkopplungsschleifen in der planetaren Maschinerie, sowie nach kritischen Elementen wie Schwellwerten, sogn. Flaschenhälsen und Schaltern im Erdsystem.

Der erste Teil dieser Dissertation behandelt die ihr zugrundeliegenden Konzepte und Methoden: Die Theorie komplexer Netzwerke, ebenso wie die netzwerkbasierte Zeitreihenanalyse. Neben einer Einführung werden insbesondere neue theoretische Beiträge zu beiden Forschungsfeldern vorgestellt, die auf allgemeine, in Natur, Gesellschaft und Technologie vorkommende Systeme mit Netzwerkstruktur anwendbar sind. Die Beiträge zur Theorie komplexer Netzwerke beinhalten Sätze konsistenter Maße und Modelle zur Analyse der Topologie (i) allgemeiner *Netzwerke von wechselwirkenden Netzwerken* und (ii) *Netzwerken mit ungleichmäßig verteilten Knotengewichten, -größen oder -wichtigkeiten*, sowie (iii) eine *analytische Theorie zur Beschreibung der speziellen Eigenschaften von räumlich eingebetteten Netzwerken*. Im Bereich der Zeitreihenanalyse werden (i) *Rekurrenznetzwerke* als eine konzeptionell einfache, vielseitige und nichtlineare Methode zum Studium multivariater Zeitreihen vorgestellt, die konzeptionell in der klassischen Mechanik, der Theorie dynamischer Systeme und der Graphentheorie begründet ist. (ii) *Gekoppelte Klimanetzwerke* werden als ein exploratives Werkzeug der Datenanalyse zur Abbildung und quantitativen Charakterisierung der komplexen statistischen Interdependenzstruktur innerhalb und zwischen verschiedenen Feldern von Zeitreihen eingeführt.

Die Entwicklung der im ersten Teil der Arbeit vorgestellten, neuartigen Konzepte und Methoden war durch ihre Anwendung auf offene Forschungsfragen und Daten im Kontext der Erdsystemanalyse motiviert. So konzentriert sich der

zweite Teil dieser Dissertation auf die Untersuchung von Kippelementen und ihren Wechselwirkungen, sowie von Kipppunkten und regionaler Vulnerabilität. Zunächst werden Rekurrenznetzwerke zur robusten Detektion von dynamischen Übergängen oder Kipppunkten in synthetischen und paläoklimatologischen Zeitreihendaten eingesetzt. Diese Analyse deutet auf mögliche Zusammenhänge zwischen großskaligen Veränderungen der afrikanischen Klimadynamik während des Plio-Pleistozäns und Ereignissen in der Menschheitsevolution, in anderen Worten auf eine Wechselwirkung von klimatischen und biologischen Kipppunkten, hin. Schließlich erlauben gekoppelte Klimanetzwerke Einblicke in die Struktur der allgemeinen Zirkulation der Atmosphäre und ermöglichen weiterhin, regionale Zentralität und Vulnerabilität im Hinblick auf Wirkbeziehungen zwischen verschiedenen Komponenten des Erdsystems zu quantifizieren.

List of publications

This dissertation is partly based on the following publications. The identifiers, *e.g.*, P1 or C1, given below are cited in the text to highlight passages that are connected to one or more of these papers.

Papers

P1 M. Wiedermann, **J.F. Donges**, J. Heitzig, and J. Kurths, *Node-weighted interacting network measures improve the representation of real-world complex systems* (subm.), preprint arxiv:1301.0805 [physics.soc-ph].

P2 **J.F. Donges**, R. V. Donner, and J. Kurths, *Testing time series reversibility using complex network methods* (subm.), preprint arXiv:1211.1162 [physics.data-an].

P3 J.H. Feldhoff, R.V. Donner, **J.F. Donges**, N. Marwan, and J. Kurths, *Geometric signature of complex synchronisation scenarios* (subm.), preprint arxiv:1301.0806 [nlin.CD].

P4 A. Radebach, R.V. Donner, J. Runge, **J.F. Donges**, and J. Kurths, *Disentangling different types of El Niño episodes by evolving climate network analysis*, Physical Review E (subm.).

P5 J.H. Feldhoff, R.V. Donner, **J.F. Donges**, N. Marwan, and J. Kurths, *Geometric detection of coupling directions by means of inter-system recurrence networks*, Physics Letters A **376**, 3504–3513 (2012).

P6 Y. Zou, J. Heitzig, R.V. Donner, **J.F. Donges**, J.D. Farmer, R. Meucci, S. Euzzor, N. Marwan, and J. Kurths, *Power-laws in recurrence networks from dynamical systems*, Europhysics Letters **98**, 48001 (2012).

P7 R.V. Donner and **J.F. Donges**, *Visibility graph analysis of geophysical time series: Potentials and possible pitfalls*, Acta Geophysica **60**, 589–623 (2012).

P8 **J.F. Donges**, J. Heitzig, R.V. Donner, and J. Kurths, *Analytical framework for recurrence network analysis of time series*, Physical Review E **85**, 046105 (2012).

P9 J. Heitzig, **J.F. Donges**, Y. Zou, N. Marwan, and J. Kurths, *Node-weighted measures for complex networks with spatially embedded, sampled, or differently sized nodes*, European Physical Journal B **85**, 38 (2012).

P10 **J.F. Donges**, R.V. Donner, M.H. Trauth, N. Marwan, H.-J. Schellnhuber, and J. Kurths, *Nonlinear detection of paleoclimate-variability transitions possibly related to human evolution*, Proceedings of the National Academy of Sciences of the United States of America **108**, 20422–20427 (2011).

P11 **J.F. Donges**, R.V. Donner, K. Rehfeld, N. Marwan, M.H. Trauth, and J. Kurths, *Identification of dynamical transitions in marine palaeoclimate records by recurrence network analysis*, Nonlinear Processes in Geophysics **18**, 545–562 (2011).

P12 C. Tominski, **J.F. Donges**, and T. Nocke, *Information visualization in climate research*, Proceedings of the International Conference Information Visualisation (IV), London, UK, IEEE Computer Society, 298–305 (2011).

P13 R.V. Donner, M. Small, **J.F. Donges**, N. Marwan, Y. Zou, R. Xiang, and J. Kurths, *Recurrence-based time series analysis by means of complex network methods*, International Journal of Bifurcation and Chaos **21**, 1019–1046 (2011).

P14 **J.F. Donges**, H.C.H. Schultz, N. Marwan, Y. Zou, and J. Kurths, *Investigating the topology of interacting networks – Theory and application to coupled climate subnetworks*, European Physical Journal B **84**, 635–652 (2011).

P15 R.V. Donner, J. Heitzig, **J.F. Donges**, Y. Zou, N. Marwan, and J. Kurths, *The geometry of chaotic dynamics – A complex network perspective*, European Physical Journal B **84**, 653–672 (2011).

P16 Y. Zou, **J.F. Donges**, and J. Kurths, *Recent advances in complex climate network analysis*, Complex Systems and Complexity Science **8**, 27–38 (2011).

P17 Y. Zou, R.V. Donner, **J.F. Donges**, N. Marwan, and J. Kurths, *Identifying complex periodic windows in continuous-time dynamical systems using recurrence-based methods*, Chaos **20**, 043130 (2010).

P18 R.V. Donner, Y. Zou, **J.F. Donges**, N. Marwan, and J. Kurths, *Ambiguities in recurrence-based complex network representations of time series*, Physical Review E **81**, 015101(R) (2010).

P19 R.V. Donner, Y. Zou, **J.F. Donges**, N. Marwan, and J. Kurths, *Recurrence networks – A novel paradigm for nonlinear time series analysis*, New Journal of Physics **12**, 033025 (2010).

P20 N. Marwan, **J.F. Donges**, Y. Zou, R.V. Donner, and J. Kurths, *Complex network approach for recurrence analysis of time series*, Physics Letters A **373**, 4246–4254 (2009).

P21 **J.F. Donges**, Y. Zou, N. Marwan, and J. Kurths, *The backbone of the climate network*, Europhysics Letters **87**, 48007 (2009).

P22 **J.F. Donges**, Y. Zou, N. Marwan, and J. Kurths, *Complex networks in climate dynamics*, European Physical Journal Special Topics **174**, 157–179 (2009).

Conference proceedings

C1 R.V. Donner, J.H. Feldhoff, **J.F. Donges**, N. Marwan and J. Kurths, *Multivariate extensions of recurrence networks: Geometric signatures of coupled nonlinear systems*, Proceedings of the IEEE International Symposium on Circuits and Systems (ISCAS 2013), Beijing, China. IEEE Xplore (2013).

C2 N. Marwan, J.H. Feldhoff, R.V. Donner, **J.F. Donges**, and J. Kurths, *Detection of coupling directions with intersystem recurrence networks*, Proceedings of the International Symposium on Nonlinear Theory and its Applications (NOLTA2012), Palma de Majorca, Spain. IEICE, Tokyo (2012), 231–234.

C3 R.V. Donner and **J.F. Donges**, *Identifying nonlinearities by time-reversal asymmetry of vertex properties in visibility graphs*, Proceedings of the International Symposium on Nonlinear Theory and its Applications (NOLTA2012), Palma de Majorca, Spain. IEICE, Tokyo (2012), 435–438 (2012).

C4 N. Marwan, **J.F. Donges**, A. Radebach, J.G.B. Runge, and J. Kurths, *Evolving climate networks*, Proceedings of the International Symposium on Nonlinear Theory and its Applications (NOLTA2010), Krakow, Poland. IEICE, Tokyo (2010) 3–6 (2010).

C5 R.V. Donner, **J.F. Donges**, Y. Zou, N. Marwan, and J. Kurths, *Recurrence-based evolving networks for time series analysis of complex systems*, Proceedings of the International Symposium on Nonlinear Theory and its Applications (NOLTA2010), Krakow, Poland. IEICE, Tokyo (2010) 87–90 (2010).

Acknowledgements

Contents

List of Figures

List of Tables

List of frequently used mathematical symbols

$\mathbf{1}_N$	N-dimensional identity matrix
$\mathbf{A} = \{A_{ij}\}_{ij}$	Adjacency matrix
$\mathbf{A}^+ = \{A_{ij}^+\}_{ij}$	Extended adjacency matrix
$\langle \cdot \rangle$	Average
b_i	(Shortest-path) betweenness centrality
$B_\varepsilon(x)$	ε-ball centered at x
$\mathcal{C}$	Global clustering coefficient
$\mathcal{C}_i$	Local clustering coefficient
c_i	Closeness centrality
d_{ij}	Length of shortest path connecting vertices i and j
δ_{ij}	Kronecker's delta
E	Set of edges in G
$\{i, j\}$	Edge linking vertices i and j
$\mathbb{E}(\cdot)$	Expectation value
ε	Recurrence threshold
f_i^* (f^*)	Node splitting invariant local (global) measures
$G = (V, E)$	Graph or network
$\Theta(\cdot)$	Heaviside function
k_i	Degree centrality
L	Number of edges in G, size of E
$\mathcal{L}$	Average path length
N	Number of vertices in G, size of V
$\mathcal{N}_i$	Neighborhood of vertex i
$\mathcal{N}_i^+$	Unpunctured neighborhood of vertex i
$\| \cdot \|$	Norm
$p(l) = p_l(l)$	Edge length distribution
$\mathcal{P}(i, j)$	Set of all paths connecting vertices i and j
ρ	Edge density
$\mathbf{R} = \{R_{ij}\}_{ij}$	Recurrence matrix
S	Set of points x
t	Time
$\mathcal{T}$	Transitivity
V	Set of vertices in G

Chapter 1.

Introduction

1.1. Earth system analysis

The Earth, enwrapped by a vanishingly thin biological layer, is recognized as a highly complex dynamical system operating far from thermodynamic equilibrium (Schellnhuber et al., 2004). The entangled interactions and feedbacks between its inanimate (*e.g.*, atmosphere, hydrosphere, and lithosphere) and living (biosphere) constituents inspired the metaphor of a self-regulating metabolism, *Gaia*, named after the primal ancient Greek goddess of the Earth (Lovelock, 1979). Gaia theory postulates that the co-evolution of life and its environment during the past 4.5 billion years gravitated towards favorable conditions for living organisms controlled by tightly entwined feedback loops (Lovelock, 2000; Lenton et al., 2004). With the dawn of the anthropocene at most a few thousand years ago (Ruddiman, 2007), a single species, *Homo sapiens*, began to interfere with this delicate balance and emerged as a formative geological force. This development gave rise to a host of planetary syndromes tending to push the Earth system out of the relatively stable Holocene state (Rockström et al., 2009), most notably, anthropogenic climate change or global warming (Solomon et al., 2007). *Earth system analysis* pursues unraveling the complex interplay between Gaia's subsystems (Schellnhuber and Wenzel, 1998; Schellnhuber et al., 2004) and, as layed out in the geocybernetic theory of Schellnhuber (1998), aims to find pathways for a sustainable long-term co-evolution of ecosphere and anthroposphere.

1.2. The network macroscope

The principal idea behind this thesis project is to explore the use of *complex networks* (Cohen and Havlin, 2010; Newman, 2010) as *macroscopes* (Schellnhuber, 1999), scientific instruments for condensing instead of magnifying information, for an integrated analysis of the Earth's planetary inventory. Networks inferred from observational data and model runs, or constructed on the basis of theoretical considerations, are conceptually well-suited for naturally addressing some of the fundamental questions highlighted in a *Hilbertian* program for Earth system science akin to the collection of basic mathematical problems put forward by David Hilbert in the 1920s (Schellnhuber et al., 2004, p. 9). These concern, among other problems, major dynamical patterns, teleconnections, and feedback loops in the planetary machinery

as well as critical elements of the Earth system such as thresholds, bottlenecks, and switches.

The idea of tackling these questions using network macroscopes rests on the assumption that (i) for adequately describing a complex system of nonlinearly interacting subsystems, its coupling structure has to be understood and (ii) to first-order approximation the subsystems' detailed dynamics is of minor importance for the networked system's global behavior. Theoretical insights into the synchronization of nonlinear dynamical systems coupled via a complex network support these claims (Arenas et al., 2008). Moreover, since its early days, network theory has focussed on quantifying the local centrality and vulnerability of subsystems with respect to the overall complex interaction structure (Albert and Barabási, 2002; Newman, 2003; Boccaletti et al., 2006). It hence provides a well-developed theoretical basis for studying the impact of global syndromes like climate change on local and regional scales, or investigating the role of particular physical, chemical, or biological processes for the Earth system's functioning. All in all, the network macroscope as an advanced tool for data analysis can be considered complementary to the three macroscopic approaches for Earth system analysis described by Schellnhuber (1999): observation from space (*The "bird's-eye" principle*), computer simulations (*The digital-mimicry principle*), and experimental investigations using small-scale models (*The "Lilliput" principle*).

1.3. Tipping elements and tipping points

Directing network macroscopes to the study of potential *tipping elements* in the Earth system is of specific interest for this dissertation (Lenton et al., 2008). Tipping elements are subsystems that can alter their dynamics qualitatively and/or abruptly in response to small changes in a control variable like global mean surface air temperature after crossing a *tipping point* (in physics, tipping points are more commonly known as bifurcations or dynamical transitions). Passing tipping points could have drastic consequences (not only) for the anthroposphere, *e.g.*, the Indian summer monsoon could switch into an irregular state with a lower total precipitation after crossing a certain temperature threshold, while increased melting of the Greenland and West Antarctic ice shields after passing a different threshold is projected to contribute to an accelerated global sea-level rise. Both events are expected to have a potentially large impact on humankind, because a substantial fraction of the global population inhabits low-lying coastal regions that are vulnerable to flooding, as well as the area of influence of the Asian monsoon system, where agriculture is dependent on monsoonal precipitation.

Now tipping elements are not independent from each other. On the contrary, complex interactions between tipping elements are known to exist, but the scientific understanding of these couplings is still in a nascent stage. Illustrative examples are the coupling between the Indian summer monsoon and the El Niño-Southern Oscillation (ENSO) (Maraun and Kurths, 2005; Krishna Kumar et al., 2006), or the interactions of deep water formation as well as other oceanographic processes with

large continental ice sheets (Stouffer et al., 2006; Nicholls et al., 2009; Straneo et al., 2010; Rignot et al., 2010).

1.4. Contents and arrangement of this thesis

The present dissertation is divided into two parts focussing on theoretical aspects (Part I) and applications thereof (Part II). After embarking on the project of applying network-theoretic concepts to Earth system analysis, it quickly became apparent that the existing tools of complex network theory and time series analysis were not sufficient to address the questions at hand. This insight lead to the development of new theoretical tools that are introduced and explained in Part I of the thesis.

On the network side, firstly, Chapter 2 starts with briefly presenting the basic elements of network theory. Secondly, the tools and measures needed to quantitatively analyze and model the complex topology of interacting networks or networks of networks are described which appear naturally when studying interdependencies between different subdomains of the Earth system. Thirdly, in many cases of interest for employing the network macroscope, subsystems or vertices within the network may be of differing size or importance, *e.g.*, they might represent differently sized regions on the planetary surface. To consistently account for this effect, vertex-weighted versions of statistical measures for standard and interacting networks based on the concept of *node splitting invariance* are introduced (see also Appendix A).

On the time series side, Chapter 3 first reviews the literature on various concepts of network-based time series analysis developed for constructing networks from multivariate time series and subsequently extracting information on the underlying dynamics from the inferred network structure (see also Appendix B). Subsequently, *recurrence networks* are introduced as a flexible method for time series analysis that is well-founded in classical mechanics and dynamical systems theory by exploiting the recurrence of states in phase space (Poincaré, 1890; Marwan et al., 2007), as well as applicable to relatively short, real-world time series such as typical geoscientific observational data (see also Appendix C). It is shown that recurrence networks can be employed to distinguish qualitatively different dynamics (*e.g.*, periodic or chaotic), trace unstable periodic orbits, or define new notions of (fractal) dimensionality of general sets like strange attractors based on transitivity in the recurrence structure (see also Appendix D). Finally, moving from single, but possibly multivariate time series to *fields* of time series data, functional networks are discussed as a general tool for mapping and investigating the statistical interdependency structure between the components of spatially extended dynamical systems like the Earth's climate. Adhering the topical setting of this thesis, special focus is put on providing a sweeping overview of the emerging field of *climate network analysis* and pointing out links to research on functional networks in other fields such as neuroscience and quantitative finance.

Chapter 4 integrates the two preceding ones by developing an analytical framework for describing networks embedded in a general space, be it physical (*e.g.*, climate

networks) or phase space (*e.g.*, recurrence networks), and applying it to various paradigmatic model systems.

The second half of this dissertation, Part II, is devoted to presenting applications of the above developed methods for inspecting the inner workings of the Earth's planetary machinery in the spirit of data analysis. Clearly, the selection of analytical techniques from the rich toolbox accessible to the researcher has to be guided by the structure of the available data as well as the research questions at hand. Paleoclimate records from geological archives as diverse as ice cores from the continental ice sheets of Antarctica and Greenland, speleothems growing in caves, or marine sediments sampled from the sea floor contain information on past climate and environmental variability that is of paramount importance for understanding Earth system dynamics (Bradley, 1999). In particular, they are indispensable sources of data needed for identifying tipping elements and uncovering the underlying mechanisms as well as their mutual interrelationships (Lenton et al., 2008).

In Chapter 5, it is shown that recurrence network analysis is well-suited for detecting nonlinear dynamical transitions, a specific class of tipping points, in short paleoclimate time series with problematic properties such as irregular sampling and dating uncertainties. The method is validated drawing on nonstationary time series generated by prototypical model systems with time-varying parameters and its robustness is tested for model systems and measured paleoclimate records. Building on these results, Chapter 6 sets out to address a long standing challenge going back to Darwin (1859): the potential effect of climatic change (geosphere) on evolutionary processes (biosphere), specifically concerning the development of human ancestors. Applying recurrence network analysis to marine records of African paleoclimate-variability during the Plio-Pleistocene reveals large-scale dynamical transitions (potential tipping points) that are put into context with known climatological and tectonic processes acting during that epoch. Relating the timing of these transitions to events in human evolution documented in the known fossil record suggests that the observed shifts between more regular and more erratic environmental variability may have acted as a trigger for rapid change in the development of humankind in Africa (see also Appendix E).

In contrast to paleoclimatology, where the accessible records are sparsely scattered in time and space, with the advent of global measurement networks and satellite observations, the amount, quality, and resolution of available climatological data has vastly increased during the 20th century and continues to rise until today. In Chapter 7, *coupled climate networks* are proposed as a further development of the network macroscope for harnessing and making sense of this wealth of available data. Combining functional network analysis and the newly introduced interacting networks framework, this approach is specifically designed for exploring the statistical interdependency structure between data sets originating from distinct components of the Earth system, *e.g.*, observables like atmospheric sea level pressure and oceanic sea surface temperature. As a first application of coupled climate network analysis, a study of the atmosphere's three-dimensional general circulation structure based on geopotential height data is presented.

Finally, Chapter 8 concludes this dissertation by recapitulating the achievements attained and sketching promising avenues for future research.

Part I.

Theoretical foundations

This first part of the thesis offers an introduction to basic concepts of complex network theory and network-based time series analysis. Furthermore, this dissertation's novel theoretical contributions to both fields are reported. Regarding complex network theory, these include consistent frameworks for analyzing general networks of interacting networks and networks with vertices of heterogeneous weights, size, or importance, as well as an analytical theory for describing the structure of spatial networks. Recurrence network analysis is put forward as a conceptually simple, but versatile, technique of nonlinear time series analysis that is well-founded in classical mechanics, as well as in dynamical systems and graph theory.

Chapter 2.

Complex network theory

2.1. Introduction

Networks are recognized as a structurally simple, yet powerful representation of the manifold complex systems consisting of large numbers of intricately interacting elements found in nature, technology and human society. Examples from these realms include food webs and genetic regulatory networks in biology, the internet and logistic networks in engineering, or online social networks in sociology (Albert and Barabási, 2002; Newman, 2003; Boccaletti et al., 2006). These, like most other real-world networks, have a complex structure that is neither regular nor fully random (Fig. 2.1).

Disorder
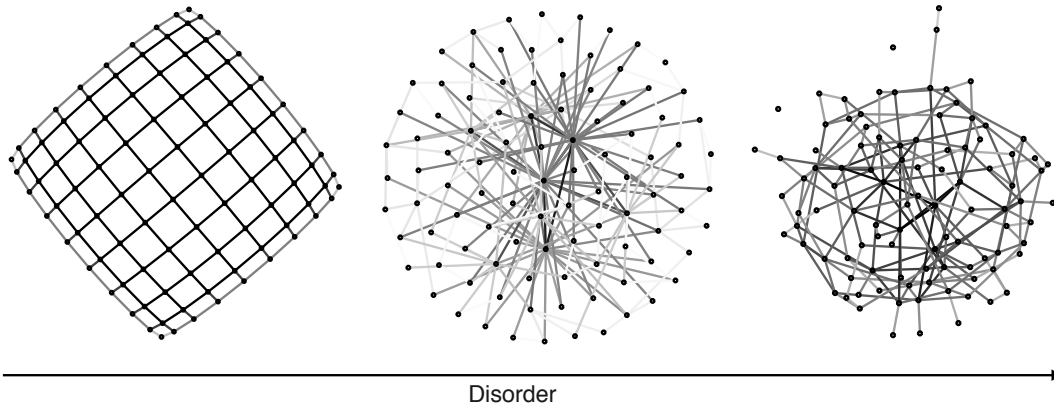
Figure 2.1.: A traverse through network space towards increasing randomness starting from a regular lattice and heading to a fully random Erdős-Rényi graph (Erdős and Rényi, 1959; Erdős and Rényi, 1960). Complex networks like the Barabási-Albert scale-free network (Barabási and Albert, 1999) in the center are encountered between both extremes. All three networks are simple graphs of $N = 100$ vertices and edge density $\rho \approx 4\%$ (note that there exist more than 10^{332} distinct networks of this kind)[1]. Vertex shading encodes degree k_v (white: small, black: large).

---

[1]There are $\left(\binom{N}{2} \atop L \right)$ distinct labeled simple graphs with N vertices and L edges.
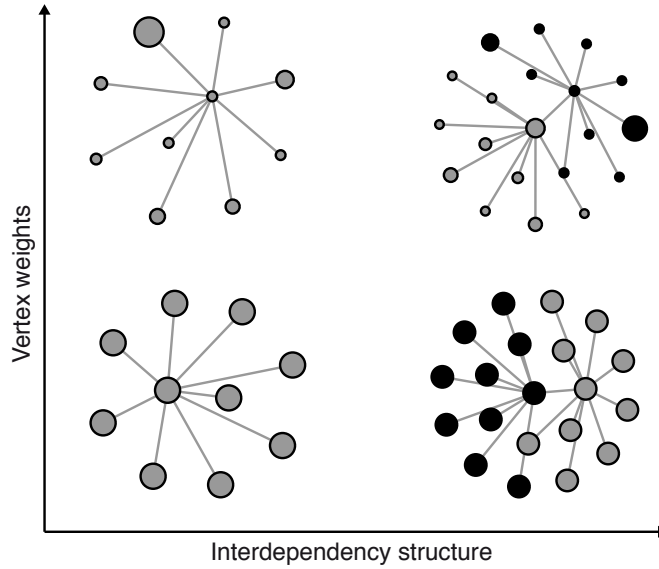
Figure 2.2.: Interdependency (or interaction) structure and vertex weights are both important properties of complex networks. Novel measures are developed in Sections 2.4, 2.5, and Appendix A to incorporate this information consistently into the statistical analysis complimenting and generalizing standard quantifiers for unweighted networks without interdependency structure (lower left quadrant). Vertex size encodes scalar weight, vertex shading distinguishes subnetworks (interdependency structure).

Drawing on ideas from mathematical graph theory, statistical physics, and other fields complex network theory allows a detailed and quantitative investigation of the topology and evolution of interlinked systems (Costa et al., 2007) as well as exploring the interplay between network structure and dynamics on the interacting elements (Arenas et al., 2008). The fundamental idea behind this theory is to discover what aspects of the observed complex behavior of real-world networked systems can be explained by focussing on their interaction structure and neglecting most other details like different types of interrelationships between or dynamics on the subcomponents. It is important to clearly distinguish between systems with a physically evident network structure like power grids or neural networks (*structural networks*) and those networks representing more abstract relationships between objects, *e.g.*, citation networks or *functional networks* constructed from electroencephalogram or climate data (see the discussion in Chapter 7). Because this work focusses on network-based data analysis, *i.e.*, on studying networks constructed from data, we will solely study networks of the latter kind throughout this thesis. For a broad overview of the state of the art in complex network theory and its applications, we direct the interested reader to the abundant literature on the topic, *e.g.*, Kolaczyk (2009); Newman (2010); Cohen and Havlin (2010).

After introducing the necessary concepts from graph theory (Section 2.2) and those needed for understanding spatially embedded networks (Section 2.3), the newly

developed methods and measures for investigating networks with interdependency structure (Section 2.4) and vertex weights (Section 2.5) are presented (Fig. 2.2).

2.2. Elements of graph theory

This section introduces the essential graph-theoretical vocabulary that will be relied on throughout this thesis, partly following Donges (2009). For a thorough treatment of the mathematical theory of (di)graphs see, *e.g.*, Bang-Jensen and Gutin (2009).

Definition 2.1 (Graph / Network). *An* undirected *graph is defined as an ordered pair $G := (V, E)$ containing a set $V = \{1, ..., N\}$ of vertices or nodes together with a set $E \subseteq V \times V$ of edges or links $\{i, j\}$ with $i, j \in V$ which are 2-element subsets of V. $N = |V|$ denotes the size (number of vertices) of G, $L = |E|$ the number of edges. The following types of graphs are considered (see also Fig. 2.2):*

(i) *In a* simple *graph, at most one edge $\{i, j\} \in E$ can exist between a pair of vertices and self-loops of the type $\{i, i\}$ are not allowed (all graphs treated in this thesis are simple). A simple graph is called* dense *if L is close to the maximum number of edges $L_{max} = \binom{N}{2}$. It is called* sparse *if $L \ll L_{max}$.*

(ii) *A* finite *graph has a finite number of vertices N.*

(iii) *An* infinite *graph carries a countably or uncountably infinite number of vertices N (Chapter 4 studies graphs of the latter kind).*

(iv) *The vertices of a* spatially embedded *graph are placed in some general metric space, inducing the notion of* length *of edges (see Section 2.3).*

(v) *A graph can be said to have* interdependency structure *if some decomposition into interconnected subgraphs is of particular interest for the investigator (see Section 2.4).*

(vi) *A* vertex-weighted *graph consists of vertices that carry a scalar weight encoding, e.g., vertex size, importance, or represented area in a domain of interest (see Section 2.5).*

We do, in this thesis, neither explicitly consider directed networks, or digraphs nor edge-weighted networks. However, possible generalizations of the discussed concepts incorporating this additional structure are pointed out wherever appropriate. In the following, hierarchically structured systems that can be viewed as networks of interacting (sub)networks will be of particular interest.

Definition 2.2 (Subgraph / Subnetwork). *A* subgraph *$G' := (V', E')$ of a graph $G = (V, E)$ contains a vertex set $V' \subseteq V$ and an edge set $E' \subseteq E$, where $\forall \{i, j\} \in E' : i, j \in V'$. A subgraph G' of a graph G is said to be* induced *if, for any pair of vertices $i, j \in V'$, $\{i, j\} \in E'$ if and only if $\{i, j\} \in E$.*

For performing calculations on a simple graph, it can be represented by an *adjacency matrix*. However, this type of representation is computationally feasible only for relatively small graphs, mostly because the memory needed to store the dense adjacency matrix on a computer grows as N^2. Therefore, while the matrix representation is primarily used for formal purposes in this work, most calculations rely on sparse adjacency list or edge list representations (see Bang-Jensen and Gutin (2009) and Appendix F).

Definition 2.3 (Adjacency matrix). *A simple (directed) graph $G = (V, E)$ without edge-weights can be represented by a binary* adjacency matrix $\boldsymbol{A} = \{A_{ij}\}_{ij}$ *with elements*

$$A_{ij} = \begin{cases} 1 & \text{if } \{i, j\} \in E, \\ 0 & \text{otherwise,} \end{cases} \tag{2.1}$$

where $i, j \in V$. For an undirected graph, $\boldsymbol{A}$ is symmetric.

Definition 2.4 (Neighborhood). *In a simple undirected graph $G = (V, E)$, the neighborhood $\mathcal{N}_i$ of a vertex $i \in V$ is defined as the set of vertices that are directly adjacent to i, i.e.,*

$$\mathcal{N}_i = \{j \in V : A_{ij} = 1\}. \tag{2.2}$$

For networks with an uncountably infinite number of vertices, we can loosely think of the adjacency matrix as a mapping $A : \mathbb{R} \times \mathbb{R} \to \{0, 1\}$ if $|V| \leq |\mathbb{R}|$.

In many applications, the potential movement of some entities on a network, *e.g.*, information packets in the internet, as well as higher-order connectivity properties, *e.g.*, for identifying community structure or critical elements like bottlenecks, are of major interest. This directly leads to the graph-theoretical notions of *walk, path, cycle*, and *component*.

Definition 2.5 (Walk). *A* walk *on the graph $G = (V, E)$ is an alternating sequence of vertices and edges that starts and ends with a vertex. The vertices that precede and follow an edge in the sequence are the end vertices of that edge. A walk is called*

(i) open *if its start and end vertices are different,*

(ii) closed *if its start and end vertices are identical,*

(iii) simple *if no vertex except of start and end vertices (and therefore no edge) is visited more than once.*

Definition 2.6 (Path). *A path $\pi(i, j)$ is a simple walk on the graph $G = (V, E)$ from start vertex $i \in V$ to end vertex $j \in V$. i is said to be* reachable *from j if a path containing both vertices exists on G. The length of the path $|\pi(i, j)|$ is defined as the number of edges the path contains. We denote the set of all existing different paths from i to j by $\mathcal{P}(i, j)$. The* shortest-path length *from i to j is then given by $d_{ij} = \min_{\pi(i,j) \in \mathcal{P}(i,j)} |\pi(i, j)|$, where $d_{ii} = 0$ and $d_{ij} = \infty$ if $\mathcal{P}(i, j) = \emptyset$.*

In this work, we generally use Dijkstra's algorithm to calculate the topological distance matrix d_{ij} (Dijkstra, 1959).

Definition 2.7 (Cycle). *A cycle is a simple and closed walk on a graph G.*

Definition 2.8 (Component). *A component is a maximally connected subgraph $G' := (V', E')$ of a graph $G = (V, E)$. That is, all vertices in V' are reachable from all other vertices in V' and no vertex $i \in V \backslash V'$ is reachable from any vertex $j \in V'$. The largest component of G with size $N' \approx N$ is referred to as the* giant component.

The standard measures of complex network theory such as degree, closeness, and shortest-path betweenness centralities (Newman, 2003) will be defined where they are needed throughout the remainder of this thesis.

2.3. Spatially embedded networks

Many networks of interest map the interrelationships between objects (vertices) residing in some metric space, be it abstract like the phase space of dynamical systems (Section 3.2) or physical space like the Earth's surface (Section 3.3). Hence, a *spatially embedded* or *spatial* network $G = (V, E)$ carries a mapping $V \to S : i \mapsto x_i$ assigning each vertex $i \in V$ to an element $x_i \in S$ of a set S and a metric $l : S \times S \to \mathbb{R} : (x_i, x_j) \mapsto l_{ij}$. x_i is called the coordinate vector of a vertex i and l_{ij} can be used as a measure of edge length whenever $\{i, j\} \in E$.

The vertices' spatial embedding can impose considerable constraints on network structure (Boccaletti et al., 2006; Bullock et al., 2010; Barthélemy, 2011) that in real-world systems manifest themselves as increasing costs or decreasing probability of edge establishment with increasing edge length and other, more subtle effects (Gastner and Newman, 2006). To first-order, the spatial structure of a complex network is captured by the *edge length distribution $p(l)$*, a probability density function (PDF), where $\int_{l-\Delta l}^{l+\Delta l} dl\, p(l)$ is the probability that an edge $\{i, j\}$ randomly chosen from E has a length $l - \Delta l \leq l_{ij} \leq l + \Delta l$. For example, in random geometric graphs only vertices that are within a certain distance from each other in S are linked (Penrose, 2003), leading to a rectangularly shaped edge length distribution $p(l) \propto \Theta(\varepsilon - l)$, where ε is a threshold distance and $\Theta(\cdot)$ denotes the Heaviside function (see Chapter 4). Other spatial networks possess a monotonously decaying $p(l)$, *e.g.*, an exponential decay $p(l) \propto \exp(l/l')$ with a typical scale l' (see Fig. 2.3 for some typical edge length distributions).

It is important to conceptually distinguish a system's *intrinsic* edge length distribution $p_I(l)$ that is exclusively determined by the internal laws governing its formation and evolution (Fig. 2.3), *e.g.*, a tendency to form edges of a particular length l, from geometric effects originating from the particular distribution of vertices in S, the global topology of S, and the influence of boundaries. The latter effects are summarized by the *geometric* edge length distribution $p_g(l)$, the PDF comprising the distances of *all possible* pairs of vertices ($p_g(l) = p(l)$ holds for fully connected networks). In other words, $p_I(l)$ gives the probability that an edge of length l is formed
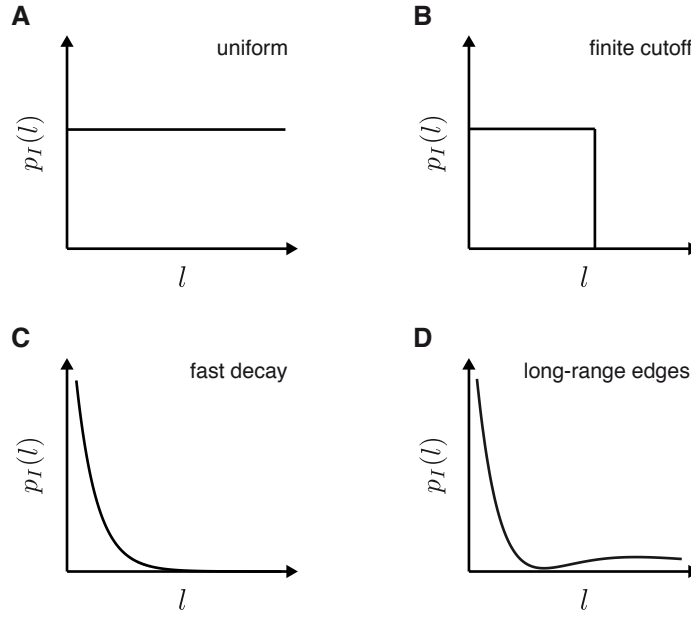
Figure 2.3.: Idealized intrinsic edge length distributions $p_I(l)$ of typical spatial networks: (A) uniform distribution pointing at a network structure that is independent from the spatial embedding, (B) distribution with a finite cutoff as in random geometric graphs and recurrence networks (Section 3.2), (C) distribution quickly decaying with l as in road networks (Gastner and Newman, 2006; Chan et al., 2011), and (D) distribution including numerous long-range edges as observed in the internet (Gastner and Newman, 2006) or climate networks (Section 3.3).

by the underlying networked system irrespective of the geometrical arrangement of vertices (tendency of edge formation), while $p_g(l)$ is the probability that an edge of length l occurs only due to the specific spatial embedding of vertices (possibility of edge formation). As a first-order approximation, assuming that system-intrinsic and geometric factors are statistically independent, one can assume that

$$p(l) = p_I(l)p_g(l). \tag{2.3}$$

By inversion, this relation can be used to correct for geometric effects when the interest is in a system's intrinsic edge length distribution $p_I(l)$, but usually only $p(l)$ and $p_g(l)$ can be observed. For example, assuming a uniform and continuous distribution of vertices on the surface of a 2-sphere with radius r yields

$$p_g(l) = \frac{1}{2r} \sin\left(\frac{l}{r}\right), \tag{2.4}$$

which is a useful correction factor when studying global networks embedded on the Earth's surface such as climate networks (Donges, 2009) (see also Section 3.3.2). An analytical framework for assessing the effects of prescribed edge length distributions on certain structural properties of spatial networks is presented in Chapter 4.
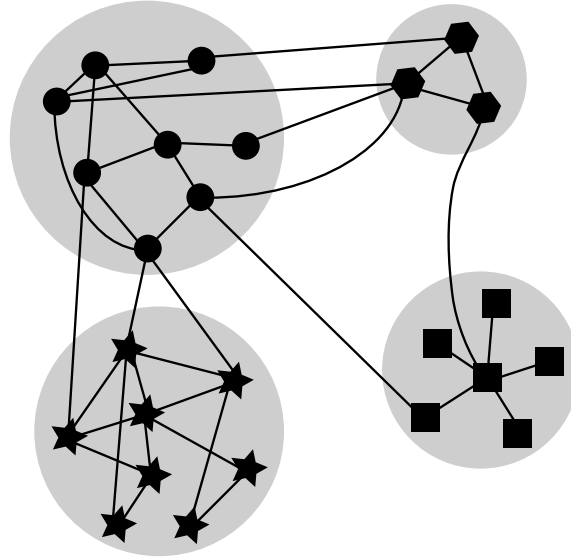
Figure 2.4.: Systems of interacting and interdependent networks or networks of networks are a natural representation of many systems found in nature, technology, and society. The partition into interacting subnetworks (indicated by vertex symbols of different shape) is either naturally induced by the considered problem, *e.g.*, consider interdependent infrastructures (Buldyrev et al., 2010) or cortical areas of the mammalian brain (Zhou et al., 2006), or may be generated by a community detection algorithm (Fortunato, 2010). Such a system is characterized by dependencies within subnetworks (internal edges, solid lines) as well as interactions between different subnetworks (cross edges, dashed lines).

2.4. Networks of interacting and interdependent networks

Most studies have so far concentrated on *isolated networks*, where vertices represent single elements or subsystems, and edges indicate interactions or relationships between vertices. However, it has recently been realized that a considerably large class of systems of interest warrants a more natural representation as *networks of interacting and interdependent networks* for an appropriate description of their structure and dynamics (Fig. 2.4).[2] Notable examples are representations of the mammalian cortex, where cortical areas form complex subnetworks that are themselves linked via a complex network topology (Zhou et al., 2006; Zhou et al., 2007), systems of interacting populations of heterogeneous oscillators (Barreto et al., 2008; So et al., 2008), or mutually interdependent infrastructure networks (Vespignani, 2010; Parshani et al., 2010) such as the power grid and electricity consuming communication

---

[2]In the following, we will use the terms *interacting* and *interdependent* interchangeably in the context of studying networks of networks. This choice is legitimate, since we focus on characterizing the complex coupling structure of these systems, but not their dynamical evolution (Gao et al., 2011a).

networks (Buldyrev et al., 2010). More generally, and particularly if the system's representation as a network of interacting networks is a less obvious choice than in the aforementioned examples, networks with a pronounced community structure may also be viewed as networks of networks, where subnetworks are constituted by communities or clusters as identified by some community detection algorithm (Fortunato, 2010). A related but distinct concept is presented by layered networks (Kurant and Thiran, 2006b; Kurant and Thiran, 2006a; Kurant et al., 2007), where essentially different sets of edges (layers) are considered connecting the same substrate of vertices, *e.g.*, describing a two-layered transportation network with roads forming a layer of physical connections between locations and a superposed layer of virtual connections induced by actual pathways of traffic flow on the physical layer. In Chapter 7, we will investigate networks of networks in the wider context of Earth system analysis by means of coupled climate network analysis.

So far research on interacting and interdependent networks has focussed on global properties and dynamics of these systems, *e.g.*, percolation thresholds and cascading failures, showing that networks of interdependent networks are much more vulnerable to cascading failures than isolated networks are (Buldyrev et al., 2010; Parshani et al., 2010; Parshani et al., 2011; Shao et al., 2011; Buldyrev et al., 2011; Bashan et al., 2011; Gao et al., 2011b). A review of recent work on the global structural characteristics of networks of interdependent random networks is given by Gao et al. (2011a). However, real-world networks of networks usually possess a well-organized, non-random interaction/interdependency structure (Parshani et al., 2010). It is hence of major interest to determine in detail the importance and role of single vertices for the interaction or communication between different subnetworks as well as to characterize their mutual interaction topology, *e.g.*, for studying the vulnerability of coupled and interdependent networked systems to random perturbations or targeted attacks (Huang et al., 2011). Here, following Donges et al. (2011b, P14), we propose a general and novel framework that allows to quantitatively investigate the interaction structure of networks of networks on multiple topological scales. We derive graph-theoretical measures that allow to answer questions like: Does a vertex have a large direct influence on and/or is it an efficient transmitter of information to a specific subnetwork? Which amount of control does a vertex have on the interaction between two subnetworks? Are two subnetworks topologically well separated or tightly intertwined and is their interaction structure well organized or random? The methodology introduced in this section therefore creates a new setting for a detailed graph-theoretical assessment of the functional roles of vertices within complex networks of networks, *e.g.*, integration or segregation of information that have been studied in corticocortical networks of cats or macaque monkeys (Zamora-López et al., 2009; Zamora-López et al., 2010).

2.4.1. Basic definitions

Consider a network $G = (V, E)$. As we wish to study a network of K interacting subnetworks, we consider a complete decomposition of the vertex set V into disjoint

sets $\{V_i\}_{i=1}^K$ such that $\bigcup_{i=1}^K V_i = V$ and $V_i \cap V_j = \emptyset \;\forall i \neq j$, where the number of vertices in subset V_i is $N_i = |V_i|$. Similarly, the edge set E is decomposed into sets E_{ii} containing edges between vertices inside V_i and sets E_{ij} of edges connecting vertices from V_i and V_j, *i.e.*, $\bigcup_{i,j=1}^K E_{ij} = E$ with $E_{ij} \cap E_{kl} = \emptyset \;\forall (i,j) \neq (k,l)$. In other words, the mutual interactions between subnetworks $G_i = (V_i, E_{ii})$ (G_i is the induced subgraph of V_i) are described by the edge sets E_{ij} for $i \neq j$. For simplicity, we restrict ourselves to undirected and unweighted simple graphs represented by a symmetric adjacency matrix $\mathbf{A}$, since the generalization of the concepts and measures introduced below is straightforward. In this section, indices i, j, k, l always denote subnetworks while v, w, p, q designate single vertices.

2.4.2. Measures for studying networks of networks

In the following we define several local as well as global network measures to quantify and investigate the interaction structure of networks of networks on different topological scales. Here, local network measures assign a real number to a vertex $v \in V_i$ in relation to (a generally different) subnetwork G_j, or to any other vertex $w \in V$ depending on two subnetworks G_i, G_j. They are inspired by the "trinity" of classical and frequently used centrality measures degree, closeness, and betweenness (Freeman, 1979; Newman, 2003; Boccaletti et al., 2006), as well as the local clustering coefficient (Watts and Strogatz, 1998), and accordingly quantify direct influence on G_j (cross-degree, Eq. (2.5)), local organization of interdependency with G_j (local cross-clustering, Eq. (2.8)), effectiveness of interaction with G_j (cross-closeness, Eq. (2.12)), and the control over communication between G_i and G_j (cross-betweenness, Eq. (2.15)), respectively. The global network measures we introduce assign a real number to a pair of subnetworks (G_i, G_j). They are derived from the well-established measures edge density, global clustering coefficient, transitivity, and average path length (Watts and Strogatz, 1998). These global network measures quantify various overall aspects of the interaction between two subnetworks such as its degree of organization (global cross-clustering coefficient and cross-transitivity, Eqs. (2.19), (2.20)), effectiveness and speed of information exchange (cross-average path length, Eq. (2.21)), or their mutual interconnectivity (cross-edge density, Eq. (2.18)).

In the following definitions, we always assume $v \in V_i$ if not indicated otherwise. The term *cross* generally relates to the interaction between subnetworks G_i, G_j, whereas *internal* refers to the structure within a single subnetwork. Furthermore, it should be noted that the formulae given below explicitly account for the general case $i \neq j$. In some cases, *e.g.*, for the cross-edge density, normalization factors need to be modified to suit the special case $i = j$.
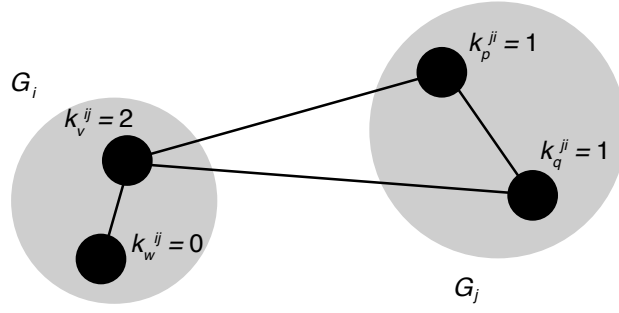
Figure 2.5.: The cross-degree k_v^{ij} counts the number of neighbors of vertex $v \in V_i$ within subnetwork G_j. In this example, the cross-edge density is given by $\rho_{ij} = 0.5$.

Local measures

Cross-degree k_v^{ij} gives the number of neighbors of the vertex $v \in V_i$ within subnetwork G_j (Fig. 2.5),

$$k_v^{ij} = k_v^j = \sum_{q \in V_j} A_{vq}. \tag{2.5}$$

This measure thus captures the importance of v for the interaction or communication between two subnetworks G_i, G_j in terms of the number of direct connections it projects between G_i and G_j. For brevity, we will in the following suppress the somewhat redundant index i whenever possible, *e.g.*, write k_v^j instead of k_v^{ij}. The standard *degree* k_v considering the full network G can be obtained by summing up the contributions from all subnetworks:

$$k_v = \sum_{j=1}^{K} k_v^j \tag{2.6}$$

$$= \sum_{p \in V} A_{vp}. \tag{2.7}$$

Parshani et al. (2010) introduce the *inter degree-degree correlation* r^{ij} measuring the correlation between the internal degrees k_p^{ii}, k_q^{jj} of vertices at the ends of all cross-edges $\{p, q\} \in E_{ij}$.

Local cross-clustering coefficient $\mathcal{C}_v^{ij}$ is the probability that two randomly drawn neighbors of v from subnetwork G_j are also neighbors (Fig. 2.6),

$$\mathcal{C}_v^{ij} = \mathcal{C}_v^j = \frac{1}{k_v^j(k_v^j - 1)} \sum_{p,q \in V_j} A_{vp} A_{pq} A_{qv}. \tag{2.8}$$
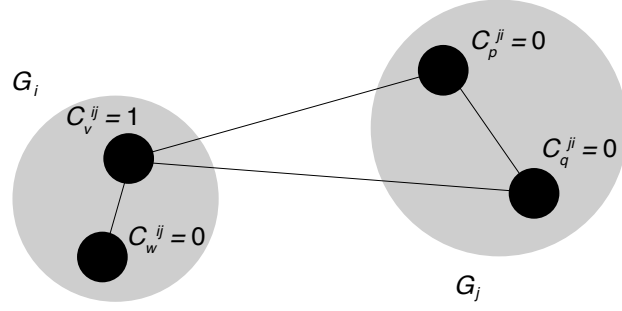
Figure 2.6.: The local cross-clustering coefficient $\mathcal{C}_v^{ij}$ is the probability that two randomly drawn neighbors of vertex v from subnetwork G_j are neighbors themselves, where v belongs to subnetwork G_i. In this example, the global cross-clustering coefficients are given by $\mathcal{C}_{ij} = 0.5$ and $\mathcal{C}_{ji} = 0$. However, for the cross-transitivities one obtains $\mathcal{T}_{ij} = 1$ and $\mathcal{T}_{ji} = 0$. Note that already in this simple example, the interaction structure of G_i and G_j is asymmetric, *i.e.*, $\mathcal{C}_{ij} \neq \mathcal{C}_{ji}$ and $\mathcal{T}_{ij} \neq \mathcal{T}_{ji}$.

For all vertices v^* with $k_{v^*}^j \in \{0, 1\}$ we set $\mathcal{C}_{v^*}^j = 0$ consistently with Newman (2003) (alternatively one could leave $\mathcal{C}_{v^*}^{ij}$ undefined). $\mathcal{C}_v^j$ quantifies the tendency of vertices to form clusters spanning two subnetworks and therefore contains important information on the interaction structure between them.

Assuming no correlations between the occurrence of edges within G_j and between G_i and G_j (described by the sets E_{jj} and E_{ij}, respectively) the expectation value for $\mathcal{C}_v^j$ is the *internal edge density* of subnetwork G_j, *i.e.*, $\mathbb{E}(\mathcal{C}_v^j) = \rho_j \; \forall v$, where

$$\rho_j = 2|E_{jj}|/(N_j(N_j - 1)). \tag{2.9}$$

This lack of correlations would arise if edges in E_{ij} were distributed randomly and independently between subnetworks V_i and V_j. Hence, $\mathcal{C}_v^j \gg \rho_j$ ($\mathcal{C}_v^j \ll \rho_j$) hints at significant correlations (anti-correlations) in the connectivity between both subnetworks that may be related to design principles or details of growth processes depending on the specific application (*e.g.*, see Section 7.5). On the contrary, as it is always the case for statistical hypothesis tests, $\mathcal{C}_v^j \approx \rho_j$ for all $v \in V_i$ does *not* imply a random directional interdependency structure between G_i and G_j, because a null hypothesis such as that of random interdependency structure can never be confirmed, but only rejected (see also Section 2.4.3).

Compared to the other local measures introduced in this section, $\mathcal{C}_v^j$ has a less direct relationship with the standard *local clustering coefficient* $\mathcal{C}_v$ (Newman, 2003), since the contributions from triangles containing vertices from three different subnetworks as well as those from triangles with two vertices in G_i and one vertex in a different

subnetwork also have to be taken into account (second summand in Eq. (2.10)),

$$\mathcal{C}_v = \frac{1}{k_v(k_v - 1)} \left(\sum_{j=1}^{K} k_v^j(k_v^j - 1)\mathcal{C}_v^j + \sum_{\substack{l=1 \\ l \neq i}}^{K} \sum_{\substack{k=1 \\ k \neq l}}^{K} \sum_{\substack{p \in V_k \\ q \in V_l}} A_{vp} A_{pq} A_{qv} \right) \tag{2.10}$$

$$= \frac{1}{k_v(k_v - 1)} \sum_{p,q \in V} A_{vp} A_{pq} A_{qv}, \tag{2.11}$$

where again this holds only if $k_v > 1$. Note that $\mathcal{C}_v^{ij}$ is conceptually related, but not equivalent to the measure *inter-clustering coefficient* proposed by Parshani et al. (2010).

Cross-closeness centrality c_v^{ij} measures the topological closeness of v to subnetwork G_j along shortest paths,

$$c_v^{ij} = c_v^j = \frac{N_j}{\sum_{q \in V_j} d_{vq}}, \tag{2.12}$$

where d_{vq} is the shortest-path length between vertices v and q. If no path exists, *i.e.*, the vertices are not mutually reachable, $d_{vq} = N$ is set as an upper bound consistently with the literature (Kolaczyk, 2009), since the longest possible path length in the considered network is $N - 1$. Alternatively, to avoid $c_v^j = 0$ for all v in disconnected networks with $d_{vq} = \infty$ for at least one pair (v, q), closeness can be computed separately for each component of G. It is important to note that for generality, we do not restrict paths to subnetworks G_i, G_j or a particular order of vertices as in earlier works (Flom et al., 2004), which might however be appropriate depending on the specific application. In contrast, the shortest paths analyzed here and below may contain any vertices $w \in V$ in any order depending on the topology of the full graph G.

Cross-closeness therefore quantifies the effectiveness of interaction between a particular vertex and a specific subnetwork taking the entire network structure into account. A vertex with high cross-closeness is likely to be important for the fast exchange of information with a certain subnetwork, even if it does not have a large number of direct neighbors in that subnetwork or a high closeness centrality with respect to the whole network. The standard *closeness centrality* c_v (Freeman, 1979) can be obtained from the c_v^j as

$$c_v = \frac{N - 1}{\sum_{j=1}^{K} N_j \left(c_v^j \right)^{-1}} \tag{2.13}$$

$$= \frac{N - 1}{\sum_{p \in V} d_{vp}}. \tag{2.14}$$
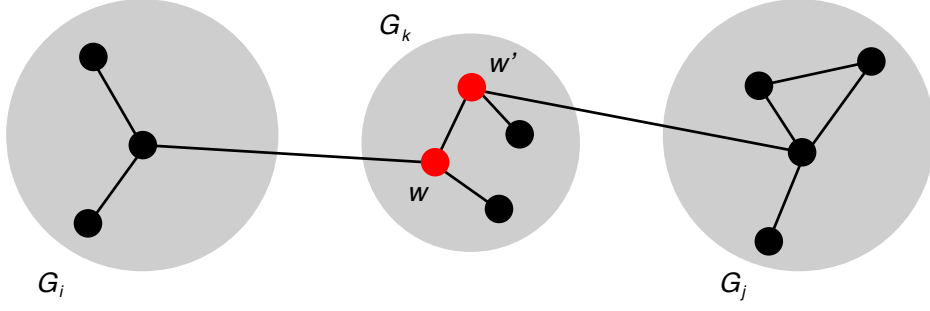
Figure 2.7.: The shortest-path cross-betweenness centrality b_w^{ij} measures the importance of a vertex $w \in V$ for mediating or controlling interactions or communication on shortest paths between two subnetworks G_i and G_j. In this example, vertices $w, w' \in V_k$ (red) have a large cross-betweenness b_w^{ij}, $b_{w'}^{ij}$, while the remaining vertices in G_k, $p \in V_k \setminus \{w, w'\}$, do not participate in shortest paths between G_i and G_j. Hence, they have a vanishing cross-betweenness $b_p^{ij} = 0$.

Cross-betweenness centrality   For any vertex $w \in V$, shortest-path cross-betweenness centrality b_w^{ij} indicates its role for mediating or controlling interactions or communication on shortest paths between two subnetworks G_i and G_j (Fig. 2.7),

$$b_w^{ij} = \sum_{\substack{p \in V_i, q \in V_j \\ p \neq q; p, q \neq w}} \frac{\sigma_{pq}(w)}{\sigma_{pq}} = b_w^{ji}, \tag{2.15}$$

where σ_{pq} gives the total number of shortest paths from p to q and $\sigma_{pq}(w)$ counts the number of shortest paths between p and q that include w (Freeman, 1979; Brandes, 2008). While a vertex with high cross-degree (*relational hub*) may function as a robust transmitter between two subnetworks, its functional redundancy for communication is evaluated by cross-betweenness centrality. *E.g.*, a network containing relational hubs with high cross-betweenness is more vulnerable to attack or failure with respect to the interaction of two subnetworks than another one with overall lower cross-betweenness and, hence, a higher redundancy of the interaction structure. The standard *betweenness centrality* b_w (Freeman, 1979) of the full network is obtained by summing up the contributions from all pairs of subnetworks,

$$b_w = \sum_{i,j=1}^{K} b_w^{ij} \tag{2.16}$$

$$= \sum_{\substack{p, q \in V \\ p \neq q; p, q \neq w}} \frac{\sigma_{pq}(w)}{\sigma_{pq}}. \tag{2.17}$$

In this sense, cross-betweenness centrality can be seen as a decomposition of the standard betweenness centrality with respect to a certain partition of the full network. Cross-betweenness is a generalization of the measure Q_2 defined by Flom et al. (2004) that is restricted to networks consisting of only two different sorts of vertices or two subnetworks in our terminology (Brandes, 2008).

Global measures

Cross-edge density ρ_{ij} measures the density of connections between distinct subnetworks G_i and G_j (Fig. 2.5),

$$\rho_{ij} = \frac{|E_{ij}|}{N_i N_j} = \frac{\langle k_v^j \rangle_{v \in V_i}}{N_j} = \rho_{ji}. \tag{2.18}$$

Two subnetworks can be considered to be well separated topologically if their internal edge densities ρ_i, ρ_j are clearly larger than their cross-edge density, *i.e.*, $\rho_{ij} \ll \rho_i, \rho_j$. More generally, subnetworks form communities of the full network (Fortunato, 2010) if this inequality holds for all pairs of subnetworks. In other words, in this situation the partition of the full network G induced by the subnetworks G_i would give rise to a high modularity (Newman and Girvan, 2004). It should be stressed, however that there exists a multitude of other definitions of communities (Fortunato, 2010). Our general framework does not require the chosen partition to be consistent with any such definition as long as it allows the resulting cross-network measures to be readily interpretable.

Global cross-clustering coefficient $\mathcal{C}_{ij}$ is the mean probability for vertices from subnetwork G_i to have mutually connected neighbors within subnetwork G_j,

$$\mathcal{C}_{ij} = \left\langle \mathcal{C}_v^{ij} \right\rangle_{v \in V_i} = \frac{1}{N_i} \sum_{v \in V_i, k_v^j > 1} \frac{\sum_{p,q \in V_j} A_{vp} A_{pq} A_{qv}}{\sum_{p \neq q \in V_j} A_{vp} A_{vq}}. \tag{2.19}$$

It is important to note that in contrast to cross-edge density and cross-average path length the cross-clustering coefficient is not a symmetric property of two subnetworks, *i.e.*, in general $\mathcal{C}_{ij} \neq \mathcal{C}_{ji}$ (Fig. 2.6). As was shown above, we expect $\mathbb{E}(\mathcal{C}_{ij}) = \rho_j$ if the interaction structure of subnetworks G_i and G_j is random, *i.e.*, cross edges are distributed randomly and independently between the two subnetworks. In contrast, $\mathcal{C}_{ij} \gg \rho_j$ or $\mathcal{C}_{ij} \ll \rho_j$ points to an organized interdependency structure.

Cross-transitivity $\mathcal{T}_{ij}$ is the probability that two vertices in subnetwork G_j are connected if they have a common neighbor in subnetwork G_i,

$$\mathcal{T}_{ij} = \frac{\sum_{v \in V_i; p,q \in V_j} A_{vp} A_{pq} A_{qv}}{\sum_{v \in V_i; p \neq q \in V_j} A_{vp} A_{vq}}. \tag{2.20}$$

Here, $\mathcal{T}_{ij} \neq \mathcal{T}_{ji}$ holds in general as well (Fig. 2.6). Like the global cross-clustering coefficient $\mathcal{C}_{ij}$, $\mathcal{T}_{ij}$ is a measure of the degree of organization of the subnetworks' topological interdependence. Analogous to the standard version of transitivity (Newman, 2003), $\mathcal{T}_{ij}$ tends to weigh contributions of vertices in G_i with low cross-degree k_v^j less heavily than $\mathcal{C}_{ij}$. From another point of view, in the average of Eq. (2.20) edges have equal weights, while Eq. (2.19) has the same property with respect to vertices. This peculiarity has to be born in mind when interpreting the values of $\mathcal{T}_{ij}$ and $\mathcal{C}_{ij}$ for general complex networks of networks (Fig. 2.6). Given a fully random interconnectivity structure, the expectation value for cross-transitivity is $\mathbb{E}(\mathcal{T}_{ij}) = \rho_j$.

Cross-average path length $\mathcal{L}_{ij}$ measures the topological closeness of two subnetworks G_i and G_j,

$$\mathcal{L}_{ij} = \frac{1}{N_i N_j - M_{ij}} \sum_{v \in V_i, q \in V_j} d_{vq} = \mathcal{L}_{ji}, \tag{2.21}$$

where M_{ij} is the number of pairs $(v, q) \in (V_i \times V_j)$ which are not mutually reachable and we prescribe $d_{vq} = 0$ for these pairs. Hence, $\mathcal{L}_{ij}$ measures the average length of existing shortest paths between the subnetworks G_i and G_j. Alternatively, akin to the definition of cross-closeness centrality, $d_{vp} = N$ could set for disconnected pairs of vertices v, p, or the calculation of $\mathcal{L}_{ij}$ could be restricted to the giant component of G.

$\mathcal{L}_{ij}$ can be interpreted as a measure of the effectiveness of interaction between two subnetworks. Subnetworks with low $\mathcal{L}_{ij}$ are closely interwoven and are likely to show a high degree of functional interdependence, while those with high $\mathcal{L}_{ij}$ are topologically more separated and likely to be dynamically and functionally more independent from each other. If $M_{ij} = 0$, $\mathcal{L}_{ij}$ is related to the cross-closeness centralities c_v^{ij} via

$$\mathcal{L}_{ij} = \frac{1}{N_i} \sum_{v \in V_i} \left(c_v^{ij} \right)^{-1}. \tag{2.22}$$

Further measures

The selection of measures introduced above was chosen to be as concise as possible, while at the same time representing all classes of commonly used network quantifiers. Similar generalizations of other local and global network properties (like local random walk betweenness, or global efficiency among many others (Albert and Barabási, 2002; Newman, 2003; Boccaletti et al., 2006)), may be derived to quantify additional nuances of the topology of interacting networks. Adaptations for directed and edge- or vertex-weighted networks (Heitzig et al., 2012, P9) can also be deduced (Appendix A and Wiedermann (2011); Wiedermann et al. (2013, P1)). Similarly, it is possible on the basis of our proposed framework to design measures to take into account different qualities or functions of vertices and edges within or between subnetworks,

e.g., the additional constraint that the functioning of vertices $v \in V_i$ depends on the functioning of vertices $v' \in V_j$ studied by Buldyrev et al. (2010).

2.4.3. Surrogate models and significance tests for networks of networks

When analyzing empirical networks of networks using the newly introduced tools described in Section 2.4.2, it is of major importance to identify those nontrivial observed structural characteristics that cannot be explained by ensembles of random surrogate networks subject to some boundary conditions such as fixed edge density, fixed degree sequence, or fixed edge length distribution (Newman, 2003; Donges, 2009). Analogously to the method of surrogate data in time series analysis (Schreiber and Schmitz, 2000), the aim of this exercise in statistical hypothesis testing is usually to identify structures within the network that are unlikely to arise with respect to the chosen random ensemble. These *statistically significant* structures are considered potentially interesting and may be subjected to further analysis. A hierarchy of surrogate tests can be constructed by imposing additional constraints on the random ensemble in several steps to discover under which particular boundary conditions the observed network's properties of interest loose their statistical significance (Zamora-López, 2009; Donges, 2009).

As for isolated networks, one can construct surrogates for networks of networks to specifically study their interdependency structure in several steps (Schultz, 2010): (i) To obtain a simple kind of surrogate for a given observed network of networks, the cross-edge structure E_{ij} is randomized conserving only the cross-edge densities ρ_{ij} for all pairs of subnetworks G_i, G_j. The corresponding null hypothesis is that a given observed cross-characteristic can be explained solely by the subnetworks' internal edge-structure E_{ii} and prescribed ρ_{ij}. The expectation values for local and global measures of cross-clustering and cross-transitivity with respect to this particular random ensemble are given in Section 2.4.2. (ii) A more restricted surrogate ensemble with prescribed cross-degree sequences k_v^{ij} for all vertices $v \in V_i$ and all pairs of subnetworks is readily generated using a random edge rewiring algorithm. This ensemble is related to the configuration model (Newman, 2003) and may be used to test the effect of the cross-degree sequences and/or distributions on higher-order cross-characteristics like local and global cross-clustering, cross-transitivity, or cross-betweenness. (iii) The next step in the surrogate hierarchy could now be constructed in an iterative fashion, *e.g.*, by additionally prescribing aspects of a spatial embedding of vertices such as the *cross-edge length distributions*[3], depending on the research question at hand.

It should be noted that the construction and analysis of ensembles of network surrogates can be computationally demanding and algorithmically challenging, partic-

---

[3]Like isolated networks, most relevant real-world networks of networks are spatially embedded, *e.g.*, consider a power grid interacting with a communication network (Buldyrev et al., 2010). The *cross-edge length distribution* $p_{ij}(l)$ can be defined as the PDF of the lengths l of all cross-edges in the set E_{ij}
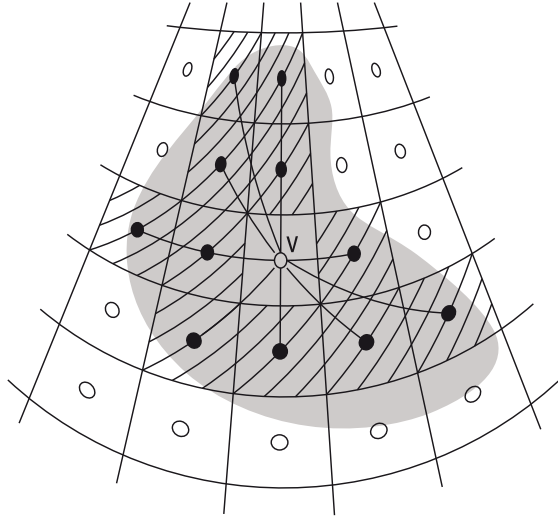
Figure 2.8.: Detail of a vertex-weighted spatial network $G = (V, E)$ obtained by sampling from an underlying infinite graph $G_0 = (V_0, E_0)$ defined on the 2-sphere, *e.g.*, G could be a climate network (Section 3.3). In this example, V is a regular latitude-longitude discretization of V_0 as it is commonly found in gridded climate data. Hence, the vertices $i \in V$ (disks) represent differently sized shares w_i (hatched areas) of the domain of interest V_0. In consequence, only the node splitting invariant degree $k_v^*(G)$ (not the standard degree $k_v(G)$) is a good estimator for the size of v's neighborhood $k_v(G_0)$ in the domain of interest V_0 (gray shaded area).

ularly given large networks and tight constraints on network structure (Zamora-López, 2009). These caveats can be circumvented at least for simple network models when analytical results are available (see, *e.g.*, Section 2.4.2 and Chapter 4). Further details on surrogates for networks of networks and their applications in significance testing are provided by Schultz (2010).

2.5. Vertex-weighted networks

In many networks of interest, vertices represent objects of heterogeneous size, weight, or importance (Figs. 2.2 and 2.8). Typical examples include networks describing (i) statistical associations between climatological time series representing the dynamics on differently sized portions of the Earth's surface (climate networks, see Section 3.3), (ii) proximities between sampled state vectors in the phase space of a dynamical system, possibly sampled at irregularly spaced points in time (recurrence networks, see Chapters 4 and 5), (iii) functional connections between regions of differing volume in the human brain (Zhou et al., 2006), or (iv) cross-references between articles of varying length and content in an online encyclopedia (Capocci et al., 2006). Following the arguments of Heitzig et al. (2012, P9), already from an intuitive point of view it is evident that the results of a statistical network analysis will be distorted by this
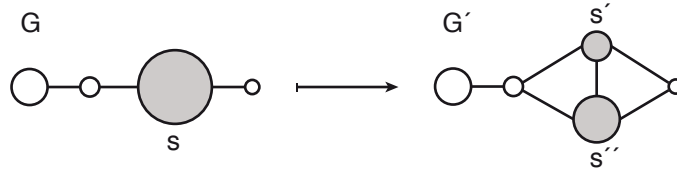
Figure 2.9.: The operation of *node splitting* transforms a network G of size N into a network G' of size $N + 1$ by replacing a vertex s of weight w_s with two linked vertices s', s'' of weights $w_{s'} + w_{s''} = w_s$. Additionally, s', s'' have the same neighborhood as s.

heterogeneity in node size, weight, or importance if the latter is taken into account inappropriately or not at all (as is usually the case in the literature).

More precisely, usually one is actually interested in the connectivity structure of a very large or even infinite set of objects of interest, *i.e.*, a finite or infinite graph $G_0 = (V_0, E_0)$. The typically finite set of vertices V of the available empirical network $G = (V, E)$ is often either a somehow selected or sampled subset of the larger set V_0, or is obtained from it by some discretization, aggregation, or coarse-graining (Fig. 2.8). *E.g.*, given an empirical global climate network, where V is a finite collection of grid points or measurement stations, the domain of interest V_0 is the set of uncountably many points on the Earth's surface and, hence, the underlying network G_0 has an uncountably infinite number of vertices and edges.

Now the task is to *estimate* the characteristics of G_0 given an empirical network G together with scalar weights w_v assigned to all vertices $v \in V$ that are together considered representative of G_0. The concept of *node splitting invariance* is a constructive axiomatic approach designed to tackle this estimation problem (Heitzig et al., 2012, P9). Assume that G and w_v already provide a sufficiently informative representation of the properties of G_0. When edges symbolize some kind of similarity (like a statistical association in climate networks), one would then expect that in a further refinement G' obtained from G by splitting a vertex s of weight w_s into two vertices s', s'' of weights $w_{s'} + w_{s''} = w_s$, those vertices would be linked, *i.e.*, $A'_{s's''} = 1$, and have the same neighborhood as s: $\mathcal{N}_{s'} = \mathcal{N}_{s''} = \mathcal{N}_s$ (Fig. 2.9). In other words, s', s'' represent objects in the domain of interest that are similar enough to have been aggregated into s in the first place, hence, it is reasonable to assume that they should be linked and have the same neighborhoods.

To derive consistently weighted variants of certain statistical network quantifiers of interest, Heitzig et al. (2012, P9) now require that the desired local and global measures $f_v(G), f(G)$ are invariant under further refining node splitting operations, because the empirical network G together with the weights w_v is already considered representative of G_0: $f(G) = f(G'), f_v(G) = f_v(G')$ for all $v \neq s$, and $f_s(G) = f_{s'}(G') = f_{s''}(G')$. Furthermore, vertices are now considered as linked to themselves because they embody a larger collection of similar and, thus, linked objects. This gives rise to the *extended adjacency matrix*

$$A_{ij}^+ = A_{ij} + \delta_{ij}, \tag{2.23}$$
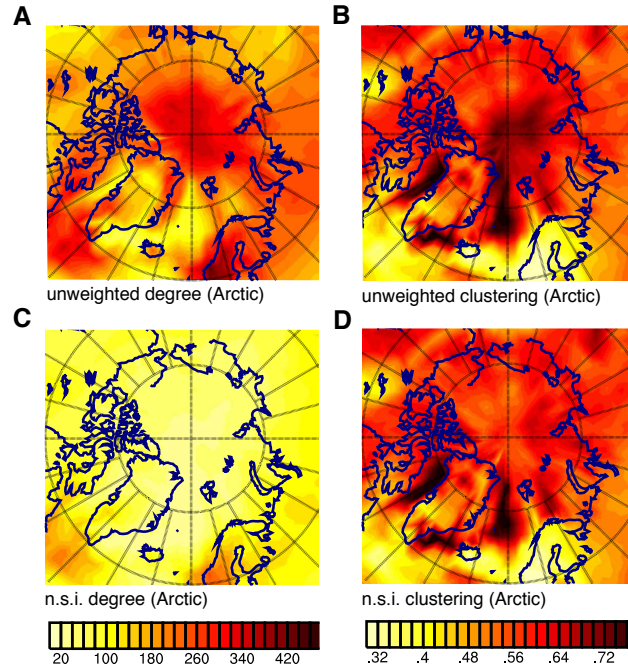
Figure 2.10.: Comparison of unweighted and weighted (node splitting invariant) versions of (A,C) degree k_v, k_v^* and (B,D) local clustering coefficient $\mathcal{C}_v, \mathcal{C}_v^*$ in the northern polar region (Lambert equal area projection) of a global climate network representing correlations in temperature dynamics (Heitzig et al., 2012, P9). The high values at the pole in (A,B) turn out to be an artifact of the increasing grid density toward the pole, as demonstrated by (C,D). Moreover, the n. s. i. results in (C,D) are confirmed by being virtually identical to results obtained for unweighted network measures from data on an icosahedral grid with homogeneous vertex density (Chapter 7).

where δ_{ij} is Kronecker's delta. Both demands induce a canonical construction mechanism for transforming statistical measures from complex network theory to their *node splitting invariant* (n. s. i.) counterparts(Appendix A and Heitzig et al. (2012, P9)). As a relatively simple characteristic, the *n. s. i. degree*

$$k_v^* = \sum_{i \in V} w_i A_{vi}^+ \tag{2.24}$$

estimates the share of objects in the domain of interest that a vertex $v \in V$ is connected to (Fig. 2.8). In turn, the *n. s. i. local clustering coefficient*

$$\mathcal{C}_v^* = \frac{\sum_{i,j \in V} w_i w_j A_{vi}^+ A_{ij}^+ A_{jv}^+}{(k_v^*)^2} \tag{2.25}$$

estimates the probability that two weight units (or *points* in terms of G_0) drawn at random from the part of the network linked to v are linked with each other (Fig. 2.10).

Even if the assumptions made above do not hold exactly for a given empirical network, we can still use the derived n. s. i. measures for consistently incorporating vertex weights into the statistical analysis. A typical example is analyzing a climate network on a regular latitude-longitude grid (Figs. 2.8 and 3.6). In this case, n. s. i. measures serve to reduce distortions in local connectivity and transitivity properties that are caused by the area represented by vertices decreasing towards the poles like $w_v = \cos(\vartheta_v)$, where ϑ_v denotes the latitude of v (Fig. 2.10). Note that for these particular vertex weights arising in climate networks, the n. s. i. degree is closely related to the heuristically defined *area weighted connectivity*[4] (Tsonis et al., 2006). Besides these more practical and applied benefits, the concepts of node splitting invariance and vertex-weighted network measures are valuable from an epistemological point of view. This is because they force the researcher to explicitly think about and specify what underlying system G_0 a given empirical network G is supposed to approximate and how the properties of G_0 can be estimated using G.

Heitzig et al. (2012, P9) further exploit the concept of node splitting invariance for deriving vertex-weighted versions of many other statistical quantifiers, algorithms, and methods of complex network theory, while Wiedermann (2011),Wiedermann et al. (2013, P1) extend it to obtain consistently weighted cross-measures for investigating networks of interacting networks with differently sized vertices (see also Fig. 2.2). Some relevant formulae are collected in Appendix A.

2.6. Summary

The basic concepts of complex network and graph theory have been introduced, motivating their benefits for the analysis of real-world complex systems encountered in many disciplines ranging from physics over biology and medicine to engineering. Subsequently, the specific properties and intricacies of spatially embedded networks appearing throughout this thesis have been discussed. Finally, we have put forward novel conceptual frameworks for consistently investigating complex networks of interacting or interdependent networks as well as general networks with weighted, differently sized, sampled, or spatially embedded vertices.

---

[4]Specifically, the area weighted connectivity $AWC_v = \sum_{i \in V} A_{ij} \cos(\vartheta_i) / \sum_{i \in V} \cos(\vartheta_i)$ of Tsonis et al. (2006) does not include area contributions from vertex v itself and involves a normalization term.

Chapter 3.

Network-based data analysis

Es gibt, seit Tagen gibt es keinen Wind.
Vielleicht, weil der Schmetterling atmet,
bewegt sich die Luft und ändern die
Abendmaschinen den Kurs. Als ginge die
Landschaft verloren, so trostlos hast du
gesprochen, aber das stimmt nicht, du weißt
es, die ganze Zeit [. . .]

Jürgen Becker (2009)

3.1. Introduction

It has become popular recently in several fields of science to apply the wealth of
concepts and measures from complex network theory for the analysis of data that
is not given explicitly in network form. In network-based data analysis, a data set
at hand, *e.g.*, consisting of time series such as electroencephalogram and climate
records or spatiotemporal point events such as earthquake aftershock swarms, first
has to be transformed to a network representation by means of a suitable algorithm
or mathematical mapping. We refer to the resulting networks quite generally as
functional networks in the course of this thesis, mainly to distinguish them clearly from
structural networks that are derived from systems with a more obvious graph structure,
e.g., social networks or power grids. Examples of functional networks include gene
regulatory networks in biology (Hempel et al., 2011), functional brain networks in
neuroscience (Bullmore and Sporns, 2009), climate networks in climatology (Donges
et al., 2009b, P21; Donges et al., 2009a, P22; Donges et al., 2011b, P14), or networks
of earthquake aftershocks in seismology (Davidsen et al., 2008).

As will be elaborated in the remainder of this chapter, the particular interest
and focus of this dissertation is on transformations from data to network that are
based on first principles and fundamental (physical) laws allowing the rigorous
analysis, interpretation, and understanding of the resulting network properties. In
this respect, the approaches of interest for this work are conceptually distinct from
rather application-oriented techniques such as neural networks (Haykin, 2008) and
(probabilistic) graphical models (Koller and Friedman, 2009) used for machine learning
and data mining mainly in engineering and computer science.

The first part of this chapter, Section 3.2, covers complex network approaches for nonlinear time series analysis of single system, but possibly multivariate time series. After giving a brief overview of the field, we specifically introduce recurrence network analysis of time series and review related results and developments attained recently. Secondly, network techniques for investigating spatiotemporal data like point processes or fields of time series are presented, with a special focus on climate networks reconstructed from fields of climatological time series such as surface air temperature and other applications in the geosciences (Section 3.3).

3.2. Single time series

3.2.1. Overview

Analogies are a fundamental motor of innovation in physics and other disciplines, since they foster the transfer of theoretical insights, results, and techniques from one field to the other. In the last years, complex network theory has been particularly successful in providing unifying concepts and methods for understanding the structure and dynamics of complex systems in many areas of science, ranging from power grids over social networks to neuronal networks (Chapter 2). Similarly, nonlinear time series analysis aims to gain insights into a wide variety of natural, technological, and experimental dynamical systems drawing on a generic body of theory and methods (Kantz and Schreiber, 2004; Pikovsky et al., 2001).

By exploiting analogies in the structure and mathematical description of complex networks and dynamical systems, a number of new network-based techniques for nonlinear time series analysis have been proposed recently (Donner et al., 2011a, P13). The first class of these methods makes use of graph representations of similarity relationships between state vectors or groups of state vectors (*e.g.*, cycles) in phase space. It includes transition networks based on a coarse-graining of phase space (Nicolis et al., 2005), cycle networks (Zhang and Small, 2006), correlation networks (Yang and Yang, 2008), k-nearest-neighbor (Shimada et al., 2008) and adaptive nearest neighbor networks (Xu et al., 2008; Xiang et al., 2012), as well as ε-recurrence networks (Marwan et al., 2009, P20; Donner et al., 2010c, P19). The latter three techniques harness the fundamental analogy between the Poincaré recurrence structure (Poincaré, 1890) of a time series in phase space, which is commonly represented by a binary recurrence matrix and allows us to recover basic dynamical invariants of the underlying system (Marwan et al., 2007), and the binary adjacency matrix describing a complex network. Other methods such as visibility graphs (Lacasa et al., 2008) work in the time domain and focus on studying stochastic properties of time series.[5] In summary, all approaches mentioned above propose a mapping from the time series to the network domain and then proceed to interpret the statistical

---

[5]The potentials and pitfalls encountered when applying visibility graphs to the analysis of geoscientific data (Donner and Donges, 2012b, P7) as well as their use in devising novel ways for detecting time-reversal asymmetry in general time series (Appendix B and Donges et al. (2012, P2); Donner and Donges (2012a, C3)) have been explored during this thesis project.
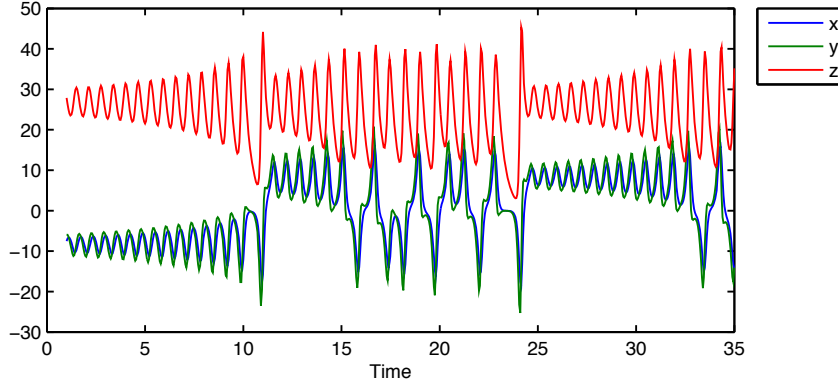
Figure 3.1.: Realization of the Lorenz system (Eq. (3.1)) with parameters $r = 28$, $\sigma = 10$, and $\beta = 8/3$ that is used for network construction in Fig. 3.2 (sampling time $\Delta T = 0.05$).

properties of the resulting (usually complex) network in terms of the underlying system's dynamical properties.

An exhaustive treatment of all above mentioned techniques for network-based time series analysis and their applications is far beyond the scope of this thesis and is already provided elsewhere (Donner et al., 2011a, P13). Here, we restrict ourselves to an illustrative visual comparison of the different network structures resulting from a single realization of the paradigmatic Lorenz system

$$\frac{d}{dt}(x, y, z) = (\sigma(y - x), x(r - z) - y, xy - \beta z) \tag{3.1}$$

exhibiting chaotic dynamics and a strange attractor with complex geometry in phase space (Figs. 3.1, 3.3). Notably, the networks resulting from all six distinct approaches all display the characteristic double-scroll structure of the Lorenz attractor (Fig. 3.2), albeit for different reasons (Donner et al., 2011a, P13).

3.2.2. Recurrence network analysis

Complementary views on Poincaré recurrence

Recurrence in phase space is a basic property of complex dynamical systems. Since the seminal work of Poincaré (1890), it is known that under rather general conditions, dynamical systems tend to return arbitrarily close to their previous states in the long-term limit. In the last decades, the recurrence property has attracted considerable interest, since it has been shown that essential information about the main dynamical properties is contained in the temporal pattern of mutual recurrences of a state (Thiel et al., 2004; Robinson, 2009). Particularly, the visual representations of recurrence plots (Eckmann et al., 1987; Marwan et al., 2007) obtained from (multivariate) time
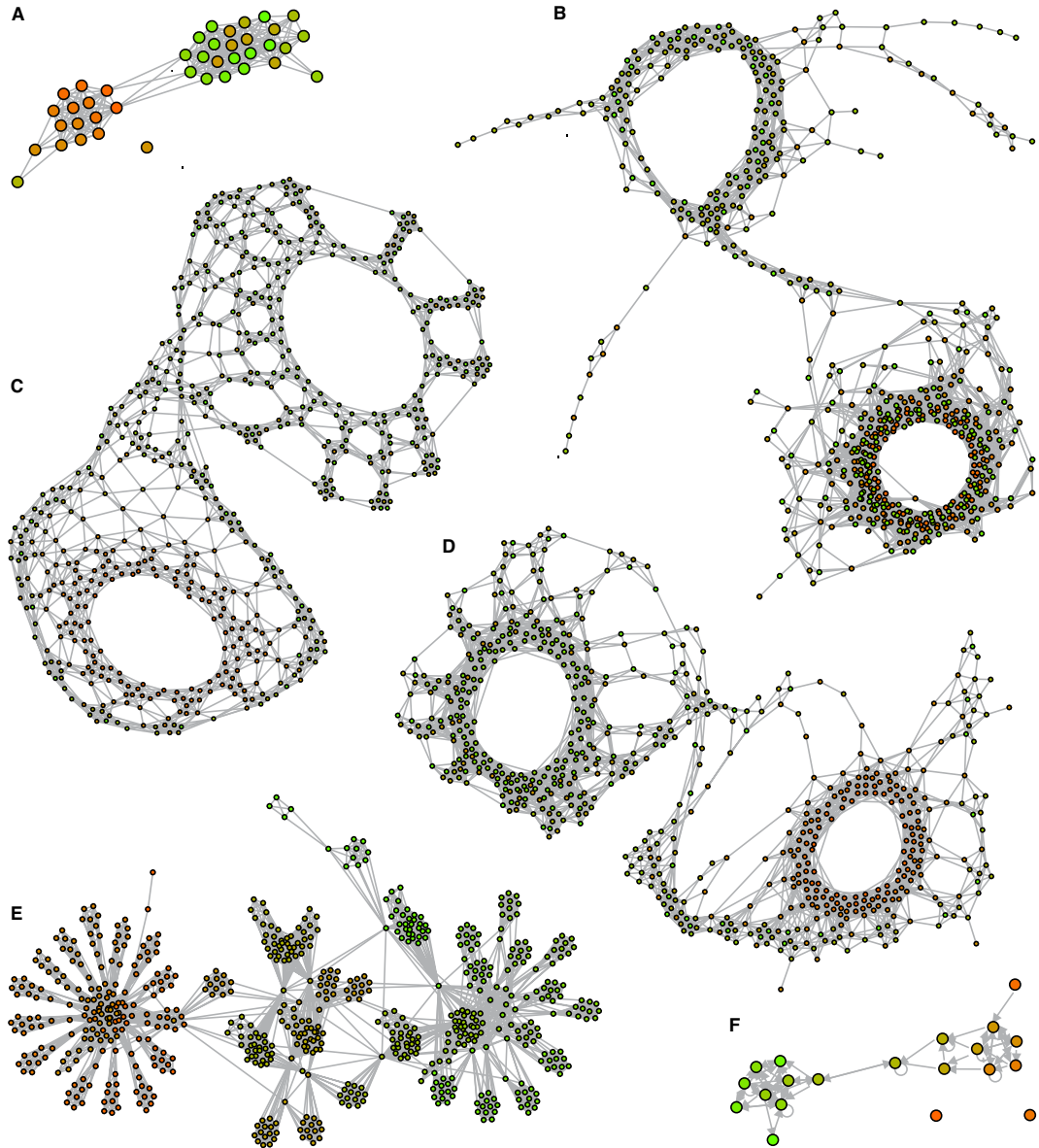
Figure 3.2.: Illustration of the different types of time series networks all constructed from the x-component of the same realization of the Lorenz system shown in Fig. 3.1 (see Donner et al. (2011a, P13) for details). (A) Cycle network, (B) correlation network, (C) k-nearest neighbor network (asymmetric version), (D) ε-recurrence network, (E) visibility graph, and (F) transition network. The graphs have been embedded into an abstract two-dimensional space using a force-directed placement algorithm (Battista et al., 1994). For panels (A)–(E), the vertex color indicates the temporal order of observations (from orange to bright green), for the transition network (panel (F)), colors correspond to the different x values. In panels (B) and (D), some individual disconnected vertices have been removed from the network representations.
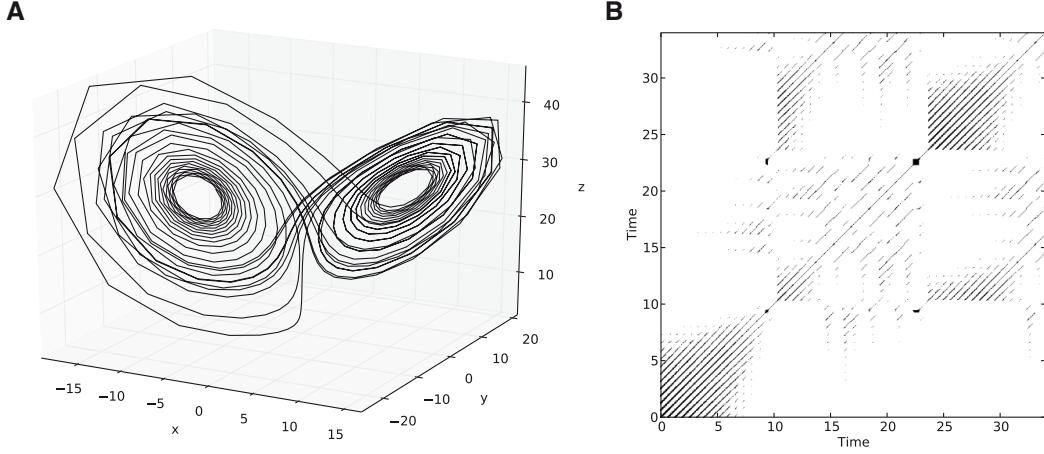
Figure 3.3.: (A) Phase space trajectory for a single realization of the Lorenz system (see Fig. 3.1 for details). (B) Recurrence plot obtained from its embedded x-component (embedding dimension $m = 3$ and delay $\tau = 3$, see Section 5.2.3) using a recurrence threshold $\varepsilon = 2$ and the supremum norm. The corresponding recurrence matrix $\mathbf{R}(\varepsilon)$ is directly related to the adjacency matrix $\mathbf{A}(\varepsilon)$ of the ε-recurrence network displayed in Fig. 3.2D via Eq. (3.3).

series $\{x(t_i)\}_{i=1}^{N}$ with $x(t_i) \in \mathbb{R}^m$, have found wide use and are commonly expressed by a binary recurrence matrix $\mathbf{R}(\varepsilon)$ with elements

$$R_{ij}(\varepsilon) = \Theta(\varepsilon - \|x(t_i) - x(t_j)\|), \tag{3.2}$$

where $\Theta(\cdot)$ is the Heaviside function, ε a threshold distance in phase space used for defining the neighborhood of a state vector $x(t_i) = x_i$, and $\| \cdot \|$ denotes some norm acting on $\mathbb{R}^m$. Given univariate observational or experimental time series $\{x(t_i)\}$, it is usually necessary to reconstruct the corresponding system's trajectory in some higher-dimensional phase space to recover its recurrence structure reliably (*e.g.*, by time-delay embedding (Packard et al., 1980; Takens, 1981), see Section 5.2.3). Additionally, a *Theiler window* (Marwan et al., 2007) can be used to eliminate trivial recurrences between temporally neighboring state vectors from $\mathbf{R}(\varepsilon)$ that are merely due to the finiteness of ε and the trajectory's continuity (tangential motion).

Recurrence plots typically show distinct line structures (Fig. 3.3), the length distributions of which can be used for defining suitable measures of complexity in terms of recurrence quantification analysis (RQA), or for estimating dynamical invariants such as the correlation dimension D_2, the 2nd-order Rényi entropy K_2, or the generalized mutual information $I_2(\tau)$ (Marwan et al., 2007). In the context of paleoclimate research, recurrence plots and RQA have been successfully applied for tracing dynamical changes (Trauth et al., 2003; Marwan et al., 2003) and aligning records with different age-depth models (Marwan et al., 2002).

Recently, it has been suggested to approach recurrence matrices from a complex network perspective by identifying

$$A_{ij}(\varepsilon) = R_{ij}(\varepsilon) - \delta_{ij} \qquad (3.3)$$

(δ_{ij} denoting Kronecker's delta) as the elements of the adjacency matrix $\mathbf{A}(\varepsilon)$ of a *ε-recurrence network* associated with the underlying time series (Marwan et al., 2009, P20; Donner et al., 2010a, P18).[6] This fundamental analogy implies that each sampled state vector is assigned to one of N vertices in the ε-recurrence network (for brevity, the term *recurrence network* will sometimes be used in the following to name the very same concept), where two vertices are linked if the corresponding state vectors are recurrent, *i.e.*, mutually close, in phase space. Due to the symmetric definition of $\mathbf{R}(\varepsilon)$ (Eq. (3.2)), the resulting ε-recurrence network $G = (V, E)$ is an undirected and simple graph.

In contrast to RQA, which considers temporal dependencies between observations in form of diagonal and vertical line structures in the recurrence plot, recurrence network analysis discards all temporal information and solely quantifies the geometry of the underlying set S (*e.g.*, an attractor) (Donner et al., 2010c, P19; Donges et al., 2011a, P11), see Chapters 4 and 5.

Global ε-recurrence network measures

The statistical properties of ε-recurrence networks (parameterized by the single parameter ε) have been shown to trace structures in phase space corresponding to dynamically invariant objects (Donner et al., 2010a, P18; Donner et al., 2011b, P15) as well as qualitative changes in the dynamical behavior of time series (Marwan et al., 2009, P20; Donner et al., 2011a, P13). For detecting bifurcations in time series, global-scale characteristics from complex network theory are of particular interest (Newman, 2003; Boccaletti et al., 2006; Costa et al., 2007). Here, we introduce a set of measures that are used for detecting dynamical transitions in model systems and paleoclimate records in Chapters 5 and 6, and additionally give heuristic interpretations of their behavior in terms of the dynamics of the underlying system. A more rigorous interpretation of the following and other statistical network measures in the context of ε-recurrence network analysis is provided in Chapter 4.

Edge density $\quad \rho$ measures which fraction of the maximum theoretically possible number $N(N-1)/2$ of undirected edges is present in the ε-recurrence network,

$$\rho = \frac{1}{N(N-1)} \sum_{i,j \in V} A_{ij}. \qquad (3.4)$$

---

[6]Note that similar approaches can also be found in other geoscientifically relevant applications of data analysis, such as dendrograms in agglomerative cluster analysis, or nonlinear decomposition of multivariate data using isometric feature mapping (Gámez et al., 2004).

It is equivalent to the *recurrence rate RR* in traditional RQA (Marwan et al., 2009, P20).

Transitivity $\mathcal{T}$ of an unweighted and undirected network characterizes the overall probability that two randomly chosen neighbors of an also randomly chosen vertex are connected (Newman, 2003),

$$\mathcal{T} = \frac{\sum_{i,j,k \in V} A_{ij} A_{jk} A_{ki}}{\sum_{i,j,k \in V; i \neq j} A_{ik} A_{jk}}. \tag{3.5}$$

In recurrence network analysis, $\mathcal{T}$ serves as a measure for the regularity of the dynamics as encoded in the ε-recurrence network's mesoscopic structure (Donner et al., 2010a, P18). Specifically, regular dynamics (*e.g.*, on a periodic orbit) is typically characterized by higher values of the transitivity $\mathcal{T}$ than chaotic dynamics (it will be shown below that $\mathcal{T}$ is closely related to a specific notion of dimensionality of the underlying attractor in phase space). When dealing with short time series (segments), *e.g.*, typical paleoclimate records, transitivity is a more robust measure than the related global clustering coefficient $\mathcal{C}$ (Watts and Strogatz, 1998; Newman, 2003), since the latter gives relatively more weight to sparsely sampled regions in phase space (vertices with low degree k_v, Eq. (2.6)) (Donner et al., 2010a, P18; Donner et al., 2011a, P13).

Average path length $\mathcal{L}$ is defined as the mean value of the shortest-path lengths d_{ij} between all mutually reachable pairs of vertices (i,j) (see Section 2.2),

$$\mathcal{L} = \langle d_{ij} \rangle_{i,j \in V : \mathcal{P}(i,j) \neq \emptyset}. \tag{3.6}$$

Since for comparable values of ε the average distances along different types of orbits typically differ significantly, changes in $\mathcal{L}$ can be used as sensitive indicators of dynamical transitions (Marwan et al., 2009, P20; Donner et al., 2010a, P18). Refer to the definition of cross-average path length in Section 2.4.2 for a discussion of alternative treatments of networks with more than one component.

Assortativity   A network is called assortative if vertices tend to connect preferentially to vertices of a similar number of connections (degree k_v). On the other hand, it is called disassortative if vertices of high degree prefer to link to vertices of low degree, and vice versa (Newman, 2002). This *assortativity* property can be quantified by the Pearson correlation coefficient

$$\mathcal{A} = \frac{\frac{1}{2L} \sum_{i,j \in V} k_i k_j A_{ij} - \left(\frac{1}{2L} \sum_{i,j \in V} \frac{1}{2}(k_i + k_j) A_{ij} \right)^2}{\frac{1}{2L} \sum_{i,j \in V} \frac{1}{2}(k_i^2 + k_j^2) A_{ij} - \left(\frac{1}{2L} \sum_{i,j \in V} \frac{1}{2}(k_i + k_j) A_{ij} \right)^2} \tag{3.7}$$

between the degrees k_i, k_j of the vertices on both ends of all L edges (Costa et al., 2007). In the recurrence network context, $\mathcal{A}$ can be considered as a measure for the

local continuity of the phase space density of state vectors (Donner et al., 2010a, P18).

Diameter $\mathcal{D}$ is the maximum geodesic (shortest-path) distance between all mutually reachable pairs of vertices in the network (Newman, 2003),

$$\mathcal{D} = \max_{\substack{i,j \in V: \\ \mathcal{P}(i,j) \neq \emptyset}} (d_{ij}) . \tag{3.8}$$

From this definition, there are obvious relationships with the average path length $\mathcal{L}$, which are expected to lead to correlations between both measures (Donner et al., 2010a, P18).

Theoretical results and applications

Recently, ε-recurrence networks have been demonstrated to be a useful tool in diverse applications of nonlinear time series analysis ranging from model systems (Marwan et al., 2009, P20; Donner et al., 2010a, P18; Donner et al., 2010c, P19; Donner et al., 2010b, C5; Senthilkumar et al., 2010; Donner et al., 2011a, P13; Donner et al., 2011b, P15; Zou et al., 2010, P17; Li et al., 2011; Strozzi et al., 2011; Zou et al., 2012) via experimental data (Gao and Jin, 2009b; Gao and Jin, 2009a; Gao et al., 2010; Marwan et al., 2010b) to recent and (paleo)climate records (Marwan et al., 2009, P20; Donner et al., 2011a, P13; Donges et al., 2011a, P11; Donges et al., 2011c, P10; Hirata et al., 2011) as well as financial time series (Donner et al., 2010b, C5). They allow one to uncover complex bifurcation scenarios (Marwan et al., 2009, P20; Donges et al., 2011a, P11) and to reliably distinguish between chaotic and non-chaotic dynamics (Zou et al., 2010, P17). Furthermore, the local and global transitivity characteristics of ε-recurrence networks have been shown to enable the tracing of unstable periodic orbits (Donner et al., 2010c, P19) as well as the definition of notions of fractal dimension (Donner et al., 2011b, P15) independently of earlier approaches (see below).

An important advantage of nonlinear ε-recurrence network analysis of time series is that it performs well in the detection of dynamical transitions within significantly shorter time series ($\mathcal{O}(10^2)$ data points (Marwan et al., 2009, P20; Zou et al., 2010, P17; Donges et al., 2011a, P11)) than required by classical techniques such as estimating the maximum Lyapunov exponent from data (Abarbanel, 1996; Kantz and Schreiber, 2004). This renders ε-recurrence networks readily applicable to the analysis of non-stationary real-world data (Chapter 5). The method has also been applied successfully to time series with irregular sampling and/or uncertain timing of observations that are commonly found in the geosciences or in astrophysics (Donges et al., 2011a, P11; Donges et al., 2011c, P10), see Chapters 5 and 6.

Notably, ε-recurrence network analysis has recently been extended to allow the investigation of interrelationships between two or more (multivariate) time series generated by distinct dynamical systems (Appendix C). Inter-system recurrence net-
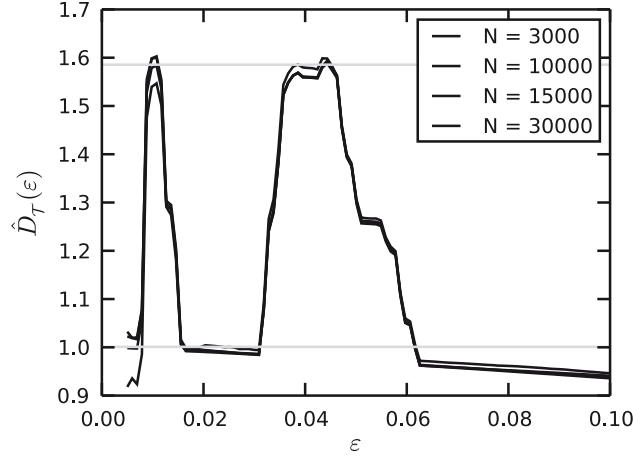
Figure 3.4.: Estimation of the transitivity dimensions $\hat{D}_{\mathcal{T}}^{u,l}$ for the generalized baker's map (Eq. 3.12) at $\alpha = 1/2$ and $\lambda_a = \lambda_b = 1/4$ for different N. Gray horizontal lines indicate numerical estimates of $D_{\mathcal{T}}^{u,l}$ obtained with $N = 30,000$ data points at small ε. See Donner et al. (2011b, P15) for details.

works have been shown to enable detecting the coupling direction between interacting dynamical systems (Feldhoff et al., 2012, P5) by exploiting the intrinsic asymmetry of the coupled network measures cross-transitivity and global cross-clustering coefficient (Section 2.4.2), while certain features of joint recurrence networks are sensitive to complex synchronization regimes like generalized synchronization (Feldhoff et al., 2013, P3).

Transitivity-based dimensions

Interestingly, transitivity-based measures like transitivity $\mathcal{T}$ and local clustering coefficient $\mathcal{C}_i$ computed from ε-recurrence networks are closely related to the underlying attractive set's effective dimensionality. For a smooth d-dimensional manifold $S \subseteq \mathbb{R}^m$, it can be shown that the expectation values of the measures are

$$\mathbb{E}(\mathcal{T}) = \mathbb{E}(\mathcal{C}_i) = \left(\frac{3}{4}\right)^d \tag{3.9}$$

when using the supremum norm in phase space (Donner et al., 2011b, P15). Focussing on the global network measure transitivity, for continuous-time systems this implies $\mathbb{E}(\mathcal{T}) = 3/4$ for a periodic orbit, but $\mathcal{T} < 3/4$ is observed for chaotic dynamics on strange attracting sets (Marwan et al., 2009, P20; Donner et al., 2010c, P19). This behavior motivates defining a novel notion of global dimensionality based on $\mathcal{T}$. However, it turns out that it is not sufficient to simply solve Eq. (3.9) for d given any recurrence threshold ε, since self-similar (fractal) features of the studied set of state vectors in phase space typically lead to oscillations of $\mathcal{T}$ with changing ε (Fig. 3.4).

These oscillations can be taken into account by defining an upper transitivity dimension $\hat{D}_{\mathcal{T}}^u$ together with a lower transitivity dimension $\hat{D}_{\mathcal{T}}^l$ (the hat $\hat{D}$ indicates that these measures are estimators of the true transitivity dimensions derived from *continuous ε-transitivity*, see Chapter 4 and Donner et al. (2011b, P15)):

$$\hat{D}_{\mathcal{T}}^u = \max_{\varepsilon \in \mathcal{E}} \frac{\log \mathcal{T}(\varepsilon)}{\log(3/4)}, \tag{3.10}$$

$$\hat{D}_{\mathcal{T}}^l = \min_{\varepsilon \in \mathcal{E}} \frac{\log \mathcal{T}(\varepsilon)}{\log(3/4)}. \tag{3.11}$$

These can be estimated from a sufficiently long sampled trajectory for a suitably large set $\mathcal{E}$ of different values of ε that are as small as possible while still providing sufficiently large values of k_i to avoid problems due to lack of neighbors in low density regions of phase space (Donner et al., 2011b, P15). Notably, the number of data points needed for reliably estimating transitivity dimensions is significantly larger than that required for detecting dynamical transitions in time series (see above). In both applications, this number depends strongly on the dimension of the considered phase space (see the arguments given in Smith (1988)).

For illustration, we estimate the newly defined upper and lower transitivity dimensions with analytically calculated bounds as well as established measures of (fractal) dimensionality like the box-counting, information, or correlation dimensions (Rényi dimensions $D_{0,1,2}$ of order 0,1,2, respectively (Hentschel and Procaccia, 1983)) for the prototypical generalized baker's map

$$x_{n+1} = \begin{cases} \lambda_a x_n & \text{if } y_n < \alpha, \\ (1 - \lambda_b) + \lambda_b x_n & \text{if } y_n > \alpha, \end{cases}$$

$$y_{n+1} = \begin{cases} y_n/\alpha & \text{if } y_n < \alpha, \\ (y_n - \alpha)/(1 - \alpha) & \text{if } y_n > \alpha \end{cases} \tag{3.12}$$

with $\alpha < 1$, $\lambda_a, \lambda_b > 0$ and $\lambda_a + \lambda_b \leq 1$ (Farmer et al., 1983; Ott, 2002). This exercise reveals that the newly defined transitivity dimensions are well-behaved and vary consistently with the classical Rényi dimensions (Fig. 3.5). However, it should be stressed that computing the latter typically involves the problematic task of estimating power law exponents γ from functions of the form ε^γ (Stumpf and Porter, 2012) (Eq. (3.14)), while the estimation of transitivity dimensions simply requires finding the minimum and maximum of a sequence $\mathcal{T}(\varepsilon)$ (Eq. (3.16) and Fig. 3.4).

It is instructive in this context to compare the definitions of the correlation and transitivity dimensions in a common notation. Given a set of points $x_i \in \mathbb{R}^m$, $i = 1, \ldots, N$, the *correlation dimension* D_2 can be estimated as a scaling exponent of the *correlation sum* $C(\varepsilon)$ (which is directly related to the corresponding ε-recurrence
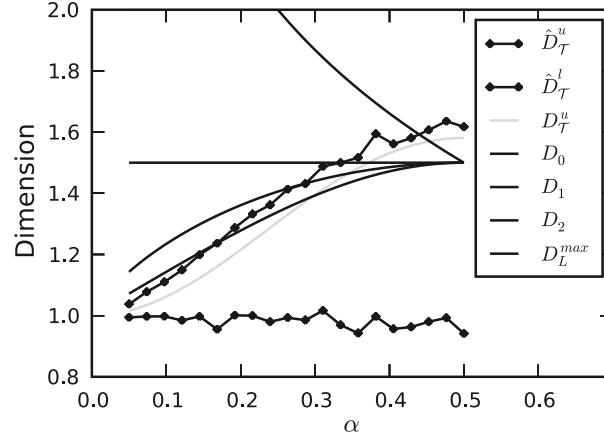
Figure 3.5.: Dependence of several global measures of dimensionality on the parameter α ($\lambda_a = \lambda_b = 1/4$) of the generalized baker's map (Eq. 3.12): Upper and lower transitivity dimensions $\hat{D}_{\mathcal{T}}^{u,l}$, Rényi dimensions $D_{0,1,2}$, and Lyapunov dimension D_L^{max}. One realization has been considered for each value of α. The gray line corresponds to an analytically calculated lower bound of $D_{\mathcal{T}}^u$. Numerical estimates have been obtained with $N = 15,000$ data points, and results are robust for various choices of N (Fig. 3.4). See Donner et al. (2011b, P15) for details.

network's link density $\rho(\varepsilon)$ (Donner et al., 2010c, P19))

$$C(\varepsilon) = \frac{1}{N^2} \sum_{\substack{i,j=1 \\ i \neq j}}^{N} \Theta\left(\varepsilon - \|x_i - x_j\|\right), \tag{3.13}$$

which scales like

$$C(\varepsilon) \propto \varepsilon^{D_2} \tag{3.14}$$

for small ε (Grassberger and Procaccia, 1983). In turn, the *recurrence network transitivity* (Eq. (3.5)) can be written as

$$\mathcal{T}(\varepsilon) = \frac{\sum_{\substack{i,j,k=1 \\ i \neq j \neq k}}^{N} \Theta\left(\varepsilon - \|x_i - x_j\|\right) \Theta\left(\varepsilon - \|x_j - x_k\|\right) \Theta\left(\varepsilon - \|x_k - x_i\|\right)}{\sum_{\substack{i,j,k=1 \\ i \neq j \neq k}}^{N} \Theta\left(\varepsilon - \|x_i - x_j\|\right) \Theta\left(\varepsilon - \|x_i - x_k\|\right)}. \tag{3.15}$$

Introducing a *scale-dependent transitivity dimension* $\hat{D}_{\mathcal{T}}(\varepsilon)$ (see Fig. 3.4) yields

$$\mathcal{T}(\varepsilon) = \left(\frac{3}{4}\right)^{\hat{D}_{\mathcal{T}}(\varepsilon)} \tag{3.16}$$

when using the supremum norm. Comparing Eqs. (3.13) and (3.15) suggests that independently from the graph-theoretical background of recurrence network analysis, $\mathcal{T}(\varepsilon)$ can be viewed as *phase space transitivity*, a generalization of the correlation sum $C(\varepsilon)$ (or correlation integral, when using the continuous ε-transitivity introduced in Chapter 4 and Donner et al. (2011b, P15)). However, and interestingly, for fractal sets of points both quantities show a fundamentally different behavior with decreasing scale parameter ε, *i.e.*, a power-law decrease for $C(\varepsilon)$ and oscillations for $\mathcal{T}(\varepsilon)$, requiring distinct approaches for estimating the related dimensions (Eqs. (3.14), (3.16), and above discussion).

Similarly to the global transitivity dimension, local clustering dimensions can be defined based on the local clustering coefficient $\mathcal{C}_i$ in Eq. (3.9), *e.g.*, for tracing invariant objects in phase space (Donner et al., 2011b, P15). Furthermore, the above introduced notions of transitivity-based dimensions can be readily generalized to obtain a sequence of higher-order dimensionality measures analogous to the Rényi dimensions (Appendix D).

3.3. Spatiotemporal data

3.3.1. Overview

Besides network-based approaches for investigating (multivariate) time series from isolated dynamical systems (Section 3.2), much efforts have been spent for developing network techniques for analyzing data from spatially extended systems like the mammalian brain or the Earth's climate system. In these data sets, observations and, consequently, vertices of the resulting functional networks are usually embedded in four-dimensional space-time. This is in contrast to the time series networks discussed in the previous section, where in most approaches vertices are either embedded in abstract phase space or on the time axis.

In methods designed for analyzing data in the form of fields of time series, networks are commonly constructed using measures of statistical association from linear (Brockwell and Davies, 2002) and nonlinear time series analysis (Sprott, 2003; Kantz and Schreiber, 2004). Examples include functional brain networks constructed from electroencephalogram (EEG) or functional magnetic resonance imaging (fMRI) data in the neurosciences (Zhou et al., 2006; Zamora-López et al., 2009; Zamora-López et al., 2010), gene expression networks (Hempel et al., 2011), climate networks derived from climatological observables (Section 3.3.2), or functional networks describing statistical interrelationships between stock indices in finance (Bonanno et al., 2003). Most works rely on "naively" quantifying the similarity of time series using measures like Pearson correlation or mutual information. Measures of different types of *synchronization* like phase or generalized synchronization are also frequently used (Pikovsky et al., 2001; Boccaletti et al., 2002; Arenas et al., 2008). Moreover, there is an increasing

interest in networks representing *causal*[7] relationships in the data, *i.e.*, excluding the influence of auto-dependencies, indirect coupling, or common-driver effects on the association measure. A commonly used, classical linear and parametric approach to this task is Granger causality (Granger, 1969). Modern non-parametric techniques drawing on information theoretic ideas include transfer entropy (Schreiber, 2000) and partial mutual information (Frenzel and Pompe, 2007). A common drawback of these *causality measures* is that they are hard to estimate in practice, particularly given large sets of relatively short and noisy real-world times series which are typically encountered in the construction of functional networks from data. Recently, Runge et al. (2012) proposed an efficient algorithm based on the framework of graphical models for consistently estimating multivariate transfer entropy in such problematic situations.

Particularly in the geosciences, research has focussed on the network analysis of spatiotemporal point events or point processes, where in contrast to the time series data discussed above, no underlying continuous process exists even in idealized situations. For example, network approaches have been used for unveiling the complex spatiotemporal dependencies between earthquakes and their aftershock sequences (Abe and Suzuki, 2004; Davidsen et al., 2008; Jiménez et al., 2009) as well as for investigating possible long-range interactions between active volcanos (Nunnari et al., 2009). Other application of network theory to geoscientific problems include the study and/or modeling of diffusion processes in porous and disordered soils and rocks (Yang, 2001; Santiago et al., 2008), erosion processes (Winter and Damron, 2009), and transport in river networks (Zaliapin et al., 2010) or systems of rock fractures (Berkowitz, 1995).

The following section attempts to provide a comprehensive review of research in the rapidly developing field of climate network analysis that has been missing in the literature so far. This review includes and puts into context own work on general climate network structure and construction (Donges et al., 2009a, P22; Donges et al., 2009b, P21; Donges, 2009; Heitzig et al., 2012, P9), regional climate networks (Donges, 2009), the signature of qualitatively distinct El Niño episodes (Zou et al., 2011, P16; Radebach et al., subm. P4) as well as climate network visualization (Tominski et al., 2011, P12). Particularly, it sets the stage for the coupled climate networks (Donges et al., 2011b, P14) that are introduced in Chapter 7.

3.3.2. Climate network analysis

Historical background

Climatologists have been long interested in studying correlations between climatological variables for gaining an understanding of the Earth's climate system's large-scale dynamics (Katz, 2002). Pioneering work in this field was done by Sir Gilbert T.

---

[7]As is common practice in the time series analysis literature, we use the notion of *causality* in a loose sense. Strictly, it is clearly impossible to infer a causal relationship from statistical reasoning alone.
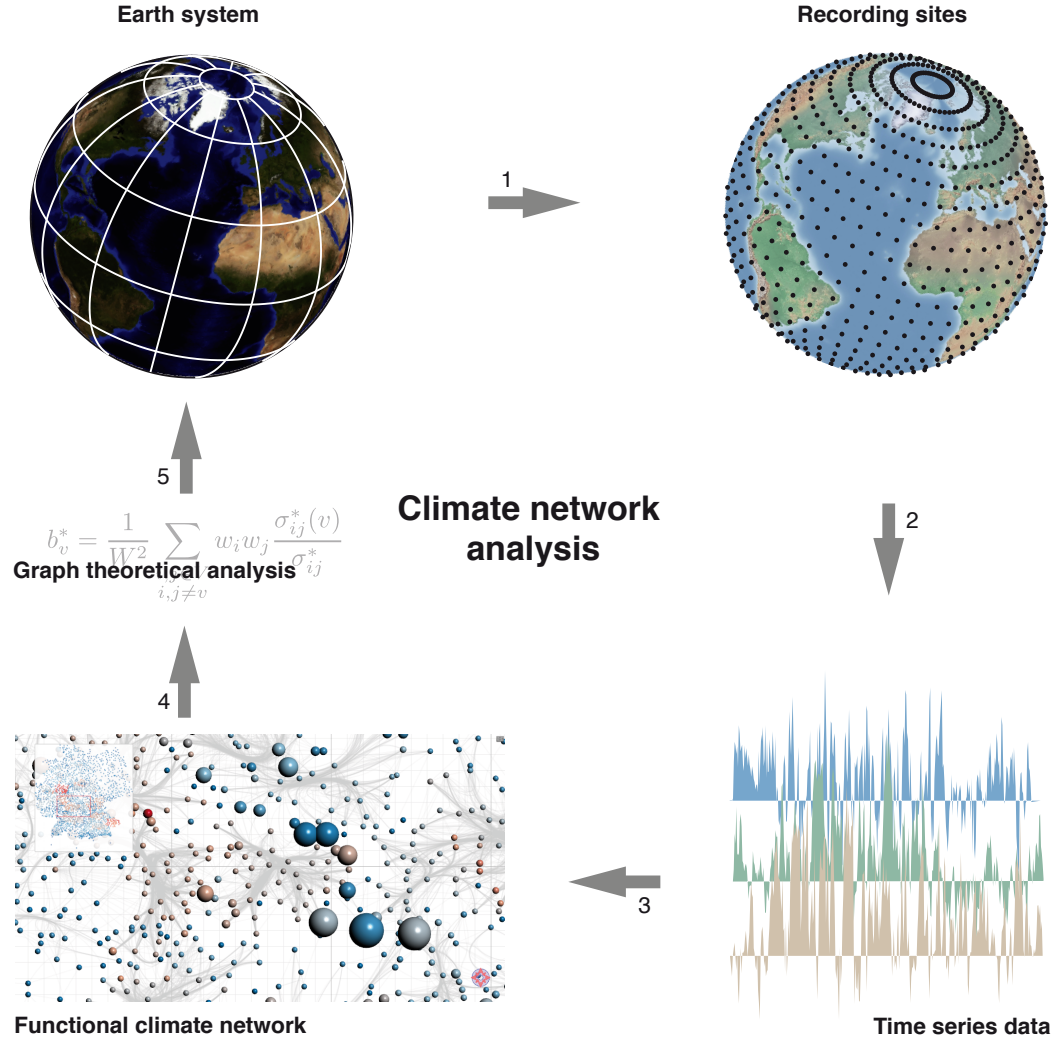
Figure 3.6.: Illustration of the workflow of climate network analysis (note the analogies to Bullmore and Sporns (2009, Box 1) concerning the analysis of structural and functional brain networks). At step 1, a discretized time series representation $\{x_i(t)\}_{i=1}^{N}$ of the climatological field(s) of interest is chosen that is usually dictated by the available gridded or station data. At step 2, coupling metrics C_{ij} are estimated for quantifying statistical interdependencies between pairs of climatological time series. At step 3, the construction of a functional climate network from the similarity matrix C_{ij} typically involves some thresholding criterion (see Tominski et al. (2011, P12) for details on the climate network shown here). At step 4, the obtained climate network is subjected to graph-theoretical analysis drawing on the toolbox of complex network theory. Finally, at step 5, the results of this analysis need to be interpreted in terms of the underlying dynamical system, the Earth, for extracting novel insights as well as iteratively refining the employed analytical tools.

Walker in the beginning of the 20th century while attempting to find precursory patterns for Indian monsoon events using statistical methods (Walker, 1910), which culminated in the discovery of the tropical Walker circulation and the Pacific Southern Oscillation (a part of the El Niño-Southern Oscillation known as ENSO). Later, the rapid increase in available computing power allowed to investigate the correlation structure of global or regional climatological fields $\{x_i(t)\}_{i=1}^{N}$ such as surface air temperature, pressure, or geopotential height. Here, i is a spatial index, *e.g.*, labeling meteorological measurement stations or grid points in an aggregated data set (see Section 2.5), and t denotes time. The aim is to find spatial as well as temporal patterns accounting for a large fraction of the field's variance, commonly relying on established linear methods such as principal component analysis (termed empirical orthogonal function (EOF) analysis in climatological parlance), singular spectrum analysis (Kutzbach, 1967; Wallace and Gutzler, 1981; Vautard and Ghil, 1989; Storch and Zwiers, 2003; Mudelsee, 2010), or nonlinear extensions thereof (Hsieh, 2004).

Climate network construction

The first functional network analysis of fields of climatological time series $\{x_i(t)\}_{i=1}^{N}$ was presented by Tsonis and Roebber (2004), introducing the term *climate network*[8]. Climate network analysis offers a complementary view and novel insights by transferring the toolbox of measures and algorithms from complex network theory to the study of climate system dynamics (Fig. 3.6). Since the field is still in a nascent stage, we will, in the following, attempt to give a comprehensive overview of the relevant literature. In all works considered here, climate networks are simple graphs consisting of N spatially embedded vertices i that correspond to time series $\{x_i(t)\}$ representing proxy reconstructions (Rehfeld et al., in press), observations (obs.), reanalyses (rean.), or simulations (mod.) of climatological variables at fixed measurement stations, grid cells, or certain predefined regions. Edges $\{i, j\}$ represent particularly strong and/or significant statistical interdependencies between two climate time series $\{x_i(t)\}$, $\{x_j(t)\}$, where usually some kind of filtering procedure is applied first to reduce the effects of the annual cycle (Donner et al., 2008). Put differently, for some pairwise measure of statistical association C_{ij}, a climate network's adjacency matrix is given by

$$A_{ij} = \begin{cases} \Theta\left(C_{ij} - T_{ij}\right) & \text{if } i \neq j, \\ 0 & \text{otherwise,} \end{cases} \tag{3.17}$$

where T_{ij} denotes a threshold parameter and $A_{ii} = 0$ is set for all vertices i to exclude self-loops. Usually, the threshold is fixed globally, *i.e.*, $T_{ij} = T$ for all vertices i, j.

---

[8]Note that the term *climate network* is also used in distinct contexts that are unrelated to graph theory or data analysis, *e.g.*, for describing collections of climatological/weather observation stations like the *Greenland climate network* (Steffen and Box, 2001) or associations of political organizations dealing with anthropogenic climate change such as the *Climate Network Europe* (Raustiala, 2001).

T_{ij} may be set for each pair individually to only include edges with values of C_{ij} exceeding a prescribed significance level, *e.g.*, determined from a statistical test using surrogate time series (Paluš et al., 2011). In most studies, symmetric measures of statistical interdependencies $C_{ij} = C_{ji}$ have been considered, leading to undirected climate networks. However, Malik et al. (2012) and Gozolchiani et al. (2011) recently exploited asymmetries in the cross-correlation function as well as in a measure of event synchronization to reconstruct directed climate networks.

A careful and differentiated treatment of the construction, graph-theoretical analysis, and interpretation (Steps 3, 4, and 5 in Fig. 3.6) of climate networks has been provided by Radebach (2010). Finally, when considering the results of climate network studies summarized in the following sections, it is important to bear in mind that certain properties of functional networks (like climate networks or functional brain networks), *e.g.*, the small-world property, can be spuriously induced by the network's spatial embedding and/or the statistical association measures used for network reconstruction (Bialonski et al., 2010; Bialonski et al., 2011). An overview of relevant studies on climate networks is compiled in Table 3.1.

Table 3.1.: Summary of the types of data, statistical interdependency measures C_{ij}, and properties of the resulting climate networks considered in studies published in or submitted to peer-reviewed journals or conference proceedings. The studies are grouped according to their main topical focus following the structure of the main text, where further relevant findings of unpublished diploma and Bachelor's theses are reported. Abbreviations for climatological observables: geopotential height (GPH), streamfunction (SF), surface air temperature (SAT), air temperature on fixed isobaric surface (AT), sea level pressure (SLP), precipitation (PR), and sea surface temperature (SST). Coupled climate networks between observables X and Y are indicated by X↔Y. Abbreviations for data source: observations (obs.), reanalysis (rean.), model (mod.). Abbreviations for statistical interdependency measures: Pearson correlation coefficient at zero lag P_{ij}, Spearman's Rho at zero lag S_{ij}, correlation strength $W_{ij} = \max_\tau(|P_{ij}(\tau)|)/\mathrm{std}(|P_{ij}(\tau)|)$ ($P_{ij}(\tau)$ is the cross-correlation function), maximum cross correlation $P_{ij}^{\max} = \max_\tau(|P_{ij}(\tau)|)$, phase synchronization strength W_{ij}^{PS}, modified correlation strength $\tilde{W}_{ij} = (\max_\tau(|P_{ij}(\tau)|) - \langle|P_{ij}(\tau)|\rangle_\tau)/\mathrm{std}_\tau(|P_{ij}(\tau)|)$, standard mutual information at zero lag M_{ij}, ordinal pattern mutual information at zero lag M_{ij}^{OP}, event synchronization strength Q_{ij}, Gaussian process regression (GPR). Spatial resolution Δx is given as latitudinal × longitudinal. Studies using grids with approximately homogenous (homogen.) vertex distribution on the sphere are indicated. Temporal resolution is denoted by Δt. In some cases, when the exact number of vertices N is not reported or several N are used, only its order of magnitude is given. n/a indicates that a specific property is not applicable or used in the respective work. It is notable that the edge density ρ varies between $\mathcal{O}(10^{-3})$ (Donges et al., 2009b, P21; Barreiro et al., 2011) and $\mathcal{O}(1)$ (Yamasaki et al., 2008) across all studies.

Reference	Data	Source	Region	Δx	Period	Δt	C_{ij}	N
Climate network construction, basic topology, and statistical analysis								
Tsonis and Roebber (2004)	GPH	rean.	global	5°×5°	1948–1999	monthly	$|P_{ij}|$	2,664
Tsonis et al. (2006)	GPH	rean.	global	5°×5°	1950–2004	monthly	$|P_{ij}|$	2,664
—"—	GPH,SF	rean.	30°–90°N	5°×5°	1950–2004	monthly	$|P_{ij}|$	864
Gong et al. (2008)	SAT	rean.	global	5°×5°	1948–2005	daily	$|P_{ij}|$	2,592
Tsonis et al. (2008b)	GPH	rean.	global	5°×5°	1950–2004	monthly	$|P_{ij}|$	2,664
—"—	GPH	rean.,mod.	30°–90°N	5°×5°	1950–2004	monthly	$|P_{ij}|$	864
Donges et al. (2009a, P22) Donges et al. (2009b, P21)	SAT	rean.	global	2.5°×2.5°	1948–2007	monthly	$|P_{ij}|$,M_{ij}	10,224
Donges et al. (2009a, P22) Donges et al. (2009b, P21)	SAT	mod.	global	2.5°×3.75°	1860–1999	monthly	$|P_{ij}|$,M_{ij}	6,816
Steinhaeuser et al. (2010b)	various	rean.	global,oceans	5°×5°	1948–2010	monthly	$|P_{ij}|$	$\mathcal{O}(10^3)$
Barreiro et al. (2011)	SAT	rean.	global	2.5°×2.5°	1949–2006	monthly	M_{ij}^{OP}	10,226

Reference	Data	Source	Region	Δx	Period	Δt	C_{ij}	N
Berezin et al. (2012)	AT,GPH	rean.	diverse	5°×5°	1948–2006	daily	$\tilde{W}_{ij}$	$\mathcal{O}(10^2)$
Zou et al. (2011, P16)	SAT	rean.	global	2.5°×2.5°	1948–2007	monthly	$|P_{ij}|, M_{ij}$	10,224
Zou et al. (2011, P16)	SAT	mod.	global	2.5°×3.75°	1860–1999	monthly	$|P_{ij}|, M_{ij}$	6,816
Heitzig et al. (2012, P9)	SAT	mod.	global	2.5°×3.75°	1860–1999	monthly	$|P_{ij}|$	6,816
Ebert-Uphoff and Deng (2012a)	GPH	rean.	global	homogen.	1948–2011	daily	PC alg.	200
Ebert-Uphoff and Deng (2012b)	Clim. ind.	rean.	diverse	n/a	1948–2011	daily	PC alg.	4
—"—	Clim. ind.	rean.	diverse	n/a	1948–2011	monthly	PC alg.	4
Runge et al. (2012)	SLP	rean.	Europe	stations	1997–2003	daily	PC alg.	4

Regional studies

Reference	Data	Source	Region	Δx	Period	Δt	C_{ij}	N
Donner et al. (2008)	SAT	obs.	Japan	stations	1975–2005	daily	P_{ij}^{max}	13
Wang and Tsonis (2009)	GPH	rean.	global	5°×5°	1949–2006	monthly	$|P_{ij}|$	2,664
—"—	SAT	obs.	China	stations	1950–1999	annual	$|P_{ij}|$	160
Jung et al. (2012)	SST	obs.	Korea	stations	2005–2009	daily	n/a	957
Rheinwalt et al. (2012)	PR	obs.	Germany	stations	1951–2007	daily	Q_{ij}	2,342

Signature of large-scale modes of climate dynamics (ENSO, NAO, monsoon, . . .)

Reference	Data	Source	Region	Δx	Period	Δt	C_{ij}	N
Tsonis et al. (2007)	Clim. ind.	obs.,mod.	diverse	n/a	1900–2000	monthly	n/a	4
Gozolchiani et al. (2008)	SAT	rean.	diverse	7.5°×7.5°	1979–2005	daily	W_{ij}	$\mathcal{O}(10^2)$
Tsonis and Swanson (2008)	SAT	rean.	global	5°×5°	1950–2005	monthly	$|P_{ij}|$	2,664
Yamasaki et al. (2008)	SAT,AT	rean.	diverse	7.5°×7.5°	1979–2006	daily	W_{ij}	$\mathcal{O}(10^2)$
Wang et al. (2009)	SAT	rean.	global	5°×5°	1966–2005	daily	$|P_{ij}|$	2,592
Yamasaki et al. (2009)	SAT,AT	rean.	diverse	7.5°×7.5°	1979–2007	daily	W_{ij}^{PS}	$\mathcal{O}(10^2)$
Marwan et al. (2010a, C4)	SAT	rean.	global	2.5°×2.5°	1948–2009	6-hourly	W_{ij}, M_{ij}	10,224
Carpi et al. (2011)	SAT	rean.	Trop. Pacific	2.5°×2.5°	1948–2009	monthly	S_{ij}	1,156
Gozolchiani et al. (2011)	AT,SAT	rean.	global	homogen.	1957–2001	daily	$\tilde{W}_{ij}$	726
Guez et al. (2012)	AT,GPH	rean.	North Atlantic	2.5°×2.5°	1948–2006	daily	$\tilde{W}_{ij}$	825
Kawale et al. (2011)	SLP	rean.,mod.	global	2.5°×2.5°	1850–2100	monthly	$|P_{ij}|$	$\mathcal{O}(10^4)$
Malik et al. (2012)	PR	rean.	South Asia	0.5°×0.5°	1951–2007	daily	Q_{ij}	1,150
Paluš et al. (2011)	SAT	rean.	global	2.5°×2.5°	1958–2000	monthly	$|P_{ij}|$	10,224
Radebach et al. (subm. P4)	SAT	rean.	global	homogen.	1948–2009	daily	various	10,242

Continued on the next page

Reference	Data	Source	Region	Δx	Period	Δt	C_{ij}	N
Rehfeld et al. (in press)	proxy	obs.	Asia	stations	Holocene	irreg.	various	28
Community structure								
Steinhaeuser et al. (2010a)	various	rean.	global	$2.5°\times2.5°$	1948–2007	monthly	custom	$10,224$
Tsonis et al. (2011)	GPH,SLP,SAT	rean.,mod.	global	$10°\times10°$	1950–2005	monthly	$|P_{ij}|$	684
Steinhaeuser et al. (2012)	various	rean.	oceans	$5°\times5°$	1948–2007	monthly	$|P_{ij}|$	$\mathcal{O}(10^3)$
Predictions								
Das and Srivastava (2011)	various	rean.	global	$0.5°\times0.5°$	1982–2002	monthly	GPR	$\mathcal{O}(10^5)$
Davis et al. (2011)	various	rean.	oceans	$5°\times5°$	1948–2007	monthly	$|P_{ij}|$	$1,701$
Pelan et al. (2011)	various	rean.	oceans	$5°\times5°$	1948–2007	monthly	various	$\mathcal{O}(10^3)$
Steinhaeuser et al. (2011b)	various	rean.	oceans	$5°\times5°$	1948–2007	monthly	$|P_{ij}|$	$\mathcal{O}(10^3)$
Steinhaeuser et al. (2011a)	various	rean.	oceans	$5°\times5°$	1948–2007	monthly	$|P_{ij}|$	$\mathcal{O}(10^3)$
Coupled climate networks								
Donges et al. (2011b, P14)	GPH$\leftrightarrow$GPH	rean.	global	homogen.	1948–2009	monthly	$|P_{ij}|$	$5,124$
Feng et al. (2012)	GPH$\leftrightarrow$SST	rean.	60°S–60°N	$4/5°\times4/5°$	1948–2010	monthly	$|P_{ij}|$	$4,670$
Visualization								
Tominski et al. (2011, P12)	SAT	mod.	global	$2.5°\times3.75°$	1860–1999	monthly	$|P_{ij}|$	$6,816$
—"—	SAT	obs.	Germany	stations	1951–2006	daily	$|P_{ij}|$	$2,342$

Studies on basic topology and methodological options

The first functional network studies of climatological data reported global properties like the small-world effect, scale-free like degree distributions, typical edge length distributions as well as distinctively different large-scale network structure in the tropics and extratropics (Tsonis and Roebber, 2004; Tsonis et al., 2006; Tsonis, 2007). A detailed study of the local structural characteristics and vertex centralities in surface air temperature climate networks (Donges et al., 2009a, P22) led to the discovery of a pronounced geodesic backbone (Fig. 3.7) in the field of shortest-path betweenness centrality that is possibly related to a significantly increased matter and energy flow in major oceanic and atmospheric circulation patterns (Donges et al., 2009b, P21).[9] Recent results support this view by studying numerical fluid dynamical experiments (Kutza, 2012) as well as theoretically showing in a simplified setting that edges parallel to the main direction of flow are typically longer than those perpendicular to it (Molkenthin et al., 2012). Also considering the basic topology of climate networks, Berezin et al. (2012) focussed on investigating the temporal stability of their structure, while Steinhaeuser (2011) compared the inter- and intra-model variability of climate network topology based on simulations from multiple climate models and evaluated the effect of model resolution on larger-scale structural features.

Other studies concentrated on exploring and comparing various options for constructing climate networks. Linear Pearson correlation applied to temporally aggregated data (Gong et al., 2008) as well as ordinal pattern mutual information have been used to construct networks representing statistical associations in climate dynamics on different time scales (Barreiro et al., 2011). The performance of several linear and nonlinear measures C_{ij} has been compared (Donges et al., 2009a, P22; Pelan et al., 2011) and the effect of the common auto-dependencies in climatological time series investigated (Paluš et al., 2011). Runge et al. (2012); Ebert-Uphoff and Deng (2012a); Ebert-Uphoff and Deng (2012b) discussed the potentials for inferring climate networks mapping causal dependencies between time series (see the comments in Section 3.3.1). An overview of methodological options for constructing and analyzing climate networks has been given by Steinhaeuser et al. (2010b) and Zou et al. (2011, P16).

Regional studies

A small number of climate network studies focussed on regional climatological phenomena relying on meteorological station data or high resolution gridded fields from reanalysis projects or simulations, *e.g.*, covering Japan (Donner et al., 2008), China (Wang and Tsonis, 2009), South Asia (Malik et al., 2012), Korea (Jung et al., 2012), the Indian (Donges, 2009) and North Atlantic Oceans (Guez et al., 2012), and

---

[9]Analogously, shortest-path betweenness centrality can be interpreted as a measure of information flow in complex brain networks under the assumption that signals travel preferentially on shortest paths (Bullmore and Sporns, 2009). In the context of climatological fields, the term information flow can be used to describe the advective or diffusive transport of fluctuations from one location to the other (Vastano and Swinney, 1988).
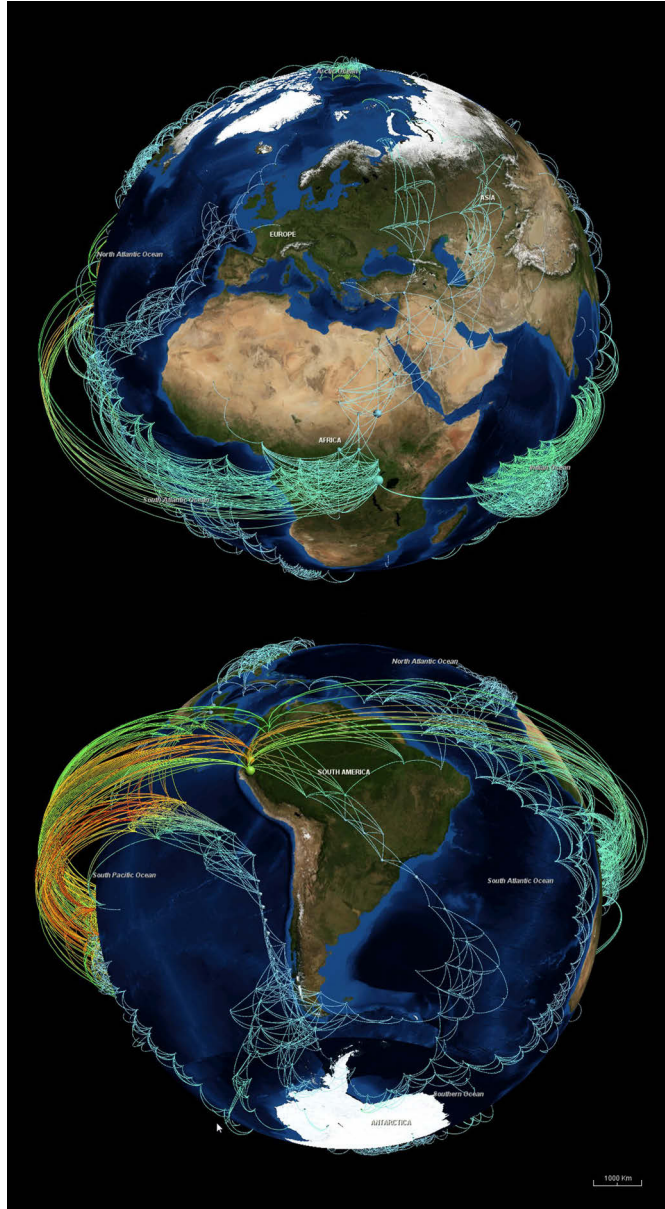
Figure 3.7.: Visualization of a global surface air temperature climate network taking into account the spatial embedding of vertices on the Earth's surface (Tominski et al., 2011, P12). Vertex color and size encode degree k_v (green: small, red: large) and shortest-path betweenness centrality b_v, respectively (visualization created with CGV (Tominski et al., 2009)). Edge color interpolates between the colors of both vertices adjacent to each edge. The network has been filtered by masking out vertices and edges with small shortest-path (edge) betweenness to reveal its geodesic backbone (Donges et al., 2009b, P21), the most central regions and their interdependencies in terms of shortest paths connecting different parts of the network.

A

B

N.s.i. degree

0.2 0.4 0.6 0.8 1 1.2

N.s.i. shortest-path betweenness (log scale)

0.5 1 1.5 2 2.5 3 3.5 4 4.5
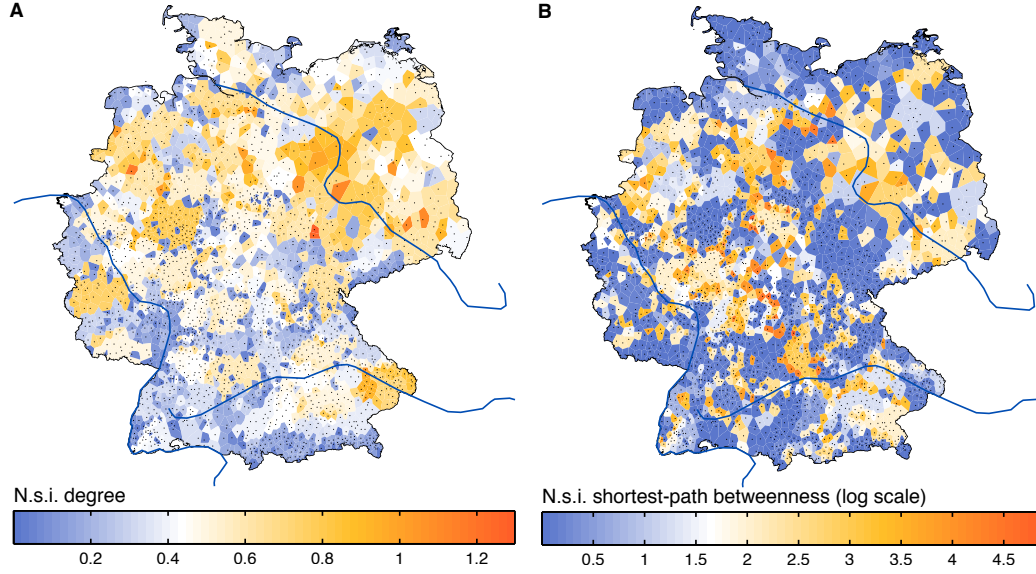
Figure 3.8.: Structural characteristics (A) n. s. i. degree k_v^* and (B) n. s. i. shortest-path between-ness b_v^* on a decadal log scale (Appendix A) for a regional climate network for Germany constructed from observational weather station data of daily mean surface air temperature covering the years 1951 to 2006. The raw data was provided by the German Weather Service and subsequently processed for improving its quality and consistency (Werner and Gerstengarbe, 2011). Pearson correlation at zero lag P_{ij} was used as the measure of statistical association and a global threshold T was selected to yield an edge density $\rho \approx 0.01$ (Tominski et al., 2011, P12). To account for the inhomogeneous distribution of meteorological stations (vertices, black dots) over Germany, the node splitting invariant network measures are computed using as weights w_i the area of the Voronoi cell (colored polygons) associated to each vertex.

the Arctic (Wiedermann, 2011; Heitzig et al., 2012, P9). Climate networks constructed from observational data over Germany have been investigated by Tominski et al. (2011, P12) and Rheinwalt (2011); Rheinwalt et al. (2012). Among others, notable features in a regional climate network constructed from daily surface air temperature (SAT) data over Germany include: (i) a pronounced northeast to southwest gradient in n. s. i. degree k_v^* pointing at a comparably larger correlation length in the SAT field over the North German Plain (Fig. 3.8A) as well as (ii) structures of large n. s. i. shortest-path betweenness b_v^* that locally coincide with orographic features such as the Black Forest or the Middle Rhine Highlands (Fig. 3.8B). Furthermore, Rheinwalt (2011); Rheinwalt et al. (2012) devised and applied a surrogate-based method for eliminating the boundary effects unavoidably arising in regionally limited networks (see Section 2.3 and Chapter 4).

Signature of large-scale modes of climate dynamics

Uncovering and understanding the signatures of large-scale modes of climate variability like the El Niño-Southern Oscillation (ENSO), the North Atlantic Oscillation (NAO), and other major teleconnection patterns, or the Asian monsoon in climate data is of paramount interest for climate network research. Linking this novel approach of climate data analysis to more classical techniques, Tsonis et al. (2008b) investigated the imprints of known teleconnection patterns defined by classical EOF analysis on climate network structure, and among others identified prominent supernodes (vertices with large degree k_v) related to NAO and the Pacific-North American (PNA) pattern. Donges (2009) pointed out some formal connections between the degree and eigenvector centralities of climate network analysis and the empirical orthogonal functions commonly studied in climatology. Furthermore, climate networks have been used to devise novel approaches for discovering known as well as previously unknown dipole structures in climate variability (Kawale et al., 2011; Steinhaeuser, 2011) that are conceptually similar to the classical teleconnection patterns of Wallace and Gutzler (1981).

The pronounced global effects of ENSO on the statistical interdependency structure of various climatological fields as represented by climate networks constructed from moving time windows (*evolving climate networks*) or data separated into El Niño and La Niña episodes have been studied by several authors (Gozolchiani et al., 2008; Tsonis and Swanson, 2008; Yamasaki et al., 2008; Yamasaki et al., 2009; Wang et al., 2009; Marwan et al., 2010a, C4; Radebach, 2010; Berezin et al., 2012; Carpi et al., 2011; Gozolchiani et al., 2011; Paluš et al., 2011; Zou et al., 2011, P16; Radebach et al., subm. P4). One main finding is that climate dynamics appears to become more spatiotemporally complex and, hence, less predictable during El Niño events (Tsonis and Swanson, 2008; Yamasaki et al., 2008). Moreover, investigating the behavior of global characteristics of evolving climate networks like transitivity $\mathcal{T}$ or average path length $\mathcal{L}$, Radebach et al. (subm. P4) were able to disentangle the signatures of La Niña events, volcanic eruptions, and distinct types of El Niño episodes, namely Eastern Pacific and Central Pacific events.

Similarly, climate networks have been employed to study the temporal evolution and global imprints of the North Atlantic Oscillation (Guez et al., 2012; Paluš et al., 2011). They furthermore provide valuable insights into the spatial organization, scales, and structure of extreme rainfall events during the Indian summer monsoon, identifying, *inter alia*, water vapor pathways and decadal-scale moisture sinks over the South Asian region (Malik et al., 2012). Tsonis et al. (2007) used a climate network-like approach to detect global climate shifts during the 20th century based on a small number of climate indices describing the dynamics of large-scale modes like ENSO or NAO.

Community structure

Searching for community structure (Fortunato, 2010) in climate networks is a promising data-driven approach for dividing the Earth's climate system into dynamically related regions. Studies based on univariate (Tsonis et al., 2011; Steinhaeuser et al., 2012) and multivariate (Steinhaeuser et al., 2010a) data as well as employing different algorithms for community detection in networks reported a small number of robust significant communities for most climatological variables. This suggests that the complexity of the climate system may reduce to a small number of interacting components beyond synoptic time scales (Tsonis et al., 2011). From a methodological point of view, it can be argued that network-based community detection is better suited for climate data analysis tasks such as defining climate indices than classical methods like k-means clustering algorithms (Steinhaeuser et al., 2010a; Steinhaeuser et al., 2011a).

Predictions

While most research on climate networks has been of a descriptive nature, the information on complex interrelationships in climate dynamics contained in the networks can be exploited for making predictions. Climate indices derived from significant communities detected in climate networks have been successfully used for predicting regional climate variability (Steinhaeuser et al., 2011b) and enabled significantly better predictions than standard clustering algorithms applied directly to the underlying climate data (Steinhaeuser et al., 2011a; Pelan et al., 2011). Without relying on community detection, probabilistic graphical models allowed to construct climate networks with predictive power (Das and Srivastava, 2011; Banerjee, 2011). Furthermore, Malik et al. (2012) drew on directed climate networks for forecasting monsoonal rainfall events on short time scales. In contrast to the previously mentioned studies that focussed on predictions of climate time series, a comparison of methods for predicting the appearance or disappearance of edges in evolving climate networks has been presented by Davis et al. (2011).

Multivariate and coupled climate networks

One option for condensing information from more than one climatological observable in a climate network is to define edges based on statistical interdependencies between multivariate time series describing the dynamics of multiple observables recorded at the same locations/vertices. For example, Steinhaeuser et al. (2010a) analyzed a climate network constructed from surface air temperature, pressure, relative humidity, and precipitable water to extract regions of related climate variability (see above). In contrast to this multivariate approach, coupled climate networks are designed to represent statistical dependencies within and between multiple climatological fields or within and between different regions (Chapter 7). For this purpose, all univariate time series from each of the involved climatological fields are associated to vertices in the resulting network. Coupled climate networks have been applied for studying

interactions between Earth system tipping elements (McKechnie, 2010), the Earth's atmosphere's general circulation structure (Schultz, 2010; Donges et al., 2011b, P14), processes linking climate variability in the North Atlantic and North Pacific regions via the Arctic (Wiedermann, 2011), and global atmosphere-ocean interactions (Feng et al., 2012). The theoretical foundations for studying coupled climate networks are elaborated in Section 2.4.

Challenges in estimating climate network properties and their solutions

In the many climate network studies relying on regular latitude-longitude grids or station data (Table 3.1), vertices typically represent differently sized shares of the Earth's surface, *i.e.*, they carry non-uniformly distributed weights (Section 2.5). To correct for the resulting distortions in standard measures of complex network theory, Tsonis et al. (2006) first proposed an area-weighted version of the degree centrality. Extending and generalizing this idea, a framework for deriving consistently weighted versions of any network property of interest based on the concept of node splitting invariance has been developed and validated in the context of climate network analysis (Heitzig et al., 2012, P9) (see Fig. 3.8). Consistently weighted variants of interacting network measures have been shown to be relevant for the investigation of coupled climate networks (Wiedermann, 2011; Wiedermann et al., 2013, P1), particularly when studying local network properties close to the poles, where the vertex density of regular latitude-longitude grids varies most strongly with latitude (Wiedermann, 2011; Heitzig et al., 2012, P9) (see Figs. 2.8 and 3.6).

Since a climate data set is a discrete representation of a spatially continuous field, the resulting climate network properties should not depend strongly on the chosen spatial resolution. This was shown to be indeed the case, as long as the number of vertices N is large enough (Sexton, 2009).

Another factor potentially distorting the statistical analysis of climate networks is the local spatial correlation structure of most climatological variables, *i.e.*, the dynamics at neighboring locations is usually more similar than that at more distant points (Radebach et al., subm. P4). A modified version of the local clustering coefficient that aims to correct for this effect has been introduced by Tsonis et al. (2008a). As an alternative and more general approach to solve this problem, ensembles of network surrogates with a prescribed edge length distribution $p(l)$ may be used to test for the effect of spatial correlations on any climate network property of interest (Donges et al. (2012, P8) and Section 4.5).

Visualization

For complementing the analysis of climate networks, it is beneficial to directly visualize their structure either including or discarding the spatial embedding of vertices. In the spirit of explorative data analysis, this procedure can be helpful for gaining an overview of the network structure, discovering traces of underlying climatological processes, and generating hypotheses that can then be tested by other means. However, visualizing

the full network structure is usually only feasible for networks with a small number of vertices, *e.g.*, in the climate network constructed from 13 Japanese weather station records by Donner et al. (2008). Larger networks, such as those usually encountered in climate network studies (Table 3.1), typically lead to cluttered views that obscure most useful information (Feng et al., 2012, Fig. 7). One solution to enable the visual exploration of large climate networks in the face of these problems is interactive visualization involving techniques like edge bundling (Fig. 3.6, lower left panel) or filtering for vertices and edges that do not meet prescribed requirements such as centrality, size, or length (Tominski et al., 2011, P12) (Fig. 3.7).

3.4. Summary

This chapter provided an overview of methods for the complex network-based analysis of both isolated time series and spatiotemporal data sets. While we emphasized theoretical and methodological aspects, a review of applications has been given focussing on geoscientific studies that are (sometimes remotely) related to Earth system analysis. Concerning isolated time series, special attention has been payed to recurrence network analysis, a versatile nonlinear technique that can be, among other uses, harnessed for detecting subtle dynamical transitions in time series or defining novel measures of dimensionality of chaotic attractors and general point sets. With respect to spatiotemporal data sets such as climatological fields, special focus was put on providing a thorough review of research in the rapidly developing field of climate network analysis. This review included own work on general climate network structure and construction, regional climate networks, the signature of qualitatively distinct El Niño episodes as well as climate network visualization. Particularly, it set the stage for the coupled climate networks introduced in Chapter 7.

Chapter 4.

A general analytical framework for describing spatial networks

4.1. Introduction

Most kinds of data-based networks proposed so far, *e.g.*, the recurrence and climate networks reviewed in the previous chapter, are spatial networks (Barthélemy (2011) and Section 2.3), since vertices are embedded either in phase space, on the time axis, or in real physical space. This implies that general results obtained for this large class of networks representing many of the complex systems found in nature, technology, and society are applicable to time series networks as well. Following Donges et al. (2012, P8), the main aim of this chapter is to introduce and apply for the first time an analytical theory for recurrence network analysis of time series (Section 3.2.2). However, the concepts and measures developed here can be readily generalized to describe the structure of a wider class of spatial networks, *e.g.*, random networks with an arbitrary prescribed edge length distribution $p_l(l) = p(l)$[10] (Section 4.5), which is of interest for statistically investigating and modeling climate networks and other types of networks encountered in Earth system analysis.

As discussed in Section 3.2, all methods of network-based time series analysis first construct a mapping from time series to network space and, subsequently, attempt to interpret the statistical characteristics of the resulting (typically complex) networks in terms of the properties of the underlying dynamical system. While these interpretations are mostly based on empirical findings for paradigmatic model systems and heuristic arguments, only a few rigorous results are available. So far, Lacasa et al. (2009) have pointed out a relationship between the scaling exponent of the degree distribution $p_k(k) \propto k^{-\gamma}$ in visibility graphs constructed from fractional Brownian motion and the Hurst exponent. Exact results are also available for horizontal visibility graphs constructed from random time series (Luque et al., 2009). Furthermore, close relationships between the transitivity properties (network transitivity and local clustering coefficients) (Donner et al., 2011b, P15) as well as the degree distribution's power-law scaling exponent γ (Zou et al., 2012, P6) of ε-recurrence networks and the (fractal) global and local dimensionality of the attracting set underlying the time series have been found. Constituting random geometric graphs (Dall and Christensen,

---

[10]Throughout this chapter, $p_l(l)$ is used indicate the edge length distribution to avoid confusing the latter with the probability density function $p(x)$ that is defined on the set S for all $x \in S$.

2002), ε-recurrence networks represent the geometry induced by the time series in phase space in a simple and well-defined way. This enabled Donner et al. (2010c, P19); Donner et al. (2011b, P15) to define continuous transitivity properties depending solely on the geometry of the (attracting) set S and the probability density function $p(x)$. These can in turn be calculated analytically for paradigmatic model systems with smooth and self-similar geometry and are approximated by the corresponding discrete ε-recurrence network measures.

Given the diverse and successful applications of ε-recurrence network analysis reported in the literature (see Chapter 3.2), it is important to establish a firm theoretical foundation for advancing the understanding of the method. Building on earlier work (Donner et al., 2011b, P15), we propose here an analytical framework for ε-recurrence network analysis of time series encompassing neighborhood-based transitivity measures, mesoscopic measures relying on network motifs (Milo et al., 2002), path-based network characteristics as well as spectral and random walk-based measures. Specifically, our theory describes all graph-theoretical recurrence network quantifiers that have been used in the literature so far (Donner et al., 2010c, P19). Beyond forming a solid theoretical basis for this modern nonlinear approach to time series analysis and fostering its detailed understanding in a way comparable to that of standard linear time series analysis (Brockwell and Davies, 2002), our analytical framework opens several avenues for practically improving the method when dealing with finite (real-world) time series: (i) We are able to obtain closed-form analytical results for paradigmatic model systems with stochastic (uniform and Gaussian noise) and deterministic (periodic, quasi-periodic, and chaotic) dynamics. These can in turn be harnessed as a benchmark for the discrete standard estimators from complex network theory which have been employed so far (Donner et al., 2010c, P19), *e.g.*, for assessing the estimators' bias and variance. (ii) This bottom-up approach allows us to design improved, weighted statistical estimators (Heitzig et al., 2012, P9) which may be more appropriate in specific situations. (iii) Moreover, our framework enables us to derive rigorous bounds for feasible values of the recurrence threshold ε, the most important parameter of the method, the choice of which is critical when analyzing finite (experimental) time series (Donner et al., 2010a, P18).

This chapter is organized as follows: We introduce a continuous framework for recurrence network analysis in Section 4.2. After reviewing the corresponding discrete estimators (Section 4.3), we present examples ranging from periodic and quasi-periodic dynamics and higher-dimensional symmetric sets over chaotic maps to stochastic processes and compare some of the results to discrete estimates (Section 4.4). We conclude with a discussion of these achievements and elaborate on generalizations of the proposed framework for describing more general spatial networks (Section 4.5).
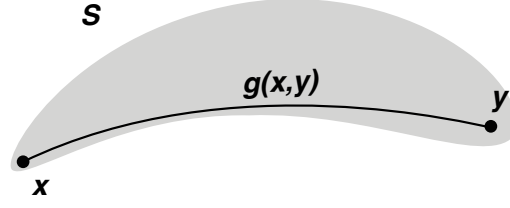
Figure 4.1.: Illustration of a set S (gray), where $g(x, y)$ denotes the geodesic distance between $x, y \in S$.

4.2. Continuous framework

4.2.1. General setting

Let us consider a path-connected Lebesgue-measurable subset $S \subset X$ of an m-dimensional compact smooth manifold X with a non-vanishing continuous probability density function $p : S \to (0, \infty)$ with $\int_S d^m x \, p(x) = 1$. We will use the abbreviation $\int d\mu(x) = \int_S d^m x \, p(x)$ throughout this chapter, where μ is a probability measure on S (Fig. 4.1). Then we can define "continuous" equivalents of all relevant graph-theoretical measures for ε-recurrence networks which may be approximated by calculating their discrete counterparts in the limit $\varepsilon \to 0$, $N \to \infty$ (Section 4.3). Here ε is the threshold used for network construction (Eq. (3.3)) and N denotes the number of data points (samples, phase space vectors, ...) considered. These measures capture the properties of a "continuous" network with uncountably many vertices and edges which may be defined (see Section 2.2) by a continuous analog of the adjacency matrix, the *adjacency function*

$$A(x, y) = \Theta(\varepsilon - \|x - y\|) - \delta_{xy} \tag{4.1}$$

for all $x, y \in S$. It is important to realize that the framework introduced here is not restricted to ε-recurrence networks alone, but may be more generally applied to describe random geometric graphs (aka spatial networks) (Dall and Christensen, 2002; Herrmann et al., 2003; Penrose, 2003) and other types of networks with strong spatial constraints (Barnett et al., 2007; Itzkovitz and Alon, 2005).

In the following we will formally define the proposed continuous recurrence network measures and discuss their properties, interrelationships, and interpretations (see Table 4.1 for an overview). Statements made for the limits $\varepsilon \to 0$ and $x \to y$ for $x, y \in S$ should be understood to hold for smooth S and p. We do not consider them for fractal geometries explicitly.

4.2.2. Neighborhood-based measures

Among other interesting properties, it has been shown that the local and global transitivity properties of ε-recurrence networks measured by the local clustering coefficient $\mathcal{C}_i$ and the global transitivity $\mathcal{T}$, respectively, are closely related to a

Table 4.1.: A summary of the continuous geometric properties of the set S (Fig. 4.1) and its associated probability density p defined in Section 4.2 (the adjective "continuous" is omitted for brevity). The heuristic interpretations follow Donner et al. (2010c, P19); Donner et al. (2011a, P13). See main text for formal probabilistic interpretations. SP abbreviates "shortest path".

Class	Name	Heuristic interpretation
Neighborhood-based		
Local	ε-degree density (Eq. (4.2))	Local density
	local ε-clustering (Eq. (4.3))	Local dimension
	ε-matching index (Eq. (4.4))	Local density gradient
Global	ε-edge density (Eq. (4.5))	Average local density
	ε-transitivity (Eq. (4.6))	Global dimension
	global ε-clustering (Eq. (4.7))	Average local dimension
	ε-assortativity (Eq. (4.8))	Average local density gradient
Mesoscopic	ε-motif density (Eq. (4.9))	Higher-order density structure
		Density anisotropy
Path-based		
Local	ε-closeness (Eq. (4.12))	Geometric centrality
	ε-efficiency (Eq. (4.13))	—"—
	ε-SP betweenness (Eq. (4.14))	Geometric bottleneckishness
	ε-SP edge betweenness (Eq. (4.18))	—"—
Global	ε-average path length (Eq. (4.25))	Average separation
	global ε-efficiency (Eq. (4.27))	—"—
	ε-diameter (Eq. (4.32))	Geometric diameter
	ε-radius (Eq. (4.33))	Geometric radius

certain notion of the fractal dimension of an underlying set S and its associated probability density $p(x)$ with $x \in S$ (Donner et al., 2011b, P15). To capture this theoretically, continuous versions of both measures denoted $\mathcal{C}(x; \varepsilon)$ and $\mathcal{T}(\varepsilon)$ have been defined together with a continuous degree density $\rho(x; \varepsilon)$.

Local measures

Definition 4.1. *The* continuous ε-degree density

$$\rho(x; \varepsilon) = \int_{B_\varepsilon(x)} d\mu(y) \tag{4.2}$$

measures the probability that a point y randomly drawn according to p lies in an ε-neighborhood $B_\varepsilon(x) = \{y \in S : \|x - y\| \leq \varepsilon\}$ of x.

Definition 4.2. *In turn, the* continuous local ε-clustering coefficient *of any point* $x \in S$,

$$\mathcal{C}(x;\varepsilon) = \frac{\iint_{B_\varepsilon(x)} d\mu(y)\, d\mu(z)\Theta(\varepsilon - \|y - z\|)}{\rho(x;\varepsilon)^2}, \tag{4.3}$$

is the probability that two points y and z randomly drawn according to p are closer than ε given they are both closer than ε to x.

Definition 4.3. *The* continuous ε-matching index $\mathcal{M}(x, y, \varepsilon)$ *measures the overlap between the neighborhoods of $x, y \in S$,*

$$\mathcal{M}(x,y;\varepsilon) = \frac{\int_{B_\varepsilon(x)\cap B_\varepsilon(y)} d\mu(z)}{\int_{B_\varepsilon(x)\cup B_\varepsilon(y)} d\mu(z)}. \tag{4.4}$$

It gives the probability that a point z drawn randomly from $B_\varepsilon(x)$ according to p is also contained in $B_\varepsilon(y)$ and vice versa.

For $x \to y$, $\mathcal{M}(x, y; \varepsilon) \to 1$. Furthermore, $\mathcal{M}(x, y; \varepsilon) = 0$ if $\|x - y\| > 2\varepsilon$.

Global measures

Definition 4.4. *The* continuous ε-edge density

$$\begin{aligned}\rho(\varepsilon) &= \int_S d\mu(x)\rho(x;\varepsilon) \\ &= \int_S d\mu(x) \int_{B_\varepsilon(x)} d\mu(y)\end{aligned} \tag{4.5}$$

is the expectation value of the continuous ε-degree density $\rho(x; \varepsilon)$.

Definition 4.5. *As a global measure of geometric transitivity, we define the* continuous ε-transitivity *of S as*

$$\mathcal{T}(\varepsilon) = \frac{\iiint_S d\mu(x)\, d\mu(y)\, d\mu(z)\Theta(\varepsilon - \|x - y\|)\Theta(\varepsilon - \|y - z\|)\Theta(\varepsilon - \|z - x\|)}{\iiint_S d\mu(x)\, d\mu(y)\, d\mu(z)\Theta(\varepsilon - \|x - y\|)\Theta(\varepsilon - \|x - z\|)}, \tag{4.6}$$

which is the probability that among three points x, y, z drawn randomly according to p, y and z are closer than ε given they are both closer than ε to x.

Definition 4.6. *Similarly, the* continuous global ε-clustering coefficient

$$\mathcal{C}(\varepsilon) = \int_S d\mu(x)\mathcal{C}(x;\varepsilon) \tag{4.7}$$

is defined as the expectation value of the continuous local ε-clustering coefficient $\mathcal{C}(x; \varepsilon)$ (Eq. (4.3)).

Note that the above defined measures of transitivity have been mainly considered for the supremum norm L_∞ in Donner et al. (2011b, P15).

Definition 4.7. Continuous ε-assortativity

$$\mathcal{A}(\varepsilon) = r\left(\rho(x;\varepsilon), \rho(y;\varepsilon) \;\mid\; \|x-y\| < \varepsilon\right) \tag{4.8}$$

gives the Pearson product-moment correlation coefficient (Brockwell and Davies, 2002) of the degree densities $\rho(x;\varepsilon)$ and $\rho(y;\varepsilon)$ of all points x,y that are closer than ε to each other.

$\mathcal{A}(\varepsilon)$ can be considered as a measure of the smoothness of the set S and the probability density p (Donner et al., 2010c, P19). In the limit $\varepsilon \to 0$, $\mathcal{A}(\varepsilon) \to 1$ holds.

4.2.3. Mesoscopic measures

Motifs of order α are small connected subgraphs of α vertices that are embedded within the topology of a complex network (Milo et al., 2002). For combinatorial reasons, usually $\alpha < 5$ is considered. Measuring motif densities is a useful approach for quantifying higher-order neighborhood relationships in complex geometries (Xu et al., 2008) and may be seen as a generalization of the transitivity concepts introduced above.

Definition 4.8. *The* continuous ε-motif density

$$M_\beta^\alpha = \left(\prod_{i=1}^\alpha \int_S d\mu(x_i)\right) \prod_{(j,k)\in E_\beta^\alpha} \Theta(\varepsilon - \|x_j - x_k\|) \tag{4.9}$$

quantifies the frequency of occurrence of a certain motif of order α described by the corresponding edge set E_β^α, where $\beta = 1,\ldots,n(\alpha)$ and $n(\alpha)$ is the total number of distinct motifs of order α. M_β^α is the probability that α points drawn randomly according to p are arranged according to the motif described by E_β^α.

For example, the density $M_\sqcup^4$ of the motif $\sqcup$ of order 4 is measured by

$$M_\sqcup^4 = \left(\prod_{i=1}^4 \int_S d\mu(x_i)\right) \Theta(\varepsilon - \|x_1 - x_2\|)\Theta(\varepsilon - \|x_2 - x_3\|)\Theta(\varepsilon - \|x_3 - x_4\|). \tag{4.10}$$

In contrast to the study of motifs for other general complex networks (Milo et al., 2002), it is neither meaningful nor necessary to normalize motif densities by their expectation values for randomized networks here. The reason is that the M_β^α already have a natural probability interpretation. To render the results for different α more comparable, one may consider to use relative motif densities normalized by $\sum_{\beta=1}^{n(\alpha)} M_\beta^\alpha$.

We conjecture that motif densities as generalizations of the continuous ε-transitivity are like the latter related to certain notions of the dimensionality of the set S and its associated probability density p (Donner et al., 2011b, P15). This would allow us to define and study a new class of motif-based measures of dimensionality analogously
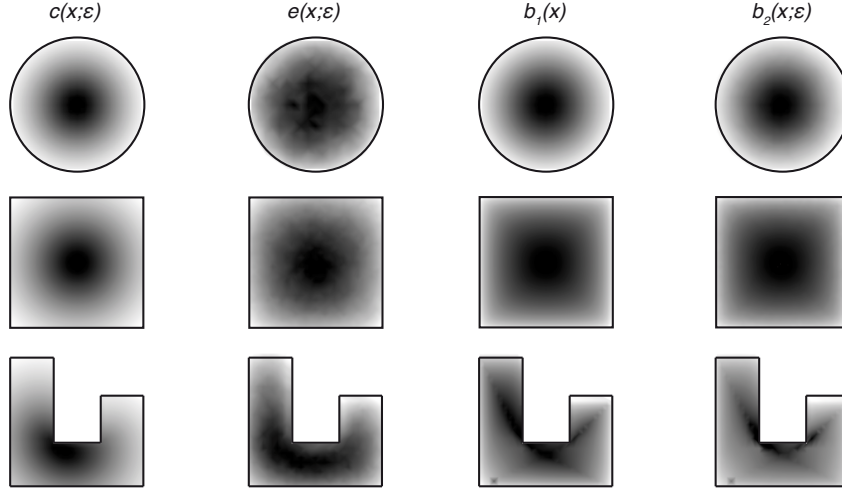
Figure 4.2.: Local path-based measures continuous ε-closeness $c(x;\varepsilon)$, ε-efficiency $e(x;\varepsilon)$, and ε-shortest-path betweenness $b_1(x)$ (based on Eq. (4.15)), $b_2(x;\varepsilon)$ (based on Eq. (4.16)) in three example sets S with a uniform density p: two convex sets (circle and square) and a nonconvex set. The grayscale indicates the value of the measures (white: small, black: large) obtained by Monte Carlo numerical integration using the Euclidean norm for small ε to avoid boundary effects. Note the more complex structure of the betweenness field, displaying particularly large values (dark) at the inward corners where many shortest paths must pass. In contrast to the path-based measures shown here, continuous ε-degree $\rho(x;\varepsilon)$ and local ε-clustering coefficient $\mathcal{C}(x;\varepsilon)$ are constant in the interior of S due to the uniform p. Variations of these measures due to boundary effects occur only closer than ε to the boundary of S (Donner et al., 2011b, P15).

to the sequence of Rényi dimensions from dynamical systems theory (Hentschel and Procaccia, 1983) (see Appendix D).

4.2.4. Path-based measures

While the neighborhood-based properties defined above describe the small-scale geometry of the set S and probability density p, path-based measures quantify their global geometry in terms of global geodesics (see Fig. 4.2 for examples). Most of the path-based concepts defined below do not conceptually depend on the threshold ε. Nevertheless, we introduce the appropriate scaling with ε into the definitions for consistency with the corresponding discrete estimators from complex network theory (Section 4.3) and the recurrence network literature.

As in standard topological terminology, a *path* in S is a continuous function $f : [0, 1] \to S$, and its *path length* $l(f) \in [0, \infty]$ is the supremum of $\sum_{i=1}^{n} d(f(t_{i-1}), f(t_i))$ over all $n > 0$ and all tuples $0 = t_0 \leq \ldots \leq t_n = 1$, where $d(\cdot, \cdot)$ is some metric. Note that $l(f)$ can be infinite in which case the path is called *non-rectifiable*. For points x, y, the *geodesic distance* $g(x, y) \in [0, \infty]$ is the infimum of $l(f)$ over all paths in

S from x to y (*i.e.*, with $f(0) = x$ and $f(1) = y$).[11] A corresponding path of this length is called a *global geodesic* or shortest curve (O'Neill, 2006). Depending on the geometry of S, there may be none, one, or multiple distinct global geodesics connecting x and y, but in a sufficiently well-behaved set S, there will usually be a unique global geodesic for almost every pair x, y (Fig. 4.1) and almost every metric (in particular, for the Euclidean metric). By "almost every" we mean as usual that the set of exceptions has zero measure. Note that, however, for some pathological metrics global geodesics are rarely unique, including the L_1 and L_∞ metrics.

To understand the reasoning behind the following definitions, one has to note that discrete shortest paths in random geometric graphs approximate global geodesics connecting two points $x, y \in S$ for small ε and large N. Then the shortest-path length $d_{ij}(\varepsilon)$ (the minimum number of edges that have to be traversed to reach vertex i from vertex j (Newman, 2003)) approximates $g(x(t_i), x(t_j))$, *i.e.*,

$$\varepsilon d_{ij}(\varepsilon) \approx g(x(t_i), x(t_j)), \tag{4.11}$$

where $x = x(t_i)$ and $y = x(t_j)$ (Fig. 4.1). In the limit $\varepsilon \to 0$, and if $N \to \infty$ sufficiently fast, we argue in Section 4.6.1 that indeed $\varepsilon d_{ij}(\varepsilon) \to g(x(t_i), x(t_j))$, independently of which metric is used for constructing the ε-recurrence network.

Local measures

Definition 4.9. *Given that a point y is drawn randomly according to p,* continuous ε-closeness

$$c(x; \varepsilon) = \left(\int_S d\mu(y) \frac{g(x, y)}{\varepsilon} \right)^{-1} = \varepsilon \left(\int_S d\mu(y) g(x, y) \right)^{-1} \tag{4.12}$$

is the inverse expected geodesic distance of y to another chosen point x in units of ε.

Definition 4.10. *Similarly,* continuous local ε-efficiency

$$e(x; \varepsilon) = \int_S d\mu(y) \left(\frac{g(x, y)}{\varepsilon} \right)^{-1} = \varepsilon \int_S d\mu(y) g(x, y)^{-1} \tag{4.13}$$

gives the expected inverse geodesic distance of y to x measured in units of ε.

---

[11]Note that when defined in this way, $g(x, y)$ may change discontinuously under continuous changes of the probability density p. This is because we require the geodesics to stay within S which consists of all points x where $p(x) \neq 0$. When $p(x)$ is continuously changed to zero, the length of geodesics running through x for $p(x) > 0$ may change abruptly once $p(x) = 0$ is reached, *e.g.*, when x constitutes some kind of geometric bottleneck. If this behavior is undesirable, one may consider generalized p-weighted notions of the geodesic distance. These could be motivated by an analogy to the optical path length in heterogeneous and non-isotropic media in physics, where the probability density p would play the role of the spatially varying refractive index.

Both $c(x; \varepsilon)$ and $e(x; \varepsilon)$ quantify the geometric closeness of x to any other point in S given a probability density p. Hence, points in the center of S will carry larger values of $c(x; \varepsilon)$ and $e(x; \varepsilon)$ than those on its boundaries (see Fig. 4.2 and below).[12]

Definition 4.11. Continuous ε-shortest-path betweenness

$$b(x; \varepsilon) = \iint_S d\mu(y)\, d\mu(z) \frac{\sigma(y, z; x; \varepsilon)}{\sigma(y, z)}, \tag{4.14}$$

is the probability that a point x lies on a randomly chosen global geodesic connecting two points y, z drawn randomly from S according to p. Here, $\sigma(y, z; x; \varepsilon)$ denotes the number of times $x \in S$ lies on a global geodesic between $y, z \in S$ and $\sigma(y, z)$ is the total number of global geodesics between y, z (Fig. 4.3).

In pathological situations, *e.g.*, for certain open sets S, $\sigma(y, z)$ may be zero even when the geodesic distance $g(y, z)$ is well-defined and finite. We ignore these cases for now. There are several ways to formally define $\sigma(y, z; x; \varepsilon)$. Using a parametrization $f_\kappa(t)$ of the family of global geodesics connecting y and z, with $t \in [0, 1]$ and $f_\kappa(0) = y$, $f_\kappa(1) = z$, we may write

$$\sigma_1(y, z; x; \varepsilon) = \sum_{\kappa=1}^{\sigma(y,z)} \int_0^1 dt\, \delta(f_\kappa(t) - x) = \sigma_1(y, z; x), \tag{4.15}$$

where $\delta(\cdot)$ is Dirac's multi-dimensional delta function. Alternatively, we can include the finite ε-effect by counting all shortest paths that pass through the ε-neighborhood of x by setting

$$\sigma_2(y, z; x; \varepsilon) = \sum_{\kappa=1}^{\sigma(y,z)} \int_0^1 dt\, \Theta(\varepsilon - \|f_\kappa(t) - x\|). \tag{4.16}$$

Both variants of $\sigma(y, z; x; \varepsilon)$ yield different, yet qualitatively similar results for $b(x; \varepsilon)$ as is illustrated in Fig. 4.2.

Given convex domains S, $\sigma(y, z) = 1$ always holds, *i.e.*, there is only one straight line connecting y and z, parametrized by $f(t) = y + t(z - y)$. For one-dimensional, convex sets S and using $\sigma_1(y, z; x)$, continuous ε-shortest-path betweenness simplifies to

$$b(x) = 2 \iint_S d\mu(y)\, d\mu(z) \Theta(x - y)\Theta(z - x). \tag{4.17}$$

Definition 4.12. Continuous ε-shortest-path edge betweenness

$$b(x, y; \varepsilon) = \iint_S d\mu(z)\, d\mu(w) \frac{\sigma(z, w; x, y; \varepsilon)}{\sigma(z, w)}, \tag{4.18}$$

---

[12] An analogous behavior is observed for visibility graphs that are embedded on the time axis (Donner and Donges, 2012b, P7).

A   **B**
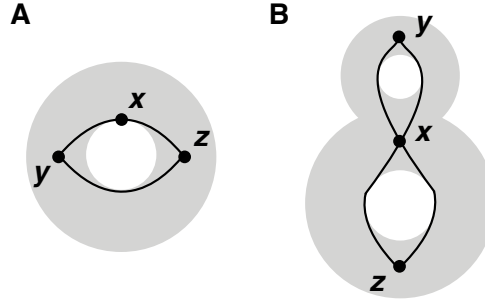
Figure 4.3.: Illustration of the definition of continuous ε-shortest-path betweenness (the set S is indicated by gray shading). (A) There are $\sigma(y, z) = 2$ global geodesics connecting $y, z \in S$, but only $\sigma(y, z; x; \varepsilon) = 1$ includes $x \in S$. (B) In this example, x lies on all four global geodesics between x and y, i.e., $\sigma(y, z) = \sigma(y, z; x; \varepsilon) = 4$.

is the probability that two points x, y both lie on a randomly chosen global geodesic connecting two points z, w drawn randomly according to p. $\sigma(z, w; x, y; \varepsilon)$ counts the number of global geodesics between z, w which contain x, y.

Analogously to continuous ε-shortest-path betweenness $b(x; \varepsilon)$, we can define this quantity as

$$\sigma_1(z, w; x, y; \varepsilon) = \sum_{\kappa=1}^{\sigma(z,w)} \left(\int_0^1 dt\, \delta(f_\kappa(t) - x) \right) \left(\int_0^1 dt\, \delta(f_\kappa(t) - y) \right), \qquad (4.19)$$

$$= \sigma_1(z, w; x, y).$$

Further generalizations for including the finite ε-effect may be deduced as shown above for continuous ε-shortest-path betweenness.

For one-dimensional convex sets S and using $\sigma_1(z, w; x, y; \varepsilon)$, Eq. (4.18) reduces to

$$b(x, y) = 2 \iint_S d\mu(z)\, d\mu(w) \Theta(x - z)\Theta(y - z)\Theta(w - x)\Theta(w - y). \qquad (4.20)$$

In the limit $x \to y$ we always have $b(x, y; \varepsilon) \to b(x; \varepsilon)$. We note that $b(x, y; \varepsilon)$ does not require the condition $\Theta(\varepsilon - \|x - y\|)$ as is the case for the corresponding discrete estimator (Table 4.2). Related generalized concepts of co- and group betweenness have been described for discrete complex networks (Kolaczyk et al., 2009).

For general well-behaved S we almost surely have $\sigma(z, w) = 1$, i.e., the probability that there is more than one global geodesics connecting z and w drawn randomly from S according to p is zero. For example, in both Figs. 4.3A and B, the set of pairs z, w with $\sigma(z, w) = 2$ and $\sigma(z, w) = 4$, respectively, is of measure zero. In these cases, $b(x; \varepsilon)$ and $b(x, y; \varepsilon)$ reduce to

$$b(x; \varepsilon) = \iint_S d\mu(y)\, d\mu(z) \sigma(y, z; x; \varepsilon) \qquad (4.21)$$

and

$$b(x, y; \varepsilon) = \iint_S d\mu(z)\, d\mu(w) \sigma(z, w; x, y; \varepsilon). \tag{4.22}$$

It should be noted that for general S and p, the center of mass

$$X = \int_S d\mu(x) x \tag{4.23}$$

does not necessarily extremize $c(x; \varepsilon)$, $e(x; \varepsilon)$, or $b(x; \varepsilon)$. However, for convex S, the generalized continuous ε-closeness

$$c_\eta(x; \varepsilon) = \left(\int_S d\mu(y) \left(\frac{g(x, y)}{\varepsilon} \right)^\eta \right)^{-1} = \varepsilon^\eta \left(\int_S d\mu(y) g(x, y)^\eta \right)^{-1} \tag{4.24}$$

can be shown to assume a global maximum at $x = X$ for the special case $\eta = 2$. In turn, the standard continuous ε-closeness $c(x; \varepsilon)$ ($\eta = 1$) is maximized at the geometric median or Fermat-Weber point (Fekete et al., 2005).

Global measures

Definition 4.13. *The* continuous ε-average path length

$$\mathcal{L}(\varepsilon) = \iint_S d\mu(x)\, d\mu(y) \frac{g(x, y)}{\varepsilon} = \varepsilon^{-1} \iint_S d\mu(x)\, d\mu(y) g(x, y). \tag{4.25}$$

measures the expected geodesic distance in units of ε between two points x and y drawn randomly according to p.

From Eq. (4.25), the equivalence of this formulation of continuous average path length to the intensively studied problem in probabilistic geometry (Bailey et al., 2006) of finding the expectation value of the distance between two randomly drawn points $x, y \in S$ according to the probability density p becomes evident. Our definitions imply the relationship

$$\mathcal{L}(\varepsilon) = \int_S d\mu(x) c(x; \varepsilon)^{-1}. \tag{4.26}$$

Definition 4.14. *Similarly, the* continuous global ε-efficiency

$$\mathcal{E}(\varepsilon) = \left(\iint_S d\mu(x)\, d\mu(y) \left(\frac{g(x, y)}{\varepsilon} \right)^{-1} \right)^{-1} \tag{4.27}$$

$$= \varepsilon^{-1} \left(\iint_S d\mu(x)\, d\mu(y) g(x, y)^{-1} \right)^{-1}.$$

is the inverse of the expected inverse geodesic distance between two points x, y drawn randomly according to p measured in units of ε.

Here, we have

$$\mathcal{E}(\varepsilon) = \left(\int_S d\mu(x)e(x;\varepsilon) \right)^{-1}. \tag{4.28}$$

More generally, let $\Delta_{S,p}(\eta)$ be the expectation value of a power η of the geodesic distance $g(x,y)$ between two points $x, y \in S$ randomly drawn according to p:

$$\Delta_{S,p}(\eta) = \iint_S d\mu(x)\,d\mu(y)g(x,y)^\eta. \tag{4.29}$$

Then, continuous ε-average path length and global ε-efficiency may be expressed as

$$\mathcal{L}(\varepsilon) = \varepsilon^{-1}\Delta_{S,p}(1) \tag{4.30}$$

and

$$\mathcal{E}(\varepsilon) = \varepsilon^{-1}\left(\Delta_{S,p}(-1) \right)^{-1}. \tag{4.31}$$

Definition 4.15. *The ε-diameter*

$$\mathcal{D}(\varepsilon) = \varepsilon^{-1} \sup_{x,y \in S} g(x,y) \tag{4.32}$$

and the ε-radius

$$\mathcal{R}(\varepsilon) = \varepsilon^{-1} \inf_{x \in S} \sup_{y \in S} g(x,y) \tag{4.33}$$

are global geometric characteristics of the set S that are independent of p (O'Neill, 2006).

4.2.5. Further measures

To illustrate that the proposed framework can be extended in several directions, we shortly discuss spectral and random-walk-based measures in the context of continuous recurrence networks. Motivated by the study of eigenvector centrality in complex networks (Newman, 2003), we first consider spectral properties of the set S and probability density p.

Definition 4.16. *The linear Laplace operator*

$$\left(\mathbb{L}_\varepsilon h \right)(x) = \int_S d\mu(y) \left[\Theta(\varepsilon - \|x - y\|) - \delta(x - y)\rho(y;\varepsilon) \right] h(y) \tag{4.34}$$

is a continuous equivalent of the discrete Laplacian matrix in network theory (Newman, 2003).

We are interested in its eigenfunctions $h(x)$ and eigenvalues λ satisfying

$$(\mathbb{L}_\varepsilon h)(x) = \lambda h(x) \tag{4.35}$$

for all $x \in S$.[13] For example, considering an arbitrary S with uniform p, one obtains an eigenfunction $h(x) = C$ for some $C \in \mathbb{R}$ associated with the eigenvalue $\lambda = 0$. This is analogous to the eigenvector $(1, 1, \ldots, 1)$ with eigenvalue 0 which is always present for the discrete Laplacian matrix of general networks (Newman, 2003). We can expect more interesting results for non-uniform p. For example, one may define a continuous analog of the eigenvector centrality of complex network theory (Bonacich, 1972) by considering the eigenfunction $\tilde{h}(x)$ corresponding to the largest eigenvalue $\tilde{\lambda}$.

For discrete networks, there are several measures of betweenness based on random walks rather than shortest paths (Arenas et al., 2003; Newman, 2005). Continuous versions of these measures would be based on continuous analogs of random walks on S that start and end at points y and z randomly chosen from p. Since in a discrete network the limit distribution of a random walk without a sink is proportional to the degree distribution, a natural choice for a continuous analog is an Itō diffusion process, the limit distribution of which is proportional to $\rho(x; \varepsilon)$, with a source at y and a sink at z (Øksendal, 2003). Such a process can most easily be defined as a gradient flow $dX_t = -\nabla \Psi(X_t)\, dt + \sqrt{2T}\, dB_t$ that combines a Brownian motion B with a local drift coefficient $-\nabla \Psi(X_t)$ which comes from a potential $\Psi(x)$ that is the product of a temperature $T > 0$ and the information corresponding to $\rho(x; \varepsilon)$, which is $-\ln \rho(x; \varepsilon)$. The resulting process

$$dX_t = T\frac{\nabla \rho(X_t; \varepsilon)}{\rho(X_t; \varepsilon)}\, dt + \sqrt{2T}\, dB_t \tag{4.36}$$

can then be interpreted as a diffusion that drifts in the direction of increasing density. The continuous version of Arenas' random walk betweenness (Arenas et al., 2003) would then be the expected density of the process at x when the source and sink are drawn from p. Similarly, the continuous version of Newman's random walk betweenness (Newman, 2005) would be the expected absolute value of the resulting flux density at x for a random source and sink.

4.2.6. Behavior under affine transformations

All continuous measures defined above are based on neighborhood relationships in S and geodesic distances between points therein. They are therefore invariant with respect to the subclass of affine transformations which leaves these properties unchanged, *i.e.*, $x \to Dx + s$ for $x \in S$ with D being a combination of rotation and isotropic scaling operations and s a translation. This is to be understood in the sense that for a measure f, $f(Dx + s; a\varepsilon) = f(x; \varepsilon)$ holds, where a is the scaling factor.

---

[13] Alternatively, one could study the spectral properties of a linear *adjacency operator* $(\mathbb{A}_\varepsilon h)(x) = \int_S d\mu(y)\Theta(\varepsilon - \|x - y\|)h(y)$.

The measures considered here are generally not invariant under non-isotropic scaling and shear operations.

4.3. Discrete estimators

Given the continuous framework defined above, we are able to treat the commonly used recurrence network quantifiers (Donner et al., 2010c, P19; Donner et al., 2011a, P13) taken from standard complex network theory (Newman, 2003; Boccaletti et al., 2006) as the most straightforward *discrete estimators* of the continuous quantities for a finite number of observations N and finite ε. The discrete estimators will be denoted using hats, *e.g.*, the discrete estimator of continuous average path length $\mathcal{L}(\varepsilon)$ is $\hat{\mathcal{L}}(\varepsilon, N)$ (we will in the following omit the estimators' dependency on ε and N to simplify the notation). Their detailed properties have been numerically studied in detail in earlier works (Donner et al., 2010a, P18; Donner et al., 2010c, P19; Donner et al., 2011b, P15; Donner et al., 2011a, P13; Marwan et al., 2009, P20; Zou et al., 2010, P17). The characteristics of these standard measures for discrete and finite complex networks have also been studied for random geometric graphs and more general network models with strong spatial contraints (Barnett et al., 2007; Herrmann et al., 2003; Itzkovitz and Alon, 2005), *e.g.*, the degree distribution (Herrmann et al., 2003), network motifs (Itzkovitz and Alon, 2005), as well as clustering coefficient and degree correlations (Barnett et al., 2007).

Here, we briefly review the estimator's definitions (Table 4.2). For some specific examples, the estimators will be compared to the results theoretically derived from their continuous counterparts in Section 4.4. This will also allow us to gain certain insights into their bias and variance for finite data sets.

Table 4.2.: A summary of standard unweighted network estimators for the continuous geometric properties defined in Section 4.2. $\hat{\sigma}_{kl}$ denotes the number of shortest paths connecting $k, l \in V$, $\hat{\sigma}_{kl}(i)$ of those include $i \in V$ and $\hat{\sigma}_{kl}(i,j)$ contain $i,j \in V$. Modifications of path-based measures accounting for disconnected networks are discussed in Section 2.4.2. For a detailed treatment, see (Donner et al., 2010c, P19; Newman, 2003; Boccaletti et al., 2006; Costa et al., 2007). SP abbreviates "shortest path".

Class	Name	Definition
Neighborhood-based		
Local	Degree	$\hat{k}_i = \sum_{j=1}^N A_{ij}$
	Degree density	$\hat{\rho}_i = \frac{1}{N-1}\hat{k}_i$
	Local clustering coefficient	$\hat{C}_i = \dfrac{\sum_{j,k=1}^N A_{ij}A_{jk}A_{ki}}{\hat{k}_i(\hat{k}_i-1)}$
	Matching index	$\hat{\mu}_{ij} = \dfrac{\sum_{l=1}^N A_{il}A_{jl}}{\hat{k}_i+\hat{k}_j-\sum_{l=1}^N A_{il}A_{jl}}$
Global	Edge density	$\hat{\rho} = \frac{1}{N(N-1)}\sum_{i,j=1}^N A_{ij}$
	Transitivity	$\hat{\mathcal{T}} = \dfrac{\sum_{i,j,k=1}^N A_{ij}A_{jk}A_{ki}}{\sum_{i,j,k=1}^N A_{ki}A_{kj}}$
	Global clustering coefficient	$\hat{\mathcal{C}} = \left\langle \hat{\mathcal{C}}_i \right\rangle_{i=1}^N$
	Assortativity	$\hat{\mathcal{A}} = \dfrac{\frac{1}{2L}\sum_{i,j=1}^N \hat{k}_i \hat{k}_j A_{ij} - \left(\frac{1}{2L}\sum_{i,j=1}^N \frac{1}{2}(\hat{k}_i+\hat{k}_j)A_{ij}\right)^2}{\frac{1}{2L}\sum_{i,j=1}^N \frac{1}{2}(\hat{k}_i^2+\hat{k}_j^2)A_{ij} - \left(\frac{1}{2L}\sum_{i,j=1}^N \frac{1}{2}(\hat{k}_i+\hat{k}_j)A_{ij}\right)^2}$
Path-based		
Local	Closeness	$\hat{c}_i = \dfrac{N-1}{\sum_{j=1}^N d_{ij}}$
	Local efficiency	$\hat{e}_i = \frac{1}{N-1}\sum_{j=1}^N d_{ij}^{-1}$
	SP betweenness	$\hat{b}_i = \binom{N-1}{2}^{-1}\sum_{j,k\neq i}^N \dfrac{\hat{\sigma}_{jk}(i)}{\hat{\sigma}_{jk}}$
	SP edge betweenness	$\hat{b}_{ij} = \binom{N-1}{2}^{-1}\sum_{k,l\neq i,j}^N \dfrac{\hat{\sigma}_{kl}(i,j)}{\hat{\sigma}_{kl}}$
Global	Average path length	$\hat{\mathcal{L}} = \langle d_{ij}\rangle_{i,j=1}^N$
	Global efficiency	$\hat{\mathcal{E}} = \left(\langle d_{ij}^{-1}\rangle_{i,j=1}^N\right)^{-1}$
	Diameter	$\hat{\mathcal{D}} = \max_{i,j=1}^N (d_{ij})$
	Radius	$\hat{\mathcal{R}} = \min_{i=1}^N \max_{j=1}^N (d_{ij})$

4.3.1. Weighted network statistics and node splitting invariant measures

We may now ask how the estimation of the above defined continuous geometric properties from a finite data set can be improved with respect to the measures from complex network theory that have been used so far for this purpose. One way to go in line with standard estimation theory is vertex-weighted network statistics, as proposed by Heitzig et al. (2012, P9). For a full application of that theory, weights w_i for all vertices i have to be chosen in a suitable way which we leave as a subject of future research. But even with constant weights $w_i \equiv 1$, the axiomatic theory developed in Heitzig et al. (2012, P9) allows us to improve estimation by using so-called node splitting invariant (n. s. i.) versions of network measures to reduce the estimation bias that results from excluding self-loops from the network (Section 2.5). Let us illustrate this for the case of continuous ε-degree density, $\rho(x; \varepsilon) = \int_{B_\varepsilon(x)} d\mu(y)$. If x is a vertex, p is approximately constant in $B_\varepsilon(x)$, and the latter contains $\hat{k}_i$ additional vertices (see Table 4.2), then $\rho(x; \varepsilon) \approx p(x) \mathrm{Vol}(B_\varepsilon(x)) \approx (\hat{k}_i + 1)/N$ since $B_\varepsilon(x)$ contains $\hat{k}_i^* = \hat{k}_i + 1$ out of N vertices. In other words, $\hat{k}_i^*/N$ is a better estimator for $\rho(x; \varepsilon)$ than $\hat{k}_i/N$, since the latter has a bias of $\sim \mathcal{O}(1/N)$. Likewise, the transitivity measure $\hat{\mathcal{T}}$ (see Table 4.2) can be improved by using instead the n. s. i. transitivity $\hat{\mathcal{T}}^* = \sum_{i,j,k=1}^{N} A_{ij}^+ A_{jk}^+ A_{ki}^+ / \sum_{i,j,k=1}^{N} A_{ki}^+ A_{kj}^+$ (see Appendix A), where $A_{ij}^+ = A_{ij} + \delta_{ij} = R_{ij}$, showing that this approach is also more in line with recurrence plot analysis. This would also reduce the bias in the estimation of the *transitivity dimension* that was observed in Fig. 3.5. The measures $\hat{k}_i^*$ and $\hat{\mathcal{T}}^*$ are examples of n. s. i. measures with unit weights which can basically be interpreted as variants of the classical measures in which vertices are considered to be linked to themselves (Heitzig et al., 2012, P9).

4.3.2. Threshold selection in recurrence network analysis

A careful choice of the recurrence threshold ε is critical for faithfully estimating the continuous recurrence network properties defined above (Donner et al., 2010a, P18). For too large ε, *i.e.*, on the order of the diameter of S, boundary effects dominate, the discrete recurrence network used for estimation becomes too dense and is unable to capture the geometry induced by S and p (see Section 4.4.1). In contrast, the network's giant component breaks down for too small ε with a phase transition at the critical value ε_c. This obstructs our ability to properly estimate mesoscopic and path-based measures for $\varepsilon < \varepsilon_c$. Therefore we expect a good performance of the discrete estimators for thresholds just above the critical ε_c, where much of the geometric fine structure is still resolved (Donner et al., 2011b, P15).

The problem of selecting ε therefore reduces to deriving the percolation threshold ε_c which is directly related to the critical edge density $\rho_c = \rho(\varepsilon_c)$ of the theory of random geometric graphs (Penrose, 2003) via Eq. (4.5). ρ_c is linked to the commonly

studied critical mean degree z_c by

$$\rho_c = \frac{z_c}{N-1}. \tag{4.37}$$

The Erdős-Rényi graph is the simplest random network model (Newman, 2003). Since any pair of vertices is linked with the same probability ρ independently of their distance, it neglects the effects of spatial embedding. Therefore the Erdős-Rényi model is inadequate for describing d-dimensional random geometric graphs, and the corresponding critical mean degree $z_c = 1$ (Newman, 2003) turns out to be too low except for the limiting case $d \to \infty$ (Dall and Christensen, 2002) (see Section 4.4.1 for an example). Taking into account the effects of clustering of vertices induced by the spatial embedding (Bialonski et al., 2010) yields improved analytical bounds on the true z_c obtained from numerical simulations (Kong and Yeh, 2007). Exact analytical results for arbitrary d are not available so far, but Dall and Christensen (2002) have empirically found the scaling law

$$z_c(d) = z_c(\infty) + A d^{-\gamma} \tag{4.38}$$

from extensive numerical simulations, where $z_c(\infty) = 1$, $\gamma = 1.74(2)$ and $A = 11.78(5)$. Inverting $\rho_c = \rho(\varepsilon_c)$ (which is possible as $d\rho(\varepsilon)/d\varepsilon > 0$ in non-pathological situations) yields the associated critical threshold

$$\varepsilon_c(d) = \rho^{-1}\left(\frac{z_c(d)}{N-1}\right). \tag{4.39}$$

To our best knowledge this is the most useful result available so far for our aim of choosing the recurrence threshold ε. However, one should be aware that the results of (Dall and Christensen, 2002) were obtained for the box $S = [0,1]^d$ with uniform probability density p which is the most commonly studied setting in random geometric graph theory. When considering general S and p they may be appropriate as a first educated guess for properly selecting ε in line with the guidelines discussed in (Donner et al., 2010a, P18; Donner et al., 2011b, P15). Deriving analytical bounds on z_c for such geometries remains an open problem.

4.4. Examples

We illustrate the above defined continuous geometric quantities and their estimators for paradigmatic examples by giving closed-form analytical results and relating them to numerical evidence from ε-recurrence networks constructed from time series. The focus will be on examples where all quantities of interest can be calculated either analytically or semi-analytically (relying on numerical evaluation of some integrals), *i.e.*, possessing smooth sets S and density functions $p(x)$. This implies that when considering the Euclidean norm (which we will use for all examples below) and

neglecting boundary effects (Donner et al., 2010c, P19; Donner et al., 2011b, P15), we obtain

$$
\begin{aligned}
\mathcal{C}(x;\varepsilon) = 1 - \frac{d\Gamma(d/2)}{2\sqrt{\pi}\Gamma((d+1)/2)} &\left[{}_2F_1\left(\frac{1}{2}, \frac{1-d}{2}; \frac{3}{2}; \frac{1}{4}\right) \right. \\
&\left. - \frac{1}{d+1}{}_2F_1\left(\frac{1-d}{2}, \frac{d+1}{2}; \frac{d+3}{2}; \frac{1}{4}\right) \right] \\
&= \mathcal{C}(\varepsilon) = \mathcal{T}(\varepsilon)
\end{aligned}
\tag{4.40}
$$

for all transitivity-based measures, where ${}_2F_1(\cdot)$ is the hypergeometric function and d the manifold dimension of S. A simpler exponential scaling with d can be found for the supremum metric (Eq. (3.9)). Nontrivial transitivity-based properties for fractal sets S and densities $p(x)$ allowing for non-integer d, where an analytical calculation of path-based measures is problematic, have been treated exhaustively by Donner et al. (2011b, P15) (see Section 3.2.2 and Appendix D).

The results given here hold in the limit $\varepsilon \to 0$. For simplicity we ignore boundary effects which have been discussed by Donner et al. (2010c, P19); Donner et al. (2011b, P15). In all examples, we use the parametrization $\sigma_1(y, z; x)$ to compute continuous ε-shortest-path betweenness.

4.4.1. One-dimensional chaotic maps and stochastic processes

All examples considered in the following are defined on convex sets S embedded on the real axis. Therefore, the geodesic distance of $x, y \in \mathbb{R}$ reduces to $g(x, y) = |x - y|$. Since for one-dimensional S the integral $\int_S dy\, p(y)\, |x - y|^{-1}$ diverges for all p and all $x \in S$, we get $\mathcal{E}(\varepsilon) = 0$ and $e(x; \varepsilon) = \infty \ \forall x$ in all examples of this section. In contrast, the corresponding integral always converges for non-fractal S with $d \geq 2$ and general p.

Bernoulli map / uniformly distributed noise

The Bernoulli map $x_{n+1} = (2x_n) \mod 1$ defined on the interval $S = [0, 1)$ induces $p(x) = 1$. This yields

$$
\begin{aligned}
\mathcal{T}(\varepsilon) &= \mathcal{C}(\varepsilon) = \mathcal{C}(x; \varepsilon) = \frac{3}{4} \\
\mathcal{L}(\varepsilon) &= \frac{1}{3}\varepsilon^{-1} \\
c(x; \varepsilon) &= \frac{2\varepsilon}{1 - 2x + 2x^2} \\
b(x) &= 2x(1 - x).
\end{aligned}
$$

The same results hold for uniformly distributed noise on the interval $[0, 1]$, since S and $p(x)$ are identical to those of the Bernoulli map (an exemplary calculation for this setting is shown in Section 4.6.2). This equality clearly illustrates that recurrence

network analysis is purely geometric and, hence, by design masks out the auto-dependency structure of dynamical systems. Stochastic and deterministic dynamics can be distinguised when embedding techniques are used prior to recurrence network analysis (Donner et al., 2010c, P19).

Gaussian noise

Considering Gaussian noise with zero mean and standard deviation σ, *i.e.*, $p(x) = \left(1/\sqrt{2\pi\sigma^2}\right)\exp\left(-x^2/(2\sigma^2)\right)$, on the real axis $S = (-\infty, +\infty)$ we obtain

$$\mathcal{T}(\varepsilon) = \mathcal{C}(\varepsilon) = \mathcal{C}(x; \varepsilon) = \frac{3}{4}$$

$$\mathcal{L}(\varepsilon) = \frac{2\sigma}{\sqrt{\pi}}\varepsilon^{-1}$$

$$c(x; \varepsilon) = \frac{\varepsilon}{\sqrt{\frac{2}{\pi}}\sigma\exp\left(-\frac{x^2}{2\sigma^2}\right) + x\,\mathrm{erf}\left(\frac{x}{\sqrt{2}\sigma}\right)}$$

$$b(x) = \frac{1}{2}\left(1 - \mathrm{erf}\left(\frac{x}{\sqrt{2}\sigma}\right)^2\right),$$

where $\mathrm{erf}(x) = \frac{2}{\sqrt{\pi}}\int_0^x e^{-t^2}dt$ is the error function. The results for mean $\chi \neq 0$ can be derived by substituting $x \to x - \chi$ on the right side of the equations for the local measures given above (see also Section 4.2.6).

Logistic map

We can also give exact analytical solutions for the logistic map in the fully chaotic regime, $x_{n+1} = 4x_n(1 - x_n)$, defined on the interval $S = [0, 1]$. Using the probability density $p(x) = \pi^{-1}\sqrt{x(1-x)}^{-1}$ (Alligood et al., 2000) yields

$$\mathcal{T}(\varepsilon) = \mathcal{C}(\varepsilon) = \mathcal{C}(x; \varepsilon) = \frac{3}{4}$$

$$\mathcal{L}(\varepsilon) = \frac{4}{\pi^2}\varepsilon^{-1}$$

$$c(x; \varepsilon) = \pi\varepsilon\left(2\sqrt{x(1-x)} + (1 - 2x)\left(\arccos\left(\sqrt{x}\right) - \arcsin\left(\sqrt{x}\right)\right)\right)^{-1}$$

$$b(x) = \frac{8\,\mathrm{Im}\left[\mathrm{arcosh}\left(\sqrt{x}\right)\right]\arcsin\left(\sqrt{x}\right)}{\pi^2}.$$

Comparison to numerical results

Within an intermediate range of ε, the continuous ε-average path length $\mathcal{L}(\varepsilon)$ is approximated well by the estimators $\hat{\mathcal{L}}(\varepsilon)$ calculated from ε-recurrence networks for both the Bernoulli and logistic map (Fig. 4.4). For small ε, the estimator breaks down due to the finite number of samples used (finite size effect) after the network's giant
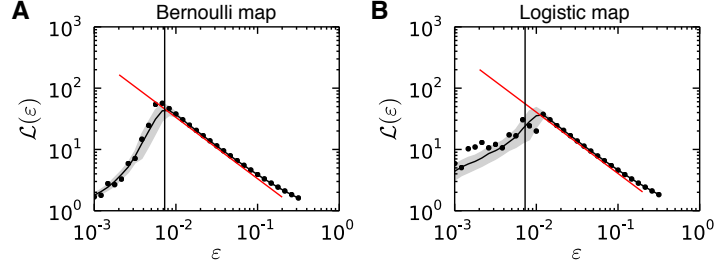
Figure 4.4.: Continuous ε-average path length $\mathcal{L}(\varepsilon)$ for (A) the Bernoulli map and (B) the logistic map. Analytical results are indicated by solid red lines. Estimates $\hat{\mathcal{L}}(\varepsilon)$ have been obtained from ε-recurrence networks constructed from one realization of $N = 1,000$ samples, respectively, for each map (black dots). Ensemble mean (dash-dotted black line) and standard deviation (gray band) for different ε have been obtained from a set of 100 realizations of each model with initial conditions uniformly distributed in the interval $[0, 1]$. Vertical lines indicate the estimated percolation thresholds ε_c (Eq. (4.39)).

component decomposes into smaller and smaller disconnected components. The Erdős-Rényi approximation yields a critical percolation threshold $\varepsilon_c = 1/(2(N-1)) \approx 5 \cdot 10^{-4}$ for both maps using the parameters of Fig. 4.4 which is one order of magnitude smaller than the numerically observed phase transition point (Fig. 4.4). As explained in Section 4.3.2, this is because the Erdős-Rényi model does not account for the effects of spatial embedding and clustering. To be able to use the relationship of Eq. (4.39) based on the empirical results of Dall and Christensen (2002) for $m = 1$, we approximate $\rho(\varepsilon) = 2\varepsilon$ (Bernoulli map) and $\rho(\varepsilon) = 8\varepsilon \operatorname{artanh}(1 - 2\varepsilon)/\pi^2$ (logistic map) for small ε. This yields $\varepsilon_c \approx 6.4 \cdot 10^{-3}$ for the Bernoulli map and $\varepsilon_c \approx 6.2 \cdot 10^{-3}$ for the logistic map, which is consistent with the phase transition points observed numerically (Fig. 4.4). The good agreement of predicted and observed phase transition for the Bernoulli map can be explained by the fact that the latter exactly meets the assumptions underlying the theory of Dall and Christensen (Section 4.3.2). These observations indicate that Eq. (4.39) is indeed useful for deriving an educated guess on the proper choice of ε, even for strongly varying probability densities p. Moreover, the phase transition for the logistic map occurs at notably larger ε than for the Bernoulli map. Consistently with the results of Kong and Yeh (2007), this indicates that the increased spatial clustering induced by peaks in the density p leads to larger values of the critical mean degree z_c and therefore the associated percolation threshold ε_c. However, the results of Barnett et al. (2007) suggest that there may be in fact no true phase transition in giant component size for non-uniform p in the limit $N \to \infty$.

For large ε, the approximation in Eq. (4.11) is not valid anymore and, hence, the discrete estimator breaks down in this regime. Note that $\mathcal{L}(\varepsilon_{c'}) = 1$ for a critical $\varepsilon_{c'}$. Since $\mathcal{L}(\varepsilon) < 1$ whereas $\hat{\mathcal{L}}(\varepsilon) = 1$ for $\varepsilon > \varepsilon_{c'}$, the definition of the discrete estimator is not meaningful anymore for thresholds larger than the critical threshold. For the Bernoulli map we have $\varepsilon_{c'} = 1/3$, while for the logistic map, $\varepsilon_{c'} = 4/\pi^2$ follows.

The continuous ε-closeness $c(x; \varepsilon)$ is approximated well by the estimator $\hat{c}(x_i; \varepsilon)$
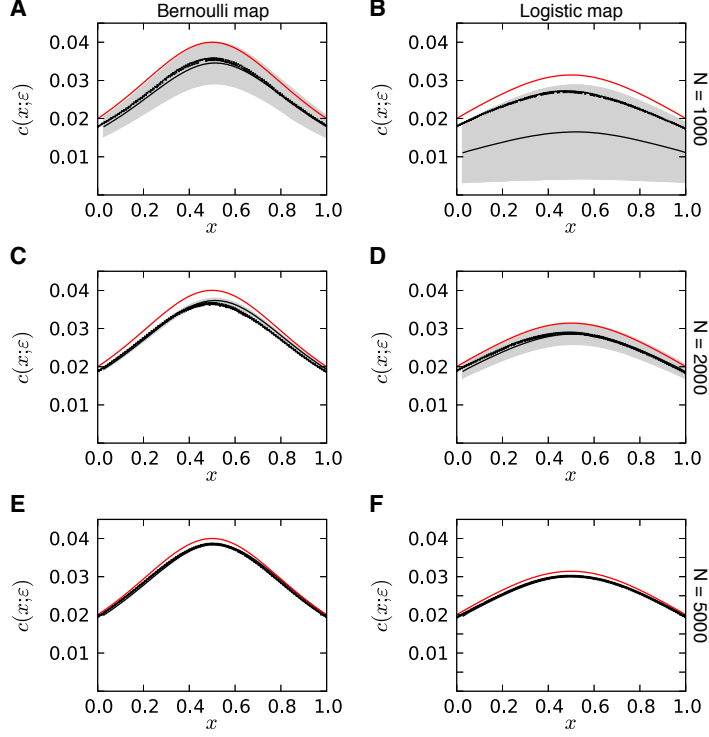
Figure 4.5.: Continuous ε-closeness $c(x;\varepsilon)$ for (A,C,E) the Bernoulli map and (B,D,F) the logistic map. Analytical results are indicated by red solid lines. Estimates $\hat{c}(x_i;\varepsilon)$ have been obtained from ε-recurrence networks at $\varepsilon = 0.01$ constructed from single realizations of (A,B) $N = 1,000$, (C,D) $N = 2,000$, and (E,F) $N = 5,000$ samples (all: black squares). Ensemble mean (black dash-dotted lines) and standard deviation (gray bands) have been calculated as in Fig. 4.4. The standard deviation is too small to be visible in the plots for $N = 5,000$ (E,F).

for both the Bernoulli and logistic maps (Fig. 4.5). However, $\hat{c}(x_i;\varepsilon)$ is notably smaller than the true theoretical value particularly in the center of S at $x = 1/2$, implying that shortest paths are longer in the empirical ε-recurrence network than expected theoretically. This is clearly a finite size effect as the bias and variance of the estimator decrease for growing N and fixed ε (Fig. 4.5).

The shape of continuous ε-shortest-path betweenness $b(x)$ is approached well by the estimator $\hat{b}(x_i;\varepsilon)$ for both maps (Fig. 4.6). However, there is a large bias that increases with the number of samples N, while the variance decreases with growing N. That the estimator $\hat{b}(x_i;\varepsilon)$ is generally smaller than the theoretical value $b(x)$ for all x can be explained by the skipping of vertices due to the finite ε in the empirical ε-recurrence network. This effect is expected to increase for growing N when ε is fixed, since more and more vertices can be skipped along a shortest path for the same recurrence radius ε, which also explains the growing bias in this setting. Accordingly, the bias decreases for decreasing ε when N is sufficiently large regarding
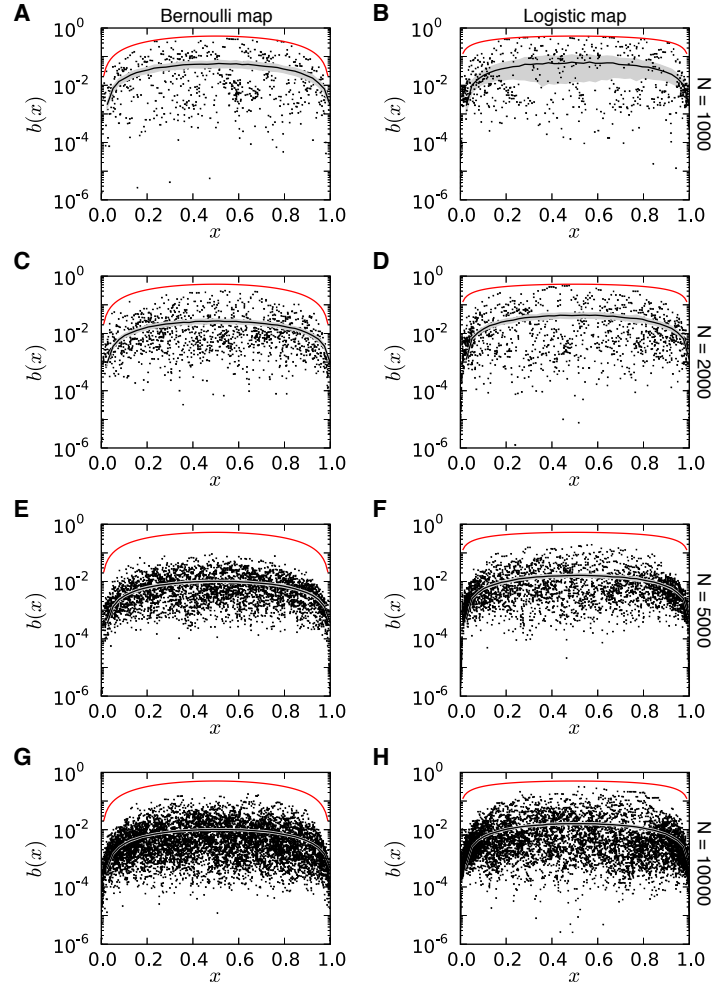
Figure 4.6.: Continuous ε-shortest-path betweenness $b(x)$ for (A,C,E,G) the Bernoulli map and (B,D,F,H) the logistic map. Analytical results are indicated by red solid lines. Estimates $\hat{b}(x_i; \varepsilon)$ have been obtained from ε-recurrence networks at $\varepsilon = 0.01$ constructed from single realizations of (A,B) $N = 1,000$, (C,D) $N = 2,000$, and (E,F) $N = 5,000$ samples (all: black squares). Panels (G,H) show results for $\varepsilon = 0.005$ and $N = 10,000$. Ensemble mean (black dash-dotted lines) and standard deviation (gray bands) have been calculated as in Fig. 4.4. Note that $\hat{b}(x_i; \varepsilon)$ is the discrete shortest-path betweenness of Donner et al. (2010c, P19), but normalized by its theoretical maximum value $(N-1)(N-2)/2$ (Table 4.2).

the discussion of suitable choices of ε in Section 4.3.2 (Fig. 4.6G,H). However, the bias is not a problem in practical situations, because for local measures we are usually only interested in relative differences between vertices and not in the absolute values.

4.4.2. Periodic and quasi-periodic dynamics

Periodic orbit

We analyze next a periodic orbit (general closed curve) of curve length l embedded in an m-dimensional phase space, *i.e.*, $S = \{x \in \mathbb{R}^m : x = f(s); s \in [0, l]; f(0) = f(l)\}$, with uniform probability density $p(x) = 1/l$. The geodesic distance of two points $x(s), x(t)$ along the curve is then given by $g(x(s), x(t)) = |s - t|$. This yields

$$\mathcal{T}(\varepsilon) = \mathcal{C}(\varepsilon) = \mathcal{C}(x; \varepsilon) = \frac{3}{4}$$

$$\mathcal{L}(\varepsilon) = \frac{l}{4} \varepsilon^{-1}$$

$$c(x; \varepsilon) = \frac{4\varepsilon}{l}$$

$$b(x) = \frac{1}{4}.$$

As the periodic orbit is a one-dimensional set we have $\mathcal{E}(\varepsilon) = 0$ and $e(x; \varepsilon) = \infty$ as in the examples in Section 4.4.1. *E.g.*, a circular orbit of radius R as generated by a harmonic oscillator with $S = \{x \in \mathbb{R}^2 : x_1 = R \sin(s/R), x_2 = R \cos(s/R); s \in [0, 2\pi R]\}$ and $p(x) = 1/(2\pi R)$ gives the above results with $l = 2\pi R$.

Flat 2-torus

Quasi-periodic dynamics is displayed by a system oscillating with two incommensurable frequencies ω_1 and ω_2, *i.e.*, where the ratio ω_1/ω_2 is not a rational number. The phase space trajectory fills a 2-torus $S = \{x = (s, t) : s \in [0, 2\pi R], t \in [0, 2\pi r]\}$ uniformly with $p(s, t) = p = 1/(4\pi^2 Rr)$. The radii R, r are related to the oscillation's amplitudes. With the geodesic distance

$$g((s,t),(s',t')) = \sqrt{\min\left(|s - s'|, 2\pi R - |s - s'|\right)^2 + \min\left(|t - t'|, 2\pi r - |t - t'|\right)^2}$$

we obtain

$$\mathcal{T}(\varepsilon) = \mathcal{C}(\varepsilon) = \mathcal{C}(x; \varepsilon) = 1 - \frac{3\sqrt{3}}{4\pi} \approx 0.5865$$

$$\mathcal{L}(\varepsilon) = \frac{\pi\varepsilon^{-1}}{12rR}\left(4rR\sqrt{r^2 + R^2} + 3r^3\mathrm{arsinh}\left(\frac{R}{r}\right) + 2R^3\mathrm{artanh}\left(\frac{r}{\sqrt{r^2 + R^2}}\right)\right.$$

$$\left. - r^3\mathrm{artanh}\left(\frac{R}{\sqrt{r^2 + R^2}}\right)\right)$$

$$\mathcal{E}(\varepsilon) = 2\pi r R \varepsilon^{-1} \left(2r \operatorname{artanh} \left(\frac{R}{\sqrt{r^2 + R^2}} \right) + R \ln \left(\frac{r + \sqrt{r^2 + R^2}}{-r + \sqrt{r^2 + R^2}} \right) \right)^{-1}.$$

Because of symmetry, the local path-based measures do not depend on x as for the periodic orbit discussed above and we have

$$c(x; \varepsilon) = \mathcal{L}(\varepsilon)^{-1}$$
$$e(x; \varepsilon) = \mathcal{E}(\varepsilon)^{-1}$$
$$b(x) = \frac{1}{4\pi^2 R r} = p.$$

As expected, in the limit $r \to 0$ the average path length converges to the value obtained for a circle of radius R (see above), *i.e.*, $\lim_{r \to 0} \mathcal{L}(\varepsilon) = (\pi R / 2) \varepsilon^{-1}$.

4.4.3. Higher-dimensional symmetric sets

The m-dimensional hyperball and hypercube may be viewed as tractable idealizations of higher-dimensional attracting sets of dynamical systems (in this section we set $d = m$, since the considered sets S all have integer dimension d). Their study highlights that continuous path-based measures may depend sensitively and non-trivially on the global geometry of the set. In contrast, their neighborhood and transitivity-based counterparts just depend on the dimension m and are therefore identical for the hyperball and hypercube (Eq. (4.40)), consistently with the dimensionality interpretation of $\mathcal{C}(x; \varepsilon)$ and $\mathcal{T}(\varepsilon)$ (Section 3.2.2 and Donner et al. (2011b, P15)). The sets considered here are convex, hence, $g(x, y) = \|x - y\|_2$ holds when using the Euclidean norm.

m-dimensional hyperball

We consider the m-dimensional hyperball $S = \mathbb{S}^m$ with the uniform probability density $p(x) = p = 1 / \int_S dx = \operatorname{Vol}(\mathbb{S}^m)^{-1} = \Gamma\left(\frac{m}{2} + 1\right) / \pi^{\frac{m}{2}}$. Following Hammersley (1950), the r-th moment of the distribution of point-to-point distances $\|x - y\|_2$ in $\mathbb{S}^m$ is given by

$$\mu_{mr} = 2 \frac{m \Gamma(m+1)}{\Gamma\left(\frac{1}{2}m + \frac{1}{2}\right)} \frac{\Gamma\left(\frac{1}{2}m + \frac{1}{2}r + \frac{1}{2}\right)}{(m+r)\Gamma\left(m + \frac{1}{2}r + 1\right)}. \tag{4.41}$$

Then the continuous ε-average path length is

$$\mathcal{L}(\varepsilon) = \mu_{m1}\varepsilon^{-1} = 2 \frac{m}{m+1} \frac{\Gamma(m+1)}{\Gamma\left(\frac{1}{2}m + \frac{1}{2}\right)} \frac{\Gamma\left(\frac{1}{2}m + 1\right)}{\Gamma\left(m + \frac{3}{2}\right)} \varepsilon^{-1}, \tag{4.42}$$
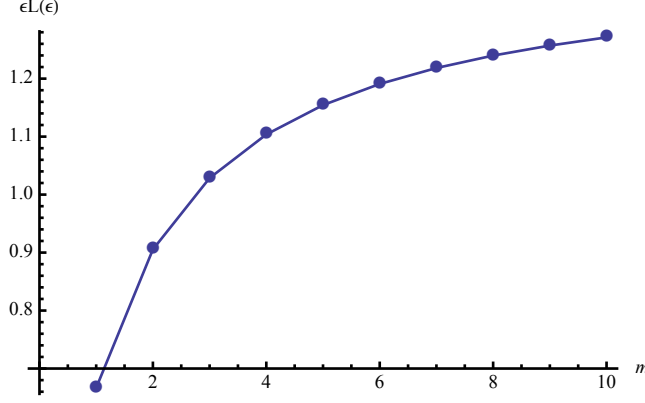
Figure 4.7.: Continuous ε-average path length $\varepsilon\mathcal{L}(\varepsilon)$ of the hyperball $\mathbb{S}^m$ with uniform probability density, obtained from Eq. (4.42).

and all its higher moments are known via Eq. (4.41) (see Fig. 4.7). Some examples for lower-dimensional spheres follow:

$$
\varepsilon\mathcal{L}(\varepsilon) =
\begin{cases}
\frac{2}{3} & m = 1 \\
\frac{128}{45}\pi^{-1} & m = 2 \\
\frac{36}{35} & m = 3 \\
\frac{16384}{4725}\pi^{-1} & m = 4 \\
\frac{800}{693} & m = 5
\end{cases}.
$$

Note that the result for $m = 1$ agrees with the corresponding one for the Bernoulli map when considering the stretching of the domain by a factor of 2, since $\mathbb{S}^1 = [-1, 1]$. In the limit $m \to \infty$ the continuous ε-average path length is $\mathcal{L}(\varepsilon) = \sqrt{2}\varepsilon^{-1}$ (see Fig. 4.7). We can also derive in closed form an expression for the continuous ε-closeness $c(0; \varepsilon)$ of the center of $\mathbb{S}^m$, taking advantage of the spherical symmetry:

$$
c(0; \varepsilon)^{-1} = \varepsilon^{-1} \int_{\mathbb{S}^m} dx_1 \dots dx_m\, p\sqrt{x_1^2 + \dots + x_m^2} = \varepsilon^{-1}\Omega_m p \int_0^1 dr\, r^{m-1}r.
$$

With the full solid angle in m dimensions $\Omega_m = m\pi^{\frac{m}{2}}/\Gamma(\frac{m}{2} + 1)$ this leads to

$$
c(0; \varepsilon) = \frac{m+1}{m}\varepsilon. \tag{4.43}
$$

The limit $\varepsilon c(0; \varepsilon)^{-1} \to 1$ for $m \to \infty$ shows that almost all of the measure $\mu(\mathbb{S}^m)$ of the unit radius hyperball $\mathbb{S}^m$ is concentrated at its surface for large m. For the special case of $m = 2$ (unit disk with uniform $p(x)$), Lew et al. (1978) give a nearly closed-form expression for the continuous ε-closeness at $x(q) = (q, 0)$,

$$
c(x(q); \varepsilon)^{-1} = \frac{1}{9\pi}\left(16(q^2 - 1)K(q^2) + 4(q^2 + 7)E(q^2)\right)\varepsilon^{-1},
$$

where $0 \leq q \leq 1$ and the value for arbitrary $x \in \mathbb{S}^2$ may be obtained after an appropriate rotation. $K(m)$ and $E(m)$ are complete elliptic integrals of the first and second kind (see §17.3 in Abramowitz and Stegun (1964)).

For the continuous local ε-efficiency $e(0; \varepsilon)$ of the center of $\mathbb{S}^m$ we get for $m > 1$

$$
\begin{aligned}
e(0; \varepsilon) &= \varepsilon \int_{\mathbb{S}^m} dx_1 \ldots dx_m \, p \sqrt{x_1^2 + \ldots + x_m^2}^{-1} = \varepsilon \Omega_m p \int_0^1 dr \, r^{m-1} r^{-1} \\
&= \frac{m}{m-1} \varepsilon.
\end{aligned}
$$

A somewhat more involved calculation of the continuous ε-betweenness $b(0)$ of the center of $\mathbb{S}^m$ yields (see Section 4.6.3)

$$
b(0) = \frac{1}{\Omega_m} = \frac{\Gamma(\frac{m}{2} + 1)}{m \pi^{\frac{m}{2}}}. \tag{4.44}
$$

The high degree of symmetry of $\mathbb{S}^m$ allows to derive closed-form results for local path-based measures at its center for many $p(x) = p(r, \Omega)$, as long as the probability density separates into a radial and an angular part, *i.e.*, $p(r, \Omega) = p(r)p(\Omega)$.

m-dimensional hypercube

The hypercube $S = \mathbb{K}^m = [0, 1]^m$ with uniform probability density $p(x) = p = \mathrm{Vol}(\mathbb{K}^m)^{-1} = 1$ is much harder to treat analytically than the hyperball $\mathbb{S}^m$. Hence, rigorous results are only available for isolated dimensions m and a subset of the continuous measures defined above (Anderssen et al., 1976; Bailey et al., 2006; Bailey et al., 2007; Bailey et al., 2010). Solving the resulting general box integrals remains a largely unsolved problem of applied and experimental mathematics.

The following closed-form expressions for the continuous ε-average path length $\mathcal{L}(\varepsilon)$ are based on the expectation values for point-to-point distances $\Delta_{\mathbb{K}^m}(1) = \varepsilon \mathcal{L}(\varepsilon)$ (see Eq. (4.29)) listed in Bailey et al. (2010):

$$
\varepsilon \mathcal{L}(\varepsilon) = \begin{cases} \frac{1}{3} & m = 1 \\ \frac{1}{15} \left(2 + \sqrt{2} + 5 \ln \left(1 + \sqrt{2} \right) \right) & m = 2 \\ -\frac{118}{21} - \frac{2}{3}\pi + \frac{34}{21}\sqrt{2} - \frac{4}{7}\sqrt{3} + 2\ln(1 + \sqrt{2}) + 8\ln(\frac{1+\sqrt{3}}{\sqrt{2}}) & m = 3 \end{cases}.
$$

Some numerical results for $m = 1, \ldots, 10$ are displayed in Fig. 4.8. Anderssen et al. (1976) proved the bounds

$$
\frac{1}{3}\sqrt{m} \leq \varepsilon \mathcal{L} \leq \sqrt{\frac{1}{6}m} \sqrt{\frac{1}{3} \left(1 + 2\sqrt{1 - \frac{3}{5m}} \right)} \tag{4.45}
$$

implying $\varepsilon \mathcal{L} \to \infty$ for $m \to \infty$. This is in contrast to the hyperball, where this limit is finite (see above). Using expectation values for the inverse point-to-point
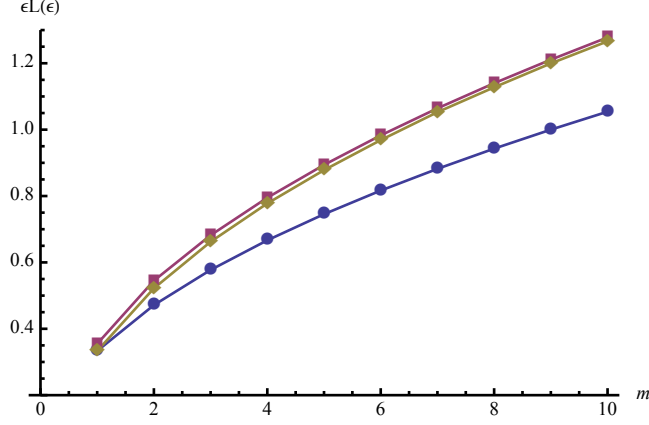
Figure 4.8.: Continuous ε-average path length $\varepsilon\mathcal{L}(\varepsilon)$ of the hypercube $\mathbb{K}^m$ with uniform probability density, obtained by numerical Monte Carlo integration using Mathematica (yellow diamonds). Analytical lower (blue disks) and upper (red squares) bounds from (Anderssen et al., 1976) are also shown.

distances $\Delta_{\mathbb{K}^m}(-1) = \varepsilon^{-1}\mathcal{E}(\varepsilon)^{-1}$, we are able to give the following expressions for the continuous ε-efficiency $\mathcal{E}(\varepsilon)$:

$$(\varepsilon\mathcal{E}(\varepsilon))^{-1} = \begin{cases} \infty & m = 1 \\ \frac{4}{3}(1 - \sqrt{2}) + 4\ln(1 + \sqrt{2}) & m = 2 \\ \frac{2}{5} - \frac{2}{3}\pi + \frac{2}{5}\sqrt{2} - \frac{4}{5}\sqrt{3} + 2\ln(1 + \sqrt{2}) + 12\ln\left(\frac{1 + \sqrt{3}}{\sqrt{2}}\right) & m = 3 \\ \quad - 4\ln(2 + \sqrt{3}) \end{cases}.$$

Note that as $S = \mathbb{K}^1 = [0, 1]$, the results for $m = 1$ agree with the corresponding ones for the Bernoulli map for both continuous ε-average path length and efficiency. Further expressions for $\Delta_{\mathbb{K}^m}(1)$ and $\Delta_{\mathbb{K}^m}(-1)$ for $m = 4, 5$ are given in Bailey et al. (2010). Another object of interest in the theory of box integrals is the integral

$$B_m(\eta) = \int_{\mathbb{K}^m} dx \|x\|_2^\eta, \tag{4.46}$$

which is related to the continuous ε-closeness $c(0; \varepsilon)$ of the origin $x = 0$ (and, by symmetry, to that of all the 2^m corners of the hypercube) for $\eta = 1$ and to the local efficiency $e(0; \varepsilon)$ of the same points for $\eta = -1$:

$$c(0; \varepsilon) = B_m(1)^{-1}\varepsilon \tag{4.47}$$
$$e(0; \varepsilon) = B_m(-1)\varepsilon. \tag{4.48}$$

We can now once again use results from Bailey et al. (2010) to give some closed forms for small m:

$$\varepsilon c(0;\varepsilon)^{-1} = \begin{cases} \frac{1}{2} & m = 1 \\ \frac{1}{3}(\sqrt{2} + \ln(1 + \sqrt{2})) & m = 2 \\ \frac{1}{4}\sqrt{3} - \frac{1}{24}\pi + \frac{1}{2}\ln(2 + \sqrt{3}) & m = 3 \end{cases}$$

and

$$\varepsilon^{-1}e(0;\varepsilon) = \begin{cases} \infty & m = 1 \\ 2\ln(1 + \sqrt{2}) & m = 2 \\ -\frac{1}{4}\pi + \frac{2}{3}\ln(2 + \sqrt{3}) & m = 3 \end{cases} .$$

Further solutions for $m = 4, 5$ are given in Bailey et al. (2010).

4.5. Discussion

We have shown that the definitions of continuous geometric measures provided in this chapter are feasible for describing ε-recurrence networks for time series analysis as well as, more generally, random geometric graphs (Dall and Christensen, 2002; Herrmann et al., 2003; Penrose, 2003). Our theoretical framework may readily be generalized to encompass other classes of random networks with spatial constraints (*i.e.*, spatial networks) (Barnett et al., 2007; Itzkovitz and Alon, 2005; Barthélemy, 2011), *e.g.*, those with an edge length distribution of the form $p_l(l) \propto \exp(-l/\xi)$ describing among others the substrate of climate networks (Tsonis and Swanson, 2008; Donges et al., 2009a, P22) (in contrast to the sharp cutoff $p_l(l) \propto \Theta(\varepsilon - l)$ for random geometric graphs). For the neighborhood-based measures, this generalization can be achieved by substituting terms containing the Heaviside function or $B_\varepsilon(x)$ with suitably chosen expressions involving $p_l(l)$. For example, a measure of transitivity in generalized spatial random networks with prescribed $p_l(l)$ would be

$$\mathcal{T}'(\varepsilon) = \frac{\iiint_S d\mu(x)\,d\mu(y)\,d\mu(z)p_l(\|x-y\|)p_l(\|y-z\|)p_l(\|z-x\|)}{\iiint_S d\mu(x)\,d\mu(y)\,d\mu(z)p_l(\|x-y\|)p_l(\|x-z\|)}. \tag{4.49}$$

One possible application to real-world spatial networks is computing expectation values for the characteristics of an ensemble of spatial random network surrogates to assess which properties of a given empirical network can be explained by $p_l(l)$ alone. Additionally, more general metrics could be used for measuring the distance l between connected vertices. Research along these lines may also help to shed light on the specific topology and dynamics of growing spatial complex networks (cf. Kaiser and Hilgetag (2004); Zhang and Small (2006)).

Furthermore, we have demonstrated that the resulting continuous properties can be approximated by estimators calculated from empirical ε-recurrence networks reasonably well, even for relatively small N and large ε. The continuous framework promotes

considerable advances in the theoretical understanding of ε-recurrence network-based time series analysis. Among others, from the examples of hyperballs and hypercubes in various dimensions m, the claim that path-based measures depend explicitly on the global geometry of the set S is theoretically justified. This is in contrast to the continuous notions of local and global transitivity, as at least the continuous local ε-clustering coefficient $\mathcal{C}(x; \varepsilon)$ depends on the local dimensionality of the set S (Appendix D and Donner et al. (2011b, P15)). Along these lines, in the future we may gain an understanding of the differing performance of transitivity-based and path-based measures in classifying qualitatively different behavior of dynamical systems (Marwan et al., 2009, P20; Zou et al., 2010, P17; Zou et al., 2012). For example, more complex dynamical systems such as the Lorenz and Rössler models or noisy dynamical systems, where no closed-form expression for the invariant probability density p exists, may be studied by estimating $\hat{p}$ from simulated trajectories. ε-recurrence network measures could then be calculated by numerical integration techniques relying on $\hat{p}$ and the integral expressions given in this chapter. Circumventing the computational limitations of discrete ε-recurrence network analysis when $N \to \infty$, this approach would in principle allow us to approximate the continuous geometric quantities defined above as closely as desired.

The examples of hyperballs and hypercubes establish links to some current research problems in probabilistic geometry and applied mathematics, among others, to the theory of box integrals (Anderssen et al., 1976; Bailey et al., 2006; Bailey et al., 2007; Bailey et al., 2010). Perhaps these highly symmetric model sets could serve to understand theoretically some qualitative features of path-based ε-recurrence network measures for strange attractors such as the Lorenz or Rössler attractors. It remains an open question whether it is possible to solve the integrals for continuous path-based measures in the case of self-similar sets S and more complex, potentially also self-similar densities p.

The theoretical framework put forward in this chapter enables several practical advances, which are particularly relevant for applications to time series analysis of real-world data. Analytical solutions for continuous ε-recurrence network measures allow us to assess the bias and variance of the discrete estimators from complex network theory that have been used in the literature so far. These insights led to devising improved discrete estimators based on the concept of vertex-weighted network statistics (Heitzig et al., 2012, P9). Furthermore, for the first time we were able to formulate a theoretically motivated criterion for the selection of the recurrence threshold ε based on the critical percolation threshold ε_c, which for a given system can be estimated using our theory.

Finally, we should note that we now have a comprehensive continuous theory for essentially all relevant measures of ε-recurrence networks. This foundation will help to further increase our understanding as well as strengthen the general confidence in the method of ε-recurrence network analysis in practical situations, *e.g.*, the analysis of real-world time series. Our results suggest that ε-recurrence network analysis is among the simplest and best understood network-based approaches to nonlinear time series analysis available so far.

4.6. Mathematical supplement

4.6.1. Sketch of proof of Eq. (4.11)

For $\varepsilon > 0$, we define the *continuous ε-distance* $d(x, y; \varepsilon)$ between $x \neq y \in S$ to be the smallest integer $k > 0$ such that there are points $z_0, \ldots, z_k \in S$ with $z_0 = x$, $z_k = y$, and $||z_{i-1} - z_i|| < \varepsilon$ for $i = 1 \ldots k$. Note that because S is path-connected, $d(x, y; \varepsilon)$ is finite. We also put $d(x, x; \varepsilon) = 0$. Let $d_{ij}(\varepsilon, N) \geq d(x_i, x_j; \varepsilon)$ be the network distance between x_i and x_j in the ε-recurrence network constructed from the first N points of a sequence of independent draws from p. One can then prove that for fixed ε, fixed vertices x_i, x_j, and $N \to \infty$, it has probability one that $d_{ij}(\varepsilon, N) = d(x_i, x_j; \varepsilon)$ eventually (*i.e.*, there is some $N(i, j, \varepsilon)$ so that $d_{ij}(\varepsilon, N) = d(x_i, x_j; \varepsilon)$ for all $N > N(i, j, \varepsilon)$). This is because for $k = d(x_i, x_j; \varepsilon)$, there is $\delta > 0$ and $z_0, \ldots, z_k \in S$ with $z_0 = x$, $z_k = y$, and $||z_{i-1} - z_i|| < \varepsilon - 2\delta$ for $i = 1 \ldots k$, and with probability one, the sequence contains points $w_0, \ldots, w_k \in S$ with $w_0 = x_i$, $w_k = x_j$, and $||w_i - z_i|| < \delta$ for $i = 1 \ldots k - 1$, so that also $||w_{i-1} - w_i|| < \varepsilon$ for $i = 1 \ldots k$, implying $d_{ij}(\varepsilon, N) \leq k$ when $N > N(i, j, \varepsilon)$ where $N(i, j, \varepsilon)$ is the index of the last of the w_i to occur in the sequence.

Moreover, $d(x, y; \varepsilon) \leq g(x, y)/\varepsilon + 1$ and $\varepsilon d(x, y; \varepsilon) \leq g(x, y)$ if $g(x, y)$ is not an integer multiple of ε. This is because for all $\delta > 0$ and $\varepsilon' < \varepsilon$, there is a path from x to y of length $\leq g(x, y) + \delta$, hence for $k = \lceil (g(x, y) + \delta)/\varepsilon' \rceil$ ($\lceil x \rceil$ is the smallest integer not less than x), there are $z_0, \ldots, z_k \in S$ with $z_0 = x$, $z_k = y$, and $||z_{i-1} - z_i|| \leq \varepsilon' < \varepsilon$ for $i = 1 \ldots k$, so that $d(x, y; \varepsilon) \leq k$. On the other hand if S is sufficiently well-behaved, one will also have $\varepsilon d(x, y; \varepsilon) \nearrow g(x, y)$ for $\varepsilon \to 0$. More precisely, assume S is "locally almost convex" in the sense that for all $L > 1$, there is some $\varepsilon > 0$ so that for all $x, y \in S$ with $||x - y|| < \varepsilon$, we have $g(x, y) < L\varepsilon$. Then for all $L > 1$, there is some $\varepsilon > 0$ so that $\varepsilon d(x, y; \varepsilon) > g(x, y)/L$. Putting all these facts together, we see that $\varepsilon d_{ij}(\varepsilon, N)$ is a plausible estimate of $g(x, y)$.

4.6.2. Continuous ε-average path length for Bernoulli map and uniformly distributed noise

For illustration, we give the detailed calculation of $\mathcal{L}(\varepsilon)$ for the Bernoulli map and, equivalently, uniformly distributed noise:

$$
\begin{aligned}
\varepsilon \mathcal{L}(\varepsilon) &= \int_0^1 \int_0^1 dxdy \, |x - y| \\
&= \int_0^1 dx \left(\int_x^1 dy \, |x - y| + \int_0^x dy \, |x - y| \right) \\
&= \int_0^1 dx \left(\int_x^1 dy \, (y - x) + \int_0^x dy \, (x - y) \right) \\
&= \int_0^1 dx \left(\left[\frac{1}{2}y^2 - xy \right]_x^1 + \left[xy - \frac{1}{2}y^2 \right]_0^x \right)
\end{aligned}
$$

$$= \int_0^1 dx \left(\frac{1}{2} - x + x^2 \right)$$

$$= \left[\frac{1}{3}x^3 - \frac{1}{2}x^2 + \frac{1}{2}x \right]_0^1 = \frac{1}{3}.$$

4.6.3. Continuous ε-betweenness for the center of a hyperball

$$b(0) = p^2 \iint_S dy\, dz \int_0^1 dt\, \delta(f(t))$$

$$= p^2 \iint d\Omega\, d\Omega' \int_0^1 \int_0^1 dr dr'\, r^{m-1} r'^{m-1} \delta(\Omega - \Omega')$$

$$= p^2 \int d\Omega \left(\int_0^1 dr\, r^{m-1} \right)^2$$

$$= p^2 \Omega_m \frac{1}{m^2}$$

$$= \frac{\Gamma\left(\frac{m}{2} + 1 \right)}{m\pi^{\frac{m}{2}}} = \frac{1}{\Omega_m}$$

4.7. Summary

Recurrence networks are a powerful nonlinear tool for time series analysis of complex dynamical systems. While there are already many successful applications ranging from medicine to paleoclimatology, a solid theoretical foundation of the method has still been missing so far. Here, we have interpreted an ε-recurrence network as a discrete subnetwork of a "continuous" graph with uncountably many vertices and edges corresponding to the system's attractor. This step allowed us to show that various statistical measures commonly used in complex network analysis can be seen as discrete estimators of newly defined continuous measures of certain complex geometric properties of the attractor on the scale given by ε. In particular, we have introduced local measures such as the ε-clustering coefficient, mesoscopic measures such as ε-motif density, path-based measures such as ε-betweennesses, and global measures such as ε-efficiency. This new analytical basis for the so far heuristically motivated network measures also provides an objective criterion for the choice of ε via a percolation threshold, and it shows that estimation can be improved by so-called node splitting invariant versions of the measures. We finally illustrated the framework for a number of archetypical chaotic attractors such as those of the Bernoulli and logistic maps, periodic, and two-dimensional quasiperiodic motions, and for hyperballs and hypercubes by deriving analytical expressions for the novel measures and comparing them with data from numerical experiments. More generally, the theoretical framework describes random geometric graphs and other networks with spatial constraints which appear frequently in disciplines ranging from biology to climate science.

Part II.

Applications

The novel concepts and techniques developed in Part I
call for their application to real-world problems and
data in the context of Earth system analysis. This sec-
ond part focusses on tipping elements and their inter-
actions, tipping points, as well as regional vulnerability.
Recurrence network analysis is employed to detect dy-
namical transitions or tipping points in synthetic and
paleoclimate data. This reveals a possible influence
of large-scale shifts in Plio-Pleistocene African climate
variability on events in human evolution, *i.e.*, an in-
teraction of climatic and evolutionary tipping points.
Finally, coupled climate networks yield insights into the
atmosphere's general circulation structure and allow
to quantify regional centrality and vulnerability with
respect to interactions between disparate parts of the
Earth system.

Chapter 5.

Identification of dynamical transitions in paleoclimate records

My eye is better than any statistical test.

Well-known paleoceanographer, circa 2001

(after Wunsch (2007))

5.1. Introduction

Paleoclimate proxy data representing past variations of environmental conditions can be obtained from various types of geological archives distributed over the Earth's surface. The study of time series of such proxies, *i.e.*, data that encode the temporal variability of physical, chemical, biological, or sedimentological properties, is a major source of information fostering our understanding of the functioning of the complex Earth system in the past, present, and future. However, non-equidistant sampling, uncertain age models, multi-scale, and multi-stable state variability as well as relatively high noise levels render the study of these proxy records a challenging problem for time series analysis. Most certainly, these complications contest the meaningfulness of a purely visual inspection of paleoclimate data (see the quote from Wunsch (2007) cited above).

Methods used for time series analysis can be roughly classified as linear or non-linear. On the one hand, linear methods are based on the evaluation of certain classical statistical characteristics and assume the presence of an underlying linear stochastic process with eventually some superimposed deterministic (*e.g.*, periodic) components (Brockwell and Davies, 1991; Brockwell and Davies, 2002; Hamilton, 1994). Prominent examples that are frequently used for the analysis of real-world time series, including such obtained from geological archives (Schulz and Stattegger, 1997; Schulz and Mudelsee, 2002; Mudelsee et al., 2009; Rehfeld et al., 2011), are correlation functions and power spectra. On the other hand, nonlinear methods follow a dynamical systems point of view, implicitly assuming the presence of certain types of deterministic behavior (Abarbanel, 1996; Kantz and Schreiber, 2004; Donner et al., 2008).

The vast majority of existing linear or nonlinear methods of time series analysis relies on the quantification of patterns of temporal dependencies between observations $\{x(t)\}$ made at times t, *i.e.*, aims to quantify functional relationships of the form

$$x(t) = \sum_{\tau > 0} f(x(t - \tau), \tau, t) + \eta(t), \tag{5.1}$$

where $f(x, \tau, t)$ is a general deterministic function and $\{\eta(t)\}$ a stochastic process (often assumed to be fully uncorrelated, *i.e.*, δ-correlated, in time). For a stationary system, the functional dependence f does not explicitly depend on time t. In standard linear methods of time series analysis, f is often assumed to be a linear function; in this case, the parameters of f encode linear temporal correlations. More generally, one may consider arbitrary (*i.e.*, not explicitly specified) deterministic relationships f, which may be characterized using nonlinear concepts such as mutual information (Kantz and Schreiber, 2004).

In the following, we will refer to methods of time series analysis that are based on the quantification of temporal interrelationships between observations, *e.g.*, correlation and mutual information functions or power spectra, as *correlative* methods. These clearly depend on how well the observation points are specified. In particular, in case of a non-uniform sampling of the considered time series, estimates of even simple linear characteristics can often not be expressed in a straightforward analytical way. For example, if one wishes to avoid interpolation (which leads to additional uncertainties), power spectra can be estimated using harmonic regression of the data (*e.g.*, by means of the Lomb-Scargle periodogram (Lomb, 1976; Scargle, 1982)), projection methods (Foster, 1996a; Foster, 1996b), or a variety of alternative approaches (Babu and Stoica, 2010; Rehfeld et al., 2011). However, in the specific case of paleoclimate data where typically not even the exact timing of the individual observations is sufficiently well known (Telford et al., 2004), correlative methods can have strong conceptual disadvantages.

In contrast to this large class of methods (which characterize time series from a more or less rigorous statistical point of view), alternative concepts such as fractal dimensions and generalizations thereof have been first developed in different mathematical disciplines and later applied to the characterization of the properties of certain dynamical systems (Sprott, 2003). Statistical estimates of such measures can be obtained by a variety of different approaches, most of which take into account the spatial arrangement of observations in the (possibly reconstructed) phase space. From this perspective, the mentioned methods do not directly require knowledge about the timing of observations, *i.e.*, can be considered as non-correlative or *geometric* methods, since they rely on geometric attractor properties in phase space rather than on explicit dynamical information. In the case of paleoclimate data with uncertain age models, geometric methods may provide a considerable alternative for statistical analysis. However, as a particular disadvantage, we note that the proper estimation of fractal dimensions usually requires a considerably larger amount of data than necessary for most correlative methods (Sprott, 2003) which is typically not available in paleoclimatology.

Some fundamental relationships between the geometric properties of attractors in phase space (*e.g.*, Hausdorff and box dimensions) and important invariants of the associated dynamics (*e.g.*, Lyapunov exponents) are known to exist (Chlouverakis and Sprott, 2005). Note that certain measures of dimensionality include both geometric and dynamical information, *i.e.*, all Rényi dimensions D_q for $q > 1$ including the information dimension D_1 (Sprott, 2003). However, besides fractal dimension estimates based on attractor topology there are only very few suitable and purely geometric methods available.

Recently, it has been suggested to characterize the mutual proximity relationships of all pairs of state vectors from the sampled attractor in phase space by means of complex network methods (Section 3.2). Among others, the concept of ε-recurrence networks (Marwan et al., 2009, P20; Donner et al., 2010a, P18; Donner et al., 2010c, P19) has been proven particularly useful for this purpose (Section 3.2.2). Since ε-recurrence networks take only spatial information into account, they can be considered as important examples of geometric methods of time series analysis. Recurrence networks provide a set of nonlinear measures characterizing the complexity of dynamical systems (Donner et al., 2010a, P18; Donner et al., 2011a, P13), *e.g.*, allowing to distinguish periodic from chaotic dynamics (Zou et al., 2010, P17). While recent findings demonstrate close interrelationships between certain recurrence network properties and fractal dimensions (Donner et al., 2011b, P15), the graph-theoretical measures can often be estimated with high confidence from much shorter time series than fractal dimensions. This warrants their application as a tool for window-based analysis of non-stationary data (Marwan et al., 2009, P20; Donner et al., 2011a, P13). In contrast to ε-recurrence networks and conceptually related techniques, transition networks (Nicolis et al., 2005) and visibility graphs (Lacasa et al., 2008) are correlative methods in the sense that they depend explicitly on the temporal ordering of observations (Donner and Donges, 2012b, P7).

When considering network-based methods of time series analysis, so far only recurrence networks (Marwan et al., 2009, P20; Donner et al., 2011a, P13; Hirata et al., 2011) and visibility graphs (Elsner et al., 2009; Telesca and Lovallo, 2012; Donner and Donges, 2012b, P7) have been used to analyze geoscientific data. Following Donges et al. (2011a, P11), in this chapter we discuss the application of recurrence networks to studies of paleoclimate records, with a special focus on the identification of structural changes in the dynamics that are not easily found when relying on simple linear statistics. As a benchmark example, we will mainly utilize three marine records of aeolian dust flux from Northern Africa during the last 5 million years (Myr) (Trauth et al., 2009; Marwan et al., 2009, P20; Donner et al., 2011a, P13; Donges et al., 2011c, P10).

In Section 5.2, we present a detailed description of the considered data sets, the necessary preprocessing steps, and the general idea of applying the quantitative analysis of ε-recurrence networks in a sliding-windows framework. Application to typical nonlinear model systems with a systematic drift of the control parameters in Section 5.3 suggests that network statistics are well suited for identifying dynamical transitions from finite time series. Finally, in Section 5.4, we describe the results of
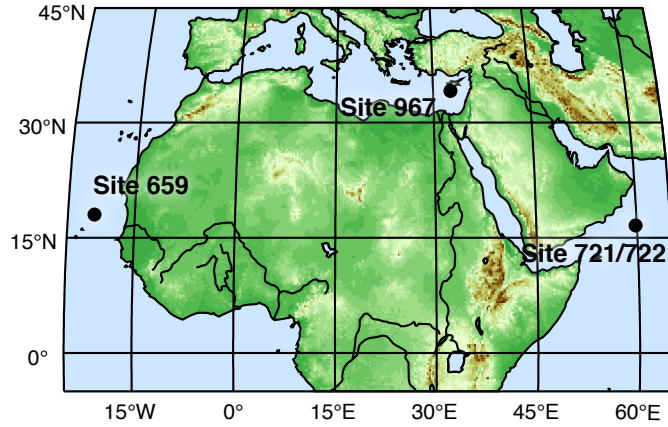
Figure 5.1.: Map displaying the locations of the three ODP drilling sites considered in this chapter (Tiedemann et al., 1994; deMenocal, 1995; deMenocal, 2004; Larrasoaña et al., 2003).

our investigations obtained for the different paleoclimate time series and discuss their robustness with respect to the fundamental parameters of our method.

5.2. Data and methods

5.2.1. Description of the data

Marine records of terrigenous dust flux from North Africa are an important source of information on the long-term aridification of the continent during the Plio-Pleistocene (Trauth et al., 2009). Continuous time series $\{x_i = x(t_i)\}_{i=1}^{N}$ sampled at times t_i, where i is an index variable and N the number of samples, are available from three sediment cores: ODP 659 (Atlantic Ocean offshore subtropical West Africa) (Tiedemann et al., 1994), ODP 721/722 (Arabian Sea) (deMenocal, 1995; deMenocal, 2004), and ODP 967 (Eastern Mediterranean Sea) (Larrasoaña et al., 2003) (Fig. 5.1). These records allow the reconstruction of North African dust mobilization and transport over the last 5 Myr and, hence, encode temporal changes in both the aridity of the region and the strength and direction of dominant regional atmospheric circulation patterns (Trauth et al., 2009). We chose these records as they are well studied in the literature (deMenocal, 1995; deMenocal, 2004; Larrasoaña et al., 2003; Tiedemann et al., 1994; Trauth et al., 2009) and are at the same time representatively distributed around North Africa (Fig. 5.1). Terrigenous dust flux has been estimated using different approaches: from the relative abundance of the non-carbonate fraction and the dry-bulk density for ODP site 659, via linear regression from magnetic susceptibility (which can be measured much more easily) for ODP site 721/722 (Bloemendal and deMenocal, 1989), to artificially induced magnetic remanescence for ODP site 967 (for more details, see Trauth et al. (2009)).
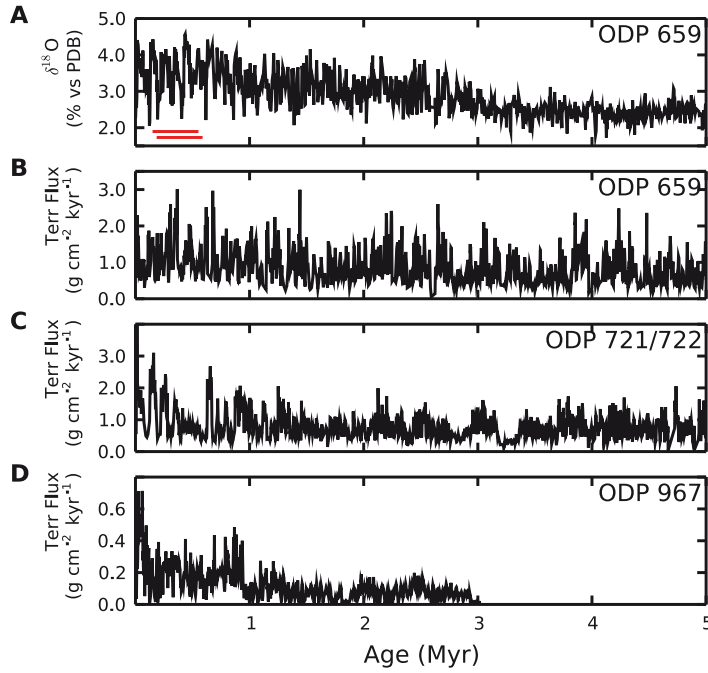
Figure 5.2.: Plio-Pleistocene variability of (A) δ^{18}O at ODP site 659 (Tiedemann et al., 1994), and of terrigenous dust flux from North Africa at ODP sites (B) 659 (Tiedemann et al., 1994), (C) 721/722 (deMenocal, 1995; deMenocal, 2004), and (D) 967 (Larrasoaña et al., 2003). The horizontal red bars in panel (A) indicate two consecutive recurrence windows of length $W^* = 410$ kyr and mutual offset $\Delta W^* = 41$ kyr as used in the analysis of Section 5.4 and in Figs. 5.9–5.12.

In addition, the benthic oxygen isotope (δ^{18}O) record from ODP site 659 (Tiedemann et al., 1994) will be studied as a proxy for variations in global ice volume which can be assumed to have a considerable impact on the continental aridification via a southward displacement of climate and vegetation zones. All time series are shown in Fig. 5.2.

5.2.2. Detrending

All considered time series $\{x_i\}$ show a nonlinear trend of increasing amplitude and variance towards the present. This trend reflects the successive aridification of North and East Africa and the intensification of Northern Hemisphere glacial cycles during the Plio-Pleistocene (Trauth et al., 2009). To prevent corruption of the results of our analysis and significance test due to this nonlinear trend, we attempt to remove it to first-order by subtracting from x_i the mean of a sliding window of size $W_D(t_i)$

centered at t_i for all time points t_i, *i.e.*,

$$\hat{x}_i = x_i - \frac{1}{2\lfloor W_D(t_i)/2 \rfloor + 1} \sum_{j=-\lfloor W_D(t_i)/2 \rfloor}^{\lfloor W_D(t_i)/2 \rfloor} x_{i+j}, \qquad (5.2)$$

where for a chosen *detrending window size* W_D,

$$W_D(t_i) = \begin{cases} 2(i-1) & \text{if} & i < W_D, \\ W_D & \text{if} & W_D \leq i \leq N - W_D, \\ 2(N-i) & \text{if} & i > N - W_D. \end{cases} \qquad (5.3)$$

That is, the effective detrending window size decreases towards the time series' boundaries, resulting in $\hat{x}_1 = \hat{x}_N = 0$. This simple approach avoids the complication of locally or globally fitting higher-order polynomials or performing high-pass filtering given irregular sampling and uncertain dating of measurements to remove the nonlinear trend. Since recurrence network analysis as our method of choice is a non-correlative technique and its results are permutation invariant (Section 5.2.6), spurious autocorrelations which may be introduced by the sliding window detrending do not pose a serious problem here. We will show in Section 5.4.2 that our results are robust with respect to a large range of reasonable choices of W_D. Except of the detrending, no further preprocessing was applied to the data. Particularly, we do not resample the time series to obtain an evenly spaced record in the time domain, since the necessary interpolation could corrupt the results of the further analysis to be performed below (see, *e.g.*, Rehfeld et al. (2011)).

5.2.3. Embedding

Univariate time series often reflect the dynamics of a higher-dimensional system as viewed through some observation function. In typical situations, it is possible to reconstruct the phase space trajectory using time-delay embedding, *i.e.*, considering state vectors

$$y_i^{(m,\tau)} = \left(\hat{x}_i, \hat{x}_{i+\tau}, \dots, \hat{x}_{i+(m-1)\tau} \right) \qquad (5.4)$$

instead of the univariate observations $\{\hat{x}_i\}$ themselves (Packard et al., 1980; Takens, 1981). Due to the finite length of the available time series, the index i is now restricted to the range $i = 1, \dots, N - (m-1)\tau$. The embedding parameters (embedding dimension m and delay τ) have to be appropriately determined from the available data, *e.g.*, using approaches such as the false nearest-neighbors (Kennel et al., 1992) and average mutual information (Fraser and Swinney, 1986) methods, respectively. Although there are good reasons for applying embedding techniques, it is known that this approach also has conceptual disadvantages and may induce spurious structures in recurrence plots and corresponding misleading results of recurrence quantification analysis (RQA) (Thiel et al., 2006). In contrast, many important dynamical invariants
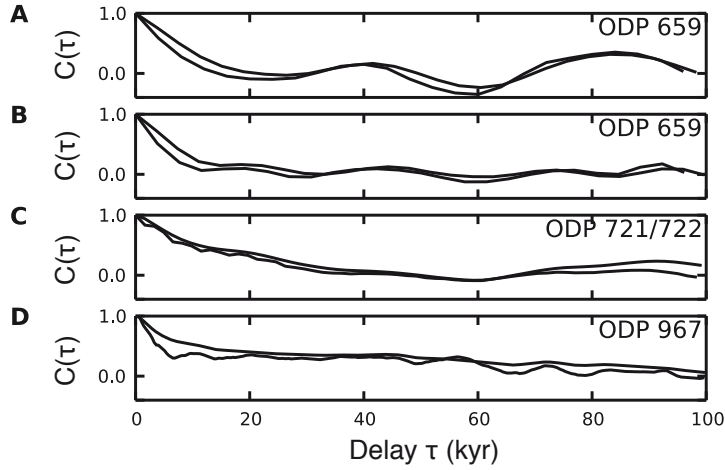
Figure 5.3.: Linear autocorrelation functions $C(\tau)$ for (A) the δ^{18}O record at ODP site 659 and the dust flux records from ODP sites (B) 659, (C) 721/722, and (D) 967. The autocorrelation functions were estimated using a Gaussian kernel-based estimator (Rehfeld et al., 2011) adapted to irregularly sampled data (solid line) and directly from time series linearly interpolated to a regular sampling with sampling time $\langle \Delta T \rangle$ (dash-dotted line). For the Gaussian kernel-based estimator we used the recommended optimum bandwidth $h = \langle \Delta T \rangle /4$ (Rehfeld et al., 2011), where h is the standard deviation of the Gaussian kernel. These results show that the estimator based on linear interpolation tends to overestimate autocorrelation at most time delays.

can be estimated from non-embedded time series as well, especially using recurrence plot-based methods (Thiel et al., 2004). From here on we will use the simplified notation y_i for reconstructed state vectors and assign to them the ages t_i, respectively.

While the standard approaches for determining the optimum embedding parameters typically provide feasible results in the case of many applications, the situation is considerably more challenging for paleoclimate records: On the one hand, traditional embedding methods require equally spaced observations, so that interpolation of the available data might become necessary with all corresponding conceptual disadvantages. On the other hand, in the presence of dating uncertainties, even such interpolation is hardly possible and would lead to an enormous enhancement of uncertainty in the embedded record.

Given these methodological difficulties we attempt a compromise: (i) The embedding dimension $m = 3$ is a trade-off given the relatively short time series forbidding larger embedding dimensions (Eckmann and Ruelle, 1992; Kantz and Schreiber, 2004) and the underlying high-dimensional dynamics as suggested by the false nearest-neighbors criterion (Kennel et al., 1992; Marwan et al., 2009, P20). (ii) Using a Gaussian kernel-based estimator of the autocorrelation function adapted to irregularly sampled time series (Rehfeld et al., 2011), we find that the autocorrelation of all four time series has decayed markedly after 10 kyr (Fig. 5.3). Hence, we choose the delay

Table 5.1.: Basic properties of the analyzed paleoclimate time series. N is the number of samples contained in the time series, $\langle \Delta T \rangle$ the mean sampling interval, and $\sigma(\Delta T)$ the standard deviation of sampling intervals. For a desired window size $W^* = 410$ kyr and step size $\Delta W^* = 41$ kyr (as chosen in Section 5.4.1 for recurrence network analysis), W and ΔW give the corresponding window and step size (in numbers of observations), $\langle W^* \rangle$ and $\langle \Delta W^* \rangle$ the average effective window and step size, and $\sigma(W^*)$ and $\sigma(\Delta W^*)$ the associated standard deviations (in units of time).

	ODP 659 δ^{18}O	ODP 659 dust	ODP 721/722 dust	ODP 967 dust
N	1170	1221	2757	8417
$\langle \Delta T \rangle$ (kyr)	4.28	4.10	1.81	0.36
$\sigma(\Delta T)$ (kyr)	2.88	2.69	1.52	0.31
W	95	100	226	1139
ΔW	9	10	22	113
$\langle W^* \rangle$ (kyr)	400.37	408.16	401.97	409.10
$\sigma(W^*)$ (kyr)	46.58	33.09	62.66	78.04
$\langle \Delta W^* \rangle$ (kyr)	38.37	41.25	39.29	40.67
$\sigma(\Delta W^*)$ (kyr)	4.36	3.22	6.09	7.51

τ to cover approximately the same time scale $\tau^* = 10$ kyr for all considered records, *i.e.*,

$$\tau = \lfloor \tau^* / \langle \Delta T \rangle \rfloor, \tag{5.5}$$

where $\langle \Delta T \rangle$ is the average sampling time (Table 5.1). This yields $\tau_1 = 2$ for ODP site 659, $\tau_2 = 5$ for site 721/722, and $\tau_3 = 27$ for site 967 corresponding to $\tau^* = 10$ kyr. Promising and more sophisticated techniques for consistent embedding of irregularly sampled time series are based on Legendre polynomials (Gibson et al., 1992) or Bayesian regression (Heitzig, 2012) and should be explored in future studies.

5.2.4. Windowed analysis

For detecting structural changes in the dynamics encoded by the time series, we slide a window over the embedded record $\{y_i\}$ and perform the subsequent analysis for the data contained in each window separately. However, the records under study are quite heterogeneous with respect to their basic sampling properties (Table 5.1). The average sampling time $\langle \Delta T \rangle$ differs widely across the records. In order to assure comparability of our results uncovered from the different time series, the most natural approach is to choose windows of a fixed size W^* in units of time. However, this approach has two disadvantages: The exact timing t_i of the available observations is not known as is the case for most geological proxy records, and due to the non-uniform sampling rates, different windows would contain different amounts of data. While the latter is not problematic for statistical tests for homogeneity of the distribution of values in different windows, a quantitative comparison of statistical characteristics of
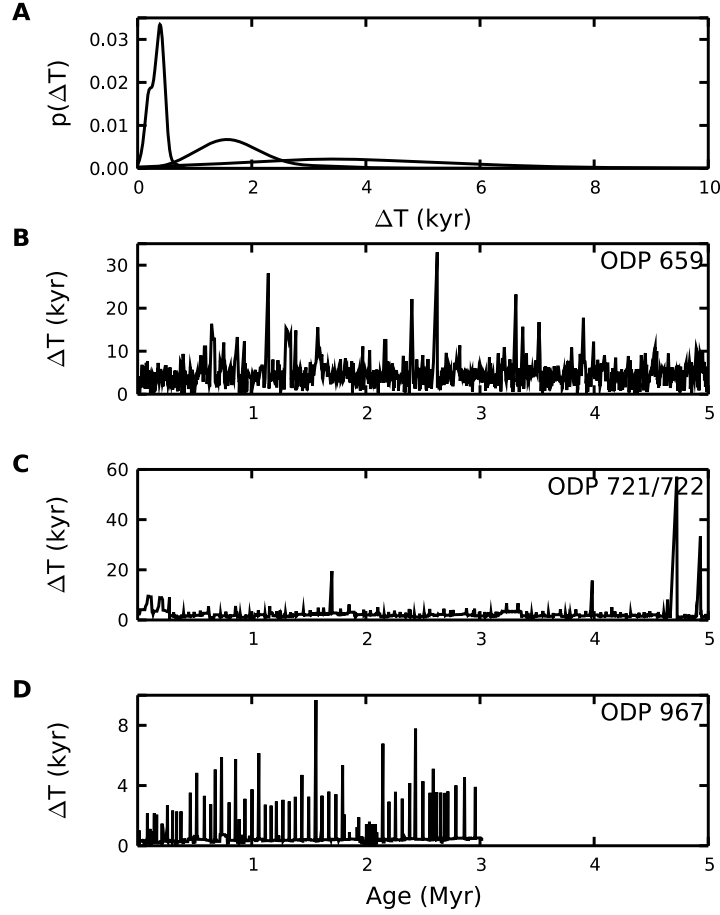
Figure 5.4.: (A) Probability distribution (PDF) $p(\Delta T)$ of the sampling intervals of the three dust flux records according to their established age models (ODP sites 659: solid line, 721/722: dash-dotted, 967: dashed). The distribution for the $\delta^{18}O$ record at ODP site 659 is visually almost indistinguishable from that of the corresponding dust flux record and therefore not shown. The PDFs were estimated using a Gaussian kernel with bandwidth $h = \sigma(\Delta T)(N-1)^{-1/5}$ (Table 5.1) following Scott's rule (Scott, 1982). (B,C,D) Temporal variation of the sampling times ΔT for the three dust flux records.

the associated recurrence networks (see Section 5.2.5) is not possible. Therefore, in the following, we will proceed in a different way by prescribing both the window size W and step size ΔW for recurrence network analysis measured in units of sampling points. In order to derive W and ΔW from the desired quantities in units of time, W^* and ΔW^*, we divide by the average sampling time,

$$W = \lfloor W^* / \langle \Delta T \rangle \rfloor, \tag{5.6}$$
$$\Delta W = \lfloor \Delta W^* / \langle \Delta T \rangle \rfloor, \tag{5.7}$$

where $\lfloor x \rfloor$ denotes the integer part of x. In turn, the actual window size $W^*(t_i)$ is determined by the average sampling time in the size-W window centered around t_i. For a particular choice of W^* and the associated step size ΔW^* in units of time, the resulting values of W and ΔW, the mean window widths, and step sizes as well as the corresponding standard deviations are given in Table 5.1.

The simple approach for determining the window size described above guarantees that the windows cover approximately the same time span for all records and positions within the time series. While most sampling intervals take values close to the mean, there are distinct outliers which most likely correspond to missing data due to incomplete core recovery, hiata, or disturbances of the sediment such as turbidites (Fig. 5.4A). Nevertheless, the standard deviation of window size $\sigma(\Delta W^*)$ is still small in comparison to the average window size $\langle \Delta W^* \rangle$ (Table 5.1), suggesting that statistical characteristics computed for different windows can still be quantitatively compared in a reasonable way.

Formally, the data series $\{y_i^\mu\}$ within the μ-th window, $\mu = 1, 2, \ldots$, is given by

$$\{y_i^\mu\} = \{y_{(\mu-1)\Delta W + i}\}, \tag{5.8}$$

where from here on $i = 1, \ldots, W$. We use the window's mid-point's timing

$$t^\mu = t_{(\mu-1)\Delta W + \lfloor W/2 \rfloor} \tag{5.9}$$

to attach an age to the scalar network measures f^μ calculated from the data within the μ-th window.

5.2.5. Recurrence network analysis

Following the general methodology of ε-recurrence network analysis described in Section 3.2.2, the recurrence matrices $\mathbf{R}^\mu$ with elements

$$R_{ij}^\mu(\varepsilon) = \Theta(\varepsilon - \|y_i^\mu - y_j^\mu\|) \tag{5.10}$$

are computed from the state vectors $\{y_i^\mu\}$ in the μ-th window (see Fig. 5.5 for examples), where the appropriate choice of the recurrence threshold parameter ε is discussed below. The corresponding recurrence networks (see Fig. 5.6 and the
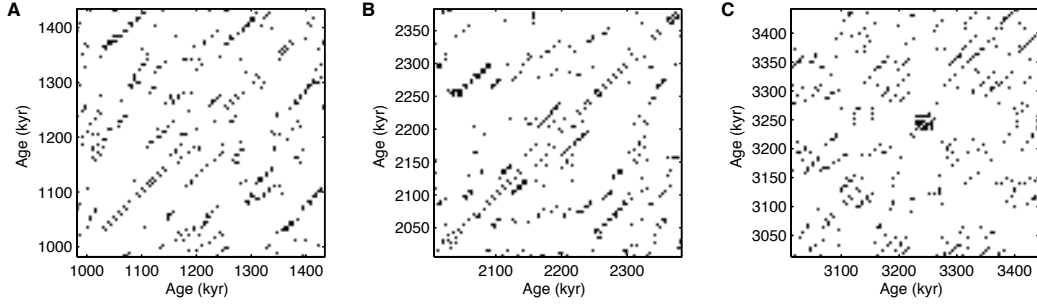
Figure 5.5.: Recurrence plots (equivalently adjacency matrices of the recurrence networks shown in Fig. 5.6) obtained from the dust flux record at ODP site 659, centered around (A) 1.2, (B) 2.2, and (C) 3.2 Myr BP (before present), using window size $W^* = 410$ kyr, step size $\Delta W^* = 41$ kyr, and embedding parameters $m = 3$, $\tau^* = 10$ kyr. ε was chosen in a data-adaptive way to yield a fixed edge density $\rho(\varepsilon) = 0.05$ for each window.

corresponding discussion in Section 5.4.1) are then fully described by the adjacency matrices $\mathbf{A}^\mu$ with elements

$$A_{ij}^\mu(\varepsilon) = R_{ij}^\mu(\varepsilon) - \delta_{ij}. \tag{5.11}$$

According to the conventions of Section 5.2.3, each vertex i in the μ-th window has an age $t_i^\mu = t_{(\mu-1)\Delta W + i}$ attached to it. To simplify the notation when referring to network measures, we will drop the window index μ in the following.

In order to apply recurrence networks in a sliding window analysis, a reference framework is necessary. Here, we consider a data-adaptive choice of ε that guarantees for a fixed edge density ρ of 5% which has been characterized as a reasonable choice in previous studies (Donner et al., 2010c, P19; Donges et al., 2012, P8) (see the related discussion in Section 4.3.2). One should note, however that even with this choice the characteristics of recurrence networks can only be compared in a meaningful way if the network size W is kept fixed (see Section 5.2.1). Among the considered complex network measures, transitivity $\mathcal{T}$ and assortativity $\mathcal{A}$ are mainly affected by finite-sample problems otherwise, whereas average path length $\mathcal{L}$ and diameter $\mathcal{D}$ explicitly depend on ε and W (Section 3.2.2 and Donner et al. (2010a, P18)).

5.2.6. Significance test

We perform a relatively simple statistical test of whether the network characteristics (see Section 3.2.2) in a certain time interval differ significantly from the general network characteristics expected given the phase space distribution of state vectors y_i from the whole detrended and embedded record and a certain recurrence window size W. The corresponding null hypothesis is that the network measures observed for a certain window are consistent with being calculated from a random draw of W
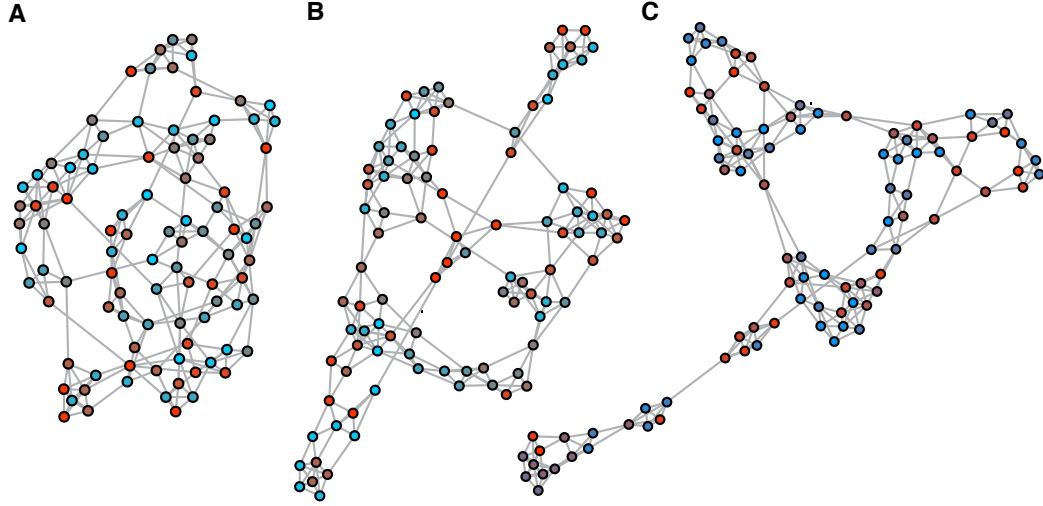
Figure 5.6.: Recurrence networks obtained from the dust flux record at ODP site 659, centered around (A) 1.2, (B) 2.2, and (C) 3.2 Myr BP and corresponding to the recurrence plots of Fig. 5.5. Vertex color indicates the age t_i^μ associated to single state vectors μ (from blue [=old] to red [=young]). The two-dimensional graph visualization has been obtained with the software package GUESS using a force-directed placement algorithm (see Appendix F). It is important to note that in this visualization, node positions are determined by the aforementioned algorithm and do not correspond to a projection of the node coordinates in the reconstructed three-dimensional phase space.

state vectors from the prescribed phase space distribution induced by the complete detrended time series. We can justly assume a thus randomized embedded time series without losing essential information, because all network measures $f(\cdot)$ considered here are permutation-invariant when considering a fixed subset of state vectors $y_1, \ldots, y_W$. More formally, $f(y_1, \ldots, y_W) = f(y_{\pi(1)}, \ldots, y_{\pi(W)})$ for arbitrary permutations π. A similar test for RQA measures requires a more advanced method (Schinkel et al., 2009). In order to create an appropriate null model, we use the following approach:

(i) Draw randomly W state vectors from the embedded time series (corresponding to the window size chosen for the original data).

(ii) Construct a recurrence network from this set of state vectors.

(iii) Compute the network measures of interest.

Repeating this procedure sufficiently many times, we obtain a test distribution for each of the network measures and choose to estimate its 0.05 and 0.95 quantiles that can be interpreted as 90% confidence bounds. These conservative symmetric confidence bounds were selected because due to the relatively small number of state vectors y_i available for bootstrapping, the Monte Carlo draws are not sufficiently independent to allow the reliable estimation of stricter confidence bounds.

The proposed significance test can be interpreted as a test for stationarity of the higher-order geometrical properties of the time series that are quantified by qualitatively different recurrence network measures. It is conceptually distinct from the network surrogate-based hypothesis tests put forward in Section 2.4.3, since the latter essentially rely on network surrogates obtained by directly randomizing the network structure under certain constraints. In contrast, the test proposed here operates by first generating multivariate time series surrogates by bootstrapping from all available state vectors and subsequently constructing recurrence networks from these surrogates.

5.3. Dynamical transitions in model systems

To validate the proposed methodology for detecting transitions in time series based on recurrence networks, we apply it to the logistic map and the Lorenz system with drifting bifurcation parameter as paradigmatic examples of discrete and continuous-time dynamical systems, respectively. While step-like changes of bifurcation parameters have already been studied for discrete (Marwan et al., 2009, P20) and continuous-time dynamical systems (Zou et al., 2010, P17; Donner et al., 2011a, P13), here we are particularly interested in the effect of transients, which are expected to be present in real-world systems and, hence, data extracted from them. We will check whether the global network quantifiers described above are able to detect transitions in the system's dynamics induced by bifurcations due to a slowly changing control parameter. For this purpose we are specifically looking for time intervals (or equivalently, values of the bifurcation parameter), where one or more of the considered network quantifiers undergo sudden changes. This requires taking into account the measures' interpretation in terms of dynamical systems theory (Section 3.2.2). Furthermore, we will study how their performance and the level of resolved detail depend on the window size W. This analysis particularly shows that the window sizes W chosen for the recurrence network analysis of terrigenous dust flux records (Table 5.1) are indeed appropriate for detecting bifurcations.

5.3.1. Logistic map

We iterate the logistic map

$$x_{i+1} = r_i x_i (1 - x_i)$$
$$r_{i+1} = r_i + \Delta r \tag{5.12}$$

while varying the bifurcation parameter linearly from $r_1 = 3.8$ to $r_M = 3.9$ in $M = 10,000$ equidistant steps setting $\Delta r = 1 \times 10^{-5}$ (Fig. 5.7), similar to Trulla et al. (1996). We analyze the resulting time series $\{x_i\}$ without embedding or detrending. The transition from chaotic to 3-periodic dynamics after an interior crisis at $r = 1 + \sqrt{8} \approx 3.8284$ (Wackerbauer et al., 1994) is clearly displayed by all four measures. As expected from theoretical considerations for discrete-time systems (Marwan et al.,
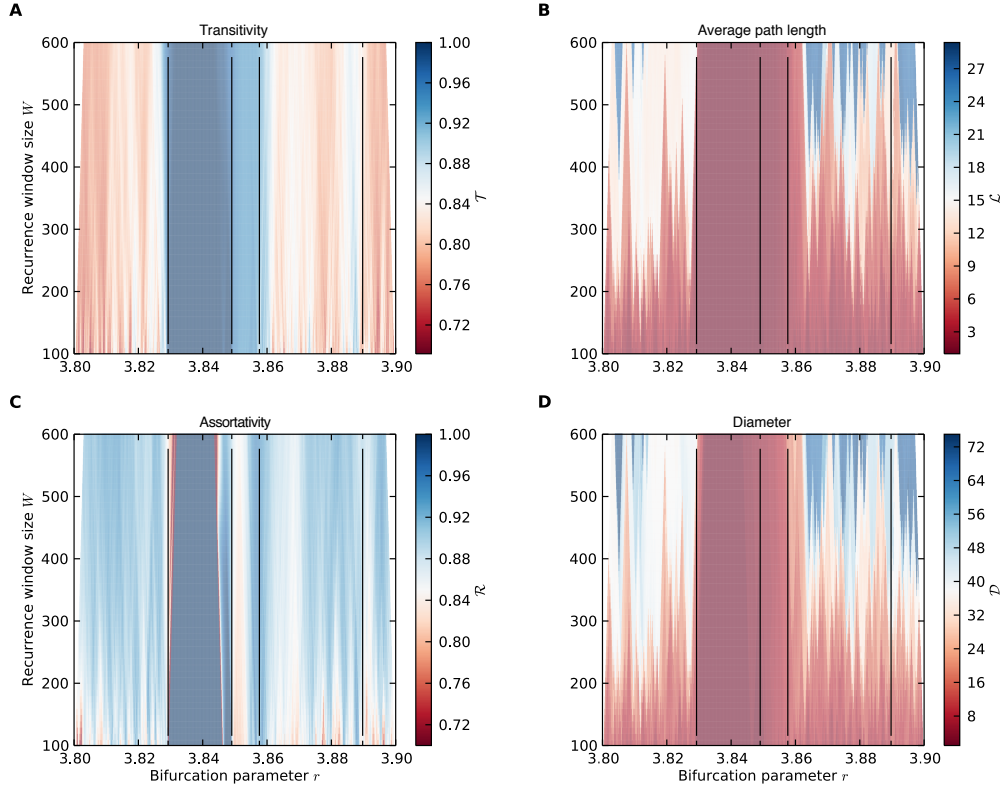
Figure 5.7.: (A) Transitivity $\mathcal{T}$, (B) average path length $\mathcal{L}$, (C) assortativity $\mathcal{A}$, and (D) diameter $\mathcal{D}$ for varying recurrence window size W for the logistic map (Eq. (5.12)) with drifting bifurcation parameter r (see text) and initial condition $x_1 = 0.7$. W was varied linearly in the interval $[100, 600]$, the recurrence window step size was fixed to $\Delta W = 10$ time steps. No embedding was used and the threshold set to $\varepsilon = 0.05\sigma$ (Marwan et al., 2009, P20), where σ denotes the standard deviation of the time series segment within the recurrence window. Vertical dashed lines indicate the critical values of r discussed in the text.

2009, P20; Donner et al., 2010a, P18; Donner et al., 2011b, P15), $\mathcal{T}$ and $\mathcal{A}$ abruptly increase to their maximum value of 1 following this transition, whereas at the same time $\mathcal{L}$ and $\mathcal{D}$ sharply decrease to their minimum value of 1. Among all four measures, $\mathcal{T}$ and $\mathcal{A}$ most clearly detect the termination of the period-doubling cascade following the period-3 behavior at the accumulation point $r \approx 3.849$, while $\mathcal{T}$, $\mathcal{L}$, and $\mathcal{D}$ highlight the merger of the subsequently formed three chaotic bands at the interior crisis at $r \approx 3.857$ (Wackerbauer et al., 1994). The latter transition is only weakly visible in $\mathcal{A}$. Additionally, much fine-structure is resolved by the network measures, *e.g.*, a narrow period-4 window at $r \lesssim 3.89$ that is most clearly indicated by an increased transitivity $\mathcal{T}$ across all W. Generally, the transitions appear more and more blurred as W increases, which is due to the growing number of samples from both periodic and chaotic dynamical regimes contained in the recurrence windows

when sliding over the bifurcation point. In consequence, some of the narrow periodic windows appearing for $r < 3.83$ and $r > 3.86$ are only visible for small recurrence window sizes W. As a rule of thumb, we can expect a periodic (chaotic) window of width w_r embedded within a chaotic (periodic) background to be detectable if $w_r \gtrsim W \Delta r$.

Another notable feature is that both $\mathcal{L}$ and $\mathcal{D}$ show a clear tendency to increase with growing W in the chaotic parameter ranges (Fig. 5.7B,D). This is theoretically expected, since both measures are extensive, *i.e.*, they depend explicitly and non-linearly on the number of vertices W in the recurrence network for a general phase space distribution of state vectors as induced by chaotic dynamics (Donner et al., 2010a, P18). In contrast, $\mathcal{L}$ and $\mathcal{D}$ do not change with W in the periodic windows, most notably in the large period-3 window of the logistic map (Fig. 5.7B,D). We can explain this behavior by recalling that for discrete-time systems in a p-periodic regime, the recurrence network reduces to a set of p fully connected components (Donner et al., 2010a, P18). Following the definitions in Section 3.2.2, this in turn leads to $\mathcal{L} = \mathcal{D} = 1$ in any periodic regime and independent of W.

5.3.2. Lorenz system

To illustrate the performance of windowed recurrence network analysis for detecting transitions in continuous-time dynamical systems, we consider the Lorenz system (see Figs. 3.1 and 3.2) with a time-dependent bifurcation parameter $r = r(t)$,

$$\frac{d}{dt}(x, y, z) = \left(10(y - x), x(r - z) - y, xy - \frac{8}{3}z\right). \tag{5.13}$$

While the system is evolving, r increases linearly from $r_0 = 160$ at time $t_0 = 0$ to $r_f = 170$ at time $t_f = 500$, *i.e.*,

$$r(t) = r_0 + \frac{r_f - r_0}{t_f - t_0}(t - t_0). \tag{5.14}$$

For consistency with the analysis of scalar paleoclimate time series to be performed in Section 5.4, we use an embedding of the x-component time series for recurrence network analysis without prior detrending (see caption of Fig. 5.8 for details). The recurrence network measures indicate two major transitions towards increasingly irregular dynamics at $r \approx 161$ and $r \approx 166.5$ (Fig. 5.8). The former possibly reflects an initial transient due to the chosen initial condition. The latter agrees well with the major shift from periodic (large $\mathcal{T}$, large $\mathcal{L}$ and $\mathcal{D}$ for continuous-time systems, see Chapter 4 and Donner et al. (2010a, P18); Donner et al. (2011b, P15); Zou et al. (2010, P17); Donges et al. (2012, P8)) to chaotic (small $\mathcal{T}$, small $\mathcal{L}$ and $\mathcal{D}$) behavior which is present in the Lorenz system's non-transient bifurcation scenario at $r \approx 166$ (Barrio and Serrano, 2007; Donner et al., 2011a, P13). On a shorter time scale, the path-based measures $\mathcal{L}$ and $\mathcal{D}$ among others detect weaker transitions at $r \approx 163.5$, $r \approx 164.5$ and $r \approx 166$. Note that one has to be careful when comparing
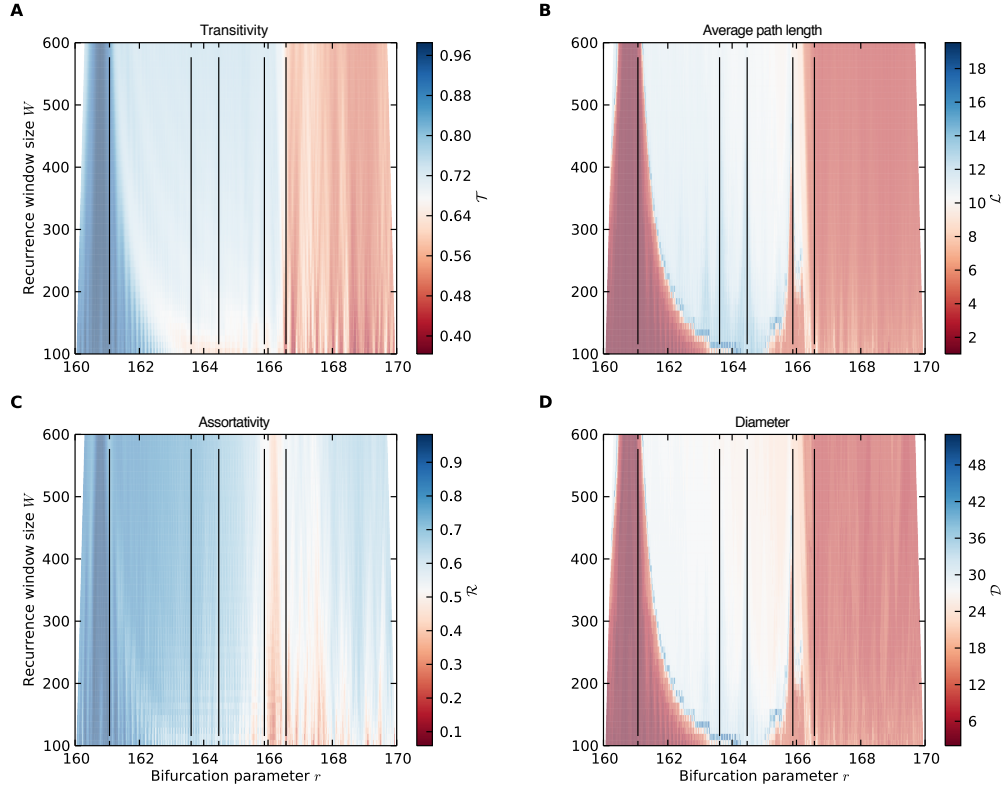
Figure 5.8.: (A) Transitivity $\mathcal{T}$, (B) average path length $\mathcal{L}$, (C) assortativity $\mathcal{A}$, and (D) diameter $\mathcal{D}$ for varying recurrence window size W for the Lorenz system (Eq. (5.13)) with drifting bifurcation parameter r (see text) and initial condition $(x_0, y_0, z_0) = (10, 10, 10)$. Because we are interested in the performance of our method for scalar time series, we chose the x-component of the trajectory sampled with sampling time $\Delta T = 0.05$ and embed it with embedding dimension $m = 3$ and delay $\tau = 15$. W was varied linearly in the interval $[100, 600]$, the recurrence window step size was fixed to $\Delta W = 10$ samples. We varied the recurrence threshold ε to yield a fixed edge density $\rho = 0.05$ (Donner et al., 2010c, P19). Vertical dashed lines indicate the critical values of r discussed in the text.

these results to bifurcation studies, where distinct realizations of the Lorenz system with fixed parameter r (not varying in time) are studied (*e.g.*, Donner et al. (2011a, P13)), since transients influence the results and cannot be excluded by construction when r is continuously varied in time. However, our results are consistent with the work of Trulla et al. (1996) who observed that in transient scenarios bifurcations may appear for larger bifurcation parameters than in their non-transient equivalents. The dependence of the results on the recurrence window size W is more pronounced than that described above for the logistic map. This is likely due to the fact that transients play a larger role in continuous-time systems like the Lorenz model than in discrete-time systems.

5.4. Dynamical transitions in paleoclimate records

Our studies in the previous section demonstrated that recurrence network analysis can be meaningfully applied for detecting dynamical transitions in non-stationary time series from different model systems by applying this kind of analysis to running windows. This is a necessary, but not sufficient condition for ensuring the feasibility of recurrence network analysis for detecting regime shifts in paleoclimate records as well. However, the application of our simple significance test (Section 5.2.6) diminishes the danger of confusing statistical fluctuations with proper dynamical changes substantially. Time series from geological archives are typically characterized by a variety of different types of nonstationarities, including (i) changes in the long-term mean or variance of the recorded proxies, (ii) variations in the amplitudes of almost periodic variability components (*e.g.*, such attributed to Milankovich-type variations caused by periodic changes in the Earth's orbital parameters), or (iii) even multimodal behavior (*e.g.*, transitions between glacial and interglacial periods, see Section B.5.2). All these three types of nonstationarities are contained in our data (Fig. 5.2 and Trauth et al. (2009)). While these different phenomena can be analyzed using more specific methodological approaches, we propose recurrence network analysis as a general exploratory tool for detecting time intervals containing changes in the dominating type of dynamical behavior. In the following, we will illustrate the robustness of this approach for the four marine records introduced in Section 5.2.1 and briefly discuss the possible climatological background of the observed dynamical changes. These results are elaborated in detail and put into context with additional paleoclimate and paleontological data in Chapter 6 and Donges et al. (2011c, P10).

5.4.1. Time-dependence of network properties

We consider the four marine paleoclimate records embedded in a three-dimensional reconstructed phase space with a time delay of approximately $\tau^* = 10$ kyr, resulting in the embedding parameters described in Section 5.2.3. For an initial inspection, we use recurrence windows of size $W^* = 410$ kyr with a mutual offset of subsequent windows $\Delta W^* = 41$ kyr. Note that the latter two parameter choices correspond to

those used in previous work on the ODP site 659 dust flux record (Marwan et al., 2009, P20; Donner et al., 2011a, P13). The selection of both parameters results from a compromise between high temporal resolution of the finally produced recurrence network measures (small W^*, ΔW^*) and larger statistical confidence in the results (large W^*). The choice of W^* is more critical than that of ΔW^*, because the former directly influences the number of vertices W in the recurrence networks via Eq. (5.6). Since a formal criterion for determining an optimal choice of W^* and ΔW^* is not available so far, we study the robustness of our results with respect to variations in the more critical parameter W^* in Section 5.4.2.

We additionally apply local detrending by removing the long-term average taken over windows of $W_D^* = 500$ kyr, where

$$W_D = \lfloor W_D^* / \langle \Delta T \rangle \rfloor, \tag{5.15}$$

which has not been considered in the aforementioned studies. As we will show in the following, the main features recovered by our analysis are not qualitatively changed when applying detrending. However, this step appears relevant in other kinds of statistical analyses, *e.g.*, for estimating spectrograms or time-dependent coefficients of autoregressive processes, since the data show considerable long-term trends in both mean and variance (Fig. 5.2).

Regarding the transitivity (Fig. 5.9), we find a synchronous behavior of the two geographically distinct records at ODP sites 659 and 721/722 during the Pliocene ($\sim$5.3–2.6 Myr BP (before present)) and Early Pleistocene[14] (2.6–1.0 Myr BP), including two periods of extraordinarily large values of $\mathcal{T}$ at about 3.45–3.05 and 2.2–2.1 Myr BP, related to pronounced clusters of vertices shown in Figs. 5.6B,C. The first of these periods results from a time interval of strongly suppressed and almost constant dust flux in the Mid Pliocene (see Figs. 5.2,6.3), while the latter one coincides with a period of almost periodic Milankovich-type variations (Trauth et al., 2009). We note that it is known that both types of dynamics typically lead to large values of $\mathcal{T}$ (Marwan et al., 2009, P20; Donner et al., 2010a, P18; Donner et al., 2011b, P15; Zou et al., 2010, P17), so that this result is consistent with theoretical expectations (Chapter 4). During the Early Pleistocene, the signatures at both sites decouple from each other, which could be the result of an enhancement of the atmospheric Walker circulation (Ravelo et al., 2004). For the last about 1.5 Myr, the variations of transitivity become more similar between ODP sites 721/722 and 967, particularly highlighting the Mid Pleistocene transition between 1.2 and 0.7 Myr BP (Fig. 5.6A), which corresponds to a change in the dominating Milankovich-type periodicity. The results obtained for the average path length $\mathcal{L}$ (Fig. 5.10) are mostly consistent with these findings, also highlighting the Mid Pliocene, Early Pleistocene, and Mid Pleistocene as periods with changes in the long-term dust flux variability. Specifically, $\mathcal{L}$ tends to show significant peaks at abrupt change points between regular

---

[14]Here "Early Pleistocene" does not refer to any of the archetypical stages (Upper, Middle and Lower Pleistocene). Its timing 2.6–1.0 Myr BP is not motivated stratigraphically, but climatologically, *i.e.*, by the onset of the Mid-Pleistocene transition around 1.0 Myr BP.
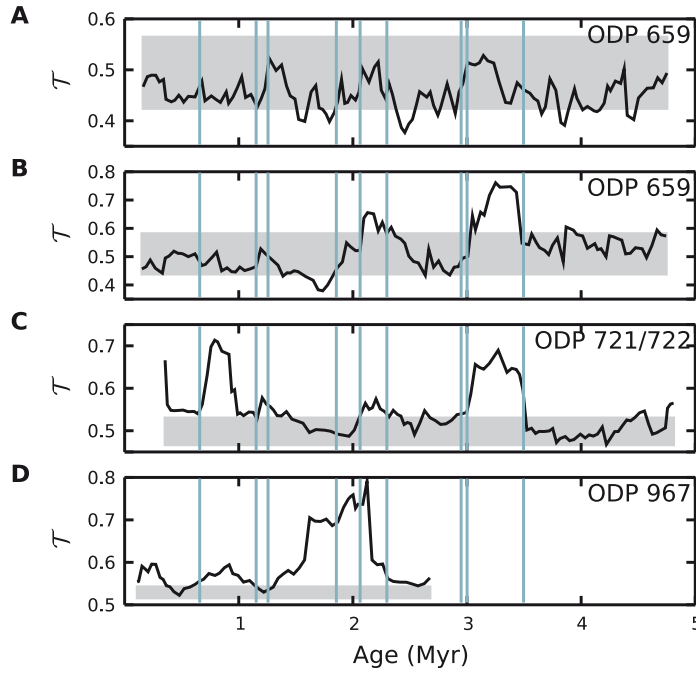
Figure 5.9.: Evolution of recurrence network transitivity $\mathcal{T}$ for (A) the $\delta^{18}O$ record from ODP site 659, and the dust flux records from ODP sites (B) 659, (C) 721, and (D) 967. $\mathcal{T}$ reveals changes in the regularity of African climate during the Plio-Pleistocene. Here we used a detrending window size $W_D^* = 500$ kyr, recurrence window size $W^* = 410$ kyr and step size $\Delta W^* = 41$ kyr, embedding dimension $m = 3$ and delay $\tau^* = 10$ kyr. The recurrence threshold ε was chosen adaptively to yield a fixed edge density $\rho = 0.05$. The gray bars represent the 5% and 95% quantiles with respect to the test distribution obtained from 10,000 realizations of our null model for each record separately. Vertical dashed lines indicate the detected epochs of transitions discussed in the main text.

and more erratic climate variability, as indicated by $\mathcal{T}$ (see Marwan et al. (2009, P20) for a theoretical explanation of this behavior).

The oxygen isotope anomaly obtained from the analysis of benthic foraminifera characterizes a distinctively different climatic parameter (*i.e.*, global ice volume) than terrigenous dust flux, so that it can be expected that the variability recorded by this proxy differs from that of the dust flux. An inspection of the recurrence network properties indeed confirms this expectation. Specifically, the transitivity $\mathcal{T}$ does not show any systematic maxima at all (indicating time intervals with regular long-term dynamics) (Fig. 5.9A), which is in clear contrast to the aeolian dust flux. The average path length $\mathcal{L}$ shows significant maxima around 2.9 Myr BP (possibly being related to the intensification of Northern Hemisphere glaciation at around this time), between 1.8 and 1.3 Myr BP (consistent with the corresponding results for the dust flux records, suggesting a high-latitude mechanism behind the large-scale
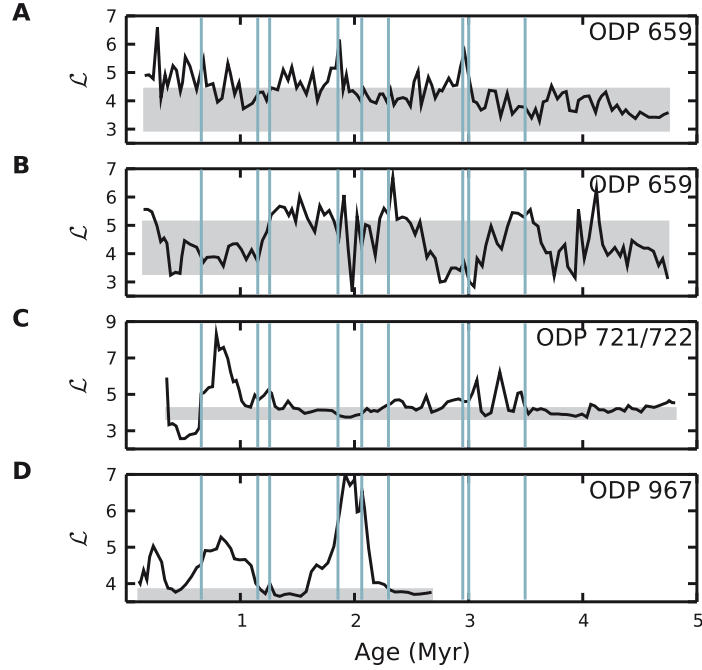
Figure 5.10.: Evolution of recurrence network average path length $\mathcal{L}$ for (A) the $\delta^{18}O$ record from ODP site 659, and the dust flux records from ODP sites (B) 659, (C) 721, and (D) 967, indicating transitions in African climate dynamics during the Plio-Pleistocene. Parameters, significance test, and vertical lines are the same as in Fig. 5.9.

climatic changes during this time period), and after about 900 kyr BP (possibly resulting from the glacial terminations and inceptions with a rather long – roughly 100 kyr – periodicity) (Fig. 5.10A).

Figures 5.11 and 5.12 additionally show the time variability of the two other recurrence network properties assortativity $\mathcal{A}$ and diameter $\mathcal{D}$. Since the latter one is closely related to the average path length $\mathcal{L}$ (Donner et al., 2010a, P18), the variability of both measures is very similar. Moreover, we also find some much weaker similarities between the temporal variability patterns of transitivity $\mathcal{T}$ and assortativity $\mathcal{A}$, which are less pronounced, since both properties characterize not so obviously related aspects of the network geometry in phase space. Specifically, the time interval of suppressed dust flux in ODP 659 and 721/722 during the Mid Pliocene (Fig. 6.3) results not only in an increased transitivity, but also a high assortativity. The latter feature can be explained by the fact that a relatively large cluster of state vectors representing this laminar regime emerges in the network, which is rather densely connected (Fig. 5.6C).

We conclude that the recurrence network measures are not statistically independent in their time evolution (Table 5.2). For the ODP site 659 $\delta^{18}O$ and dust flux records, the correlations between transitivity $\mathcal{T}$ and assortativity $\mathcal{A}$ as well as between
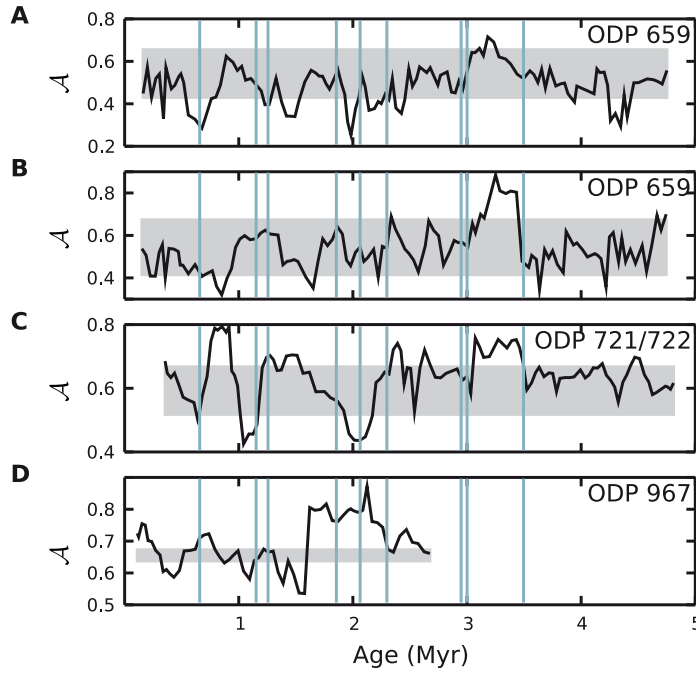
Figure 5.11.: Evolution of recurrence network assortativity $\mathcal{A}$ for (A) the $\delta^{18}O$ record from ODP site 659, and the dust flux records from ODP sites (B) 659, (C) 721, and (D) 967 during the Plio-Pleistocene. Parameters, significance test, and vertical lines are the same as in Fig. 5.9.

average path length $\mathcal{L}$ and diameter $\mathcal{D}$ as measured by Spearman's ρ are most pronounced, which is consistent with theoretical expectations (Donner et al., 2010a, P18). Correlations are more clearly developed between all four measures in case of the more highly sampled dust flux records from ODP sites 721/722 and 967 (Table 5.1). However, for all records the four measures can be considered sufficiently independent to justify including all of them for a broad and thorough nonlinear time series analysis of oxygen isotope and terrigenous dust flux variability.

5.4.2. Robustness of the results

To assure the reliability and robustness of our results, we systematically study their dependence on the relevant algorithmic parameters of our method, in particular, the widths of the recurrence window (W^*) and the detrending window (W_D^*) as well as the embedding delay (τ^*). In Figs. 5.13–5.15, the results of the significance test are presented as contours at two prescribed significance levels obtained from the observed measure's quantiles with respect to the corresponding test distribution. Green contours represent the lower prescribed quantile (5%), while black contours indicate the upper one (95%). This implies that values of the measure under study
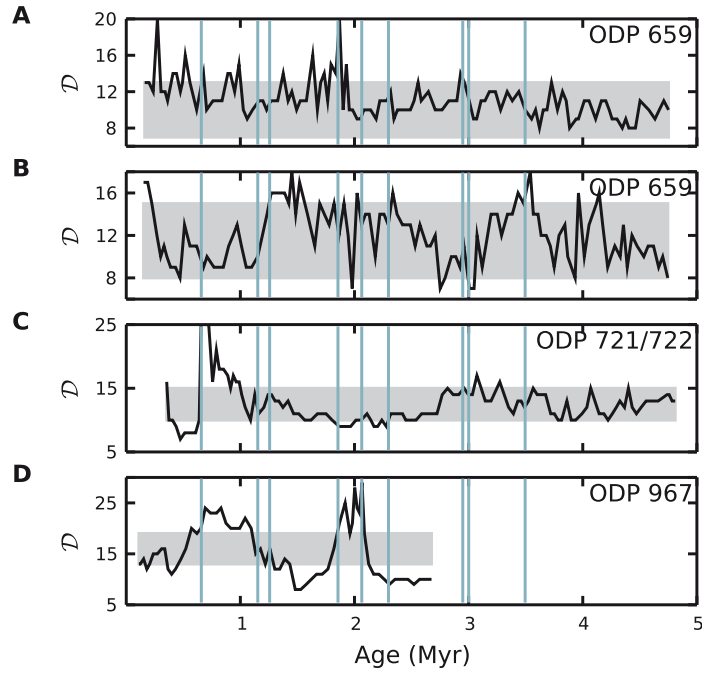
Figure 5.12.: Evolution of recurrence network diameter $\mathcal{D}$ for (A) the δ^{18}O record from ODP site 659, and the dust flux records from ODP sites (B) 659, (C) 721, and (D) 967 during the Plio-Pleistocene. Parameters, significance test, and vertical lines are the same as in Fig. 5.9.

enclosed by green contours can be considered as exceptionally low, while those lying within black contours are exceptionally large, recalling the interpretation of the applied null model given in Section 5.2.6. It is, however, important to recognize that the null hypothesis of stationarity has been tested pointwise, while physical significance requires the null hypothesis to be rejected over a certain period of time, *i.e.*, for several subsequent time points (Maraun et al., 2007). Therefore, certain line-like structures, particularly those seen in Fig. 5.15, are likely to reflect statistical fluctuations rather than physically significant dynamical transitions. In the following, we will only present the results for the ODP site 659 dust flux record.

Recurrence window size W^*

As for the model systems in Section 5.3, we first discuss the sensitivity of our results to the changing width of the recurrence window W^*. The corresponding results for the four chosen recurrence network measures are shown in Fig. 5.13. We recognize that the most significant features persist under varying W^*, although the relevant structures become broader and less significant for larger windows. This is to be expected since more and more data from time intervals not directly affected by the

Table 5.2.: Spearman's ρ measuring monotonic correlations in the time evolution of recurrence network measures for (A) the ODP site 659 δ^{18}O record, and the dust flux records from ODP sites (B) 659, (C) 721/722, and (D) 967. Significant correlations having a p-value smaller than 0.05 under the assumption of uncorrelated data of the same length are marked in bold.

		$\mathcal{T}$	$\mathcal{L}$	$\mathcal{A}$	$\mathcal{D}$			$\mathcal{T}$	$\mathcal{L}$	$\mathcal{A}$	$\mathcal{D}$
	$\mathcal{T}$	**1.00**	−0.08	**0.38**	0.00		$\mathcal{T}$	**1.00**	**0.50**	**0.40**	**0.37**
(A)	$\mathcal{L}$	−0.08	**1.00**	−0.06	**0.92**	(C)	$\mathcal{L}$	**0.50**	**1.00**	**0.37**	**0.74**
	$\mathcal{A}$	**0.38**	−0.06	**1.00**	0.03		$\mathcal{A}$	**0.40**	**0.37**	**1.00**	**0.35**
	$\mathcal{D}$	0.00	**0.92**	0.03	**1.00**		$\mathcal{D}$	**0.37**	**0.74**	**0.35**	**1.00**
		$\mathcal{T}$	$\mathcal{L}$	$\mathcal{A}$	$\mathcal{D}$			$\mathcal{T}$	$\mathcal{L}$	$\mathcal{A}$	$\mathcal{D}$
	$\mathcal{T}$	**1.00**	−0.05	0.12	0.03		$\mathcal{T}$	**1.00**	**0.65**	**0.61**	0.23
(B)	$\mathcal{L}$	−0.05	**1.00**	−0.08	**0.77**	(D)	$\mathcal{L}$	**0.65**	**1.00**	**0.54**	**0.78**
	$\mathcal{A}$	0.12	−0.08	**1.00**	**0.23**		$\mathcal{A}$	**0.61**	**0.54**	**1.00**	0.16
	$\mathcal{D}$	0.03	**0.77**	**0.23**	**1.00**		$\mathcal{D}$	0.23	**0.78**	0.16	**1.00**

origin of specific network properties (*e.g.*, a laminar phase in the dynamics) contribute to the longer windows. As the window width is increased linearly, cone-like structures emerge (which is especially well visible for the Mid Pliocene transitivity maximum as the most relevant feature). In general, we observe that for our example the transitivity is most robust with respect to changes of W^*, whereas the other network measures may lose significance if this parameter of our analysis method is varied. We note, however, that the periods of interest identified in Section 5.4.1 are robust for a wide range of recurrence window sizes, presenting a trade-off between good localization of identified features (small windows) and reasonable statistical confidence of the calculated network properties (large windows).

Detrending window size W_D^*

Regarding the dependence of our observations on the choice of the detrending window, Fig. 5.14 shows that the general temporal variability pattern of the different network measures remains unchanged as W_D^* is altered, whereas the actual significance levels are more strongly influenced. In general, we can conclude, however, that the most significant time periods persist under variations of W_D^*, which is particularly well expressed for the transitivity during the Mid Pliocene. Together with the fact that recurrence network analysis of the three dust flux records without detrending produces consistent results (Donges et al., 2011c, P10) this suggests that trends do not have a significant influence on the outcomes of recurrence network analysis as long as $W^* \ll N \langle \Delta T \rangle$. However, this should be checked in any particular application by comparing the results for the time series data before and after detrending. Note that the results for undetrended time series are approximated by those displayed in Fig. 5.14 for $W_D^* \approx N \langle \Delta T \rangle$, since recurrence network analysis is invariant to nearly uniform translations of the data (Section 4.2.6).

Embedding delay τ^*

Our results are also robust with respect to reasonable variations of the embedding delay τ^* around the previously chosen delay time $\tau^* = 10$ kyr (Fig. 5.15). However, for the embedding delay exceeding $\tau^* = 20$ kyr the results and significance levels change considerably. This is expected as for delays larger than 20 kyr, autocorrelations in the time series do not decrease significantly anymore. In the case of the δ^{18}O record from ODP site 659 they even increase again due to pronounced periodicities (Fig. 5.3), so that the autocorrelation criterion for the choice of τ^* does not apply here anymore.
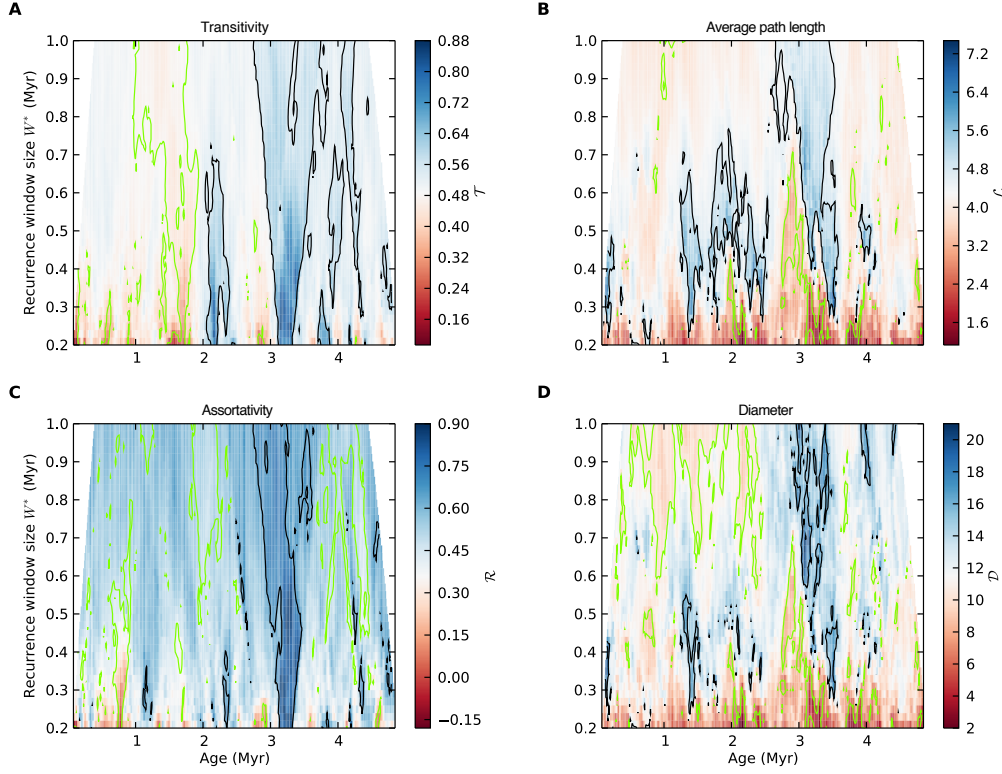
Figure 5.13.: Dependence of (A) transitivity $\mathcal{T}$, (B) average path length $\mathcal{L}$, (C) assortativity $\mathcal{A}$, and (D) diameter $\mathcal{D}$ on the recurrence window size W^* for the dust flux record from ODP site 659. The recurrence window step size is fixed to $\Delta W^* = 41$ kyr, the detrending window size to $W_D^* = 500$ kyr. Green and black contours correspond to the 5% and 95% quantiles with respect to the test distribution obtained from 10,000 realizations of our null model. Other parameters were: embedding dimension $m = 3$ and delay $\tau^* = 10$ kyr, the threshold was chosen to yield a fixed edge density $\rho = 0.05$. The white bands indicating "no value" at the left and right margins of each panel appear because we plot the network measures f^{μ,W^*} at the mid-points t^μ of the windows μ used for recurrence network analysis (Section 5.2.4). As the mid-points of the first (last) window move further into the past (present) for increasing W^*, the white bands grow linearly for linearly increasing W^*.
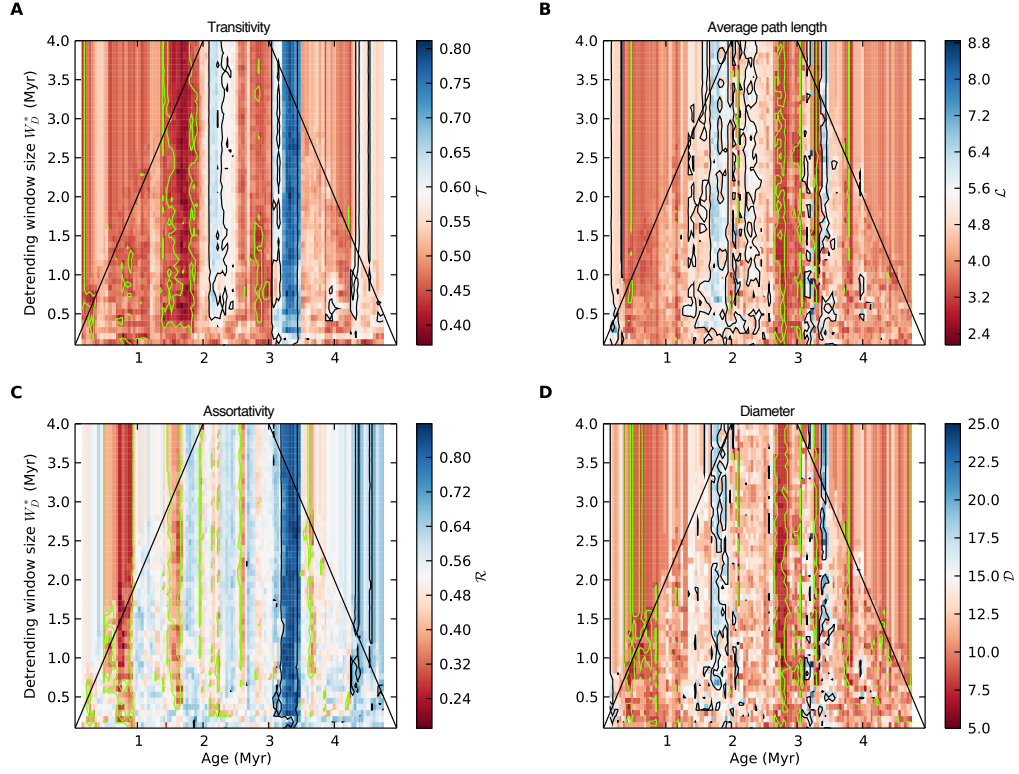
Figure 5.14.: Dependence of (A) transitivity $\mathcal{T}$, (B) average path length $\mathcal{L}$, (C) assortativity $\mathcal{A}$, and (D) diameter $\mathcal{D}$ on the detrending window size W_D^* for the dust flux record from ODP site 659. The recurrence window size is fixed to $W^* = 410$ kyr with a step size of $\Delta W^* = 41$ kyr. Green and black contours correspond to the 5% and 95% quantiles with respect to the test distribution obtained from $10,000$ realizations of our null model. Other parameters were: embedding dimension $m = 3$ and delay $\tau^* = 10$ kyr, the threshold was chosen to yield a fixed edge density $\rho = 0.05$. In regions outside the black dashed lines the results are influenced by boundary effects, since the effective detrending window size $W_D(t)$ has to decrease towards the time series' limits (Eq. (5.3)). The white bands indicating "no value" at the left and right margins of each panel appear because we plot the network measures f^{μ,W_D^*} at the mid-points t^μ of the windows μ used for recurrence network analysis (Section 5.2.4). In contrast to Fig. 5.13 their width does not change as W^* is fixed here.
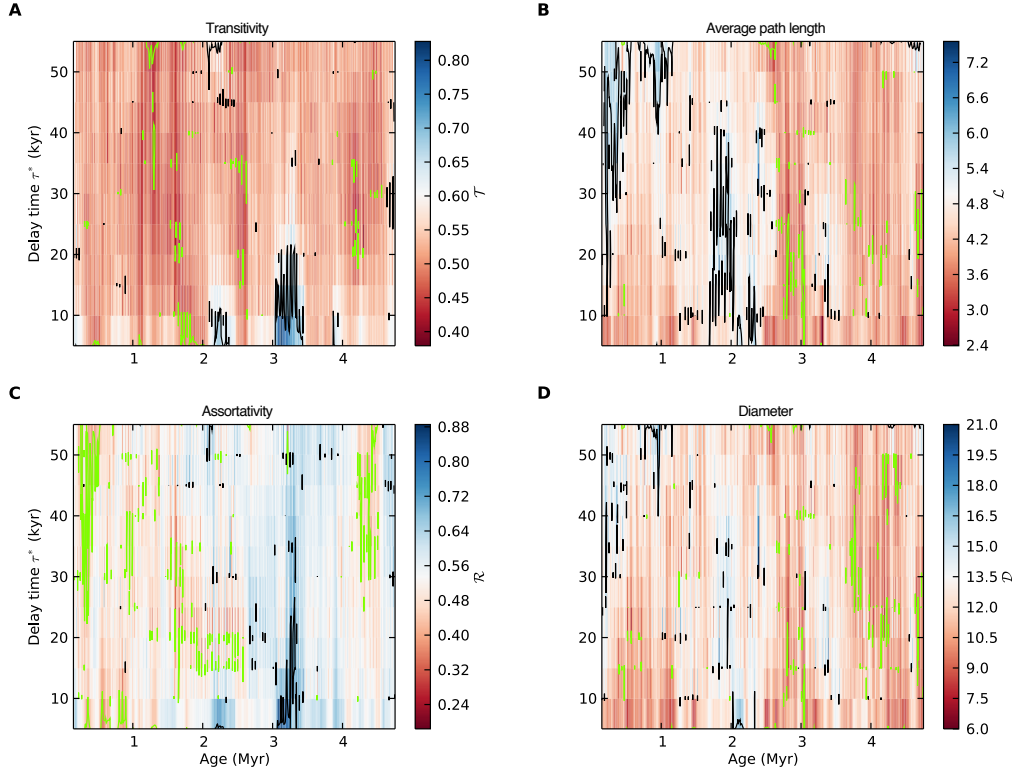
Figure 5.15.: Dependence of (A) transitivity $\mathcal{T}$, (B) average path length $\mathcal{L}$, (C) assortativity $\mathcal{A}$, and (D) diameter $\mathcal{D}$ on the embedding delay time τ^* for the dust flux record from ODP site 659. The recurrence window size is fixed to $W^* = 410$ kyr with a step size of $\Delta W^* = 41$ kyr, the detrending window size to $W_D^* = 500$ kyr. Green and black contours correspond to the 5% and 95% quantiles with respect to the test distribution obtained from 10,000 realizations of our null model. Vertical line-shaped contours are likely to correspond to statistical fluctuations rather than physically significant time intervals (see text). Other parameters: embedding dimension $m = 3$, the threshold was chosen to yield a fixed edge density $\rho = 0.05$.

5.5. Discussion

We have demonstrated that recurrence network analysis allows detecting dynamical transitions in non-stationary model systems as well as real-world paleoclimate data. Transitivity and average path length have been previously discussed as appropriate network properties indicating qualitative changes in the dynamics of the underlying system (Marwan et al., 2009, P20; Donner et al., 2010c, P19). Here, we have provided examples that also other global network measures such as assortativity and network diameter trace qualitative changes in dynamical systems, where, specifically, assortativity does not have a similarly straightforward interpretation in terms of basic system properties as the other mentioned quantities (see Chapter 4).

Our results show that the outcomes of recurrence network analysis are quite robust if the fundamental parameters of the method (detrending and recurrence window sizes, embedding delay) are varied within a reasonable range. Unlike for other methods of time series analysis, the consideration of embedding with properly chosen parameters is necessary in order to obtain feasible results.

In contrast to other techniques, recurrence network analysis does not characterize temporal interrelationships within the analyzed records (although time information enters indirectly through embedding parameters, however, mostly on short time scales as typically $m\tau^* \ll N\langle\Delta T\rangle$), but quantifies geometric properties of the sampled dynamical system in its (reconstructed) phase space. The only implicit assumption is that the available sample of observed state vectors $\{y_i^\mu\}$ represents the spatial distribution of the *true* state vectors in the (properly reconstructed) phase space of the underlying dynamical system sufficiently well (see Chapter 4).

In this respect, our approach is very generally applicable and has comparably moderate requirements in terms of the requested number of data (*i.e.*, windows with $\mathcal{O}(100)$ data points are sufficient for a reasonable analysis of non-stationary systems). In case of paleoclimate records, this complementary way for characterizing time series avoids conceptual problems of other approaches due to uncertain age models and non-uniform sampling. *E.g.*, the results of recurrence network analysis $\{f^\mu\}$ are invariant to changes in the age model $\{t_i\}$, only the associated windows' mid-points $\{t^\mu\}$ change with variations in $\{t_i\}$ (Eq. (5.9)). However, the aforementioned problems indirectly persist in terms of the necessary embedding of the data and have to be finally resolved in corresponding future work. While the present chapter focussed on the technical aspects of applying recurrence network analysis to paleoclimate time series, an in-depth discussion of the results obtained for the three dust flux records in the light of additional proxy records and paleontological evidence is given in Chapter 6 and Donges et al. (2011c, P10).

5.6. Summary

The analysis of paleoclimate time series is usually affected by severe methodological problems, resulting primarily from non-equidistant sampling and uncertain age models.

As an alternative to existing methods of time series analysis, in this chapter we have argued that the statistical properties of recurrence networks are promising candidates for characterizing the system's nonlinear dynamics and quantifying structural changes in its reconstructed phase space as time evolves. The results of recurrence network analysis are invariant under changes in the age model and are not directly affected by non-equidistant sampling of the data. Specifically, we have investigated the behavior of recurrence network measures for both paradigmatic model systems with non-stationary parameters and four marine records of long-term paleoclimate variations. We have shown that the obtained results are qualitatively robust under changes of the relevant parameters of our method, including detrending, size of the running window used for analysis, and embedding delay. We have demonstrated that recurrence network analysis is able to detect relevant regime shifts in synthetic data as well as in problematic geoscientific time series. This suggests its application as a general exploratory tool of time series analysis complementing existing methods.

Chapter 6.

Paleoclimate-variability transitions possibly related to human evolution

> *Fan the flames of controversy.*
> Roger Revelle (after Inman (2003))

6.1. Introduction

Recent comparisons of terrestrial and marine paleoclimate archives have resulted in an intense debate concerning global vs. regional forcing of East Africa's climate and its relationship to human evolution during the last 5 Myr (deMenocal, 1995; deMenocal, 2004; Trauth et al., 2007; deMenocal, 2011). The gradual long-term retreat of equatorial rain forests and the emergence of drier environments in East Africa (Clemens et al., 1991; Trauth et al., 2003; deMenocal, 2004) were interrupted by distinct epochs of increased humidity indicated by paleo-lake levels in different basins of the East African Rift System (EARS) displaying synchronous highs at about 2.7–2.5 Myr, 1.9–1.7 Myr, and 1.1–0.9 Myr BP (before present) (Trauth et al., 2005). Notably, these epochs coincide well with certain global-scale climate transitions like the final closure of the Panama isthmus (Haug and Tiedemann, 1998; Bartoli et al., 2005; Sarnthein et al., 2009), the intensification of the atmospheric Walker circulation (Ravelo et al., 2004), and the shift from a predominance of obliquity-driven glacial variability (41 kyr period) to glacial-interglacial cycles with a 100 kyr period (Berger and Jansen, 1994; Mudelsee and Schulz, 1997). Further reconstructions revealed additional relevant lake periods at 4.7–4.3 Myr, 4.0–3.9 Myr, 3.4–3.3 Myr, and 3.2–2.95 Myr BP (Trauth et al., 2007). Previous findings suggest that the dominating summer aridity in East African climate was controlled mainly by orbitally driven changes in the local irradiation driving regional monsoon activity via changes of sea surface temperatures (SSTs) (Kutzbach and Streetperrott, 1985; Clemens et al., 1991; Kutzbach and Liu, 1997; Ruddiman, 2008; Trauth et al., 2009; Trauth et al., 2010) rather than by high-latitude glacial dynamics. In addition, tectonic activity and the resulting complex topography of East Africa could have triggered particularly variable climate conditions during the Plio-Pleistocene (Trauth et al., 2010; Reynolds et al., 2011).
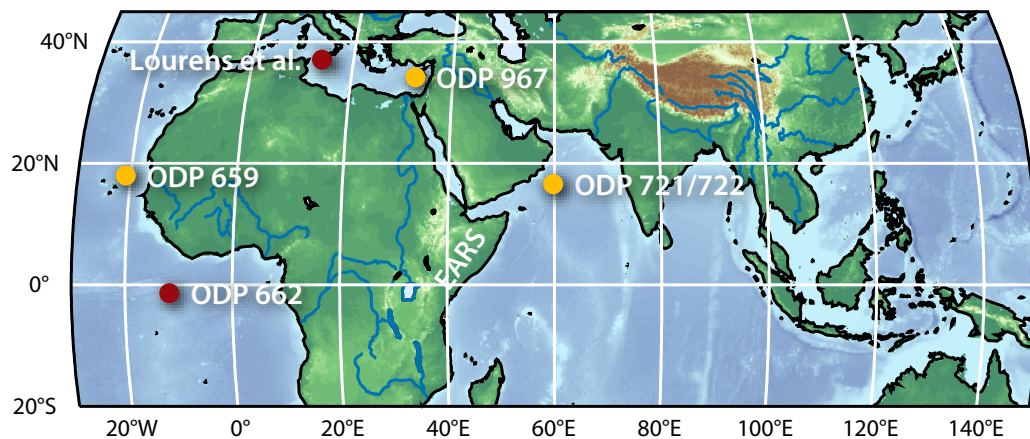
Figure 6.1.: Map displaying the locations of the marine sediment cores analyzed in this chapter (orange): ODP 659 (East Atlantic) (Tiedemann et al., 1994), 721/722 (Arabian Sea) (deMenocal, 1995; deMenocal, 2004), and 967 (Eastern Mediterranean Sea) (Larrasoaña et al., 2003). In addition, locations of additional complementary records of Plio-Pleistocene climate evolution (red) in the Atlantic (ODP site 662 (Herbert et al., 2010)) and the Mediterranean (composite sequence of marine sediments at the Sicilian and Calabrian coast (Lourens et al., 1996)) as well as the East African Rift System (EARS) are shown.

As early as Darwin (1859), scholars have speculated on if and how climate change shaped human evolution (deMenocal, 2011). Based on the present-day knowledge of Plio-Pleistocene African climate, three general hypotheses concerning mechanisms of climate-induced mammalian evolutionary processes are currently discussed (Trauth et al., 2010): (i) The *turnover pulse hypothesis* postulates progressive habitat changes (Vrba, 1985; Vrba, 1993) due to abrupt climate shifts (deMenocal, 1995; deMenocal, 2004) enforcing the adaptation of existing and the evolution of new species. (ii) The *variability selection hypothesis* proposes an increasing instability of environmental conditions as a driver for the simultaneous emergence of species (Potts, 1996; Potts, 1998). (iii) Finally, the *pulsed climate variability hypothesis* promotes spikes of more variable climate conditions unrelated to high-latitude glacial cycles as a key driver of evolutionary selection (Trauth et al., 2003; Trauth et al., 2005; Trauth et al., 2007; Maslin and Trauth, 2009). With the currently available paleoclimate and paleoanthropological records, it has not been possible to provide clear evidence for one of these hypotheses by means of traditional (linear) statistical analysis.

Although there is an unequivocal correlation of terrestrial and marine paleoclimate records, to date, marine sediments (Fig. 6.1) provide the only archive that allows the study of Plio-Pleistocene African climate on all relevant time scales. However, earlier analyses of terrigenous dust flux records using traditional time series analysis techniques to detect important transitions in African climate yielded contradictory results with respect to the signature and timing of these events (deMenocal, 1995;

deMenocal, 2004; Trauth et al., 2009). Difficulties like these are to be expected when applying linear methods to the highly nonlinear climate system underlying paleoclimate proxy records. Linear techniques of time series analysis by definition are limited to the study of linear dynamics. To circumvent this problem and explore the vast remainder of nonlinear phenomena, following Donges et al. (2011c, P10) here we present results based on recurrence network analysis (see Section 3.2.2). As shown in Chapter 5, this nonlinear technique enables us to reliably detect qualitative changes within observational time series which are largely indiscernible for linear methods of data analysis (Xu et al., 2008; Donner et al., 2010c, P19; Donner et al., 2011a, P13). This instrument leads to an improved detection of a particular flavor of Plio-Pleistocene African climate change and its potential influence on the habitats of early humans. Based on concepts of dynamical systems and graph theory, recurrence network analysis is particularly efficient in applications where the number of observations is limited and the data points are unevenly spaced, which is common for paleoclimate proxy records such as time series of dust accumulation rates (Donges et al., 2011a, P11). Specifically, recurrence network analysis is sensitive to general changes in the dynamics, rather than those in the amplitudes of the entire record (*e.g.*, trends in mean or variance) or modes with a certain periodicity. Therefore it is well suited for detecting tipping points or, more generally, bifurcations in the behavior of nonlinear complex systems like the Earth's climate (Marwan et al., 2009, P20; Donner et al., 2011a, P13; Donges et al., 2011a, P11).

6.2. Results

For detecting significant shifts in the dynamics of Plio-Pleistocene African climate as reflected by terrigenous dust flux (see Section 5.2.1) we rely on two established measures of complex network theory: transitivity and average path length (Newman, 2003). It has been theoretically and empirically shown in several studies that, when calculated for recurrence networks of selected time series segments (see Chapter 5), transitivity reflects the regularity of the dynamics within this segment or time window (Marwan et al., 2009, P20; Donner et al., 2011a, P13; Zou et al., 2010, P17; Donges et al., 2012, P8). Noisy or chaotic dynamics gives rise to low values, while (almost) periodic or laminar behavior induces high values of transitivity. We therefore refer to it as a climate regularity (CR) index in the following. Along the same lines, extreme values of the average path length indicate an abrupt dynamical change (ADC) between different dynamical regimes within the considered time window (Marwan et al., 2009, P20; Donner et al., 2011a, P13; Zou et al., 2010, P17) (see Section 3.2.2). It is a crucial feature of our approach that CR and ADC do not reflect changes in long-term trends, but are in contrast sensitive to the regularity of short-term fluctuations (CR) and general abrupt changes in this short-term dynamics (ADC).[15] Both measures are hence responsive to different nonlinear aspects of the time series

---

[15]However, it should be born in mind that in the context of this study on geological time scales, short-term fluctuations actually reflect millennial-scale climate variability.
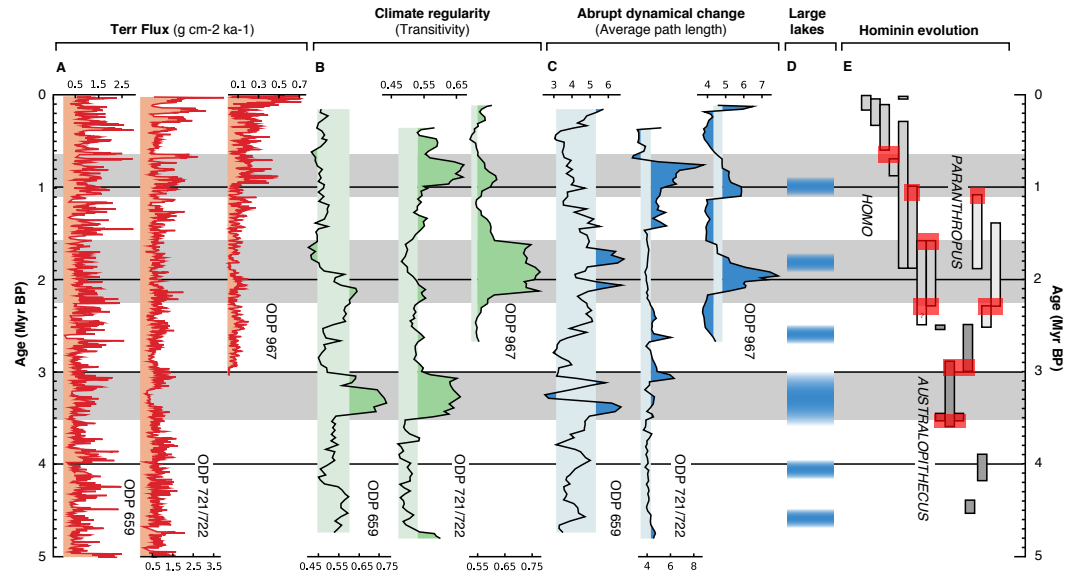
Figure 6.2.: (A) Terrestrial dust flux records from the three considered ODP sites (Tiedemann et al., 1994; deMenocal, 1995; deMenocal, 2004; Larrasoaña et al., 2003). (B,C) Results of recurrence network analysis of the three dust flux records including 90% confidence bands (vertical shadings) of a stationarity test (Section 5.2.6). Comparing both measures for all records reveals significant and synchronous large-scale regime shifts in dust flux dynamics (horizontal shadings). (D) Time intervals with geological evidence for large lakes in East Africa, comprising collected information from different areas in the EARS (Trauth et al., 2007) and additional results from the Afar basin (Hailemichael et al., 2002; Campisano and Feibel, 2007). (E) Major known steps of human evolution in East Africa (simplified from Trauth et al. (2007)). Red bars indicate epochs where the possible emergence and/or extinction of known hominin species coincides with detected climate transitions (Appendix E).

data and do not necessarily show transitions at the same epochs (Marwan et al., 2009, P20; Donner et al., 2010c, P19; Donges et al., 2011a, P11). If they do so, however, this points at a particularly relevant feature in the data.

The results reported below are obtained using the methods and parameters that are documented in detail in Section 5.2, but omitting the detrending step described in Section 5.2.2 consistently with earlier work on ODP site 659 (Marwan et al., 2009, P20; Donner et al., 2011a, P13). This change in procedure is justified by the manifest robustness of our results with respect to variations of the detrending window size (Section 5.4.2).

For representative dust flux records from the Atlantic as well as the Indian Ocean (ODP sites 659 and 721/722, Fig. 6.2A), CR reveals surprisingly similar long-term change in short-term fluctuations before about 1.5 Myr BP (in contrast to the Mediterranean ODP site 967, Fig. 6.2A), although both sites are strongly geographically separated and, hence, characterized by distinct wind systems and dust sources (de-

Menocal, 1995; Prospero et al., 2002; Trauth et al., 2009) (Fig. 6.2B). Specifically, the Saharan Air Layer, African Equatorial Jet, and trade winds contribute at ODP site 659 (Tiedemann et al., 1994), while the Shamal winds from the Arabian Peninsula, which are connected to the western branch of the Asian monsoon system, dominate at ODP site 721/722 (Clemens et al., 1996). This indicates that changes in CR during the Pliocene and early Pleistocene are robust manifestations of long-term variations in the dynamics of large-scale African dust mobilization and transport.

As a particularly striking feature, we identify a pronounced maximum of CR between 3.5–3.0 Myr BP at both ODP sites 659 and 721/722 signaling a period of exceptionally regular dust flux dynamics. The epochs highlighted by ADC support these findings (Fig. 6.2C). The time interval 3.5–3.0 Myr BP is characterized by three distinct and highly significant extrema (two maxima, one minimum) in the ODP site 659 record, indicating shifts between regimes of higher and lower regularity in the variations of environmental conditions (Marwan et al., 2009, P20). Similar observations can be made for the ODP site 721/722 data, however, the increased values of ADC are less well pronounced but persist considerably longer (until 2.8 Myr BP).

In general, the variations of ADC observed at ODP sites 659 and 721/722 differ remarkably (Fig. 6.2C), although CR traces consistent shifts between more and less regular variability until about 1.5 Myr BP. Considering the Mediterranean record (ODP site 967), further synchronous events are identified. Specifically, we find an extended, highly significant maximum of CR between about 2.25 and 1.6 Myr BP, and of ADC between 2.2 and 1.7 Myr BP. The latter one roughly coincides with the observations made at ODP site 659. Moreover, between about 1.1 and 0.7 Myr BP, both CR and ADC show significant maxima for ODP site 967 and ODP site 721/722, but not for ODP site 659.

In summary, our analysis identifies three main epochs of interest: 3.5–3.0, 2.25–1.6, and 1.1–0.7 Myr BP (Fig. 6.2). All three are characterized by significant extrema of CR and/or ADC in at least two of the analyzed records. In addition, there are further shorter time periods of considerably increased/decreased CR/ADC observed in different records which are, however, typically less pronounced. Our results do not change significantly if the basic parameters of our analysis method are modified (Section 5.4.2 and Donges et al. (2011a, P11)).

6.3. Nonlinear identification of critical transitions in paleoclimate

Tipping points in the climate system, *i.e.*, values of system parameters at which critical transitions in climate dynamics take place, have gained increasing attention in the course of the ongoing debate on potential impacts of anthropogenic climate change (Lenton et al., 2008; Schellnhuber, 2009; Levermann et al., 2012). Given the large risk (product of impact and likelihood) associated with the activation of certain climate tipping elements (*e.g.*, the Greenland and West Antarctic ice-sheets),

understanding and anticipating future qualitative changes in climate tipping elements is of major importance and requires a good knowledge of past transitions recorded in paleoclimate data (Lenton, 2011). Previous research revealed different kinds of characteristic precursory signatures associated with climate tipping points (Kuehn, 2011; Thompson and Sieber, 2011[b]; Lenton, 2011). Predominantly, changes in the variance structure of relevant observables represent a critical slowing down of intrinsic transient responses within the data prior to the instabilities (Held and Kleinen, 2004; Livina and Lenton, 2007; Dakos et al., 2008; Scheffer et al., 2009; Scheffer, 2009).

Recurrence network analysis is a particularly promising exploratory tool for detecting structural changes in paleoclimate dynamics potentially associated with certain tipping elements in the Earth's climate system. It has several advantages above other frequently used techniques for detecting (incipient) bifurcations in time series: (i) Recurrence network analysis is *not* explicitly based on temporal correlations, but on geometric considerations (Donner et al., 2011b, P15; Donges et al., 2011a, P11). Hence it is more robust with respect to noisy and non-uniformly sampled paleoclimate time series with uncertain timing than methods relying on temporal correlations (Held and Kleinen, 2004; Donner and Witt, 2006; Livina and Lenton, 2007; Dakos et al., 2008) like degenerate fingerprinting (Held and Kleinen, 2004) and detrended fluctuation analysis (Livina and Lenton, 2007). (ii) As a nonlinear technique, recurrence network analysis is not restricted to detecting only changes in linear statistical properties (*i.e.*, the autocovariance structure) of a time series (Held and Kleinen, 2004; Dakos et al., 2008; Scheffer et al., 2009; Scheffer, 2009). In contrast, it characterizes more general variations in the recorded dynamics which may become particularly relevant close to bifurcation points. (iii) Recurrence network analysis has been shown to reliably perform with a comparably small number of data points (Donges et al., 2011a, P11; Zou et al., 2010, P17), particularly when contrasting it with linear spectral methods (deMenocal, 1995; deMenocal, 2004) or certain nonlinear stochastic models of climate fluctuations for detecting noisy bifurcations (Livina et al., 2010; Thompson and Sieber, 2011[a]).

We emphasize that all existing methods for detecting tipping points from paleoclimate time series (including recurrence network analysis) make use of sliding window techniques. By construction, such methods have a limited temporal resolution of the variations of the statistics of interest. Hence, identified dynamical transitions can only be attributed to epochs rather than distinct points in time. This strategy has the advantage of a higher robustness with respect to uncertainties in the data themselves as well as the associated age models, rendering the results of recurrence network analysis particularly robust and statistically reliable (Donges et al., 2011a, P11).

6.4. Climatological interpretation

The three identified transition periods (Fig. 6.2), which are only partially known from previous studies, can be clearly related to distinct and known climatic mechanisms.

Specifically, the interval 1.1–0.7 Myr BP corresponds to the Mid-Pleistocene transition (MPT) characterized by a change from glacial cycles predominantly related to obliquity variations of the Earth's orbit (approximately 41 kyr period) to such with an approximately 100 kyr periodicity. The timing of this transition and its underlying mechanisms have been extensively studied elsewhere (Mudelsee and Schulz, 1997; Clark et al., 2006). That the MPT is not detected in the record from ODP site 659 by recurrence network analysis does not imply that it did not have any climatic impact in the corresponding dust-source areas in North-West Africa. It just shows that our technique is not sensitive to the local signature of the transition if present, *e.g.*, if it manifests itself in some change of trend (deMenocal, 1995; deMenocal, 2004; Trauth et al., 2009) (see the discussion in Section 6.2). Alternatively the locally available data may be insufficient in quality and/or resolution to reveal the subtle type of events recurrence network analysis is focussing on. This reasoning holds for any other known transition that is not detected by our method in any of the considered records. Regarding the transition period in the Early Pleistocene (2.25–1.6 Myr BP), the timing well coincides with known large-scale changes in atmospheric circulation associated with an intensification and spatial shift of the Walker circulation (Ravelo et al., 2004).

The third identified transition period includes the Mid Pliocene (3.3–3.0 Myr BP), the last long period during which global mean temperatures have been consistently higher than present day (Haywood et al., 2005). This epoch is thus considered as an analog for future climate of the late 21st century if anthropogenic emissions of greenhouse gases continue to rise (Solomon et al., 2007). It was characterized by a strongly reduced meridional temperature gradient due to an intermittent poleward shift of the North Atlantic overturning resulting in a strong warming of the Arctic by oceanic surface currents (Robinson, 2009; Dowsett et al., 2009). At the same time, recurrence network analysis reveals an enhanced regularity of African dust flux variations in both the Arabian Sea and Atlantic Ocean. At ODP site 721/722, this observation is predominantly caused by a well-pronounced epoch of relatively weak and approximately constant dust flux between about 3.36 and 3.17 Myr BP (Fig. 6.3E). A similar – but shorter – feature is found at ODP site 659 between about 3.25 and 3.19 Myr BP (Fig. 6.3D) as well as at ODP sites 661 and 662 in the Eastern Equatorial Atlantic (deMenocal, 1995; deMenocal, 2004). The presence of such very similar features with a clearly different timing suggests the presence of either one common climatological mechanism influencing the Arabian Peninsula *much earlier than* Northwest Africa, or two distinct (but eventually interrelated) factors, where the first only affected the Northeast African and/or Arabian dust flux dynamics.

A first important candidate factor is the marine isotope stage (MIS) M2 (Shackleton et al., 1995), an unusually cold period (3.32–3.28 Myr BP) prior to the Mid Pliocene warm period (Lisiecki and Raymo, 2005; Steph et al., 2006), cf. Fig. 6.3A. This cooling was most likely triggered by a significant reduction of northward heat transport via the North Atlantic Current between 3.33 and 3.283 Myr BP (de Schepper et al., 2009) – possibly due to intermittent closures and re-openings of the Panamaian Seaway (Sarnthein et al., 2009) – and led to a strong increase in global ice volume and
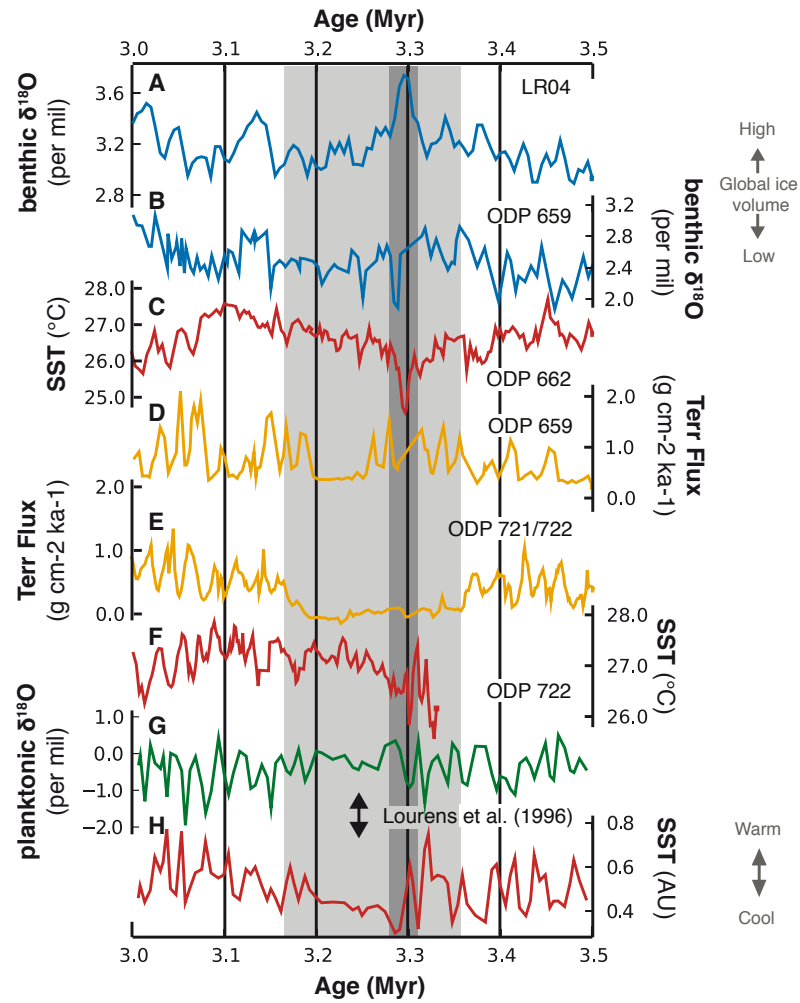
Figure 6.3.: Comparison of Mid Pliocene (3.5–3.0 Myr BP) global ice volume, sea surface temperature, and dust flux reconstructions: (A) δ^{18}O benthic stack record LR04 (Lisiecki and Raymo, 2005), (B) benthic δ^{18}O record from ODP site 659, (C) Alkenone-based SST reconstruction from ODP site 662 (Herbert et al., 2010), (D) terrigenous dust flux at ODP site 659 (Tiedemann et al., 1994), (E) terrigenous dust flux at ODP site 721/722 (deMenocal, 1995; deMenocal, 2004), (F) Alkenone-based SST reconstruction from ODP site 722 (Herbert et al., 2010), (G,H) planktonic δ^{18}O and SST reconstruction from ensembles of planktonic foraminifera for a composite sequence from Southern Italy (Lourens et al., 1996). The dark gray vertical bar indicates the MIS M2 (preceding an epoch with cold SST in the Mediterranean Sea and reduced dust flux into the Atlantic Ocean), the light gray bar indicates the interval of reduced dust flux into the Arabian Sea.

a global sea-level fall to up to 60 m below present-day values (Dwyer and Chandler, 2009). As a consequence, global SST decreased by 2–3 K (de Schepper et al., 2009), with a 1–2 K decrease in the tropics (Herbert et al., 2010), see Fig. 6.3C,F. This low-latitude cooling could be related to the reduced dust flux offshore of Northwest Africa, but can hardly explain the much earlier signature in the Arabian Sea.

A second possible triggering mechanism is the successive northward displacement of New Guinea, due to which instead of warmer Equatorial Pacific water presently only less saline and colder North Pacific water can pass the Indonesian throughflow (Cane and Molnar, 2001). Recent paleoceanographic reconstructions revealed that during the Pliocene, subsurface waters in the eastern tropical Indian Ocean freshened and cooled by about 4K, including a major cooling step between 3.5 and 2.95 Myr BP (Karas et al., 2009). Although SST was much less affected in most parts of the Indian Ocean, the southern coast of the Arabian Peninsula as well as the region around the horn of Africa are known as (wind-driven seasonal) upwelling regions (Schils and Coppejans, 2003; Herbert et al., 2010), which suggests that cold subsurface waters could have (at least intermittently) reached the ocean surface in this area and, thus, have led to a considerable decrease in the average regional SST. Recent alkenone-based SST reconstructions for ODP site 721/722 (Herbert et al., 2010) actually confirm strong SST variations with partially extremely low values between at least 3.33 Myr BP (the beginning of the respective record) and 3.28 Myr BP (see Fig. 6.3F), which cannot be explained by the known pattern of early glacial activity (Lisiecki and Raymo, 2005).

In summary, both aforementioned factors would have led to decreasing SSTs and, hence, to lower surface air temperatures and potential changes in the evaporation-precipitation balance. As a consequence, less convective rainfall, but also a shift (and possible weakening) of dominating atmospheric circulation patterns was likely. Since in the potential source areas of terrigenous dust lower temperatures foster the formation of a closed vegetation cover, erosion and, hence, dust mobilization would have decreased. This interpretation is supported by the existence of large lakes in East Africa between 3.4 and 2.95 Myr BP (including the most pronounced lake episode in the Afar region (Campisano and Feibel, 2007) at about 3.33–3.23 Myr BP) pointing towards a very humid climate (Fig. 6.2D). However, we have to emphasize that our considerations above are speculative so far and need confirmation from modeling studies and complementary paleoclimate archives.

6.5. Climate variability and human evolution

To study the influence of African climate variability on human evolution, we compare the major large-scale transitions in African climate identified above with the currently available fossil record (Fig. 6.2E). Particularly, we observe that transitions in hominin evolution indicated by the appearance and disappearance of hominin species tend to cluster close to the identified climate shifts. These observed coincidences are unlikely to arise by chance even when taking into account dating uncertainties and

the inherent incompleteness of the fossil record, as can be shown using a suitable statistical significance test (Appendix E).

The presented results therefore shed some light on the possible interrelationships between long-term climate change and hominin evolution. Specifically, we suggest that shifts between periods of more regular and more erratic environmental variability have been particularly important triggers for the development of humankind in East Africa. On the one hand, epochs of higher regularity could have led to a stabilization and gradual increase of a population and, thus, a spread of a species over a larger area. On the other hand, subsequent periods of more irregular climate variability, possibly associated with changes in long-term trends, would have created an additional evolutionary pressure via a fragmentation of habitats and, thus, adaptation and diversification leading to speciation (Trauth et al., 2010).

Supporting and extending Potts' variability selection hypothesis on environmental control of human evolution (Potts (1996); Potts (1998) and hypothesis (ii) in Section 6.1), our point of view strongly suggests that in addition to the mean climate conditions and the amplitude of variations of environmental parameters, (intermittent) changes in the regularity of climate fluctuations should be considered in future, more refined theories. In line with Potts' hypothesis, this mechanism on orbital time-scales would benefit generalists like *Homo* which are able to cope with strongly varying environmental conditions, but penalize specialists like *Paranthropus* (Potts, 1996). We must however keep in mind that the time scales of variations that are possibly relevant for migration of populations are not yet resolved in the available paleoclimate data. The necessity for further testing the extended variability selection hypothesis put forward here against other hypotheses (see Section 6.1) calls for future efforts to obtain high-resolution (decadal to centennial scale) data on Plio-Pleistocene African climate history.

6.6. Discussion

Recurrence network analysis has proven its ability to unravel large-scale changes in the temporal variability of African environmental conditions on super-millennial time scales. Comparing our results with findings from linear studies (Trauth et al., 2009) demonstrates that past climate change in Africa includes a significant, previously overlooked nonlinear component. This complementary information supports the conclusions of Trauth et al. (2009) in that we do not find evidence for sustained and irreversible step-like changes in climate variability that were proposed by deMenocal (1995); deMenocal (2004).[16]

Our results provide clear evidence for subtle, but significant transitions in the dynamics of mineral dust transport from the African continent to the adjacent oceans at about 3.35–3.15, 2.25–1.6, and 1.1–0.7 Myr BP. These transitions unanimously correlate with important global climate transitions, such as changing ocean circulation (after 3.5 Myr BP), the intensification of the low-latitude Walker Circulation (ca. 1.7

---

[16]A different view on the reversibility properties of time series is presented in Appendix B.

Myr BP) and the onset of 100 kyr glacial-interglacial cycles during the Mid-Pleistocene transition (ca. 1.25–0.7 Myr BP). The three episodes are characterized by radical changes in the ocean-atmosphere conditions, and hence the timing, magnitude, and style of wet-dry-wet transitions in tropical and subtropical Africa, without doubt influencing the regional climate and environment of early humans.

Indeed we observe statistically significant coincidences between the detected climate shifts and transitions in human evolution in the geological record. By analogy, this may be regarded as a warning considering the large risks for future human societies associated with climate tipping elements undergoing potentially irreversible, qualitative transitions due to anthropogenic climate change during the 21st century, even if the time scales involved are very different. However, to harness the potential of recurrence network analysis and other nonlinear techniques to provide early warning of climate tipping points on these centennial time scales remains a challenge for future research.

6.7. Summary

Potential paleoclimatic driving mechanisms acting on human evolution present an open problem of cross-disciplinary scientific interest. The analysis of paleoclimate archives encoding the environmental variability in East Africa during the last 5 Myr (million years) has triggered an ongoing debate about possible candidate processes and evolutionary mechanisms. In this chapter, we have successfully applied recurrence network analysis to three distinct marine records of terrigenous dust flux. Our method enabled us to identify three epochs with transitions between qualitatively different types of environmental variability in North and East Africa during the (i) Mid-Pliocene (3.35–3.15 Myr BP (before present)), (ii) Early Pleistocene (2.25–1.6 Myr BP), and (iii) Mid-Pleistocene (1.1–0.7 Myr BP). A deeper examination of these transition periods revealed potential climatic drivers, including (i) large-scale changes in ocean currents due to a spatial shift of the Indonesian throughflow in combination with an intensification of Northern Hemisphere glaciation, (ii) a global reorganization of the atmospheric Walker circulation induced in the tropical Pacific and Indian Ocean, and (iii) shifts in the dominating temporal variability pattern of glacial activity during the Mid-Pleistocene, respectively. A reexamination of the available fossil record demonstrated statistically significant coincidences between the detected transition periods and major steps in hominin evolution. This suggests that the observed shifts between more regular and more erratic environmental variability may have acted as a trigger for rapid change in the development of humankind in Africa.

Chapter 7.

Coupled climate networks and the atmosphere's general circulation

The more you tune, the less you should trust.
Michael Ghil (pers. comm.)

7.1. Introduction

Recently, climate networks representing the statistical similarity structure of spatiotemporally resolved climatological fields have been successfully employed for revealing novel aspects of climate dynamics in reanalysis data sets and in simulations of global climate models (Section 3.3.2). As argued in Chapter 1, understanding the complex interactions between different domains of the Earth system which may themselves be viewed as complex dynamical systems, *e.g.*, the atmosphere, hydrosphere, cryosphere and biosphere, remains a great challenge for modern science (Schellnhuber, 1999). The urge to make progress in this field is particularly pressing as substantial and mutually interacting components of the Earth system (tipping elements), such as the Indian Monsoon and ENSO, may soon pass a bifurcation point (tipping point) due to global climate change and consequently experience abrupt and possibly irreversible transitions in their dynamics and function (Lenton et al., 2008). Mapping the complex interdependency structure of subsystems, components or processes of the Earth system to a network of interacting networks provides a natural, simplified, condensed, and model-free mathematical representation (Section 2.4). This structure can in turn be harnessed for generating new insights by graph-theoretical analysis and, hence, fostering an improved understanding of the Earth system's vulnerability to perturbations like anthropogenic emissions of greenhouse gases (Donner et al., 2009). As a first step in this direction, in this chapter we develop a novel approach termed *coupled climate network analysis* for representing and studying the dynamical interrelationships between distinct fields of climatological observables and apply it to investigate the atmosphere's vertical dynamical structure and general circulation (Schneider, 2006; Hartmann, 2007) from a network perspective.
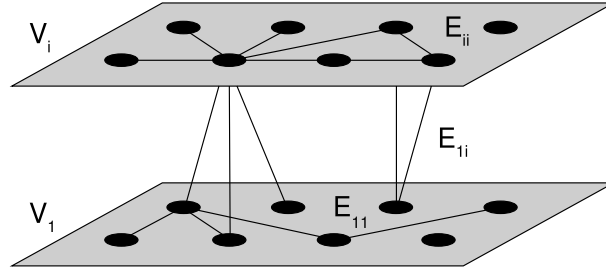
Figure 7.1.: Illustration of a coupled climate network as it is constructed in this chapter, where V_1 denotes the set of vertices in the near-ground subnetwork and V_i that of another isobaric surface higher up in the atmosphere. E_{11}, E_{ii} are sets of internal edges of the two isobaric surfaces or subnetworks describing the statistical relationships within each isobaric surface, while E_{1i} contains information on their mutual statistical interdependencies.

7.2. Coupled climate network analysis

In climatology, classical techniques such as empirical orthogonal function analysis (Storch and Zwiers (2003) and Section 3.3.2) have been generalized to detect coupled patterns in climate data for investigating the correlation structure between fields of different climatological observables using techniques such as canonical correlation analysis or singular value decomposition of the covariance matrix (Bretherton et al., 1992). In analogy to the study of coupled patterns and following Donges et al. (2011b, P14), we expand the climate network approach to analyze the dynamical interrelationships between two different climatological fields by constructing *coupled climate networks* and investigating them within the interacting networks framework introduced in Section 2.4. In other words, the correlation structure within and between two sets of discrete field observables $\{x_i(t)\}_{i=1}^{N_x}, \{y_j(t)\}_{j=1}^{N_y}$ is mapped to a complex coupled climate network (Fig. 7.1), where i and j are spatial indices and t denotes time.

In order to justify treating a coupled climate network as a network of networks, an *ab initio* physical separation of the climatological fields is necessary regarding processes responsible for internal coupling within a single field and those mediating interactions between both fields, as is elaborated in the following. The Earth's quasi-spherical shape and almost homogeneous mass distribution result in a hydrostatic equilibrium in first-order approximation, implying a stable isobaric quasi-horizontal stratification and therefore a strong buoyancy constraint (Salby, 1996). Local heating of the Earth's surface and atmosphere due to temporally and spatially varying solar radiation induces minor disturbances of the system which give rise to weather variability and are propagated by advection, diffusion (dominantly turbulent in the homosphere), and convection processes. Convection processes lead to vertical movement resulting in pressure gradients which are balanced by quasi-horizontal geostrophic winds along isobars. An important mechanism is slant convection arising as an adjustment of baroclinic instabilities (Pedlosky, 1979).

Geopotential height $Z(\vartheta, \phi, h)$ is a vertical coordinate referenced to the Earth's mean sea level which takes into account the variation of gravitational acceleration $g(\vartheta, \phi, h)$ with latitude ϑ, longitude ϕ, and geometrical height h. It is defined as

$$Z(\vartheta, \phi, h) = \frac{1}{g_0} \int_0^h dz\, g(\vartheta, \phi, z), \qquad (7.1)$$

where g_0 denotes the standard gravitational acceleration at mean sea level (Salby, 1996). $Z(\vartheta, \phi, h)$ is approximately equivalent to geometrical height h within the homosphere, *i.e.*, the lower portion of the atmosphere we consider in this work. The geopotential height $Z(\vartheta, \phi, P)$ of a certain pressure level P is defined as the geopotential height necessary to reach the given pressure P. In meteorology and climatology, the field $Z(\vartheta, \phi, P)$ is frequently used as an equivalent and convenient representation of the three-dimensional atmospheric pressure field $P(\vartheta, \phi, Z)$. Therefore the discretized and vertically resolved geopotential height field $\{Z_v^i(t)\}$, sampled at predefined points v on isobaric surfaces i at pressure P_i, captures the dynamics of both the geostrophic wind field as well as convection processes and, hence, reflects global weather and climate dynamics to a good approximation (Salby, 1996). Given the distinct physical processes behind vertical and quasi-horizontal atmospheric dynamics described above, it is hence feasible to apply the interacting networks approach, treating the induced subgraphs of vertices lying on the same isobaric surface i as distinct subnetworks G_i. In this chapter, we specifically focus on the interaction structure between near-ground and upper-level atmospheric dynamics which is particularly interesting as a large portion of the solar forcing driving atmospheric dynamics takes place on the Earth's surface (Fig. 7.1).

To better understand our coupled climate network approach, one should be aware of the strong analogy existing between the concepts of climate networks and functional brain networks studied in neuroscience (Zamora-López et al., 2009; Zamora-López et al., 2010; Zhou et al., 2006; Zhou et al., 2007; Bialonski et al., 2010; Bullmore and Sporns, 2009). Both types of networks describe statistical similarity relationships between spatially embedded time series using the same methods of time series analysis, but relying on distinct data sources, *i.e.*, the climate system and the mammalian brain. Now there exist two fundamentally different types of networks: (i) *Structural* (or *anatomical*) networks, on the one hand, reflect the topological structure of existing ties between objects (*e.g.*, computers, neurons, columns of neurons), referring to either physical connections (*e.g.*, internet, power grids, neuronal networks) or abstract relations (*e.g.*, world wide web, social networks, citation networks). (ii) *Functional networks*, on the other hand, including functional brain networks and complex climate networks, are extracted from an underlying system by detecting and assessing similarities in the dynamical behavior of its components (Section 3.3). In other words, structural networks represent *a priori* knowledge on a system's internal structure on a certain level of abstraction, whereas functional networks are inferred solely from the measured or simulated dynamics of subsystems, usually without including any additional information. Hence, in contrast to structural networks, the resulting

topological interconnections in functional networks do not directly allow to draw conclusions on a causal interrelationship between the dynamics displayed at different vertices. When constructed and compared for the same system, *e.g.*, a neuronal network, both types of networks will usually not be identical (Bullmore and Sporns, 2009). This implies that special emphasis has to be put on physical arguments when interpreting topological features of climate networks. A further noteworthy duality exists between spatial similarity networks based on fields of time series such as the climate networks discussed above, and temporal similarity networks (see Chapter 3), *e.g.*, recurrence networks (Donner et al., 2010a, P18; Donner et al., 2010c, P19; Marwan et al., 2009, P20), representing a single time series.

7.3. Data

Table 7.1.: Atmospheric pressure P_i and associated mean geopotential height Z_i (Eq. (7.2)) for each isobaric surface i in the NCEP/NCAR Reanalysis 1 reconstruction of the geopotential height field.

i	P_i (mbar)	Z_i (km)
1	1000	0.1
2	925	0.8
3	850	1.5
4	700	3.0
5	600	4.3
6	500	5.7
7	400	7.3
8	300	9.3
9	250	10.6
10	200	12.0
11	150	13.8
12	100	16.3
13	70	18.5
14	50	20.5
15	30	23.8
16	20	26.4
17	10	30.9

To construct coupled climate networks capturing longer-term dynamics of the geostrophic wind field as well as large-scale convection processes, we rely on the global monthly averaged and vertically resolved atmospheric geopotential height field covering the troposphere and the lower stratosphere. We use Reanalysis 1 data provided by the National Center for Environmental Prediction/National Center for Atmospheric Research (NCEP/NCAR) (Kistler et al., 2001). For each of the 17 isobaric surfaces, the NCEP/NCAR data is given on an angularly evenly spaced spherical grid with a latitudinal and longitudinal resolution of 2.5°× 2.5°, resulting

in 10,226 grid points for each layer. Using this type of grid for network construction would induce biases in the statistical properties of climate networks, since the area covered by each grid point is not uniform but decreases towards the poles like the cosine of latitude (Section 2.5 and Tsonis et al. (2008b); Heitzig et al. (2012, P9)). To avoid these effects, we choose to project the data to an icosahedral grid (Heikes and Randall, 1995) of $N_i = 2,562$ time series $\{Z_v^i(t)\}$ with $v \in \{1, \ldots, N_i\}$ for each isobaric surface i, respectively, at pressure P_i using the conservative interpolation scheme described by Jones (1998). Each isobaric surface i may be associated to an average geopotential height

$$Z_i = \left\langle Z_v^i(t) \right\rangle_{v,t} \tag{7.2}$$

by averaging over time t and all grid points v contained within this level (Table 7.1). The time series $\{Z_v^i(t)\}$ contain 734 monthly averaged data points from January 1948 until February 2009.

Relying on the icosahedral grid, which is used by the German Weather Service for its operational global weather forecast model *Global Modell Extended* (GME) and referred to as "triangular grid" (Majewski et al., 2002), guarantees nearly uniform grid cell areas within each isobaric surface i. The differences in grid cell area between different isobaric surfaces due to their varying distance from the Earth's surface are negligible since the maximum vertical separation of isobaric surfaces ($\approx 30\,\text{km}$, see Table 7.1) is much smaller than the Earth's mean radius $a \approx 6,370\,\text{km}$.

As a final step of preprocessing the data, we calculate climatological anomaly time series $\{\hat{Z}_v^i(t)\}$ by phase averaging (see Donges et al. (2009a, P22)) to remove the leading order effect of the annual cycle from the geopotential height time series $\{Z_v^i(t)\}$. This helps to avoid spurious correlations solely due to the solar forcing common to all time series.

7.4. Network construction

We now construct a sequence of pairwise coupled climate networks based on statistical interrelationships within the three-dimensional geopotential height anomaly field by using the linear Pearson correlation at zero lag. As was shown by Donges et al. (2009a, P22), linear correlation measures are sufficient for a first overview study like the present work, because they capture the great majority of statistical interrelationships within fields of smooth (non-intermittent) climatological variables like temperature or geopotential height. The so obtained networks describe both the intrinsic structure of a single isobaric surface as well as the interaction structure between pairs of isobaric surfaces, in other words comprising horizontal as well as vertical interdependencies of the spatially embedded time series. First the $N_i, N_j = 2,562$ time series of two isobaric surfaces i, j are relabeled using indices $p, q \in \{1, \ldots, N\}$, $N = N_i + N_j$, $\{\hat{Z}_v^i(t)\}, \{\hat{Z}_v^j(t)\} \rightarrow \{\hat{Z}_p(t)\}, \{\hat{Z}_q(t)\}$, where the fully coupled climate networks contain $N = 5,124$ vertices. The anomaly time series $\{\hat{Z}_{p,q}(t)\}$ are identified with vertices

p, q of the coupled climate network and subsequently collected in sets V_i, V_j based on their native isobaric surface. The classic Pearson correlation between any pair of $\left\{ \hat{Z}_p(t), \hat{Z}_q(t) \right\}$ is then given by

$$P_{pq}^{i,j} = \frac{\left\langle \left(\hat{Z}_p(t) - \mu_p \right) \left(\hat{Z}_q(t) - \mu_q \right) \right\rangle_t}{\sigma_p \sigma_q}, \tag{7.3}$$

where $\mu_{p,q}$ and $\sigma_{p,q}$ are the mean and standard deviation of the $\hat{Z}_{p,q}(t)$, respectively. Edges $\{p, q\}$ are introduced into the coupled climate network if the absolute value of Pearson correlation $|P_{pq}^{i,j}|$ at zero lag between both time series $\{\hat{Z}_p(t)\}$ and $\{\hat{Z}_q(t)\}$ exceeds a certain threshold value $0 \leq T \leq 1$. The threshold should be carefully chosen to ensure that only statistically significant and reasonably strong correlations are included in the network (Donges et al., 2009a, P22). Because an optimal value of T is neither easy to define nor to determine (it would even be possible to determine a threshold T_{pq} for each pair of time series p, q separately), we will present results for various thresholds below (Section 7.5). Furthermore it would be feasible to avoid the choice of a threshold altogether by including a function of the correlation measure $w_{pq}^{i,j} = \omega(P_{pq}^{i,j})$ into the network analysis as edge weights $w_{pq}^{i,j}$. However, we do not follow this research avenue here as it introduces as a new complication the choice of a meaningful transfer function ω for mapping correlations to edge weights depending on the interpretation of a specific network measure. In contrast, this chapter focusses on the topology of statistical interrelationships between different isobaric surfaces on the network level. The consideration of edge weights will be an interesting subject of future work.

Finally, the coupled climate networks are completely described by the adjacency matrices $\mathbf{A}^{i,j}$ with elements

$$A_{pq}^{i,j} = \Theta \left(\left| P_{pq}^{i,j} \right| - T \right) - \delta_{pq}, \tag{7.4}$$

where $\Theta(\cdot)$ is the Heaviside function and Kronecker's delta δ_{pq} indicates that self-loops are not considered. The subnetworks G_i, G_j representing the correlation structure within the isobaric surfaces i, j are the induced subgraphs of the sets V_i, V_j embedded within the coupled climate network $G^{i,j}$ described by the adjacency matrix $\mathbf{A}^{i,j}$. In the following, local as well as global (cross-)network measures f_v^{ij}, f_{ij} (see Section 2.4.2) will be calculated from the coupled climate network $G^{i,j}$ consisting of two isobaric subnetworks G_i and G_j and their interaction structure E_{ij}, *i.e.*, $G^{i,j} = (V_i \cup V_j, E_{ii} \cup E_{jj} \cup E_{ij})$.
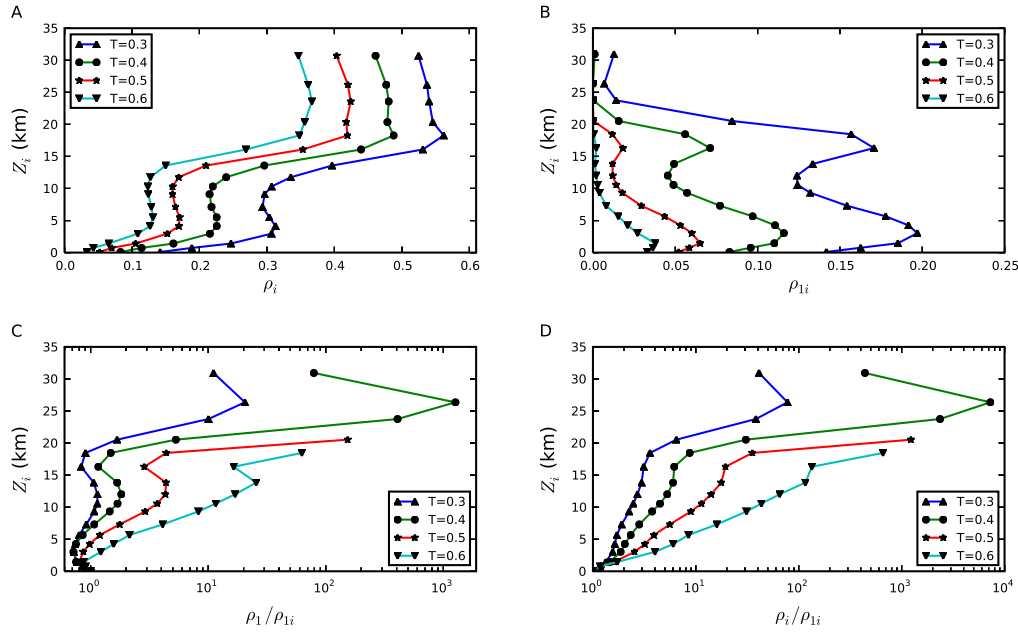
Figure 7.2.: (A) Internal edge density ρ_i of all subnetworks on isobaric surfaces i, (B) cross-edge density ρ_{1i} between the surface level 1 and all other isobaric surfaces i of average height Z_i, (C) the ratio ρ_1/ρ_{1i}, and (D) the ratio ρ_i/ρ_{1i} in the coupled geopotential height climate network for various thresholds T. Note the inversions of cross-edge density at $Z \approx$ 1–3, 12, 16 and 26 km becoming increasingly pronounced for decreasing threshold T.

7.5. Results

Global measures   The available data describes the dynamics of geopotential height in the lower homosphere, encompassing the troposphere and lower stratosphere, where most atmospheric dynamical processes relevant for the Earth's climate system are concentrated to (Salby, 1996). In the following we will investigate which aspects of atmospheric dynamics can be revealed by analyzing the sequence of coupled climate networks $G^{1,i}, i = 1, ..., 17$.

It is pivotal to be aware that for similarity networks constructed from spatiotemporal data, such as the coupled climate networks studied here, network structure is subject to statistical uncertainties (Kramer et al., 2009). One consequence is that average path length and global clustering coefficient cannot be considered as useful order parameters for network classification (Bialonski et al., 2010). Both are biased by spurious or missing links due to the network construction algorithm and local correlations between spatially close observations. Particularly, this implies that it is not meaningful to classify interaction networks as small-world networks (Watts and Strogatz, 1998), Erdős-Rényi type random networks, or grid-like regular networks, as is common practice for other networks without given spatial embedding (Newman,

2003; Boccaletti et al., 2006). Since the corresponding arguments of Bialonski et al. (2010) also hold for the modified clustering coefficients, transitivities, and average path lengths defined in Section 2.4.1, we in the following do not consider the absolute values of these measures. In contrast, here we are solely interested in their relative changes conveying information on the varying interaction structure within and between different isobaric surfaces of the atmosphere.

Our first and fundamental observation is that the cross-edge density ρ_{1i} (Fig. 7.2B) between the near-surface and all other isobaric surfaces i is always smaller than and well separated from the internal edge density of the upper isobaric subnetwork ρ_i (Fig. 7.2A) for all considered thresholds T. Moreover, the ratio of the edge densities ρ_i/ρ_{1i} and, hence, the physical separation of the underlying dynamics is increasing with height Z_i (Fig. 7.2D). Approximately the same holds for the internal edge density ρ_1 of the near-surface subnetwork which is considerably larger than ρ_{1i} for most Z_i and T (Fig. 7.2C). This observation reflects topologically the dynamical separation of atmospheric processes within and between isobaric surfaces i, respectively that led to identifying them with subnetworks in the first place (see Section 7.2). Nevertheless, ρ_1 can be slightly smaller than the cross-edge density ρ_{1i}, particularly close to the two pronounced minima of the ratio ρ_1/ρ_{1i} (the overall minimum value is $\min_{i,T} \rho_1/\rho_{1i} \approx 0.7$, see Fig. 7.2C). This finding, however, does not challenge the applicability of our method as our framework does not require that subnetworks constitute communities of the full network (Section 2.4.2).

The cross-edge density ρ_{1i} displays prominent extrema with varying height Z_i of the isobaric surface i, which become more pronounced for decreasing threshold T (Fig. 7.2B). Two maxima of ρ_{1i} are located at 1–3 km and 16 km, while a minimum is found at 12 km. A much more weakly developed inversion of cross-edge density ρ_{1i} occurs at 26 km, but it is only visible for small T. These findings indicate that correlations of large-scale quasi-geostrophic wind dynamics are significantly increased between the near-ground and higher isobaric surfaces at approximately 1–3 km and 16 km. The superficially similar inversions in internal edge density ρ_i with two maxima at 4–6 km and 18–24 km and a minimum at 7–11 km have to be carefully distinguished from those of cross-edge density ρ_{1i} (Fig. 7.2A). First, the geopotential height intervals within which the respective extrema are observed for different T do not overlap. Second, on the one hand, recall that in contrast to ρ_{1i} the internal edge density ρ_i measures dynamical correlations occurring within a quasi-horizontal isobaric surface at pressure P_i. On the other hand, the physical processes acting within isobaric surfaces (geostrophic wind, planetary Rossby waves, gravity waves) and between them (convection, turbulent mixing), which are relevant for large scale dynamical coupling, are distinctively different.

The cross-average path length $\mathcal{L}_{1i}$ between the near-ground layer and all other isobaric surfaces possesses two minima at 3 km and 16 km as well as one maximum at 11 km (Fig. 7.3). In contrast to cross-edge density, small values of $\mathcal{L}_{1i}$ imply tight dynamical relationships between two isobaric surfaces, while large values indicate a weaker coupling. Hence, cross-average path length consistently behaves complementarily to cross-edge density ρ_{1i} and internal edge-density ρ_i, as shortest paths
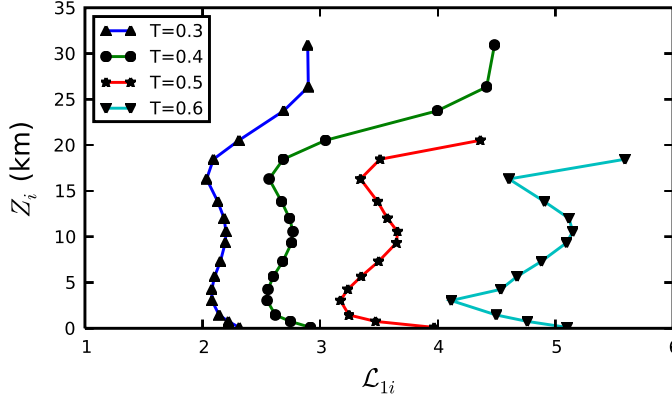
Figure 7.3.: The cross-average path length $\mathcal{L}_{1i}$ between the surface level 1 and all other isobaric surfaces i of average height Z_i in the coupled geopotential height climate network for different thresholds T. In the lower stratosphere and for larger thresholds, $\mathcal{L}_{1i}$ is not defined due to vanishing cross-edge density ρ_{1i} and, hence, the corresponding data points are not shown. $\mathcal{L}_{1i}$ shows inversions at similar height levels as the cross-edge density ρ_{1i} (Fig. 7.2), which in contrast decrease in sharpness for deceasing threshold T.

between two different subnetworks generally contain edges from both subnetworks implying their average length to decrease with increasing ρ_{1i} and ρ_i. Interestingly, in contrast to the behavior of ρ_{1i} and ρ_i, the extrema in $\mathcal{L}_{1i}$ are rendered increasingly pronounced for increasing threshold T. Cross-average path length remains sensitive to variations in the topological closeness of two isobaric surfaces even as more and more edges $\{p, q\}$ of weaker correlation strength $|P_{pq}|$ are removed from the coupled climate networks.

While the cross-network measures discussed so far are symmetric with respect to exchanging the involved subnetworks (see Section 2.4.1), the two clustering measures global cross-clustering coefficient $\mathcal{C}_{ij}$ and cross-transitivity $\mathcal{T}_{ij}$ are intrinsically directional. Hence, as for the horizontally resolved cross-measures to be treated below, we are able to distinguish $\mathcal{C}_{1i}$ and $\mathcal{T}_{1i}$ pointing "upward" from the near-ground to higher isobaric surfaces from their counterparts $\mathcal{C}_{i1}$ and $\mathcal{T}_{i1}$ projecting "downward".[17] Both $\mathcal{C}_{1i}$ and $\mathcal{T}_{1i}$ consistently uncover that the probability of vertices within the near-ground isobaric surface to have connected neighbors in higher isobaric surfaces reaches local maxima between 3–6 km and 14–16 km, whereas a local minimum is assumed at 11 km (Figs. 7.4A and C). For both measures, all three inversions are only observed for low thresholds T. It is particularly interesting to compare the measured values of $\mathcal{C}_{1i}$ and $\mathcal{T}_{1i}$ with those expected for a fully random connectivity structure between

---

[17]In this context, "upward" refers to global cross-clustering and cross-transitivity counting triangles with their apex rooted in the near-ground isobaric surface, while "downward" applies to the case when the triangles' apex is based in a higher isobaric surface.
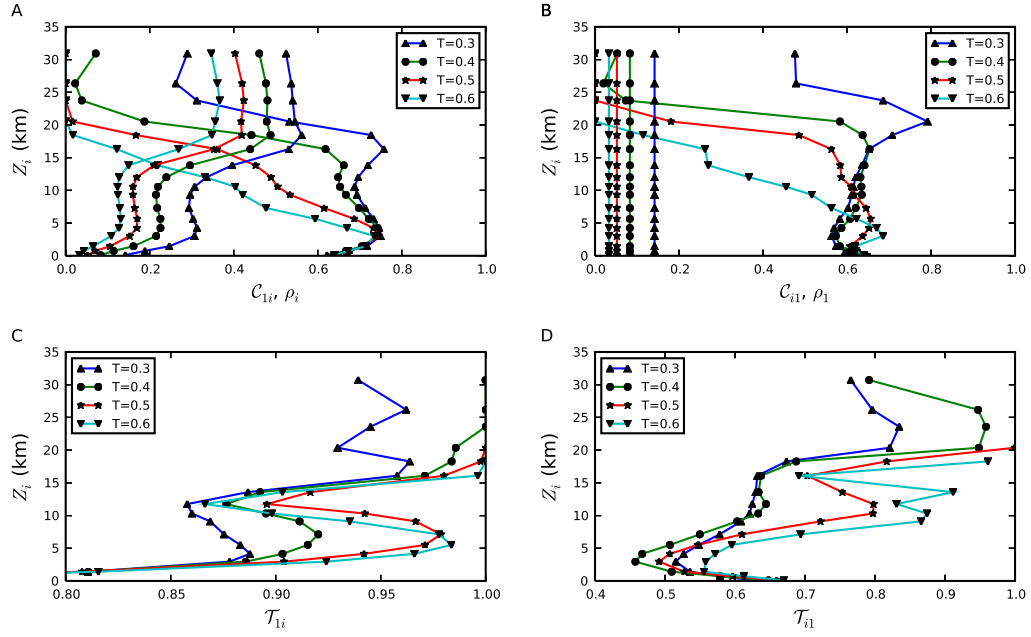
Figure 7.4.: Global cross-clustering coefficients (A) $\mathcal{C}_{1i}$ calculated "upward" from the surface level 1 to all other isobaric surfaces i and (B) $\mathcal{C}_{i1}$ defined "downward" (solid lines), as well as cross-transitivities (C) $\mathcal{T}_{1i}$ ("upward") and (D) $\mathcal{T}_{i1}$ ("downward"). For comparison with the global cross-clustering coefficients $\mathbb{E}(\mathcal{C}_{ij})$ expected for a fully random connectivity between isobaric surfaces, (A) and (B) also feature the expectation values $\mathbb{E}(\mathcal{C}_{1i}) = \rho_i$ and $\mathbb{E}(\mathcal{C}_{i1}) = \rho_1$, respectively (dashed lines).

isobaric surfaces (see Section 2.4.2). The "upward" pointing global cross-clustering coefficients $\mathcal{C}_{1i}$ are considerably larger than the expectations ρ_i (indicated by dashed lines in Fig. 7.4A) below 15 km, and markedly smaller for average geopotential heights above 20 km. Similarly, the "upward" projecting cross-transitivity $\mathcal{T}_{1i}$ is significantly larger than the expected values ρ_i for the fully random null model for all height levels (Fig. 7.4C).

Compared to their counterparts, the behavior of the "downward" projecting measures $\mathcal{C}_{i1}$ and $\mathcal{T}_{i1}$ is less consistent. The global cross-clustering coefficient $\mathcal{C}_{i1}$ possesses two extrema at 3–6 km and 16–21 km, whereas the cross-transitivity $\mathcal{T}_{i1}$ takes local minima between 2–3 km and 14–16 km and local maxima between 12–14 km and at 24 km of geopotential height (Figs. 7.4B and D). Note that "downward" pointing cross-transitivity $\mathcal{T}_{i1}$ behaves complementarily to its "upward" projecting counterpart $\mathcal{T}_{1i}$. Both clustering measures are significantly larger than their values ρ_1 expected for a fully random connectivity structure for nearly all height levels, only above 20 km the global cross-clustering coefficient $\mathcal{C}_{i1}$ is consistent with the expectation value for larger thresholds T.

In summary, the clustering measures exhibit that the interaction topology between the near-ground and higher isobaric surfaces is not consistent with a fully random

null model, except for the lower stratosphere above 20 km. The same holds when comparing the observed values of the clustering measures to those expected from a more sophisticated null model with fixed cross-degree sequences but otherwise random interaction topology (Section 2.4.3 and Schultz (2010)). These findings highlight that the coupled climate networks considered here have a nontrivial interaction topology which is consistent with known features of the atmosphere's vertical dynamical structure and stratification, and may contain additional information on previously unknown features of the atmosphere's general circulation (Schneider, 2006; Hartmann, 2007) (see Section 7.6). The large values of clustering measures observed for most height levels can be partly explained by spatial correlations between closely neighbored time series stemming from the continuity of the geopotential height field in conjunction with the intrinsic transitivity of the Pearson correlation coefficient P_{pq} used for network construction (Langford et al., 2001; Bialonski et al., 2010). Directly comparing $\mathcal{C}_{i1}$ and $\mathcal{T}_{i1}$ as well as $\mathcal{C}_{1i}$ and $\mathcal{T}_{1i}$, respectively, furthermore clearly reveals the bias in the global cross-clustering coefficient, which leads to generally lower values for increasing height through weighing more strongly the contribution of the increasing number of vertices of low cross-degree induced by the decreasing trend in cross-edge density ρ_{1i} (see Section 2.4.2). Consequently, as for the standard versions of global clustering and transitivity (Newman, 2003), special care has to be taken when interpreting absolute values of global cross-clustering and cross-transitivity. The suggested best practice is to always consider the two measures simultaneously and to draw conclusions only from qualitative features exhibited by both of them.

Local measures   For visualizing the inherently three-dimensional fields of local cross-network measures (one of the subnetwork indices i, j being fixed as in our application) $f_v^{ij} = f_{v(\vartheta,\phi)}^{ij}$, where ϑ and ϕ denote latitude and longitude, we choose to focus on their variation with height and latitude. This is most appropriate as our aim is to study from a complex network perspective aspects of the atmosphere's general circulation (Schneider, 2006; Hartmann, 2007), the dominant forcing of which is the latitudinal variation of radiative solar forcing (Salby, 1996). Hence, in the following we will consider zonal averages

$$f^{ij}(\vartheta) = \left\langle f_{v(\vartheta,\phi)}^{ij} \right\rangle_{\phi \in [0°, 360°]} \tag{7.5}$$

along circles of constant latitude. A detailed study and interpretation of the latitudinally and longitudinally resolved fields of cross-network measures will be the subject of future work (see Schultz (2010) for first results). Like the scalar measures of cross-clustering discussed above, most local cross-network measures are non-symmetric with respect to interchanging subnetworks and, hence, intrinsically directional. Therefore we distinguish "upward" cross-degree centrality $k^{1i}(\vartheta)$ from "downward" cross-degree centrality $k^{i1}(\vartheta)$, and "upward" cross-closeness centrality $c^{1i}(\vartheta)$ from "downward" cross-closeness centrality $c^{i1}(\vartheta)$. For brevity, here we present results for representative thresholds of $T = 0.4, 0.5, 0.6$ only.
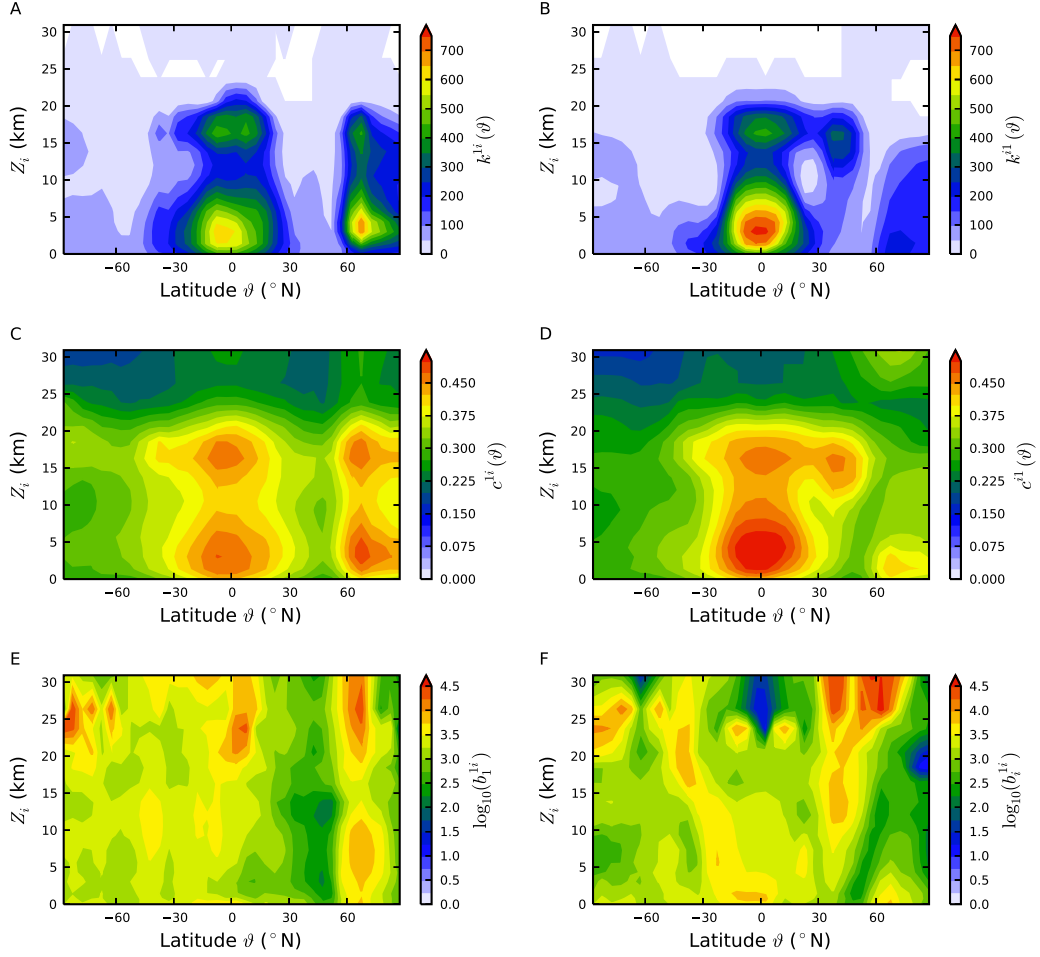
Figure 7.5.: Zonally averaged cross-degree centralities (A) $k^{1i}(\vartheta)$ pointing "upward" from the near-ground level 1 to all other isobaric surfaces i and (B) $k^{i1}(\vartheta)$ projecting "downward", zonally averaged cross-closeness centralities (C) $c^{1i}(\vartheta)$ pointing "upward" and (D) $c^{i1}(\vartheta)$ projecting "downward", (E) $b_1^{1i}(\vartheta)$ near-ground and (F) $b_i^{1i}(\vartheta)$ upper level component of zonally averaged cross-betweenness centrality for a threshold of $T = 0.4$. Panel (B) can be interpreted to show the number of cross-edges connecting a certain volume element with the whole near-ground isobaric surface, averaged along bands of approximately equal latitude (approximately because of the geodesic grid).
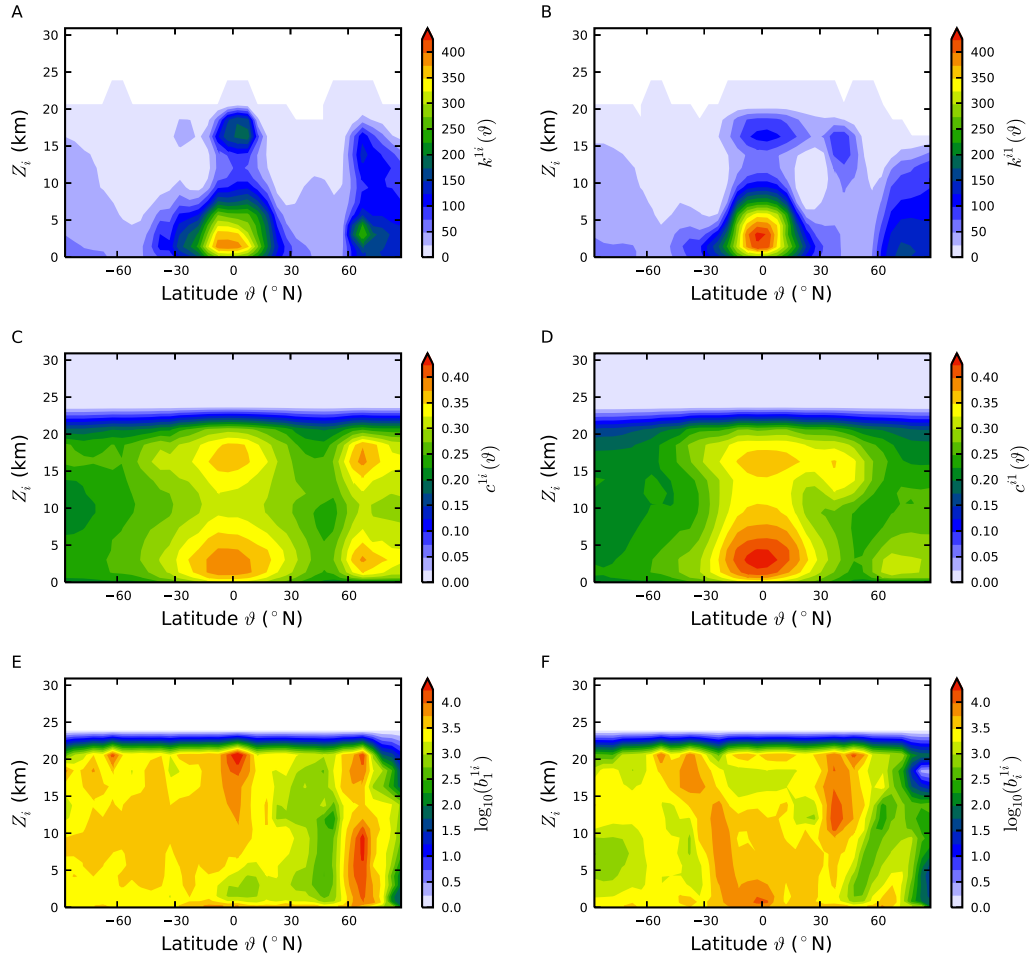
Figure 7.6.: As Fig. 7.5 with threshold $T = 0.5$.
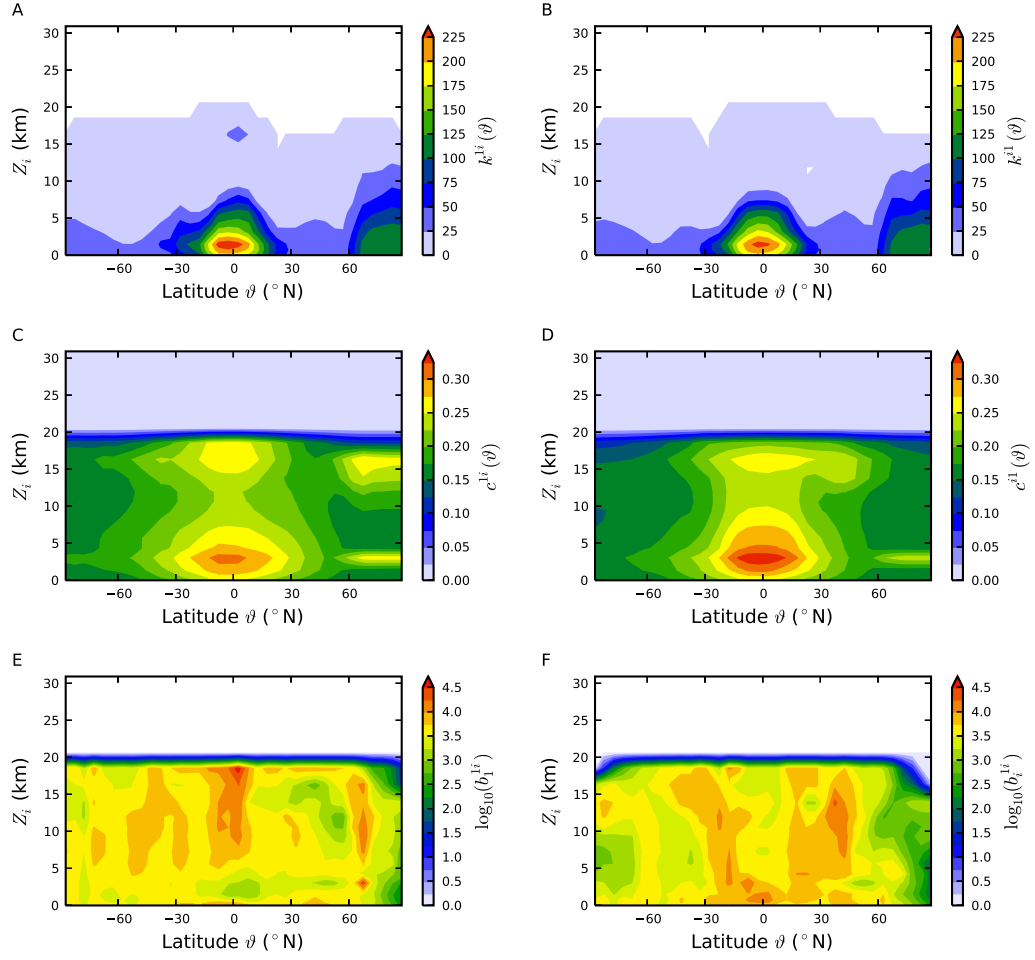
Figure 7.7.: As Fig. 7.5 with threshold $T = 0.6$

Cross-degree and cross-closeness centrality show a similar structure in both directions (Figs. 7.5, 7.6, 7.7A–D). Both measures are generally increased in the tropics and polar regions, whereas they take smaller values in the mid-latitudes. We observe a pronounced asymmetry between both hemispheres as the cross-degree and cross-closeness centralities in the northern polar regions are significantly larger than those above Antarctica and the surrounding Southern Ocean in the Southern Hemisphere. Furthermore, a structure of increased "downward" cross-degree $k^{i1}(\vartheta)$ and -closeness centrality $c^{i1}(\vartheta)$ appears above the northern mid-latitudes but not above those of the Southern Hemisphere (Figs. 7.5, 7.6, 7.7B and D).

Additionally considering the dependence of both local measures on geopotential height Z_i, the "upward" pointing cross-degree $k^{1i}(\vartheta)$ and -closeness centralities $c^{1i}(\vartheta)$ possess two distinct tropical maxima centered around 1 km and 16 km, as well as two northern polar maxima at 3 km and 16 km (Figs. 7.5, 7.6, 7.7A and C). While $k^{1i}(\vartheta)$ decreases monotonously with height in the mid-latitudes and above the polar regions of the Southern Hemisphere, $c^{1i}(\vartheta)$ maintains its bimodal structure there. The "downward" projecting cross-degree $k^{i1}(\vartheta)$ and -closeness centralities $c^{i1}(\vartheta)$ display two pronounced tropical maxima at 3 km and 16 km, and a maximum centered around 14 km in the northern mid-latitudes (Figs. 7.5, 7.6, 7.7B and D). Furthermore, $c^{i1}(\vartheta)$ reveals a maximum of topological closeness to the near-ground isobaric surface at 1 km above the northern polar regions, while $k^{1i}(\vartheta)$ decreases monotonically with height there.

It is worth noting that the observed extrema in cross-degree are directly related to those in cross-edge density via Eq. (2.18) and extrema in cross-closeness have an equivalent association to those of cross-average path length (Eq. (2.22)). Moreover, we point out that plots of cross-degree centrality like those presented in this chapter may be used to draw conclusions on the main sources and destinations of cross-edges without relying on full three-dimensional visualizations of the coupled network structure. For example, consider the region of increased "downward" cross-degree $k^{i1}(\vartheta)$ between 11 km and 18 km of geopotential height above the northern mid-latitudes (Fig. 7.5, 7.6, 7.7B). It implies that a considerably large number of cross-edges connect this region directly to the whole near-ground isobaric surface. We learn where exactly on the near-ground surface those cross-edges originate from by looking at the "upward" cross-degree $k^{1i}(\vartheta)$. It measures how many and from where on the near-ground surface cross-edges connect to some higher isobaric surface. Now the regions of increased $k^{1i}(\vartheta)$ between 11 km and 18 km above the tropics and northern polar regions imply that many cross-edges originating in the tropics and northern polar regions of the near-ground surface project to isobaric surfaces between 11 km and 18 km (Fig. 7.5, 7.6, 7.7A). As these are the only major structures in this range of geopotential height, we are lead to conclude that a significant number of cross-edges must link the tropical and northern polar near-ground isobaric surface with the northern mid-latitudes' upper troposphere to lower stratosphere between 11 km and 18 km.

In contrast to the latter two local measures, cross-betweenness b_w^{ij} with $w \in V_i \cup V_j$ is symmetric with respect to exchanging the involved subnetworks (see Eq. (2.15)),

but assigns a value to vertices of both subnetworks. Therefore we will in the following analyze zonally averaged fields of cross-betweenness

$$b_i^{ij}(\vartheta) = \left\langle b_{w(\vartheta,\phi)}^{ij} \right\rangle_{\phi, w \in V_i} \tag{7.6}$$

for vertices taken from a specific isobaric subnetwork i. It was shown earlier for climate networks constructed from surface air temperature data that betweenness centrality (Eq. (2.16)) yields additional information when compared to degree (Eq. (2.6)) and closeness centrality (Eq. (2.13)) (Donges et al., 2009b, P21). Similarly, the near-ground and higher isobaric surface components of cross-betweenness centrality $b_1^{1i}(\vartheta)$, $b_i^{1i}(\vartheta)$ reveal rich structures which are partially complementary to those seen in the zonally averaged fields of degree and closeness centrality (Figs. 7.5, 7.6, 7.7E and F). Both fields highlight how frequently certain regions on the two isobaric surfaces are traversed by shortest paths connecting the near-ground to a higher isobaric surface. Now due to our network construction procedure (Section 7.4), shortest paths correspond to sequences of strongly and significantly statistically interrelated pairs of time series with a minimum number of intermediate steps. Hence, it is conceivable to assume that to a first approximation a markedly increased cross-betweenness centrality indicates that a region is particularly important for mediating interactions between two isobaric surfaces, while the contrary is true for regions with significantly decreased cross-betweenness (Donges et al., 2009b, P21).

The hemispherically asymmetric near-ground component of cross-betweenness centrality $b_1^{1i}(\vartheta)$ reveals that the northern subpolar regions are exceptionally important for mediating interactions between the near-ground and all considered heights ranging from the lower troposphere across the tropopause to the lower stratosphere (Figs. 7.5, 7.6, 7.7E). The near-ground tropics and southern polar regions appear only to be relevant for coupling the near-ground to isobaric surfaces in the upper troposphere and above. In contrast, the upper surface component of cross-betweenness $b_i^{1i}(\vartheta)$ possesses a more pronounced inter-hemispheric symmetry (Figs. 7.5, 7.6, 7.7F). Most notable and stable for various thresholds T are the two tongues of increased $b_i^{1i}(\vartheta)$ ranging from the near-ground tropics to the mid-latitudes and subpolar regions in the lower stratosphere. These structures indicate that the latitude at which shortest paths connecting near-ground and upper isobaric surfaces arrive in the upper surface tends to increase towards the poles for growing geopotential height Z_i in both hemispheres. One should be aware that the structures detected in both components of the cross-betweenness field in the stratosphere as well as in all other local and global measures above 20 km of geopotential height should be treated with care. This is because only very few edges exist between the near-ground and isobaric surfaces in these height levels (Fig. 7.2B) and, hence, statistically expected false detections or omissions of cross-edges are likely to induce recognizable changes in the respective measures (Bialonski et al., 2010). To quantitatively assess the effects of small changes in the interaction topology between subnetworks, new types of significance tests based on network null models need to be developed in future work (see Section 2.4.3).

After describing the results of our analysis we would like to draw attention to

the fact that the observed correlations in various measures revealed by qualitatively similar structures like the inversions at mostly three different height levels are not necessarily a direct consequence of the measure's definitions (see Section 2.4.1), but point to a specific type of network structure. While correlations in different measures quantifying distinct aspects of network topology need not be present for general network structures, they are prevalent in many different types of real-world networks and network models (Costa et al., 2007). Particularly, these correlations are expected to arise in spatially embedded functional climate (and brain) networks like the coupled climate networks considered in this work, since the increased probability of spatially close vertices to be connected imposes a substantial constraint on network topology (Section 2.3 and Donges et al. (2009b, P21); Bialonski et al. (2010); Radebach (2010); Donges et al. (2012, P8)).

7.6. Climatological interpretation

We are now in a position to elaborate on the climatological implications of our coupled climate network analysis. First, recall that the coupled climate networks were constructed from monthly averaged time series of geopotential height describing the dynamics of the atmosphere's quasi-geostrophic wind field on longer than monthly time scales. Variability on shorter time scales, *e.g.*, synoptic-scale weather systems, is included in the averages but does not appear explicitly in the time series. Therefore, we can indeed expect the coupled climate networks to represent the climatological mean state of the atmosphere's three-dimensional correlation structure, excluding the direct effects of such weather phenomena with typical lifetimes of clearly less than one month.

The cross-network measures discussed in Section 7.5 reveal for a wide range of thresholds T aspects of the atmosphere's stratification and, more importantly, physical processes which couple the dynamics on different isobaric surfaces despite the strong buoyancy constraint imposed by vertical stratification. First it should be noted that in accordance with results of atmospheric physics and observations, all cross-network measures consistently indicate that most atmospheric dynamics takes place within the troposphere with comparatively weak coupling to the superjacent stratosphere (Salby, 1996). Steadily increasing (decreasing) from the near-ground to reach a first maximum (minimum) at 1 km to 3 km of geopotential height, cross-edge density ρ_{1i} and cross-average path length $\mathcal{L}_{1i}$ indicate that the near-ground and higher isobaric surfaces become dynamically more densely interwoven when ascending from the planetary boundary layer below approximately 1 km into the lower free atmosphere (Figs. 7.2B and 7.3). Bearing in mind the spatial continuity of the geopotential height field, spatially close vertices are likely to be connected and to share common neighbors. This implies that the typical correlation radius from near-ground vertices to higher isobaric surfaces and vice versa increases throughout the lower troposphere. This observation is consistent with the influence of the Earth's surface orography on atmospheric flow exponentially decreasing with height in the planetary boundary

layer via the Ekman effect. Hand in hand with the prevalence of turbulence, the formation of long-range dynamical couplings is inhibited by this essentially frictional effect. In turn, within the less turbulent free atmosphere above approximately 1 km the wind field behaves quasi-geostrophically and allows for the long-range propagation of dynamical influences between the near-ground and higher altitudes (Salby, 1996).

Within the cross-edge density (Fig. 7.2B), we observe that the first maximum shifts from approximately 4 km to 3 km for higher thresholds. This detail can be credited to the decreasing height of the planetary boundary layer with latitude, the typical zone within which convection cells form. The prominent tropical convection processes are known to be more diffusive than those in the mid-latitudes and, hence, yield lower correlation values. Thus higher thresholds rather account for mid-latitude convection phenomena rejecting the relatively low correlated processes in the tropics. The prevalence of the latter, on the other hand, is reflected in lower thresholds.

Above approximately 3 km of geopotential height, ρ_{1i} and $\mathcal{L}_{1i}$ decrease (increase) again until reaching a local minimum (maximum) between 11 km and 14 km (Figs. 7.2B and 7.3), indicating a dominating effect of a more stable vertical stratification acting to inhibit dynamical couplings between the now vertically more separated isobaric levels 1 and i. This may be understood considering that turbulent vertical mixing is significantly less prevalent in the free atmosphere than it is in the planetary boundary layer and convection is suppressed by baroclinic adjustment forcing the atmosphere to interact horizontally. The second local maximum (minimum) of ρ_{1i} and $\mathcal{L}_{1i}$ at 16 km highlights that the cumulative action of tropical penetrative convection processes (hot towers) reaching up to this height mediates markedly increased dynamical interrelationships between the near-ground and isobaric surfaces close to the tropopause (Riehl and Malkus, 1958). The tropical origin of this coupling is more readily seen in the fields of zonally averaged cross-degree and -closeness centralities (Fig. 7.5, 7.6, 7.7). When entering the stratosphere, quickly decreasing (increasing) ρ_{1i} and $\mathcal{L}_{1i}$ indicate that influences reaching from the near-ground to these heights are strongly inhibited by the dynamical barrier formed by the temperature inversion which marks the boundary between troposphere and stratosphere. This conclusion is further supported by the random-like interconnectivity structure revealed by the "downward" pointing global cross-clustering coefficient $\mathcal{C}_{i1}$ within the stratosphere (Fig. 7.4B). The behavior of internal edge density ρ_i is consistent with the foregoing argumentation in the troposphere, its striking increase above the tropopause reveals the spatially uniform dynamics of the stratospheric wind field (Fig. 7.2A) (Salby, 1996).

The zonally averaged fields of cross-degree, -closeness and -betweenness centrality uncover features of the atmosphere's general meridional circulation (Schneider, 2006; Hartmann, 2007). Most evident are the Hadley and polar cells which are indicated by markedly increased values of both measures in the tropics and polar regions (Figs. 7.5, 7.6, 7.7). Here the generally rising motion of air above the equator and subpolar latitudes couples surface wind dynamics to the upper troposphere which becomes apparent in both components of zonally averaged cross-betweenness (Figs. 7.5, 7.6, 7.7E and F). The surface component of cross-betweenness may also

be interpreted to show a signature of the Northern Hemisphere circumpolar vortex around a typical height of approximately 5 km which is known to induce vertical air motion and, hence, vertical dynamical coupling (Figs. 7.5, 7.6, 7.7E) (Andrews et al., 1987). Supporting this interpretation, a corresponding signature is not seen in the Southern Hemisphere which is consistent with the Antarctic ice shield inhibiting the formation of a polar vortex there. Cross-degree and -closeness centrality also show that the height of the tropopause decreases towards the poles by a slight poleward shift of their maximum values towards lower altitudes, as this dynamical barrier strongly inhibits the propagation of signals from the near-ground to the stratosphere. The Ferrel circulation may be involved in forming the comparably weak dynamical interrelationships between the near-ground southern subtropics and mid-latitudes with isobaric surfaces lying in the upper troposphere and lower stratosphere (Figs. 7.5, 7.6, 7.7A and C). Similarly, the remarkable coupling of wind dynamics within the upper troposphere and lower stratosphere of the northern mid-latitudes with the near-ground tropics and northern polar regions might be related to the northern Ferrel cell (Figs. 7.5, 7.6, 7.7B and D, see also the discussion in Section 7.5).

7.7. Discussion

In summary, we have developed a novel graph-theoretical framework for investigating in detail the interaction topology between pairs of subnetworks embedded within a network of networks. Applying this framework to analyze the correlation structure of a four-dimensional (spatiotemporal) data set of the climatological variable geopotential height yielded a consistent picture of the large scale circulation of the Earth's atmosphere. Particularly, the new measure cross-betweenness centrality has the potential to reveal previously unknown features of and to help address open questions on the atmosphere's general circulation (Holton, 2004; Schneider, 2006), particularly when considering its response to climate change (Lenton et al., 2008). Our results suggest that the coupled climate network approach presented in this chapter opens promising perspectives for the integrated analysis of several fields of climatological observables or, more generally, spatially embedded fields of arbitrary time series in the context of Earth system analysis. Particularly it will serve researchers as a tool complementary to established linear methods for the joint analysis of several climate data sets like canonical correlation analysis or singular value decomposition of the covariance matrix between two fields (Bretherton et al., 1992).

While it should be born in mind that the results of our study are subject to known deficiencies and limitations of the NCEP/NCAR Reanalysis 1 data, the variable geopotential height we analyze here is considered as one of the most reliable products of this reanalysis, since it is strongly determined by observations and, hence, less dependent on the particular model used for data assimilation (Kistler et al., 2001). However, we suggest that the results generated from several independent reanalysis data sets should be compared if definite climatological conclusions are to be drawn in future studies using coupled climate network analysis.

Additional information can be extracted from the available coupled climate networks by investigating the spatially fully resolved fields of local cross-network measures and relying on further measures such as the local cross-clustering coefficient (Schultz, 2010). In a next step, network null models with a randomized interaction topology could be developed and used to assess the statistical significance of observed local and global cross-network measures (see Section 2.4.3). The simplest meaningful network null model of this type that was already discussed in the context of (local) cross-clustering and cross-transitivity (Section 2.4.2) can be constructed by fully randomizing the interaction structure between two subnetworks while keeping the number of cross-edges fixed, *e.g.*, by first deleting all cross-edges and subsequently redistributing them randomly between the two subnetworks. Furthermore, the network construction methodology may be fine-tuned, *e.g.*, by using measures for detecting nonlinear or even directional interrelationships between time series or, alternatively, by including edges in the network-based on the statistical significance of their associated correlation strengths (see Section 3.3).

Summarizing the results of this first application of our framework for interacting network analysis, a particular advantage of coupled climate network analysis is that substantial conclusions can be drawn by analyzing the dynamical correlation structure of the three-dimensional geopotential height field alone, without considering fields of temperature, moisture content, or other relevant climatological variables. Subject to future research is the application of the interacting networks approach to fields of distinct climatological observables, *e.g.*, surface air temperature and sea surface salinity, to further investigate the coupled dynamical behavior of different components of the climate system. Recently, Wiedermann (2011) and Feng et al. (2012) have harnessed coupled climate networks for disentangling the complex interactions between ocean and atmosphere (for a summary, see Section 3.3.2).

7.8. Summary

Climate networks have recently been shown to be a powerful exploratory tool for the analysis of climatological data. Applying a general framework for studying networks of interacting networks, we have introduced coupled climate networks to represent and investigate the topology of statistical relationships between the fields of multiple climatological variables. Using coupled climate networks to investigate the terrestrial atmosphere's three-dimensional geopotential height field, known as well as interesting novel features of the atmosphere's vertical stratification and general circulation have been discovered. Specifically, the new measure *cross-betweenness* identified regions which are particularly important for mediating vertical wind field interactions. The promising results obtained by following the coupled climate network approach present a first step towards an improved understanding of the Earth system and its complex interacting components from a network perspective.

Chapter 8.

Conclusion

Nansen was too kind and lost his treasure.
Truly, words have no power.
Even though the mountain becomes the sea,
Words cannot open another's mind.

Ekai, called Mu-mon
(Aitken, 1991, translator)

8.1. Closing the loop

Returning to the grand background theme of this dissertation, Earth system analysis, it is now time to recapitulate what has been learnt, examine which open questions remain, and outline what paths may be followed in future research. The initial aim was to explore the potentials of complex network-based time series analysis for possibly contributing to a second Copernican revolution (Schellnhuber, 1999) needed for leveraging our understanding of the Earth system to a new operational level in the face of global warming and environmental change (Fig. 8.1). As a result of this undertaking, several of the challenges cast into a *Hilbertian program* for Earth system analysis have been addressed. It has been shown in Part I of this thesis that the network point of view is well tailored for tackling operational questions such as (Schellnhuber et al., 2004, p. 9):

> "What are the principles for constructing 'macroscopes', *i.e.*, representations of the Earth system that aggregate away the details while retaining all systems-order items?"

> "Is it possible to describe the Earth system as a composition of weakly coupled organs and regions, and to reconstruct the planetary machinery from these parts?"

Network macroscopes are designed for representing the complex structure of dynamical interactions between the manifold subdomains within the Earth system while maintaining a maximum degree of formal simplicity, adhering to the principle of Occam's razor (Chapters 1, 2, and 3). These network representations are *physical*
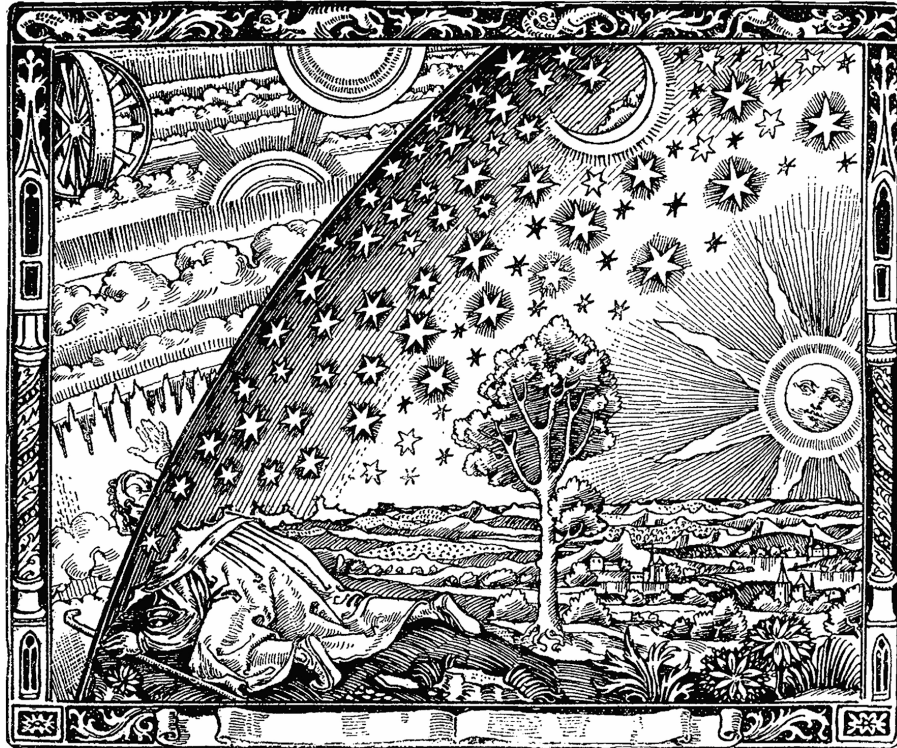
Figure 8.1.: Depiction of the enlightenment, comprising the *first* Copernican revolution, in a wood engraving by an unknown artist that first appeared in Flammarion (1888) (image source: Wikimedia Commons). If "words cannot open another's mind [. . .]" (Aitken, 1991), maybe images can.

in the sense that they embody condensed information on either functional or mechanistic dependencies within and between physical systems (Donges, 2009, Chapter 7). Notably, networks of interacting or interdependent networks are argued to allow to naturally decompose the Earth system into weakly coupled subsystems, such as the atmosphere and ocean, for diagnostic and prognostic analysis (Section 2.4 and Chapter 7).

Building on this conceptual work, in Part II we have developed and applied recurrence network (Chapters 5 and 6) and coupled climate network analysis (Chapter 7) as two powerful and versatile approaches for approaching analytical questions such as (Schellnhuber et al., 2004, p. 9):

> "What are the critical elements (thresholds, bottlenecks, switches) in the Earth System?"

> "What are the major dynamical patterns, teleconnections, and feedback loops in the planetary machinery?"

These studies relied on time series data of vastly different quality and resolution, covering Earth system dynamics from 5 million years before present until today on

continental and global scales. Specifically, recurrence network analysis allowed the detection of nonlinear transitions in African millennial-scale paleoclimate-variability during the Plio-Pleistocene which may be related to the appearance and disappearance of hominin species from the fossil record (Chapter 6). These possibly interlinked transitions in climatic and evolutionary processes point at the presence of critical elements (thresholds and switches) and their interactions (bottlenecks) within the Earth system during the considered epoch. Moreover, through a case study investigating the atmosphere's general circulation structure (Chapter 7), coupled climate network analysis has been characterized as a promising tool for extracting major dynamical patterns, teleconnections, and, possibly, feedback loops.

All in all, it is closing the positive feedback loop between applications to data-driven Earth system analysis on the one hand, and theoretical as well as methodological developments on the other hand that has inspired my work during this dissertation project. This cyclic way of doing science did not only serve to continuously sharpen my research questions together with the analytical tools designed for tackling them (Fig. 3.6), but additionally opened a number of surprising connections to other fields. For example, consider the link from searching for dynamical transitions in climatological time series via recurrence network analysis and probabilistic geometry to experimental mathematics that is drawn in Chapter 4. Conversely, and adding further to this entangled semantic network of theories and ideas, the general diagnostic concepts and methods presented in this thesis may potentially prove useful for studying the structure and dynamics of complex interdependent systems in other disciplines such as neuroscience, medicine, or infrastructure engineering. Concerning Earth system analysis, future efforts in applying and further developing ideas and techniques from complex network as well as dynamical systems theory should particularly focus on informing the improvement of prognostic models, both conceptual and comprehensive, for addressing the looming nexus of global change.

8.2. Contributions of this thesis

To conclude, in the following the contributions to the fields of graph and network theory, nonlinear time series analysis, and (paleo)climatology that have been reported in this thesis are summarized in concert with giving an outlook on open problems and promising avenues for future research. For reference, and to emphasize the collaborative efforts that come along naturally with network science, the publications (co-)authored by myself and related to each contribution are listed below the respective paragraphs.

8.2.1. Graph and network theory

Analyzing and modeling networks of networks

A consistent framework for studying in detail the complex topology of *networks of networks* providing a natural description of the manifold interacting, interdependent,

or hierarchical systems appearing in nature, society, and technology has been developed (Section 2.4). This framework comprises a rich toolbox of novel graph-theoretical measures for analyzing their structure and gives rise to specifically tailored network surrogates for developing statistical null models and significance tests.

Worthwhile future extensions may include taking into account the directionality of interactions by allowing for directed edges or *arcs* and devising advanced network surrogates for testing hypotheses on more subtle, but interesting, aspects of the interaction structure of networks of networks, possibly specifically taking into account their spatial embedding. Furthermore, building on the diagnostic work presented in this thesis, it appears promising and necessary to develop a dynamical systems theory of networks for describing and, ultimately, predicting the dynamics of temporally evolving networks.

Related publications   Donges et al. (2011b, P14); Wiedermann et al. (2013, P1)

Consistent analysis of vertex-weighted networks

We have introduced a general framework for the statistically consistent analysis of *vertex-weighted networks* based on the concept of *node splitting invariance* (Section 2.5). This result is an important step forward in the theory of general complex networks in so far as most studies in the past have simply neglected the sometimes strongly heterogeneous size, weight, or importance of the objects represented by vertices in the investigated networks, possibly leading to significant distortions in measured network properties.

The proposed framework is flexible in providing general rules for deriving consistently weighted variants of any network measures that may be of interest in future research (Appendix A). Open questions include defining meaningful weights in general situations and accounting for networks where edges do not imply a similarity or coupling between vertices.

Related publications   Heitzig et al. (2012, P9); Wiedermann et al. (2013, P1)

Analytical theory of spatial networks

As a third general contribution to graph and network theory, we have proposed an analytical theory for describing the characteristics of *spatial networks* on local, mesoscopic, and global topological scales (Chapter 4). This development leads to deeper insights into the geometrical meaning underlying many network quantifiers that are commonly used in the analysis of spatial networks. Specifically, the theory views these standard measures as estimators of the underlying geometrical properties and allows to derive analytical results for paradigmatic model systems that can serve for benchmarking and, consequently, improving the estimators.

Worthwhile tasks for future research include deriving further analytical solutions, assessing boundary effects in spatial networks, testing hypotheses on their specific

structure, or generalizing the theory to describe spatial random networks with non-isotropic edge length distributions $p(l, \Omega)$, where Ω is a solid angle in arbitrary dimensions measuring the direction an edge is pointing at.

Related publications   Donner et al. (2011b, P15); Donges et al. (2012, P8)

8.2.2. Nonlinear time series analysis

Recurrence network analysis

We have introduced *recurrence networks* as a versatile technique of nonlinear time series analysis that is rooted deeply in dynamical systems theory (by exploiting Poincaré recurrences of a dynamical system's trajectory in phase space) and graph theory (by belonging to the class of random geometric graphs). It has been shown that recurrence network analysis is capable of identifying dynamical transitions or bifurcations in time series, uncovering dynamically invariant objects in phase space as well as oddly shaped periodic islands (shrimps) in the parameter space of complex dynamical systems. Moreover, recurrence networks provide new concepts for measuring the (fractal) dimensionality of chaotic attractors and, more generally, point sets (Section 3.2.2 and Appendix D). An analytical framework for deepening the understanding of the method as well as practically improving it has been proposed (Chapter 4). Multivariate extensions of recurrence networks, namely joint and inter-system recurrence networks, allow to study complex synchronization scenarios and coupling directions in interacting dynamical systems (Appendix C). Successful applications to the analysis of real-world time series range from the fields of medicine to paleoclimatology.

Open problems include developing and testing advanced methods for the embedding of real-world times prior to recurrence network analysis for consistently taking into account irregular sampling and errors in the timing and magnitude of observations, *e.g.*, dating uncertainties. Furthermore, a systematic comparison of linear and nonlinear methods of time series analysis for detecting dynamical transitions, including recurrence network analysis, would be desirable.

Related publications   Marwan et al. (2009, P20); Zou et al. (2010, P17); Donner et al. (2010b, C5); Donner et al. (2010c, P19); Donner et al. (2010a, P18); Donner et al. (2011b, P15); Donner et al. (2011a, P13); Donges et al. (2011a, P11); Donges et al. (2012, P8); Zou et al. (2012, P6); Feldhoff et al. (2013, P3); Feldhoff et al. (2012, P5); Donner et al. (2013, C1)

Visibility graphs

In contrast to recurrence networks, *visibility graphs* are embedded in the time domain and, hence, by design capture distinctive temporal characteristics of a time series. We have exploited this feature for introducing and applying novel tests for *time-reversal symmetry (reversibility)*, an important property of dynamical systems that

is informative for model development (Appendix B). Furthermore, the potentials of visibility graphs for analyzing geoscientific time series have been explored.

Future work may focus on deriving analytical results for the proposed measures of time series reversibility and studying possible multivariate extensions of visibility graph analysis.

Related publications   Donner and Donges (2012b, P7); Donner and Donges (2012a, C3); Donges et al. (2012, P2)

Coincidence analysis

In the geosciences, researchers are often faced with processes that on sufficiently long time scales can be regarded as point events, *e.g.*, earthquakes, volcanic eruptions, abrupt climatic transitions such as Dansgaard-Oeschger and Heinrich events, or rapid jumps in the evolution of species. Based on the concept of temporal *coincidences* between point processes, we have developed (Appendix E) and applied (Chapter 6) a method for measuring the correlation of event series and testing its significance with respect to a fully random null model.

Future research may focus on deriving additional analytical results and using Monte Carlo simulations for evaluating the significance of observed coincidences based on more sophisticated null models, including, for example, the effects of auto-dependencies in event series such as bunching and antibunching.

Related publication   Donges et al. (2011c, P10)

8.2.3. (Paleo)climatology

Detection of variability transitions in African paleoclimate during the Plio-Pleistocene

We have detected large-scale and nonlinear paleoclimate-variability transitions during the Plio-Pleistocene (the past 5 million years) in Africa using proxy records obtained from marine sediment cores (Chapter 6). Paleoclimatological and -oceanographic mechanisms such as a change in the dominant periodicities of ice age cycles (the Mid-Pleistocene transition), a reorganization of the tropical Walker circulation, and a spatial shift of the Indonesian throughflow connecting the Pacific and Indian Oceans have been discussed as potential drivers of the detected transitions. A possible connection to speciation and extinction events in the fossil record of human evolution has been evaluated, favoring an extended variant of Pott's variability selection hypothesis (see also Appendix E). Importantly, the detected paleoclimate regime shifts are robust with respect to reasonable variations in parameter choices (Chapter 5).

Promising tasks for future work include analyzing additional paleoclimate records providing a higher spatial and temporal resolution, as well as quantitatively comparing

and statistically testing the various hypotheses proposed in the literature regarding the influence of climate on evolutionary processes (particularly human evolution).

Related publications   Donges et al. (2011c, P10); Donges et al. (2011a, P11)

Insights into the atmosphere's general circulation structure

Coupled climate network analysis has been established as a novel approach for unraveling the complex structure of dynamical interdependencies between different climatological fields such as surface air temperature and sea level pressure (Chapter 7). It is based on our newly established framework for investigating the topology of networks of interacting networks (Section 2.4). A first application to studying reanalysis data representing the dynamics of the three-dimensional geopotential height field yielded insights into the structural organization of the atmosphere's general circulation. These include the detection of previously known features like the Hadley circulation, but also novel signatures of vertical interaction processes, *e.g.*, over the Arctic.

Open questions for future research include applying coupled climate network analysis to study other atmospheric processes of interest and extending it to probe the intricate interactions and interdependencies between different spheres of the Earth system such as atmosphere and ocean, or atmosphere and biosphere. Furthermore, it is paramount to advance the understanding of the relationships between (coupled) climate network structure and the underlying physical processes at work in Earth system dynamics, *e.g.*, advection, diffusion, turbulence, or radiation. This goal may be achieved by both rigorous mathematical considerations and numerical simulations.

Related publications   Donges et al. (2009b, P21); Donges et al. (2009a, P22); Marwan et al. (2010a, C4); Zou et al. (2011, P16); Tominski et al. (2011, P12); Donges et al. (2011b, P14); Heitzig et al. (2012, P9); Radebach et al. (subm. P4)

Appendix

Appendix A.

Vertex-weighted network measures

For reference, we list vertex-weighted node splitting invariant (n. s. i.) versions f^* of a number of commonly used local and global network measures f that can be found in the literature (see Chapter 2). Specifically, we provide formulae for standard complex network measures (Section A.2) and cross-network measures designed for networks of networks (Section A.3). For details on their derivation and interpretation, the reader is referred to Section 2.5, Heitzig et al. (2012, P9); Wiedermann et al. (2013, P1), and Wiedermann (2011).

Here, we consider undirected and simple networks $G = (V, E)$ represented by adjacency matrices $\mathbf{A} = \{A_{ij}\}_{ij}$, where V is the set of vertices and E is the set of edges (see Chapter 2), with weights $w_v \in \mathbb{R}$ associated to all vertices $v \in V$ (Section 2.5). The notation concerning networks of networks is the same as in Section 2.4. For simplicity, specifically with respect to definitions of path-based measures, we only consider connected networks (all vertices belonging to the same component) here.

To define the n. s. i. measures in a compact notation below, a few more quantities will have to be introduced. d_{vi}^* is the *n. s. i. shortest-path length* (or *n. s. i. geodesic distance*) between vertices v and i:

$$d_{vv}^* = 1 \quad \text{and} \quad d_{vi}^* = d_{vi} \text{ for } i \neq v. \tag{A.1}$$

The *total weight* W is given by

$$W = \sum_{i \in V} w_i. \tag{A.2}$$

The *total subnetwork weight* W_i of subnetwork G_i is defined as

$$W_i = \sum_{q \in V_i} w_q. \tag{A.3}$$

A.1. General rules for deriving n. s. i. network measures

The basic construction mechanism for deriving n. s. i. network measures from their unweighted counterparts is the following (Heitzig et al., 2012, P9; Wiedermann et al., 2013, P1):

(i) Sum up weights w_v wherever the original measure counts vertices v.

(ii) Use *unpunctured neighborhoods* $\mathcal{N}_v^+ = \mathcal{N}_v \cup \{v\}$ wherever the original measure uses punctured neighborhoods $\mathcal{N}_v$ (in other words, consider v as linked to itself).

(iii) Also allow for equality of i, j wherever the original measure involves a sum over distinct vertices i, j.

(iv) "Plug-in" a n. s. i. version of a measure g wherever this g is used in the definition of another measure f.

A.2. Vertex-weighted measures for isolated networks

A.2.1. Local measures

N. s. i. degree

$$k_v^* = \sum_{i \in V} w_i A_{vi}^+ \tag{A.4}$$

N. s. i. local clustering coefficient

$$\mathcal{C}_v^* = \frac{1}{(k_v^*)^2} \sum_{i,j \in V} w_i w_j A_{vi}^+ A_{ij}^+ A_{jv}^+ \tag{A.5}$$

N. s. i. closeness

$$c_v^* = \frac{W}{\sum_{i \in V} w_i d_{vi}^*} \tag{A.6}$$

N. s. i. shortest-path betweenness

$$\sigma_{ij}^* = \sum_{\substack{(t_0,\dots,t_{d_{ij}}) \in V^{d_{ij}+1} \\ t_0=i,\ t_{d_{ij}}=j}} \left(A_{t_0 t_1} \prod_{\ell=2}^{d_{ij}} (w_{t_{\ell-1}} A_{t_{\ell-1} t_\ell}) \right)$$

$$\sigma_{ij}^*(v) = \frac{1}{w_v} \sum_{m=1}^{d_{ij}-1} \sum_{\substack{(t_0,\dots,t_{d_{ij}}) \in V^{d_{ij}+1} \\ t_0=i,\ t_m=v,\ t_{d_{ij}}=j}} \left(A_{t_0 t_1} \prod_{\ell=2}^{d_{ij}} (w_{t_{\ell-1}} A_{t_{\ell-1} t_\ell}) \right) \tag{A.7}$$

$$b_v^* = \frac{1}{W^2} \sum_{\substack{i,j \in V \\ i,j \neq v}} w_i w_j \frac{\sigma_{ij}^*(v)}{\sigma_{ij}^*} \tag{A.8}$$

A.2.2. Global measures

N. s. i. edge density

$$\rho^* = \frac{1}{W^2} \sum_{i,j \in V} w_i w_j A_{ij}^+ = \frac{1}{W^2} \sum_{v \in V} w_v k_v^* \tag{A.9}$$

N. s. i. global clustering coefficient

$$\mathcal{C}^* = \frac{1}{W} \sum_{v \in V} w_v \mathcal{C}_v^* \tag{A.10}$$

N. s. i. transitivity

$$\mathcal{T}^* = \frac{\sum_{v,i,j \in V} w_v w_i w_j A_{vi}^+ A_{ij}^+ A_{jv}^+}{\sum_{v,i,j \in V} w_v w_i w_j A_{vi}^+ A_{vj}^+} \tag{A.11}$$

N. s. i. average path length

$$\mathcal{L}^* = \frac{1}{W^2} \sum_{i,j \in V} w_i w_j d_{ij}^* \tag{A.12}$$

A.3. Vertex-weighted measures for networks of networks

A.3.1. Local measures

N. s. i. cross-degree

$$k_v^{ij*} = \sum_{q \in V_j} w_q A_{vq}^+ \tag{A.13}$$

N. s. i. local cross-clustering coefficient

$$\mathcal{C}_v^{ij*} = \frac{1}{\left(k_v^{ij*}\right)^2} \sum_{p,q \in V_j} w_p w_q A_{vp}^+ A_{pq}^+ A_{qv}^+ \tag{A.14}$$

Appendix A. Vertex-weighted network measures

N. s. i. cross-closeness

$$c_v^{ij*} = \frac{W_j}{\sum_{q \in V_j} w_q d_{vq}^*} \tag{A.15}$$

N. s. i. cross-betweenness

$$b_v^{ij*} = \frac{1}{W_i W_j} \sum_{\substack{p \in V_i; q \in V_j \\ p,q \neq v}} w_p w_q \frac{\sigma_{pq}^*(v)}{\sigma_{pq}^*} \tag{A.16}$$

A.3.2. Global measures

N. s. i. cross-edge density

$$\rho_{ij}^* = \frac{1}{W_i W_j} \sum_{p \in V_i; q \in V_j} w_p w_q A_{pq}^+ \tag{A.17}$$

N. s. i. global cross-clustering coefficient

$$C_{ij}^* = \frac{1}{W_i} \sum_{q \in V_i} w_q C_v^{ij*} \tag{A.18}$$

N. s. i. cross-transitivity

$$\mathcal{T}_{ij}^* = \frac{\sum_{v \in V_i; p,q \in V_j} w_v w_p w_q A_{vp}^+ A_{pq}^+ A_{qv}^+}{\sum_{v \in V_i; p,q \in V_j} w_v w_p w_q A_{vp}^+ A_{vq}^+} \tag{A.19}$$

N. s. i. cross-average path length

$$\mathcal{L}_{ij}^* = \frac{1}{W_i W_j} \sum_{p \in V_i; q \in V_j} w_p w_q d_{pq}^* \tag{A.20}$$

Appendix B.

Visibility graphs for testing reversibility of time series

Reversibility or time-reversal symmetry is a fundamental property of time series. Among other applications, it can be harnessed for selecting models that are consistent with experimental time series data (Timmer et al., 1993; Diks et al., 1995). We propose a novel set of statistical tests for reversibility based on visibility graphs constructed from time series as well as on time-directed variants of common graph-theoretical measures like degree and local clustering coefficient (Donges et al., 2012, P2; Donner and Donges, 2012a, C3). Unlike other tests for reversibility, the technique proposed here has the advantage that it does not require the construction of surrogate time series. We investigate the performance of our statistical tests for time series from paradigmatic model systems with known time-reversal properties and compare it to a traditional test for reversibility. Finally, our tests are applied to characterize the temporal structure of electroencephalogram (EEG) time series representing normal and pathological dynamics of the human brain as well as to study paleoclimate dynamics during the last 100,000 years and transitions within it.

Note that independently from the work presented here, Lacasa et al. (2012) have proposed a test for reversibility of time series based on horizontal visibility graphs as well as using different network measures and test statistics.

B.1. Visibility graph analysis

Visibility graphs provide a simple mapping from the time series to the network domain by exploiting certain convexity characteristics of scalar time series $\{x(t_i)\}_{i=1}^N$ (Lacasa et al., 2008). Vertices i in a visibility graph represent observations $x_i = x(t_i)$ at time t_i. Two vertices i, j are linked by an edge $\{i, j\}$ if

$$x_k < x_j + (x_i - x_j)\frac{t_j - t_k}{t_j - t_i} \tag{B.1}$$

holds for all vertices k with $t_i < t_k < t_j$ (Fig. B.1). That is, the corresponding adjacency matrix $\mathbf{A}$ is given by the elements

$$A_{ij} = \prod_{k=i+1}^{j-1} \Theta\left(x_j + (x_i - x_j)\frac{t_j - t_k}{t_j - t_i} - x_k\right). \tag{B.2}$$

The construction algorithm implies that visibility graphs are spatial networks (Section 2.3) with vertices embedded on the one-dimensional time axis, *e.g.*, giving rise to boundary effects on commonly studied network measures (Donner and Donges, 2012b, P7). For example, visibility graphs have been employed for studying memory in stochastic time series (Lacasa et al., 2009) or for investigating geophysical time series (Elsner et al. (2009); Donner and Donges (2012b, P7), see also Section 3.2).

B.2. Time-directed visibility graph characteristics

Since visibility graphs are embedded on the one-dimensional time axis, their structure is intrinsically interwoven with the direction of time. This insight leads us to defining novel statistical network quantifiers for visibility graphs taking the time direction into account.

As the simplest possible network characteristic, the *retarded degree*

$$k_i^r = \sum_{j<i} A_{ij} \tag{B.3}$$

counts the number of samples that are visible in the past of a measurement at time t_i. Likewise, the *advanced degree*

$$k_i^a = \sum_{j>i} A_{ij} \tag{B.4}$$

gives the number of data points in its future from which x_i is visible.

The local clustering coefficient $\mathcal{C}_i$ is a higher-order statistic describing the neighborhood structure of vertex i (Newman, 2003). To allow studying the neighborhood structure in the past and future of i separately, we define the *retarded local clustering coefficient*

$$\mathcal{C}_i^r = \binom{k_i^r}{2}^{-1} \sum_{j,k<i} A_{ij} A_{jk} A_{ki} \tag{B.5}$$

as well as the *advanced local clustering coefficient*

$$\mathcal{C}_i^a = \binom{k_i^a}{2}^{-1} \sum_{j,k>i} A_{ij} A_{jk} A_{ki}, \tag{B.6}$$
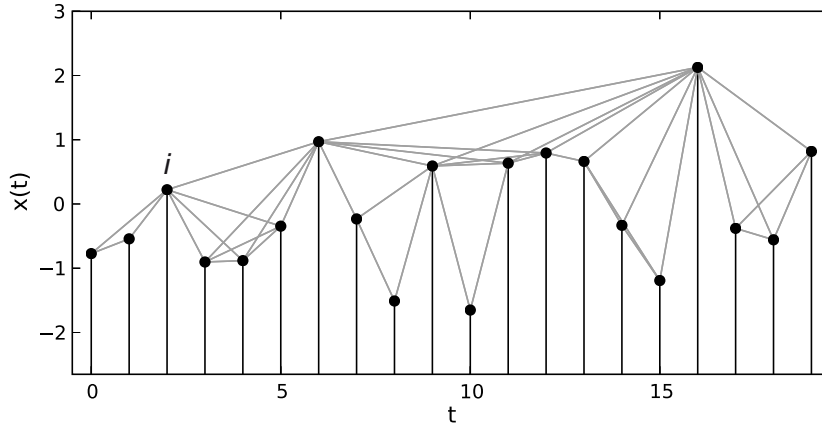
Figure B.1.: A visibility graph generated from uncorrelated Gaussian noise $\xi(t_i)$ (mean $\mu = 0$ and standard deviation $\sigma = 1$). Vertices are marked by black disks, edges by gray lines. Vertex i has retarded degree $k_i^r = 2$, advanced degree $k_i^a = 4$, and identical retarded and advanced local clustering coefficients $\mathcal{C}_i^r = \mathcal{C}_i^a = 1$.

where $\binom{k_i^{r,a}}{2}$ is a binomial coefficient. Both measure the probability that two neighbors in the past (future) of observation i are mutually visible themselves, respectively.

Further higher-order time-directed network characteristics for visibility graphs are conceivable, but are not considered here for brevity. Note that in a directed visibility graph with edges always pointing towards the future, k_i^r corresponds to the in-degree of i, while k_i^a is equivalent to its out-degree (compare Lacasa et al. (2012)). $\mathcal{C}_i^r$ and $\mathcal{C}_i^a$ are equivalent to the in- and out-clustering coefficients defined for directed networks by Fagiolo (2007).

B.3. Test for reversibility

A stationary time series x_i is said to be reversible if

$$p(x_n, x_{n+1}, \ldots, , x_{n+k}) = p(x_{n+k}, x_{n+k-1}, \ldots, , x_n) \tag{B.7}$$

holds for all n and k in the limit $N \to \infty$ (Diks et al., 1995).

The frequency distributions $p(k_i^{r,a})$ and $p(\mathcal{C}_i^{r,a})$ of our time-directed network measures are of special interest for testing the reversibility of a time series x_i. Particularly, in a reversible time series the visibility structure towards the past and future of any observation has to be statistically equivalent. That is, both observed degree sequences $\{k_i^{r,a}\}$ (or local clustering sequences $\{\mathcal{C}_i^{r,a}\}$) should be drawn from the same underlying probability distribution. The corresponding null hypothesis H_0 is

$$p(k^r) = p(k^a), \tag{B.8}$$
$$p(\mathcal{C}^r) = p(\mathcal{C}^a). \tag{B.9}$$
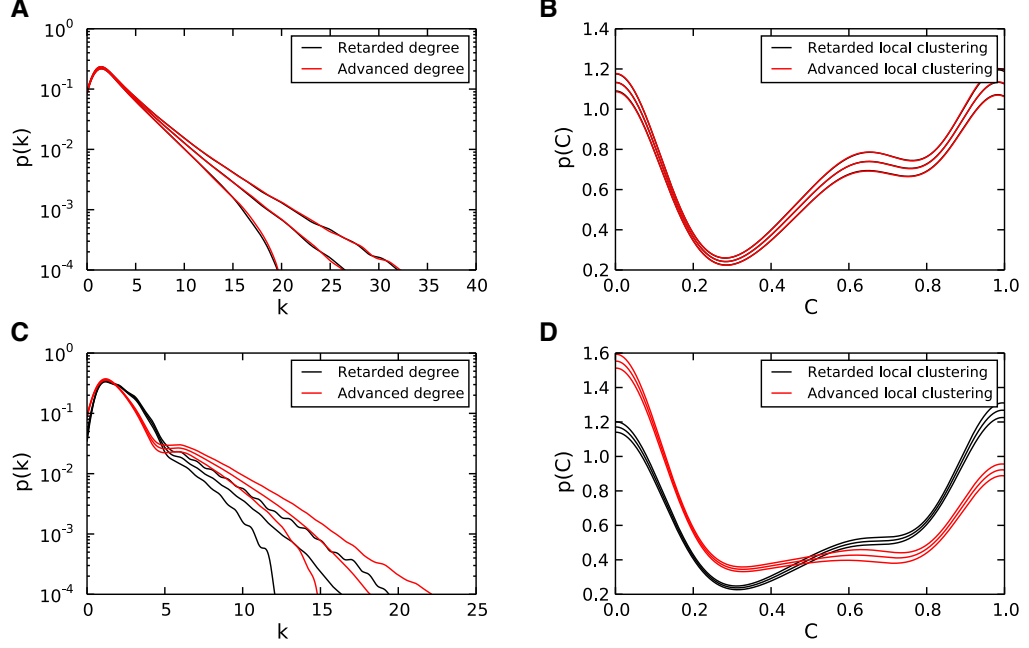
Figure B.2.: Distributions of retarded/advanced (A,C) degree $k_i^{r,a}$ and (B,D) local clustering coefficient $\mathcal{C}_i^{r,a}$ for model systems: (A,B) linear first-order auto-regressive (AR1) process and (C,D) nonlinear Hénon map (first component). Time series of length $N = 500$ have been used for estimating the probability density functions (PDF) with a kernel density estimator. The mean (solid lines) and standard deviation (dashed lines) of the PDFs have been computed based on an ensemble of $M = 1,000$ realizations with random initial conditions for both model systems.

The Kolmogorov-Smirnov (KS) test is a suitable and generally applicable means to test this null hypothesis. Now we argue that rejecting the null hypothesis that $\{k_i^{r,a}\}$ ($\{\mathcal{C}_i^{r,a}\}$) are drawn from the same probability distribution is equivalent to rejecting the null hypothesis that the time series under investigation is reversible (time-reversal symmetric). In other words, a small p-value of the KS test statistic (traditionally one considers $p < 0.05$ as small, hence, a significance level of 0.05 is used below) implies that the time series would be observed very rarely if the stochastic process or dynamical system were reversible (symmetric with respect to time-reversal).

B.4. Application to model systems

As a first step, the newly developed visibility graph tests for reversibility are applied to time series from model systems. Since the properties of these model time series are known, they can be used for assessing the performance of our tests. For illustration, we focus on the linear first-order auto-regressive (AR1) process and the nonlinear Hénon map as examples of truly reversible and irreversible dynamical systems, respectively (see, *e.g.*, Kantz and Schreiber (2004) for details). Similar results as reported below

are obtained for reversible processes such as uniformly or Gaussian distributed noise and higher-order auto-regressive processes, as well as for irreversible systems such as the chaotic logistic map or the Lorenz and Rössler systems.

An *AR1 process* is defined as

$$x_i = \alpha x_{i-1} + \xi_i, \tag{B.10}$$

and in the following, $\alpha = 0.5$ is chosen, whereas $\{\xi_i\}$ denotes a Gaussian noise process with zero mean and unit standard deviation. In turn, the chaotic *Hénon map* is given by

$$x_i^0 = A - \left(x_{i-1}^0\right)^2 + Bx_{i-1}^1$$
$$x_i^1 = x_{i-1}^0 \tag{B.11}$$

with parameter choices $A = 1.4$ and $B = 0.3$. In all cases, we use random initial conditions that are uniformly drawn from the interval $[0, 1]$ and discard 1,000 data points at the beginning of each time series to avoid transient effects. Since the proposed test is only applicable to univariate time series, the first component x_i^0 of the two-dimensional time series generated by the Hénon map is used.

As expected, for the reversible AR1 process, the empirical distributions of retarded/advanced degree $k_i^{r,a}$ and local clustering coefficient $\mathcal{C}_i^{r,a}$ collapse onto each other (Fig. B.2A,B). Consequently, the null hypothesis of reversibility is never rejected by the test based on degree (Fig. B.3A) and only rarely rejected by the clustering-based test well below the expected false rejection rate of 5% (Fig. B.3B). In contrast, for the irreversible Hénon map the distributions of retarded and advanced visibility graph measures appear distinct already by visual inspection (Fig. B.2C,D). In accordance with this observation, the null hypothesis of reversibility is nearly always (Fig. B.3C) or always (Fig. B.3D) rejected.

To evaluate the performance of the tests for varying sample sizes N, we consider the fraction $q(N)$ of time series from an ensemble for which the null hypothesis of reversibility can be rejected (Fig. B.4). It is known that the null hypothesis is true for the AR1 process, hence, $q(N)$ estimates the probability of *type I errors*[18] (incorrect rejections of true null hypothesis) for both tests (Fig. B.4A). Notably, $q(N)$ is always zero for the degree-based test, while it fluctuates below the expected type I error rate of 0.05 for the test based on local clustering. In the case of the irreversible Hénon map, the null hypothesis is known to be false. Therefore, $1 - q(N)$ estimates the probability of *type II errors*[19] (failure to reject a false null hypothesis) in this case (Fig. B.4B). Interestingly, the power $q(N)$ of the clustering-based test increases markedly earlier than that of the degree-based test. The former reaches $q(N) \approx 1$ around $N = 200$, whereas the latter requires twice as many samples to arrive at the same power.

---

[18]In this context, $1 - q(N)$ measures the *specificity* of the test.
[19]Here, $1 - q(N)$ is equivalent to the *sensitivity* of the test, while $q(N)$ is known as its *power*.
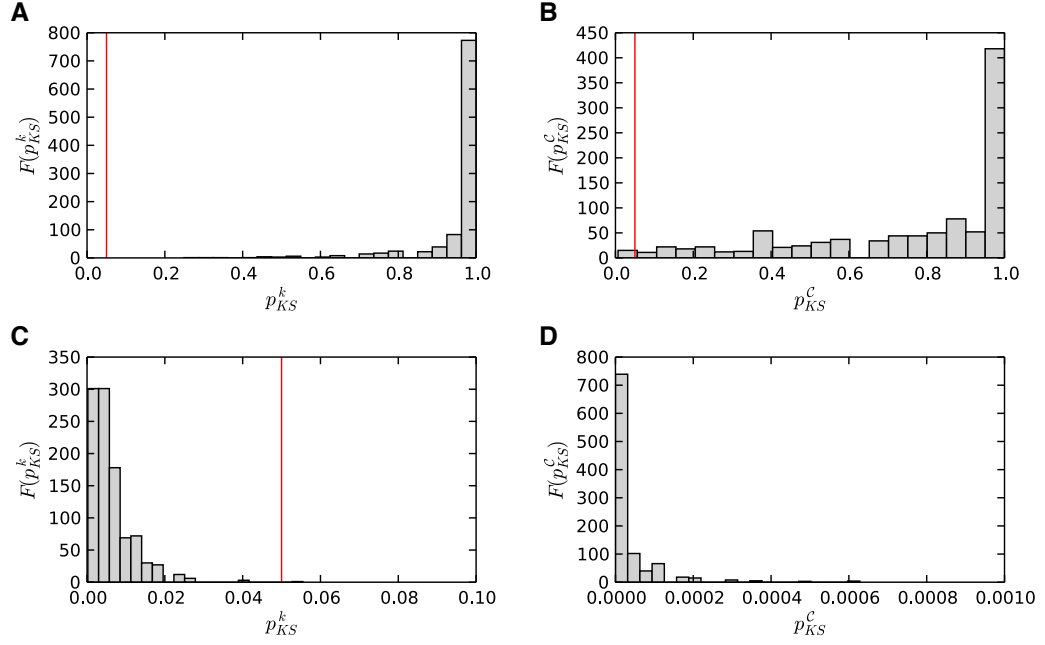
Figure B.3.: Frequency distributions of p-values of the Kolmogorov-Smirnov test statistic for comparing the distributions of retarded/advanced (A,C) degree $k_i^{r,a}$ and (B,D) local clustering coefficient $\mathcal{C}_i^{r,a}$ from an ensemble of $M = 1,000$ realizations of model system time series of length $N = 500$: (A,B) linear first-order auto-regressive (AR1) process and (C,D) nonlinear Hénon map (first component). Vertical red lines indicate the chosen significance level of 0.05.

In summary, we find that the proposed tests of reversibility of time series based on visibility graphs are well-behaved and have reasonable specificity and power for time series of a few hundred samples or more. For a given sample size N, the clustering-based test is more sensitive, but less specific than its degree-based equivalent.
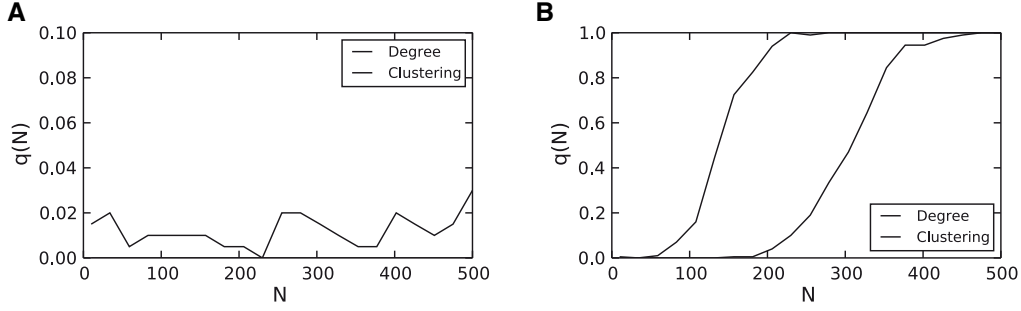
Figure B.4.: Fraction $q(N)$ of model system time series of length N from an ensemble of $M = 200$ realizations for which the null hypothesis of reversibility was rejected at the 0.05 significance level: (A) linear first-order auto-regressive (AR1) process and (B) nonlinear Hénon map (first component). Results of tests based on time-directed degree (local clustering) are marked by solid (dash-dotted) lines, respectively. The null hypothesis is never rejected for the test based on degree applied to AR1 time series (A).

B.5. Testing for time-reversal asymmetry in real-world data

B.5.1. Electroencephalogram data

To further assess the performance of our newly developed tests of reversibility for real-world data, we apply them to continuous electroencephalogram (EEG) recordings for healthy and epileptic patients that were analyzed and made publicly available by Andrzejak et al. (2001) (Fig. B.5). These authors selected five sets of $M = 100$ representative time series segments of length $N = 4,096$ comprising recordings of brain activity for different patient groups and recording regions (Table B.1). To look for traces of low-dimensional nonlinear dynamical behavior in the data, they used a nonlinear prediction error P and an effective correlation dimension $D_{2,eff}$ as statistics to test the null hypothesis H_0^{lin} that the time series are compatible with a Gaussian linear stochastic and stationary process.

Since irreversibility is a signature of nonlinear dynamics, we would expect the results of our tests to be consistent with those of Andrzejak et al. (2001). Indeed, the rate of rejections q of the null hypothesis of reversibility increases markedly from hardly any rejections for set A, where H_0^{lin} could not be rejected by Andrzejak et al. (2001), to $q \approx 1$, where H_0^{lin} was rejected using both test statistics (Table B.1). Hence, consistently with the results of Andrzejak et al. (2001), the visibility graph-based tests indicate reversible linear dynamics for healthy subjects (set A, Fig. B.5A,B) and irreversible nonlinear dynamics during epileptic seizures (set E, Fig. B.5C,D). The other data sets are intermediate with respect to the proposed tests.

In summary, it is encouraging to find that our tests perform consistently with the tests applied by Andrzejak et al. (2001) which are arguably more complicated
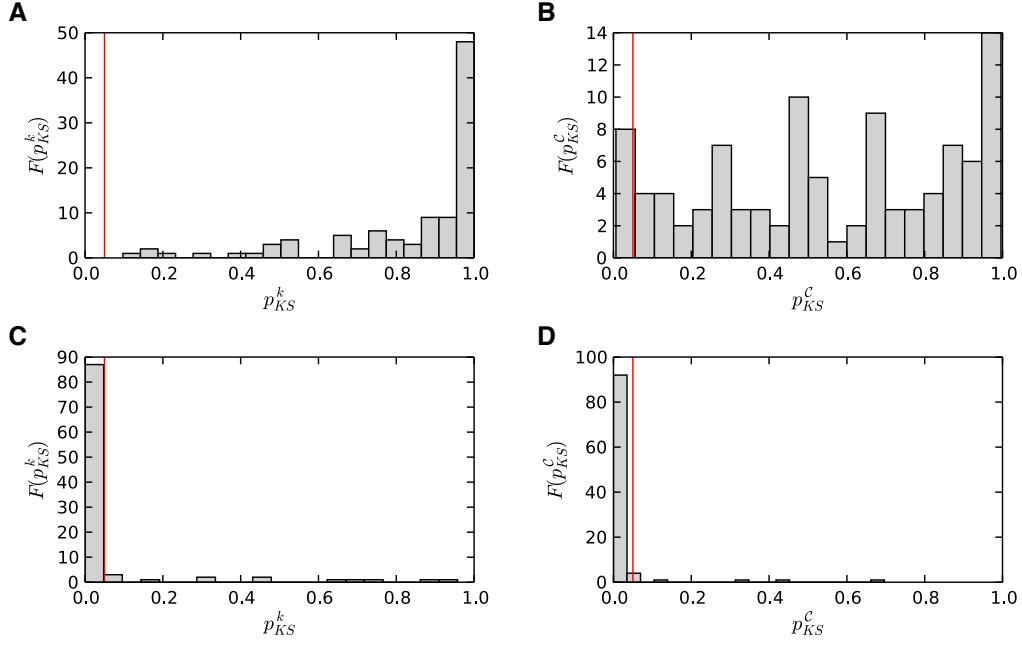
**Figure B.5.:** Frequency distributions of p-values of the Kolmogorov-Smirnov test statistic for comparing the distributions of retarded/advanced (A,C) degree $k_i^{r,a}$ and (B,D) local clustering coefficient $\mathcal{C}_i^{r,a}$ from a set of $M = 100$ electroencephalogram time series segments of length $N = 4,096$. Recordings originate from (A,B) healthy subjects with eyes open (data set A) and (C,D) epileptic patients during seizure (data set E). Vertical red lines indicate the chosen significance level of 0.05.

both technically and conceptually. Furthermore, we find that the results of the visibility graph-based tests for reversibility are consistent with those obtained using the classical Q statistic of Theiler et al. (1992, p. 84) together with standard and amplitude adjusted Fourier surrogate time series (Schreiber and Schmitz, 2000).

B.5.2. Paleoclimate time series

Since we have gained some confidence in our tests for reversibility over the last two sections, in the spirit of this thesis' background theme, Earth system analysis, we now proceed to apply them to look for signatures of nonlinearity in paleoclimate records. Visibility graph methods are particularly suitable for analyzing this type of data, because their construction does not require any assumptions on regular sampling of observations in time series. One can argue that the irregular sampling that is typical of paleoclimate records retrieved from geological archives such as marine sediment cores, ice cores, or speleothems would not strongly impact the performance of the proposed tests for reversibility given that the sampling process is stationary and the sample size is sufficiently large (Telesca and Lovallo, 2012). For now, we accept this reasoning and leave detailed tests for future research.

Table B.1.: Results of a visibility graph-based test for reversibility of electroencephalogram time series put into context with results taken from Andrzejak et al. (2001). These authors use a nonlinear prediction error P and an effective correlation dimension $D_{2,eff}$ as statistics to test the null hypothesis H_0^{lin} that the time series are compatible with a Gaussian linear stochastic and stationary process. q_k (q_C) denote the fraction of time series from a set of $M = 100$ segments for which the null hypothesis of reversibility was rejected by the proposed visibility graph tests based on time-directed degree (clustering) (see also Fig. B.5).

			Andrzejak et al. (2001)		This study	
Set	State	Recording sites	P	$D_{2,eff}$	q_k	q_C
A	healthy, eyes open	mixed	no reject H_0^{lin}	no reject H_0^{lin}	0.00	0.07
B	healthy, eyes closed	mixed	reject H_0^{lin}	no reject H_0^{lin}	0.07	0.16
C	pathological, no seizure	hippocampal formation	reject H_0^{lin}	no reject H_0^{lin}	0.13	0.22
D	pathological, no seizure	epileptogenic zone	reject H_0^{lin}	reject H_0^{lin}	0.36	0.37
E	pathological, seizure	mixed	reject H_0^{lin}	reject H_0^{lin}	0.87	0.94

We analyze four speleothem records of $\delta^{18}O$ variability during the Holocene from geographically widely separated caves serving as proxies for temperature and precipitation changes related to monsoonal activity in the past (Dykoski et al. (2005); Fleitmann et al. (2007), and Breitenbach et al., unpublished). For evaluating the robustness of the results, we create ensembles of time series from each record applying a leave-K-out cross-validation procedure by randomly removing 20% of the data points without changing their time ordering. In all four cases, the null hypothesis of reversibility cannot be rejected for a significantly large fraction of bootstrapped time series (possibly, with the exception of the record from stalagmite D1 by Fleitmann et al. (2007) with respect to the clustering-based test) (Table B.2). Similar results are obtained when randomly removing different fractions of the available data points, as long as the resulting length N remains sufficiently large. Hence, the proposed tests can be said to not detect a signature of nonlinearity in $\delta^{18}O$ variability recorded in the four considered speleothems. It is, however, impossible to determine from the present data whether this apparent lack of nonlinearity in the Holocene paleoclimate records is a direct signature of climate dynamics or an imprint of the complex physical, chemical, biological, and geological processes influencing the oxygen isotope signal deposited in the speleothems.

To address this question of distinguishing the contributions of paleoclimate dynamics and proxy genesis, it is illustrative to look at records spanning several qualitatively different climate regimes. As an example, we study the 2 m resolution $\delta^{18}O$ isotope record from the GISP2 ice core from Greenland (Grootes and Stuiver, 1997) that

Table B.2.: Results of a visibility graph-based test for reversibility of Holocene $\delta^{18}O$ variability recorded in speleothems. Ensembles of $M = 100$ realizations are created for each record by leave-K-out cross-validation with $K = 0.2N$. $\langle\Delta T\rangle$ denotes the mean sampling time, $\sigma(\Delta T)$ its standard deviation, and N the full time series length (before bootstrapping). q_k ($q_\mathcal{C}$) denote the fraction of bootstrapped time series for which the null hypothesis of reversibility was rejected by the proposed visibility graph tests based on time-directed degree (clustering).

Reference	Location	$\langle\Delta T\rangle$ (yr)	$\sigma(\Delta T)$ (yr)	N	q_k	$q_\mathcal{C}$
Fleitmann et al. (2007)	Stalagmite D1, Dimarshim Cave, Socotra, Yemen	8.3	3.1	530	0	0.24
Fleitmann et al. (2007)	Stalagmite Q5, Qunf Cave, Oman	7.1	36.4	1405	0	0.08
Breitenbach et al., unpublished	Stalagmite DHAR1, Dharamjali Cave, India	2.8	8.3	739	0	0.04
Dykoski et al. (2005)	Stalagmite D4, Dongge Cave, China	17.4	18.2	908	0	0.00

covers both the Holocene and the last glacial period (Fig. B.6). Applying the proposed test for reversibility to the Holocene and the last glacial period separately, we find that the null hypothesis of reversibility can be quite safely rejected for the last glacial, whereas it cannot be rejected for the Holocene (Table B.3). Since the conditions for the deposition of ice and snow at the drilling site are argued to have remained more or less constant throughout the entire time span covered by the record, these results point at a strong signature of nonlinear climate dynamics during the last glacial, which is not detected for the Holocene, consistently with the results for the Holocene speleothem records reported above. One visually directly accessible piece of evidence for the detected irreversible dynamics during the last glacial period are the frequently occurring Dansgaard-Oeschger events that are characterized by rapid warming (change towards more positive $\delta^{18}O$ values) and subsequent slower cooling (change towards more negative $\delta^{18}O$ values) of Greenland climate (Fig. B.6). Extending on these results, in the spirit of Chapters 5 and 6, the proposed test could be used to detect transitions between reversible (linear) and irreversible (nonlinear) dynamics in general paleoclimate records.

Note that the sampling times increase with age for the GISP2 as for all ice core proxy records, because the ice column is compressed by the ice and snow deposited on top of it over the years. It remains to be tested whether this nonstationarity has a strong impact on the results of the visibility graph test for reversibility.
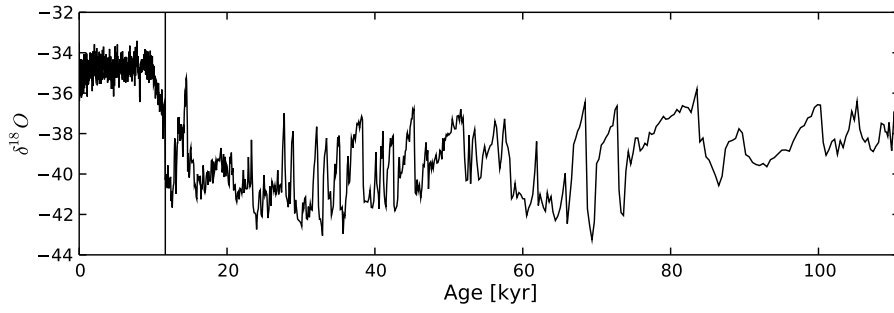
Figure B.6.: GISP2 ice core $\delta^{18}O$ record from Greenland (Grootes and Stuiver, 1997). The boundary between the last glacial and the Holocene is defined by the Younger Dryas-Preboreal transition at 11,650 years BP (Grootes and Stuiver, 1997) (vertical line).

Table B.3.: Results of visibility graph-based test for reversibility of the GISP2 ice core $\delta^{18}O$ 2 meter record from Greenland (Grootes and Stuiver, 1997). Ensembles of $M = 100$ realizations are created for each record by bootstrapping 80% of the data points without changing their time ordering. See the caption of Table B.2 for column descriptions.

Period	Time span (kyr BP)	$\langle\Delta T\rangle$ (yr)	$\sigma(\Delta T)$ (yr)	N	q_k	$q_\mathcal{C}$
Last glacial	$110.98 - 11.65$	175.8	119.6	566	0.93	0.82
Holocene	11.65 − today	14.2	6.3	824	0.00	0.00

B.6. Discussion

A test for reversibility of scalar time series based on time-directed visibility graphs has been proposed. It has been evaluated for time series generated by model systems with reversible (*e.g.*, Gaussian noise and AR1 processes) and irreversible (*e.g.*, logistic and Hénon maps) dynamics. Furthermore, the technique has been used to detect irreversibility as a signature of nonlinear dynamical behavior in electroencephalogram recordings from healthy and epileptic patients as well as paleoclimate records from speleothems and and an ice core from Greenland.

The proposed test has two notable advantages with respect to other tests for reversibility of time series reported in the literature: (i) It does not require the construction of surrogate time series for obtaining a *p*-value and (ii) it is directly applicable to irregularly sampled time series without the need of any preprocessing such as interpolation. Feature (i) serves to circumvent technical problems related to the choice and construction of surrogate time series and leads to a fast and efficient algorithm, while feature (ii) implies that the test is particularly well suited for analyzing geoscientific time series (Donner and Donges, 2012b, P7) (see the discussion of this type of data in Chapter 5).

Appendix C.

Multivariate recurrence network analysis

In the last decade, multivariate extensions of recurrence quantification analysis (RQA) have been proposed for studying interrelationships between time series from distinct systems, *e.g.*, for investigating synchronization phenomena or coupling directions (Marwan et al., 2007). Two alternative multivariate extensions of the recurrence plot (see Section 3.2.2) have been proposed: (i) joint recurrence plots (Romano et al., 2004) and (ii) cross-recurrence plots (Marwan and Kurths, 2002). Here, corresponding multivariate extensions of recurrence network analysis, which have been discussed by Feldhoff (2011) for the first time, and their applications are briefly recapitulated. Joint recurrence networks derived from joint recurrence plots are introduced in Section C.1, while inter-system recurrence networks, which are related to cross-recurrence plots, are described in Section C.2. An analytical framework for the description of their statistical characteristics, analogous to the treatment in Chapter 4, is sketched in Section C.3.

In the following, we consider K (potentially multi-dimensional) time series $\{x^k(t_i^k) = x_i^k\}_{i=1}^{N_k}$ sampled at times $\{t_i^k\}$ from dynamical systems $\{X_k\}$ with $k = 1, \ldots, K$.

C.1. Joint recurrence networks

C.1.1. Definition

The idea behind joint recurrence plots is that the simultaneous occurrence of recurrences in two or more dynamical systems $\{X_k\}$ contains information on possible interrelationships between them (Marwan et al., 2007). Consequently, based on time series $\{x_i^k\}$, the joint recurrence matrix $\mathbf{JR}$ with elements

$$JR_{ij}(\varepsilon_1, \ldots, \varepsilon_K) = \prod_{k=1}^{K} R_{ij}^k(\varepsilon_k) \tag{C.1}$$

is defined as the element-wise product of the single-system recurrence matrices $\mathbf{R}^k$ (Section 3.2.2) with elements

$$R_{ij}^k(\varepsilon_k) = \Theta(\varepsilon_k - \|x_i^k - x_j^k\|), \tag{C.2}$$

Table C.1.: Comparison of multivariate generalizations of recurrence network analysis regarding the principal requirements on the time series to be analyzed (see Donner et al. (2013, C1) for a discussion). *Identical* means that a specific property must be the same for all involved time series, while *arbitrary* implies that this does not need to be the case.

	Joint recurrence network	Inter-system recurrence network
Length	identical	arbitrary
Sampling	identical	arbitrary
Physical unit	arbitrary	identical
Phase space dimension	arbitrary	identical

where ε_k is the vector of recurrence thresholds that can be selected for each time series individually.

Analogously to single-system recurrence network analysis, we can take a graph-theoretical perspective by defining a *joint recurrence network* by its adjacency matrix

$$\mathbf{A}(\varepsilon_1, \ldots, \varepsilon_K) = \mathbf{JR}(\varepsilon_1, \ldots, \varepsilon_K) - \mathbf{1}_N, \tag{C.3}$$

where $\mathbf{1}_N$ denotes the N-dimensional identity matrix. In the undirected and simple joint recurrence network, vertices i represent points in time $t_i^k = t_i^l$, and edges $\{i, j\}$ indicate joint recurrences occurring simultaneously in all K time series under study. Alternatively, $\mathbf{A}(\varepsilon_1, \ldots, \varepsilon_K)$ may be viewed as the element-wise product the single-system recurrence networks' adjacency matrices $\mathbf{A}^k(\varepsilon_k)$.

By construction, the time series $\{x_i^k\}$ used for building a joint recurrence network need to be sampled at identical times $\{t_i^k\}$ and have to have the same length, *i.e.*, $N_1 = N_2 = \ldots = N_K$. However, since recurrences are compared instead of state vectors, the $\{x_i^k\}$ neither have to represent the same physical quantity measured in identical units, nor need they reside in the same phase space (Table C.1).

C.1.2. Applications

Joint recurrence networks can be analyzed by standard statistical measures from complex network theory (Newman, 2003; Donner et al., 2010c, P19), which, however, need to be reinterpreted in terms of the underlying systems' joint recurrence structure (Feldhoff, 2011; Feldhoff et al., 2013, P3; Donner et al., 2013, C1). The transitivity properties of joint recurrence networks have been shown to reveal complex synchronization scenarios, notably including the detection of the onset of generalized synchronization, in coupled chaotic oscillators such as Rössler systems (Feldhoff et al., 2013, P3). Moreover, the specific requirements on the time series data render joint recurrence networks a promising approach for detecting intricate interconnections between qualitatively distinct observables in observational or experimental real-world data.

C.2. Inter-system recurrence networks

C.2.1. Definition

A complementary way of extending recurrence analysis to the study of multiple dynamical systems is looking at *cross-recurrences*[20], *i.e.*, encounters of the trajectories of the systems X_k and X_l, where $x_i^k \approx x_j^l$ (Marwan et al., 2007). In contrast to the joint recurrence matrix $\mathbf{JR}$, the cross-recurrence matrix $\mathbf{CR}^{kl}$ with elements

$$CR_{ij}^{kl}(\varepsilon_{kl}) = \Theta(\varepsilon_{kl} - \|x_i^k - x_j^l\|), \tag{C.4}$$

where $i = 1, \ldots, N_k$, $j = 1, \ldots, N_l$, and ε_{kl} is the recurrence threshold, cannot be directly interpreted as the adjacency matrix of a simple graph. This is because the indices i and j label two distinct sets of state vectors belonging to systems X_k and X_l, respectively. Instead of investigating the structure of a corresponding bipartite graph[21], the information contained in the single-system recurrence matrices $\mathbf{R}^k(\varepsilon_k)$ and the cross-recurrence matrices $\mathbf{CR}^{kl}(\varepsilon_{kl})$ can be combined to construct an inter-system recurrence matrix

$$\mathbf{R}(\varepsilon) = \begin{pmatrix} \mathbf{R}^1(\varepsilon_1) & \mathbf{CR}^{12}(\varepsilon_{12}) & \ldots & \mathbf{CR}^{1K}(\varepsilon_{1K}) \\ \mathbf{CR}^{21}(\varepsilon_{21}) & \mathbf{R}^2(\varepsilon_2) & \ldots & \mathbf{CR}^{2K}(\varepsilon_{2K}) \\ \vdots & \vdots & \ddots & \vdots \\ \mathbf{CR}^{K1}(\varepsilon_{K1}) & \mathbf{CR}^{K2}(\varepsilon_{K2}) & \ldots & \mathbf{R}^K(\varepsilon_K) \end{pmatrix}. \tag{C.5}$$

Here, $\varepsilon = \{\varepsilon_{kl}\}_{kl}$ is a $K \times K$ matrix holding the single-system and cross-recurrence thresholds ε_{kl}. The corresponding *inter-system recurrence network* is fully described by its adjacency matrix

$$\mathbf{A}(\varepsilon) = \mathbf{R}(\varepsilon) - \mathbf{1}_N, \tag{C.6}$$

where $N = \sum_{k=1}^K N_k$ is the number of vertices. In the undirected and simple inter-system recurrence network, vertices represent state vectors in the phase space common to all systems X_k and edges indicate pairs of state vectors from the same or different systems that are mutually close. By construction, an inter-system recurrence network can be viewed and statistically analyzed as a network of networks (Sections 2.4 and C.3).

In contrast to joint recurrence networks, the meaningful construction and analysis of inter-system recurrence networks requires time series $\{x_i^k\}$ that reside in the same phase space and, hence, describe the same observables with identical physical units

---

[20]It is important to realize that cross-recurrences are not to be understood in the Poincaré sense, since they do not indicate the return of an isolated dynamical system to some previously assumed state. In contrast, they imply a delayed close encounter of the trajectories of two distinct systems and, therefore, should be named *cross encounters* instead. Following the same reasoning, terms such as *cross-recurrence plot* or *cross-recurrence rate* are suggestive, but potentially misleading.

[21]In a bipartite graph, only edges connecting two distinct groups of vertices exist (Newman, 2003), *i.e.*, in the terminology of Section 2.4 only cross-edges, but no internal edges occur.

(Table C.1). However, the time series under study can in principle be sampled at arbitrary times $\{t_i^k\}$ and have different lengths $\{N_k\}$, because the method discards all information on time and focusses exclusively on neighborhood relationships in the shared phase space.

C.2.2. Applications

The new class of statistical network measures designed for investigating the topology of networks of networks introduced in Section 2.4 is readily applicable for analyzing the interdependency structure of multiple complex dynamical systems. Feldhoff et al. (2012, P5) have shown that the asymmetry intrinsic to the global measures cross-transitivity $\mathcal{T}_{kl}$ and global cross-clustering coefficient $\mathcal{C}_{kl}$ (see Section C.3) can be exploited to reliably detect the direction of coupling between chaotic oscillators over a wide range of coupling strengths, requiring only a small number of samples $\mathcal{O}(N_k) = 100$. Inter-system recurrence network analysis is readily applicable to the analysis of paleoclimate data, since it does not require equidistant sampling or identical sampling times across multiple records (see above). A first successful application to detecting the predominant direction of coupling between the Indian and East Asian monsoon systems during the Holocene based on paleoclimate records of monsoonal variability from speleothems has been presented (Feldhoff et al., 2012, P5; Marwan et al., 2012, C2).

C.3. Analytical framework for inter-system recurrence network analysis

C.3.1. General framework

Given a general undirected and unweighted simple (no multiple edges, no self-loops) graph $G = (V, E)$ described by the adjacency matrix $\mathbf{A} = \{A_{ij}\}_{ij}$, consider a partition of the vertex set V into K disjunct subsets $V_k \subseteq V$ such that $\bigcup_{k=1}^{K} V_k = V$ and $V_k \cap V_l = \emptyset$ for all $k \neq l$ (see also Section 2.4). Similarly, the edge set E is decomposed into disjunct $E_{kl} \subseteq E$ with $\bigcup_{k,l=1}^{K} E_{kl} = E$ and $E_{kl} \cap E_{mn}$ for all $(k, l) \neq (m, n)$ such that $G_k = (V_k, E_{kk})$ is the induced subgraph of the vertex set V_k with respect to the full graph G. Then E_{kk} contains the (internal) edges within the subgraph or subnetwork G_k, while E_{kl} comprises (cross-) edges connecting subnetworks G_k and G_l. In the specific case of inter-system recurrence networks considered here, the G_k correspond to the single-system recurrence networks constructed from the systems X_k, whereas the cross-recurrence structure is contained in the sets of cross-edges E_{kl} for $k \neq l$.

C.3.2. Continuous measures for inter-system recurrence networks

We are now in a position to study the interconnectivity structure between two subnetworks G_k, G_l on several topological scales drawing on the lineup of local and

global graph-theoretical measures proposed in Section 2.4. In this context, local measures f_v^{kl} characterize a property of vertex $v \in V_k$ with respect to subnetwork G_l, while global measures f_{kl} assign a single real number to a pair of subnetworks G_k, G_l to quantify a certain aspect of their mutual interconnectivity structure.

All relevant graph-theoretical measures for recurrence networks can be seen as discrete approximations of more general and continuous geometrical properties of a dynamical system's underlying attractor characterized by a set S together with an associated invariant density $p(x)$, $x \in S$ (Chapter 4 and Donges et al. (2012, P8)). This point of view allows to obtain deeper insights into the geometrical meaning of the numerous and diverse network quantifiers and enables one to establish surprising connections to other fields, *e.g.*, the close relationship of transitivity measures like the local clustering coefficient and transitivity to the local and global fractal dimension of the dynamical system's attractor, respectively (Chapter 4 and Donner et al. (2011b, P15)).

In the same spirit, we can consider the graph-theoretical measures for studying the interconnections between subnetworks within inter-system recurrence networks as discrete approximations of more general geometrical properties. Let $S_k \subset Y$ be a subset of an m-dimensional compact smooth manifold Y and $p_k(x)$ represent its invariant density for all $k = 1, \ldots, K$, where $x \in S_k$. In the following, the S_k and p_k are assumed to fulfill the same requirements that are stated for S and p in Section 4.2. We will use the abbreviation $\int d\mu_k(x) = \int_{S_k} d^m x \, p_k(x)$, where μ_k is a probability measure on S_k. For simplicity, only a single recurrence threshold $\varepsilon = \varepsilon_{kl}$ for all k, l will be used.

Local measures

In all definitions, x denotes a state of system X_k, hence, $x \in S_k$ holds.

Continuous ε-cross-degree density

$$\rho_{kl}(x; \varepsilon) = \int_{B_\varepsilon(x) \cap S_l} d\mu_l(y) = \int d\mu_l(y) \Theta(\varepsilon - \|x - y\|) \tag{C.7}$$

measures the probability that a randomly chosen state from X_l is found in the recurrence neighborhood $B_\varepsilon(x)$ of $x \in S_k$. Its discrete version is the *cross-degree density*

$$\hat{\rho}_v^{kl}(\varepsilon) = \frac{1}{N_l} \sum_{i \in V_l} A_{vi}(\varepsilon) \tag{C.8}$$

with $v \in V_k$.

Continuous local ε-cross-clustering coefficient

$$\mathcal{C}_{kl}(x; \varepsilon) = \frac{\iint_{B_\varepsilon(x) \cap S_l} d\mu_l(y) \, d\mu_l(z) \, \Theta(\varepsilon - \|y - z\|)}{\rho_{kl}(x; \varepsilon)^2} \tag{C.9}$$

gives the probability that two randomly chosen states from X_l are recurrent to each other if they both lie in the recurrence neighborhood of state $x \in X_k$. $\mathcal{C}_{kl}(x; \varepsilon)$ is approximated by the discrete *local cross-clustering coefficient*

$$\hat{\mathcal{C}}_v^{kl}(\varepsilon) = \frac{1}{\hat{k}_v^{kl}(\varepsilon)(\hat{k}_v^{kl}(\varepsilon) - 1)} \sum_{i,j \in V_l} A_{vi}(\varepsilon) A_{ij}(\varepsilon) A_{jv}(\varepsilon), \tag{C.10}$$

where $\hat{k}_v^{kl}(\varepsilon) = \hat{\rho}_v^{kl}(\varepsilon) N_l$.

Continuous ε-cross-closeness centrality and -efficiency Considering the mutual global geometry of the systems X_k, X_l, we furthermore introduce *continuous ε-cross-closeness centrality*

$$c_{kl}(x; \varepsilon) = \left(\int d\mu_l(y) \frac{g(x,y)}{\varepsilon} \right)^{-1} \tag{C.11}$$

quantifying the closeness of state x of system X_k to all states of system X_l along geodesics together with the related harmonic *continuous local ε-cross-efficiency*

$$e_{kl}(x; \varepsilon) = \int d\mu_l(y) \left(\frac{g(x,y)}{\varepsilon} \right)^{-1}. \tag{C.12}$$

Here, geodesics are defined with respect to the union of all involved systems' attractors $S = \bigcup_{k=1}^K S_k$ and $g(x, y)$ is a suitable distance metric on such geodesics (Section 4.2.4). The proposed local path-based measures for inter-system recurrence networks are approximated by the discrete *cross-closeness centrality*

$$\hat{c}_v^{kl}(\varepsilon) = \left(\frac{\sum_{i \in V_l} d_{vi}(\varepsilon)}{N_l} \right)^{-1} \tag{C.13}$$

and *local cross-efficiency*

$$\hat{e}_v^{kl}(\varepsilon) = \frac{\sum_{i \in V_l} d_{vi}(\varepsilon)^{-1}}{N_l}, \tag{C.14}$$

where again $v \in V_k$. These path-based estimators break down for disconnected inter-system recurrence networks (Section 4.3.2). Section 2.4.2 discusses alternative definitions of path-based measures in this situation.

Global measures

Continuous ε-cross-edge density The simplest continuous global property describing the recurrence structure between systems X_k and X_l in phase space is the *continuous ε-cross-edge density*

$$\rho_{kl}(\varepsilon) = \iint d\mu_k(x) d\mu_l(y) \Theta(\varepsilon - \|x - y\|) = \rho_{lk}(\varepsilon) \tag{C.15}$$

that is empirically estimated by

$$\hat{\rho}_{kl}(\varepsilon) = \frac{1}{N_k N_l} \sum_{i \in V_k, j \in V_l} A_{ij}(\varepsilon) = \hat{\rho}_{lk}(\varepsilon). \tag{C.16}$$

$\hat{\rho}_{kl}(\varepsilon)$ corresponds to the definition of the *cross-recurrence rate CRR* from cross-recurrence quantification analysis (CRQA) (Marwan et al., 2007).

Continuous global ε-cross-clustering coefficient The expectation value of the local ε-cross-clustering coefficient $\mathcal{C}_{kl}(x; \varepsilon)$ is referred to as the *continuous global ε-cross-clustering coefficient*

$$\mathcal{C}_{kl}(\varepsilon) = \int d\mu_k(x) \, \mathcal{C}_{kl}(x; \varepsilon). \tag{C.17}$$

In general, the cross-transitivity structure is asymmetric and $\mathcal{C}_{kl}(\varepsilon) \neq \mathcal{C}_{lk}(\varepsilon)$ follows. The corresponding discrete estimator, *global cross-clustering coefficient* is given by

$$\hat{\mathcal{C}}_{kl}(\varepsilon) = \left\langle \hat{\mathcal{C}}_v^{kl}(\varepsilon) \right\rangle_{v \in V_k} = \frac{1}{N_k} \sum_{v \in V_k, \hat{k}_v^{kl} > 1} \frac{\sum_{i,j \in V_l} A_{vi}(\varepsilon) A_{ij}(\varepsilon) A_{jv}(\varepsilon)}{\sum_{i \neq j \in V_l} A_{vi}(\varepsilon) A_{vj}(\varepsilon)}. \tag{C.18}$$

Continuous ε-cross-transitivity Designed for quantifying transitivity in the cross-recurrence structure, the *continuous ε-cross-transitivity*

$$\mathcal{T}_{kl}(\varepsilon) = \frac{\iiint d\mu_k(x) d\mu_l(y) d\mu_l(z) \Theta(\varepsilon - \|x - y\|) \Theta(\varepsilon - \|y - z\|) \Theta(\varepsilon - \|z - x\|)}{\iiint d\mu_k(x) d\mu_l(y) d\mu_l(z) \Theta(\varepsilon - \|x - y\|) \Theta(\varepsilon - \|x - z\|)} \tag{C.19}$$

gives the probability that two randomly chosen states y, z of system X_l which are "cross-recurrent" to a randomly chosen state x of system X_k are also recurrent with respect to each other. As for the continuous global ε-cross-clustering coefficient, in general $\mathcal{T}_{kl}(\varepsilon) \neq \mathcal{T}_{lk}(\varepsilon)$. $\mathcal{T}_{kl}(\varepsilon)$ is approximated by the discrete *cross-transitivity*

$$\hat{\mathcal{T}}_{kl} = \frac{\sum_{v \in V_k; i,j \in V_l} A_{vi}(\varepsilon) A_{ij}(\varepsilon) A_{jv}(\varepsilon)}{\sum_{v \in V_k; i \neq j \in V_l} A_{vi}(\varepsilon) A_{vj}(\varepsilon)}. \tag{C.20}$$

Note that although cross-transitivity and global cross-clustering coefficient are based on a similar concept, they capture distinctively different network properties (see Section 2.4.2).

Continuous ε-cross-average path length and -efficiency While the two former measures depend only on the local recurrence structure between X_k, X_l, path-based

measures contain information on the global geometry of both systems' attractors. The *continuous ε-cross-average path length*

$$\mathcal{L}_{kl}(\varepsilon) = \iint d\mu_k(x)d\mu_l(y)\frac{g(x,y)}{\varepsilon} = \mathcal{L}_{lk}(\varepsilon) \tag{C.21}$$

gives the average length of geodesic paths starting in S_k and ending in S_l or vice versa.

Similarly, we define the *continuous ε-cross-efficiency*

$$\mathcal{E}_{kl}(\varepsilon) = \left(\iint d\mu_k(x)d\mu_l(y)\left(\frac{g(x,y)}{\varepsilon}\right)^{-1}\right)^{-1} = \mathcal{E}_{lk}(\varepsilon) \tag{C.22}$$

which is the harmonic mean geodesic distance between X_k and X_l.

Discrete approximations of these global path-based quantifiers are provided by the *cross-average path length*

$$\hat{\mathcal{L}}_{kl}(\varepsilon) = \frac{1}{N_k N_l}\sum_{i\in V_k, j\in V_l} d_{ij}(\varepsilon) = \hat{\mathcal{L}}_{lk}(\varepsilon) \tag{C.23}$$

and the *cross-efficiency*

$$\hat{\mathcal{E}}_{kl}(\varepsilon) = \left(\frac{1}{N_k N_l}\sum_{i\in V_k, j\in V_l} d_{ij}(\varepsilon)^{-1}\right)^{-1} = \hat{\mathcal{E}}_{lk}(\varepsilon), \tag{C.24}$$

where $d_{ij}(\varepsilon)$ is the graph-theoretical shortest-path length between vertices i, j in G. Refer to Section 2.4.2 for a discussion of the treatment of these measures in the case of disconnected networks.

Appendix D.

Higher-order transitivity-based dimensions

The standard local clustering coefficient and global transitivity measures, as well as their continuous equivalents (Chapter 4), have been successfully employed for defining novel notions of local and global dimensionality for general sets such as the strange (fractal) attractors of chaotic dynamical systems that are based on recurrence networks (Section 3.2.2 and Donner et al. (2011b, P15)). In Section 4.2.3 and Donges et al. (2012, P8), we formulated the idea that motif densities in recurrence networks could be used analogously to define higher-order local and global measures of dimensionality, similarly to the sequence of Rényi dimensions from dynamical systems theory (Rényi, 1961; Hentschel and Procaccia, 1983). Following this train of thought, we begin with defining a family of higher-order local κ-clustering coefficients and global κ-transitivities, respectively, based on counting clique and star motifs of order κ (Section D.1). Exploiting their behavior for smooth manifolds with integer dimension, these new classes of network quantifiers are consequently used for defining families of transitivity-based local and global dimensionality measures (Section D.2). The numerical estimation of these measures is discussed in Section D.3. Finally, we present first numerical results for paradigmatic model systems (Section D.4). Concluding remarks including a conjecture on the relationship between clustering and transitivity dimensions of different orders κ are given in Section D.5.

D.1. Higher-order clustering and transitivity

The standard (local and global) clustering coefficient and global transitivity measure locally or globally the density of triangles within a simple and undirected complex network described by a symmetric adjacency matrix $\mathbf{A} = \{A_{ij}\}_{ij}$. Triangles are cliques of order 3 (3-cliques), *i.e.*, fully connected subgraphs of 3 vertices. A more restrictive notion of clustering is obtained when measuring the local or global density of κ-cliques (fully connected subgraphs of κ nodes, see Fig. D.1). This straightforward generalization of the standard idea of clustering in networks induces a spectrum of local and global κ-clustering coefficients as well as κ-transitivities. These are distinct from other generalized clustering measures which were proposed earlier, *e.g.*, considering the density of loops of different length keeping in mind that triangles are loops of length 3 (Boccaletti et al., 2006).
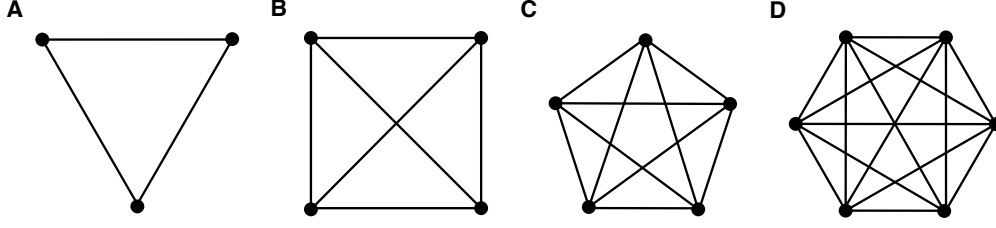
Figure D.1.: Cliques of orders (A) $\kappa = 3$, (B) $\kappa = 4$, (C) $\kappa = 5$, and (D) $\kappa = 6$.

D.1.1. Local κ-clustering coefficient

Let Z_v^κ be the number of κ-cliques vertex v participates in, H_v^κ is the maximum possible number of κ-cliques. Then we define the *local κ-clustering coefficient*

$$\mathcal{C}_v^\kappa = \frac{Z_v^\kappa}{H_v^\kappa} = \frac{Z_v^\kappa}{\binom{k_v}{\kappa-1}}, \tag{D.1}$$

where k_v denotes the degree of v. For convenience, we set $\mathcal{C}_v^\kappa = 0$ for all v with $k_v < \kappa - 1$. This implies the bounds $0 \leq \mathcal{C}_v^\kappa \leq 1$. Obviously, the local κ-clustering coefficient and all further measures given below are neither meaningful nor instructive for orders $\kappa < 3$. In the following we give explicit formulae for calculating some low-order κ-clustering coefficients. Here $\mathcal{N}_v$ denotes the set of neighbors of vertex v and N the total number of vertices in the network.

$\kappa = 3$ (Standard local clustering coefficient)

$$\mathcal{C}_v^3 = \frac{\frac{1}{2!} \sum_{i,j \in \mathcal{N}_v} A_{ij}}{\binom{k_v}{2}} \tag{D.2}$$

with $\mathcal{C}_v^3 = 0 \ \forall k_v < 2$.

$\kappa = 4$

$$\mathcal{C}_v^4 = \frac{\frac{1}{3!} \sum_{i,j,k \in \mathcal{N}_v} A_{ij} A_{jk} A_{ki}}{\binom{k_v}{3}} \tag{D.3}$$

with $\mathcal{C}_v^4 = 0 \ \forall k_v < 3$.

$\kappa = 5$

$$\mathcal{C}_v^5 = \frac{\frac{1}{4!} \sum_{i,j,k,l \in \mathcal{N}_v} A_{ij} A_{jk} A_{kl} A_{li} A_{ik} A_{lj}}{\binom{k_v}{4}} \tag{D.4}$$

with $\mathcal{C}_v^5 = 0 \ \forall k_v < 4$.

$\kappa = 6$

$$\mathcal{C}_v^6 = \frac{\frac{1}{5!} \sum_{i,j,k,l,m \in \mathcal{N}_v} A_{ij} A_{ik} A_{il} A_{im} A_{jk} A_{jl} A_{jm} A_{kl} A_{km} A_{lm}}{\binom{k_v}{5}} \tag{D.5}$$

with $\mathcal{C}_v^6 = 0 \; \forall k_v < 5$.

D.1.2. Global κ-clustering

The *global κ-clustering coefficient* $\mathcal{C}^\kappa$ is defined as the average taken over all local κ-clustering coefficients,

$$\mathcal{C}^\kappa = \langle \mathcal{C}_v^\kappa \rangle_{v \in V} . \tag{D.6}$$

We can easily derive the expectation values $\mathbb{E}(\mathcal{C}^\kappa)$ for fully random networks (Erdős-Rényi graphs (Erdős and Rényi, 1959)) given the probability q of edges to exist independently of each other. Studying this simple network ensemble allows to gain an impression of the expected magnitudes of $\mathcal{C}^\kappa$ for different orders κ in other types of networks as well.

The global κ-clustering coefficient essentially gives the mean probability that $\binom{\kappa-1}{2}$ edges exist between $\kappa - 1$ vertices in the first neighborhood of a vertex. For the Erdős-Rényi model the expectation value is then

$$\mathbb{E}(\mathcal{C}^\kappa) = q^{\binom{\kappa-1}{2}} = q^{(\kappa-1)(\kappa-2)/2}, \tag{D.7}$$

since edges are fully independent. This yields $\mathbb{E}(\mathcal{C}^3) = q$, $\mathbb{E}(\mathcal{C}^4) = q^3$, $\mathbb{E}(\mathcal{C}^5) = q^6$, $\mathbb{E}(\mathcal{C}^6) = q^{10} \ldots$. Hence, the expectation value $\mathbb{E}(\mathcal{C}^\kappa)$ decreases faster than exponentially with increasing order κ implying that higher-order cliques are unlikely to be observed in finite fully random networks. Conversely it highlights that non-zero values of $\mathcal{C}^\kappa$ are to be considered as noteworthy in empirical networks for larger κ.

D.1.3. κ-transitivity

κ-transitivity counts the global density of κ-cliques within a network. It is defined as

$$\mathcal{T}^\kappa = \frac{\kappa \times \text{Number of cliques of } \kappa \text{ nodes}}{\text{Number of stars of } \kappa \text{ nodes}} \tag{D.8}$$

and is normalized to $0 \leq \mathcal{T}^\kappa \leq 1$. The factor κ in the nominator is introduced here to correct for the fact that each κ-clique implies the presence of κ distinct κ-stars in the network. It is important to note that this definition requires that the motifs counted must be only subgraphs of the network under study, they do not need to be induced subgraphs. For example, this ensures that for each κ-clique, the number of associated κ-stars is correctly counted as κ.

Considering the expectation values $\mathbb{E}(\mathcal{T}^\kappa)$ for Erdős-Rényi graphs one can show that $\mathbb{E}(\mathcal{T}^\kappa) = \mathbb{E}(\mathcal{C}^\kappa) = q^{(\kappa-1)(\kappa-2)/2}$ by similar arguments as those given above. We now list explicit formulae for calculating some low-order κ-transitivities.

$\kappa = 3$ **(Standard transitivity)**

$$\mathcal{T}^3 = \frac{\sum_{v,i,j \in V} A_{vi} A_{ij} A_{jv}}{\sum_{v,i,j \in V} A_{vi} A_{vj}} \tag{D.9}$$

$\kappa = 4$

$$\mathcal{T}^4 = \frac{\sum_{v,i,j,k \in V} A_{vi} A_{vj} A_{vk} A_{ij} A_{ik} A_{jk}}{\sum_{v,i,j,k \in V} A_{vi} A_{vj} A_{vk}} \tag{D.10}$$

$\kappa = 5$

$$\mathcal{T}^5 = \frac{\sum_{v,i,j,k,l \in V} A_{vi} A_{vj} A_{vk} A_{vl} A_{ij} A_{ik} A_{il} A_{jk} A_{jl} A_{kl}}{\sum_{v,i,j,k,l \in V} A_{vi} A_{vj} A_{vk} A_{vl}} \tag{D.11}$$

D.2. Higher-order local clustering and transitivity dimensions

D.2.1. Behavior for smooth manifolds

In spatially embedded networks such as recurrence networks or random geometric graphs, due to spatial clustering of points particularly in high density regions (see also Section 4.3.2), $\mathcal{C}_v^\kappa$, $\mathcal{C}^\kappa$, and $\mathcal{T}^\kappa$ are expected to be significantly larger than for typical fully random Erdős-Rényi graphs with the same edge density. Indeed, analogously to the derivations carried out in Donner et al. (2011b, P15), it can be shown that the expectation values for recurrence networks constructed by drawing randomly from smooth manifolds S of integer dimension d associated with a smooth associated probability density p are given by

$$\mathbb{E}(\mathcal{C}_v^\kappa) = \mathbb{E}(\mathcal{C}^\kappa) = \mathbb{E}(\mathcal{T}^\kappa) = \left(\frac{\kappa}{2^{\kappa-1}}\right)^d \tag{D.12}$$

independently of the recurrence threshold ε, when using the supremum norm for measuring distances between points (*e.g.*, state vectors) $x \in S$. The leading term in this expression for random geometric graphs on d-dimensional smooth manifolds is $(1/2)^{d\kappa}$ which for increasing κ decays more slowly than the corresponding leading term q^{κ^2} for Erdős-Rényi graphs. For $\kappa = 3$, one obtains the expectation value $(3/4)^d$ that has been reported earlier (Section 3.2.2, Donner et al. (2010c, P19); Donner et al. (2011b, P15)).

Similarly to the continuous ε-motif densities introduced in Section 4.2.3, continuous versions of the higher-order transitivity-based measures $\mathcal{C}_v^\kappa$, $\mathcal{C}^\kappa$, and $\mathcal{T}^\kappa$ from Section D.1 can be constructed. For these continuous measures, which are not shown here for brevity, Eq. (D.12) would hold exactly, not just on average (see also Donner et al. (2011b, P15)). In line with the general treatment in Chapter 4, $\mathcal{C}_v^\kappa$, $\mathcal{C}^\kappa$, and $\mathcal{T}^\kappa$ can then be viewed as discrete estimators of their continuous equivalents.

D.2.2. Higher-order local clustering dimensions

Analogously to the case $\kappa = 3$ discussed in Section 3.2.2, a *single scale local κ-clustering dimension* can be defined as

$$\hat{D}_{\mathcal{C}^\kappa,v}(\varepsilon) = \frac{\log\left(\mathcal{C}_v^\kappa(\varepsilon)\right)}{\log\left(\frac{\kappa}{2^{\kappa-1}}\right)} \tag{D.13}$$

for a fixed scale ε, order κ, and vertex v. Here, and in the following, hats $\hat{D}$ are used to distinguish the discrete estimators presented from the true underlying dimensionalities based on continuous versions of $\mathcal{C}_v^\kappa$, $\mathcal{C}^\kappa$, and $\mathcal{T}^\kappa$ (see Donner et al. (2011b, P15) for details).

While $\mathbb{E}(\hat{D}_{\mathcal{C}^\kappa,v}(\varepsilon)) = d$ for smooth d-dimensional manifolds S independently of the scale ε, self-similarities in the set of interest, *e.g.*, a strange attractor, can lead to oscillations in $\hat{D}_{\mathcal{C}^\kappa,v}(\varepsilon)$ with changing ε (Section 3.2.2 and Donner et al. (2011b, P15)). Hence, for fully characterizing the set under study it is necessary to introduce an *upper local κ-clustering dimension*

$$\hat{D}_{\mathcal{C}^\kappa,v}^u = \max_{\varepsilon\in\mathcal{E}} \hat{D}_{\mathcal{C}^\kappa,v}(\varepsilon) \tag{D.14}$$

together with a *lower local κ-clustering dimension*

$$\hat{D}_{\mathcal{C}^\kappa,v}^l = \min_{\varepsilon\in\mathcal{E}} \hat{D}_{\mathcal{C}^\kappa,v}(\varepsilon). \tag{D.15}$$

$\mathcal{E}$ is a set of appropriately chosen recurrence thresholds ε, *i.e.*, covering at least one oscillation of $\hat{D}_{\mathcal{C}^\kappa,v}(\varepsilon)$ at as small as possible scales ε where lack of neighbors (too small edge densities) is not yet a problem (see Donner et al. (2011b, P15) for details).

D.2.3. Higher-order transitivity dimensions

Similarly, a global *single scale κ-transitivity dimension* can be defined as

$$\hat{D}_{\mathcal{T}^\kappa}(\varepsilon) = \frac{\log\left(\mathcal{T}^\kappa(\varepsilon)\right)}{\log\left(\frac{\kappa}{2^{\kappa-1}}\right)} \tag{D.16}$$

for a fixed scale ε and order κ. For the same reasons that were mentioned in Section D.2.2 (see Fig. D.2), a more representative measurement of the global (fractal) dimensionality of the set under study is provided by the *upper κ-transitivity dimension*

$$\hat{D}_{\mathcal{T}^\kappa}^u = \max_{\varepsilon\in\mathcal{E}} \hat{D}_{\mathcal{T}^\kappa}(\varepsilon) \tag{D.17}$$

and the *lower κ-transitivity dimension*

$$\hat{D}_{\mathcal{T}^\kappa}^l = \min_{\varepsilon\in\mathcal{E}} \hat{D}_{\mathcal{T}^\kappa}(\varepsilon). \tag{D.18}$$

D.3. Numerical estimation

A very simple algorithm for computing the local κ-clustering coefficient is to traverse over all vertices and check for existing edges between all groups of $\kappa - 1$ neighbors (see Schank and Wagner (2005) for a discussion of the standard local 3-clustering coefficient). For a vertex of degree k_v there are $\binom{k_v}{\kappa-1} \sim k_v^{\kappa-1}$ such groups with each $\binom{\kappa-1}{2}$ edges to check for. Hence, the running time of this algorithm for computing $\mathcal{C}_v^\kappa$ for all $v \in V$ is

$$\mathcal{O}\left(N \max_{v \in V}(k_v)^{\kappa-1}\binom{\kappa-1}{2}\right) \subset \mathcal{O}\left(N^\kappa \binom{\kappa-1}{2}\right). \tag{D.19}$$

The associated algorithms for calculating the global κ-clustering coefficient $\mathcal{C}^\kappa$ and κ-transitivity $\mathcal{T}^\kappa$ have the same running time.

Since the running time of the simple algorithm grows exponentially with κ it is impractical for computing higher-order local clustering and global transitivity dimensions for the large N needed for a reliable estimation of these quantities. More efficient algorithms and approximation procedures are available to circumvent this problem (Schank and Wagner, 2005; Wernicke and Rasche, 2006). In Section D.4, an algorithm for approximating the numbers of motifs embedded in a network that has been proposed by Wernicke and Rasche (2006) is used for estimating transitivity dimensions. In contrast, local clustering dimensions are estimated using the simple algorithm described above. Further work is needed to optimize the numerical estimation of clustering and transitivity dimensions, particularly for rendering the study of $\kappa \geq 4$ practical in the future.

D.4. Results

D.4.1. Generalized baker's map

For consistency with Section 3.2.2 and Donner et al. (2011b, P15), we study the global transitivity dimensions for $\kappa = 3, 4$ in the case of the prototypical generalized baker's map (Eq. (3.12)). Results for larger κ are not yet available due to computational limitations (see Section D.3). $\hat{D}_{\mathcal{T}^3}(\varepsilon)$ and $\hat{D}_{\mathcal{T}^4}(\varepsilon)$ behave consistently for varying ε (Fig. D.2), both showing a maximum close to $\varepsilon = 0.01$. In both cases, this maximum is most likely part of an oscillatory pattern akin to that displayed in Fig. 3.4. Notably, the variations of $\hat{D}_{\mathcal{T}^4}(\varepsilon)$ (Fig. D.2B) appear more noisy than those of $\hat{D}_{\mathcal{T}^3}(\varepsilon)$ (Fig. D.2A). This effect is due to the comparably much lower expected number of 4-cliques as compared to that of 3-cliques (see above) resulting in a larger variance of $\hat{D}_{\mathcal{T}^4}(\varepsilon)$.

Similarly, $\hat{D}_{\mathcal{T}^3}^{u,l}$ and $\hat{D}_{\mathcal{T}^4}^{u,l}$ vary comparably when changing the control parameter α (Fig. D.3). In both cases, the upper κ-transitivity dimensions tend to increase with growing α which is consistent with the behavior of the frequently studied Rényi dimensions D_0 (box-counting dimension), D_1 (information dimension), and D_2
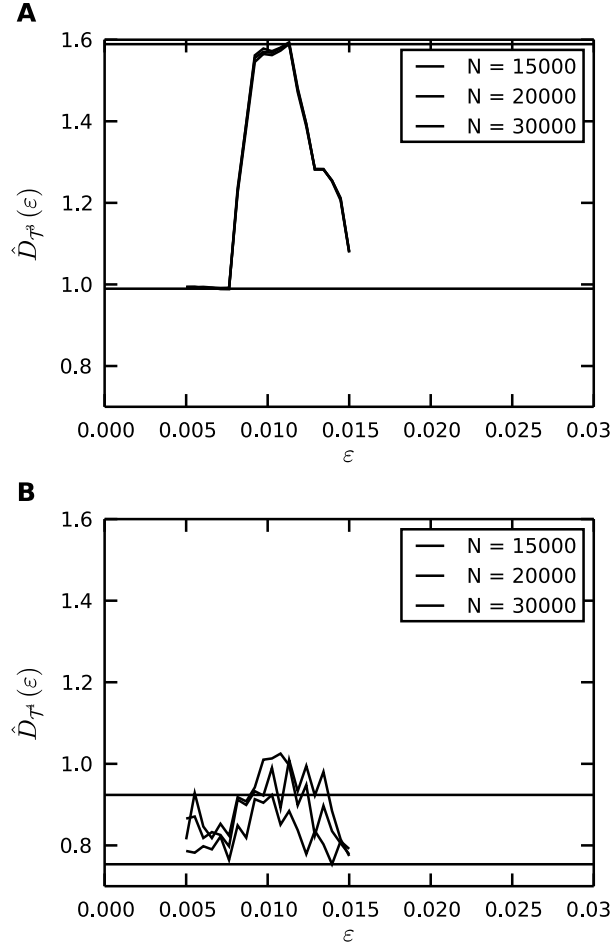
Figure D.2.: Estimation of the higher-order transitivity dimensions (A) $\hat{D}_{\mathcal{T}^3}^{u,l}$ and (B) $\hat{D}_{\mathcal{T}^4}^{u,l}$ for the generalized baker's map (Eq. (3.12)) at $\alpha = 1/2$ and $\lambda_a = \lambda_b = 1/4$ for different N. Dashed horizontal lines indicate numerical estimates of $D_{\mathcal{T}}^{u,l}$ obtained with $N = 30,000$ data points at small ε.

(correlation dimension). In contrast, the corresponding lower κ-transitivity dimensions appear to be independent of α. For the same reasons as elaborated in the previous paragraph, the results for $\kappa = 4$ (Fig. D.3B) show a higher noise level than those for $\kappa = 3$ (Fig. D.3A).

D.4.2. Rössler system

While for the generalized baker's map, the local clustering dimensions $\hat{D}^{u,l}_{\mathcal{C}^\kappa,v}$ can be theoretically shown to be constant for all points on the attractor (Donner et al., 2011b, P15), the Rössler system

$$\frac{d}{dt}(x, y, z) = (-y - z, x + ay, b + z(x - c)) \tag{D.20}$$

offers a richer structure in phase space.

It was shown earlier that the local 3-clustering coefficient $\mathcal{C}^3_v$ allows to detect unstable periodic orbits (UPOs) in recurrence networks of dynamical systems (Donner et al., 2010c, P19). This is because the local convergence of trajectories leads to a clustering of state vectors along these lower-dimensional objects. Similarly, local κ-clustering dimensions allow to trace UPOs of the Rössler system (Fig. D.4). Only the lower local clustering dimensions $\hat{D}^l_{\mathcal{C}^\kappa,v}$ are shown, because the estimation of $\hat{D}^u_{\mathcal{C}^\kappa,v}$ is complicated by $\mathcal{C}_v(\varepsilon) = 0$ (leading to $\hat{D}^u_{\mathcal{C}^\kappa,v} \to \infty$ for most v) occuring frequently for some ε due to the finite number of samples N.

The expectation is that higher-order local κ-clustering dimensions should highlight UPOs embedded within the attractor more sharply, because tight κ-clustering is very unlikely except close to UPOs where trajectories converge. One cannot see this effect very clearly for the examples presented here (Fig. D.4), but this is most likely due to the relatively small N that has been chosen for computational reasons. Furthermore, it is notable that in the considered example the median of the estimated lower local κ-clustering dimensions increases with growing κ: median($\hat{D}^l_{\mathcal{C}^3,v}$) = 1.28 < median($\hat{D}^l_{\mathcal{C}^4,v}$) = 1.41 < median($\hat{D}^l_{\mathcal{C}^5,v}$) = 1.53. For comparison, the median of the upper local 3-clustering dimensions is median($\hat{D}^u_{\mathcal{C}^3,v}$) = 2.63.
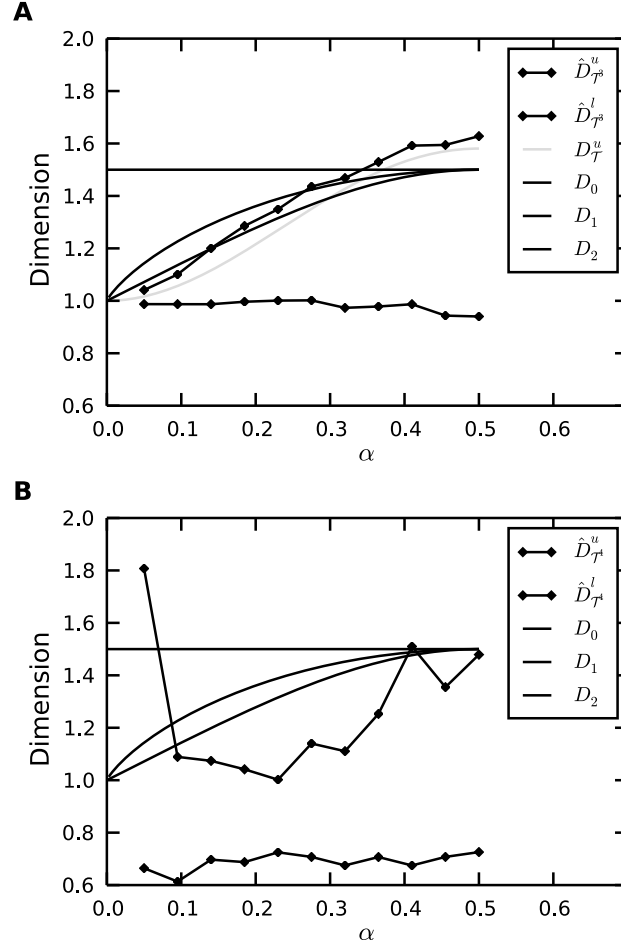
Figure D.3.: Dependence of several global measures of dimensionality on the parameter α ($\lambda_a = \lambda_b = 1/4$) of the generalized baker's map (Eq. (3.12)): Upper and lower transitivity dimensions (A) $\hat{D}_{\mathcal{T}^3}^{u,l}$, (B) $\hat{D}_{\mathcal{T}^4}^{u,l}$, and Rényi dimensions $D_{0,1,2}$. One realization has been considered for each value of α. The gray line in (A) corresponds to an analytically calculated lower bound of $D_{\mathcal{T}^3}^u$. Numerical estimates have been obtained with $N = 15,000$ data points using 50 equidistantly spaced recurrence thresholds ε in the range $[0.001, 0.015]$, and results are robust for various choices of N (Fig. D.2).
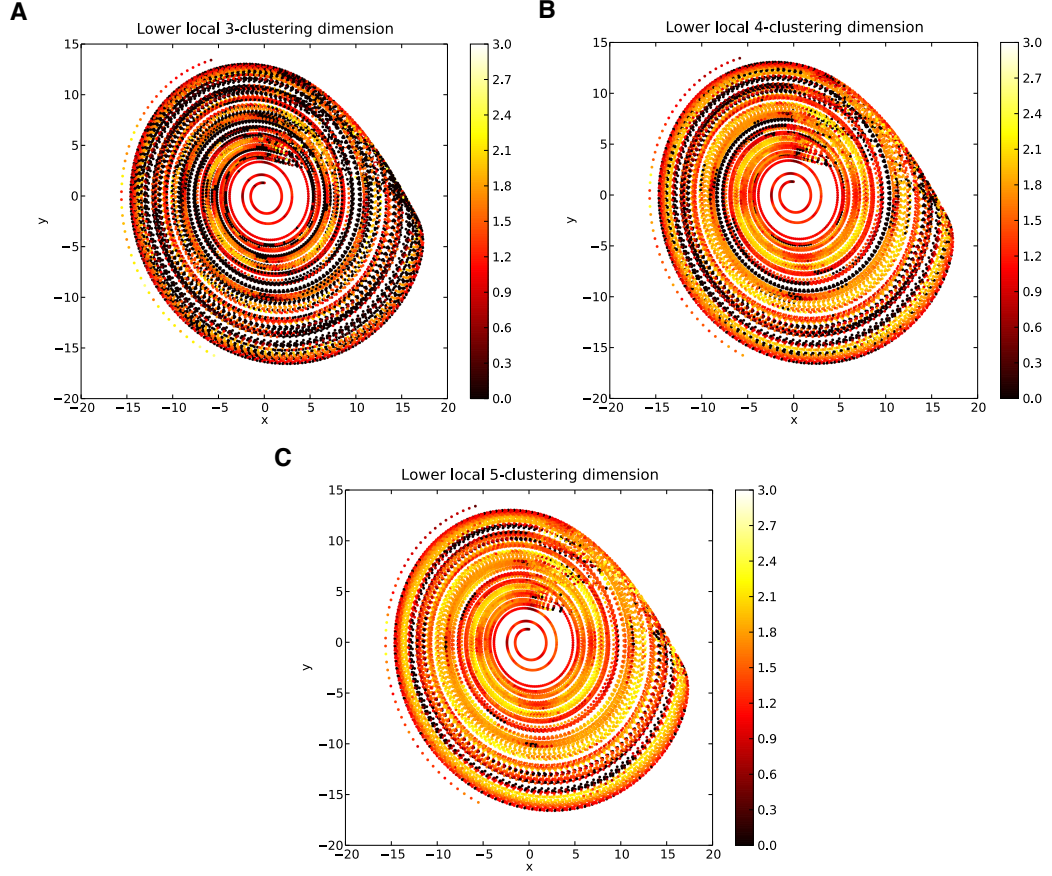
Figure D.4.: Lower local κ-clustering dimensions (A) $\hat{D}^l_{\mathcal{C}^3,v}$, (B) $\hat{D}^l_{\mathcal{C}^4,v}$, and (C) $\hat{D}^l_{\mathcal{C}^5,v}$ for the Rössler system (Eq. (D.20)) with $a = 0.15$, $b = 0.2$, and $c = 10$, shown in a projection to the x-y coordinate plane. The equations were integrated with a sampling time $\Delta T = 0.05$, where a transient of $1,000$ samples was excluded. For constructing the recurrence networks from $N = 15,000$ samples we used original coordinates (no embedding), the supremum norm, and 50 equidistantly spaced recurrence thresholds ε in the range $[0.1, 1.0]$. Vertices (state vectors) with $\hat{D}^l_{\mathcal{C}^\kappa,v} > 3$ are not shown (these values can arise in low density regions of phase space due to finite size effects or in certain exceptional geometries (Donner et al., 2011b, P15)).

D.5. Discussion

It is tempting to conjecture that the upper and lower local κ-clustering and κ-transitivity dimensions defined above should be subject to inequalities similar to those governing the behavior of Rényi dimensions D_q, *i.e.*, $D_q \geq D_{q'}$ for all $q \leq q'$ (Hentschel and Procaccia, 1983). For example, the relationship $D_{\mathcal{T}^\kappa}^{u,l} \geq D_{\mathcal{T}^{\kappa'}}^{u,l}$ for all $\kappa \leq \kappa'$ is conceivable with regard to Fig. D.3. However, the numerical results presented in this appendix are clearly insufficient to draw any conclusions on this matter. Further theoretical work and substantial numerical simulations are needed to address the conjecture.

Appendix E.

Contemplating coincidences

. . .for the "one chance in a million" will undoubtedly occur, with no less and no more than its appropriate frequency, however surprised we may be that it should occur to us.

Ronald A. Fisher (1937, p. 16)

E.1. Problem setting

We are concerned with the statistical problem of testing for coincidences of two distinct types of events: (i) shifts in climate (C-events) and (ii) the appearance and disappearance of species in the fossil record (S-events). Consider a record of N S-events $S_1, \ldots, S_N$ and M C-events $C_1, \ldots, C_M$ over a time period T, where both sequences are not necessarily ordered chronologically. A single coincidence occurs if an S-event falls within the temporal tolerance window of a C-event, *i.e.*, $|t_S - t_C| \leq \Delta T$, where t_S and t_C denote the timing of both events (Fig. E.1).

Assume that we observe in our record K_e single coincidences. Given these findings and considering the uncertainties in the timing of both types of events as well as the inherent incompleteness of the fossil record we ask the following questions: Are the observed numbers of coincidences likely to have arisen by pure chance? Can we derive a significance test by combinatorial reasoning?

E.2. Statistical null model

Our null hypothesis is that both S- and C-events are distributed randomly, independently and uniformly over the time interval T. Furthermore, we assume that $\Delta T \ll T/M \ll T$. Based on these assumptions, the probability of a specific S-event S_i falling into the tolerance window of a specific C-event C_j is

$$p = 2\frac{\Delta T}{T}. \tag{E.1}$$

Figure E.1.: Schematic representation of C-events (black vertical lines) and S-events (blue vertical lines). Red horizontal bars of length $2\Delta T$ centered around C-events indicate coincidences of one or more S-events with one C-event. This leads to $K_e = 4$ coincidences in this example.

Then the probability of a specific S-event S_i coinciding with *at least one* of the M C-events is given by

$$1 - (1-p)^M = 1 - \left(1 - 2\frac{\Delta T}{T}\right)^M . \tag{E.2}$$

Now we are in a position to compute the probability $P(K; N, 1-(1-p)^M)$ that exactly K single coincidences are observed for a given realization of the fully random null model. Since S-events are assumed to be distributed independently in the interval $[0, T]$, $P(K; N, 1-(1-p)^M)$ is the binomial distribution with N trials and success probability $1 - (1-p)^M$ (Jaynes and Bretthorst, 2003) yielding

$$P(K; N, 1-(1-p)^M) = \binom{N}{K} \left(1 - \left(1 - 2\frac{\Delta T}{T}\right)^M\right)^K \left(\left(1 - 2\frac{\Delta T}{T}\right)^M\right)^{N-K} . \tag{E.3}$$

From this distribution (Eq. (E.3)) we easily derive the expectation value $\langle K \rangle$ and standard deviation $\sigma(K)$ as

$$\langle K \rangle = N \left(1 - (1-p)^M\right) = N \left(1 - \left(1 - 2\frac{\Delta T}{T}\right)^M\right) \tag{E.4}$$

and

$$\sigma(K) = \sqrt{N \left(1 - (1-p)^M\right)(1-p)^M}$$

$$= \sqrt{N \left(1 - \left(1 - 2\frac{\Delta T}{T}\right)^M\right)\left(1 - 2\frac{\Delta T}{T}\right)^M} . \tag{E.5}$$

Table E.1.: Timing of climate shifts identified by recurrence network analysis (see Chapter 6) and related paleoenvironmental change.

Timing (Myr BP)	Paleoenvironmental change
3.50	Appearance of lakes in EARS
2.95	Disappearance of large lakes in EARS
2.25	Reorganization of Walker circulation (beginning)
1.60	Reorganization of Walker circulation (end)
1.10	Mid-Pleistocene transition (beginning)
0.70	Mid-Pleistocene transition (end)

The p-value of an observation K_e with respect to the test distribution (Eq. (E.3)), *i.e.*, the probability to obtain a number of coincidences K larger or equal to the empirically observed number K_e, is then given by

$$P(K \geq K_e) = \sum_{K^*=K_e}^{N} P(K^*; N, 1 - (1-p)^M). \tag{E.6}$$

E.3. Application

The record of interest for the case study presented in Chapter 6 and Donges et al. (2011c, P10) spans a time period of $T = 5$ Myr and contains $M = 6$ climate shifts (C-events) as well as $N = 2 \times 18 + 1 = 37$ S-events (note that *Homo sapiens* is not extinct yet). In Fig. 6.2, significant shifts in African climate (C-events) are marked by the upper and lower bounds of the gray bars spanning all data and results shown. Coincidences with the time of species appearance and disappearance (S-events) considering a temporal tolerance of $\Delta T = 0.1$ Myr are marked by red bars.

The C-events occur at approximately 3.5, 2.95, 2.25, 1.6, 1.1, and 0.7 Myr BP (Table E.1) according to recurrence network analysis (Chapter 6 and Donges et al. (2011c, P10)), while the timings of all considered S-events are listed in Table E.2. Given a tolerance $\Delta T = 0.1$ Myr, we observe $K_e = 15$ single coincidences (Fig. 6.2). This particular choice of the tolerance parameter ΔT is motivated by (i) the fact that the timings of most of the considered C- and S-events have been rounded to the first decimal point prior to the analysis, and (ii) uncertainties in dating of the analyzed dust flux records, the detected climate shifts and hominin fossils which can be assumed to be roughly of this order.

We now aim to quantify the significance of the observed number of coincidences K_e with respect to the null model formulated above, *i.e.*, assuming that both C- and S-events are distributed uniformly and independently within the time interval of interest. The null model yields an expected number of $\mathbb{E}(K) = 8.0$ coincidences with the standard deviation $\sigma(K) = 2.5$ and the empirical observation corresponding to a

A

B
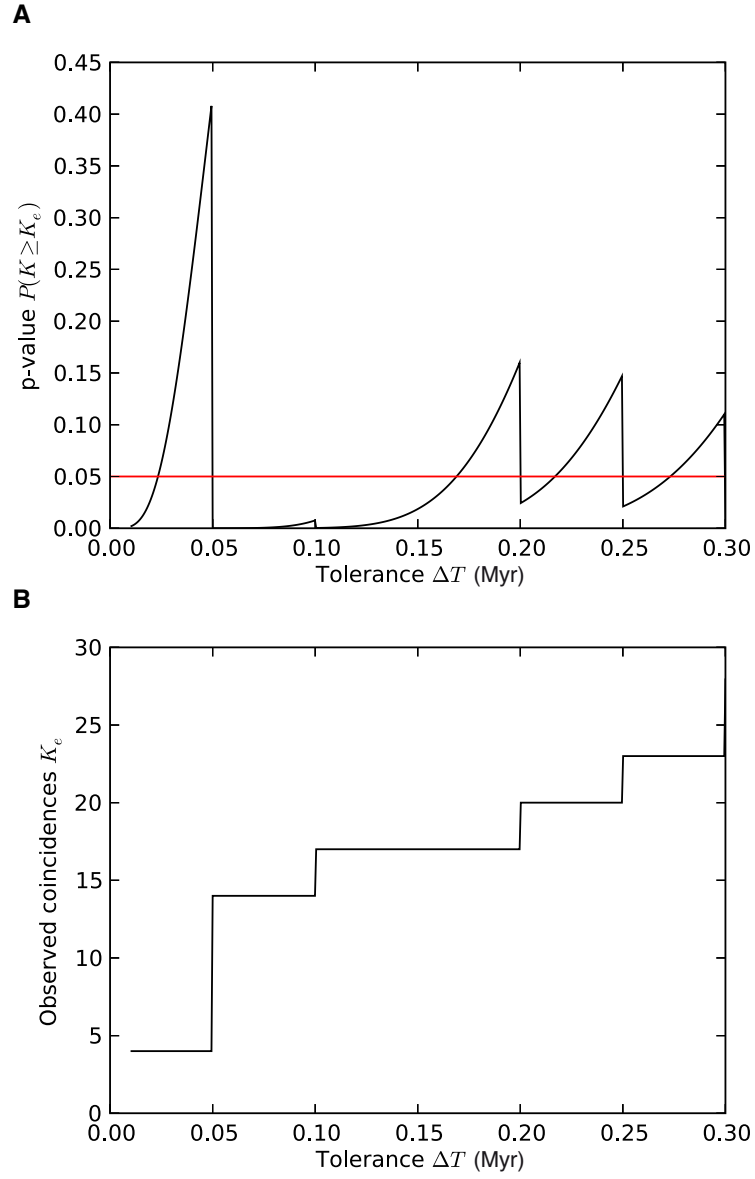
Figure E.2.: (A) p-values $P(K \geq K_e)$ of the (B) observed number of coincidences K_e for varying tolerance parameter ΔT. We consider the results to be significant if the p-value is smaller than the commonly chosen significance level of 0.05 (red horizontal line).

Table E.2.: Times of the appearance and disappearance of hominin species from the known fossil record taken from Trauth et al. (2007), based on Bromage et al. (1995); Kimbel et al. (1996); Reed (1997); White (2002); Dunsworth and Walker (2002); McHenry (2002); Antón and Swisher (2004); White et al. (2006). The timing of most of these evolutionary S-events has been rounded to the first decimal point.

Species	Appearance (Myr BP)	Disappearance (Myr BP)
Ardipithecus ramidus	4.55	4.40
Australopithecus anamensis	4.20	3.90
Kenyanthropus platyops	3.55	3.45
Australopithecus afarensis	3.60	2.90
Australopithecus bahrelghazali	3.55	3.45
Australopithecus africanus	3.00	2.50
Australopithecus garhi	2.55	2.50
Paranthropus aethiopicus	2.50	2.30
Paranthropus boisei	2.30	1.40
Homo habilis	2.30	1.60
Homo rudolfensis	2.30	1.60
Paranthropus robustus	1.90	1.10
Homo ergaster	1.90	1.00
Homo erectus	1.90	0.30
Homo antecessor	0.90	0.70
Homo heidelbergensis	0.60	0.10
Homo neanderthalensis	0.30	0.05
Homo floresiensis	0.10	0.05
Homo sapiens	0.16	n/a

p-value of $P(K \geq K_e) = 0.003$. The change of p-values $P(K \geq K_e)$ and the observed number of coincidences K_e with varying tolerance ΔT is shown in Fig. E.2.

E.4. Discussion

Our analysis reveals that the observed number of coincidences is robustly significant with p-values $P(K \geq K_e) \ll 0.05$ for a range of tolerance parameters $0.05 \leq \Delta T \leq 0.17$ with respect to the fully random null model (Fig. E.2A). Considerably larger ΔT do not meet the basic assumption $\Delta T \ll T/M \ll T$ any more. In this sense the analysis supports a statement like: *The observed coincidences between detected climate shifts and the appearance or disappearance of hominin species are unlikely to arise by chance* (Chapter 6 and Donges et al. (2011c, P10)). We should emphasize here that coincidence alone, like correlation, does not imply causality (deMenocal, 1995). It can only serve as a hint at a possible causal relationship.

Note that it is known that the appearance and/or disappearance of different species is typically correlated. This effect is not included in the null model, but could be assessed with the help of more sophisticated Monte Carlo simulations. The proposed null model should be seen as the simplest possible quantitative means to justify

discussing the influence of Plio-Pleistocene climate change on hominin evolution in the first place.

The presented statistical analysis assumes that the life spans of hominin species are approximated by the times to which their known fossils are dated, an assumption which is also routinely relied upon in the reconstruction of hominin evolutionary trees or dispersal patterns (Strait and Wood, 1999). Minor dating uncertainties and fossil sampling effects are covered by the tolerance parameter ΔT. However, as is always the case in paleontological research, new fossil evidence may dramatically alter the current view of events in hominin evolution summarized in Table E.2 (Strait and Wood, 1999). Furthermore, taphonomic biases and sampling effects may play a significant role (deMenocal, 1995). Given new evidence, the proposed statistical framework will allow future investigators to quickly evaluate the significance of observed coincidences between C- and S-events. The same is true if the timing or number of climate shifts were to be revised. Our null model could moreover prove useful to test and compare other hypotheses relating changes in climate to evolutionary events.

Finally it is important to stress that the proposed significance test is asymmetric with respect to C- and S-events which is mathematically expressed by the fact that Eq. (E.3) is asymmetric with respect to the numbers of events M and N. Above we were concerned with the clustering of S-events around C-events, thereby implicitly testing for a potential causal influence of C-events on S-events and *not* vice versa. Considering the research question under study this seems reasonable, since humans are not thought to have had a significant influence on continental and larger-scale climate change before a few thousand years ago (see, *e.g.*, the early anthropogenic hypothesis (Ruddiman, 2007)).

E.5. Related measures and concepts

The observed number of coincidences can be written as

$$K_e = \sum_{i=1}^{N} \sum_{j=1}^{M} \Theta \left(\Delta T - |t_i^S - t_j^C| \right), \tag{E.7}$$

where $\{t_i^S\}_{i=1}^N$ and $\{t_j^C\}_{j=1}^M$ are the timings of S- and C-events, respectively. This formulation highlights that K_e and coincidence analysis as a whole are closely related to certain measures of event synchronization (Kreuz et al., 2007), the cross-recurrence rate of recurrence quantification analysis (Marwan et al., 2007), and Ripley's cross-K from spatial statistics measuring the correlation of spatial point processes (Dixon, 2006). Consequently, the proposed significance test could be applied to those concepts as well, given that the requirements and basic assumptions described above are met. Finally, it should be noted that the statistical and mathematical literature contains a large number of less closely related studies of coincidences, *e.g.*, concidering the *birthday problem* (Diaconis and Mosteller, 1989).

Appendix F.

Software and implementation

The results presented in this thesis rely heavily on numerical computations. For this purpose, the software package `pyunicorn` (Donges et al., 2008-2012) written in the object oriented programing language `Python` (Rossum and Drake, 2006) and embedded `C++` code was developed (pyunicorn: Pythonic unified complex network and recurrence analysis tool box). It implements the methods, measures, and algorithms described in Part I and the appendices. The package consists of three subpackages: (i) `pygeonetwork` for the general study and modeling of complex, possibly spatially embedded networks including interacting networks or networks of networks, (ii) `pyclimatenetwork` for constructing functional networks from time series data, and (iii) `pyrecurrence` for uni- and multivariate recurrence quantification (RQA) and recurrence network analysis as well as visibility graph analysis. `pyunicorn` partly relies on the following open source packages: `NumPy` (Oliphant, 2006), `SciPy` (Jones et al., 2011), `igraph` (Csárdi and Nepusz, 2006), `pysparse` (Geus and Arbenz, 2003; Bröker et al., 2005), `PyNio` (Schmidli et al., 2011; Brown et al., 2008), `netCDF-4` (Whitaker, 2012), `Matplotlib` (Hunter, 2007), `mpi4py` (Dalcín et al., 2011), and `progressbar` (Volpato, 2011). The package `pyunicorn` will be made available to the public as an open source package in the near future.

Partially parallelized numerical calculations were performed on the IBM iDataPlex Cluster and the visualization servers at the Potsdam Institute for Climate Impact Research as well as on Apple MacBook and Dell Latitude laptops using Linux and Mac OS X operating systems.

The figures displaying quantitative information throughout this thesis were created using the `Matplotlib` package and Matlab. Network visualizations were produced in `CGV` (Tominski et al., 2009), `GUESS` (Adar, 2006), and `Gephi` (Bastian et al., 2009). `Adobe Illustrator` was employed to compose all further illustrations.

Bibliography

Abarbanel, H.D.I. (1996). *Analysis of observed chaotic data*. Springer, New York.

Abe, S. and N. Suzuki (2004). "Scale-free network of earthquakes". In: *Europhysics Letters* 65.4, pp. 581–586. DOI: 10.1209/epl/i2003-10108-1.

Abramowitz, M. and I.A. Stegun (1964). *Handbook of mathematical functions*. U.S. Government Printing Office, Washington, DC.

Adar, E. (2006). "GUESS: A language and interface for graph exploration". In: *Proceedings of the SIGCHI Conference on Human Factors in Computing Systems (CHI)*. ACM. DOI: 10.1145/1124772.1124889.

Aitken, R. (1991). *The gateless barrier: The Wu-Men Kuan (Mumonkan)*. North Point Press, New York.

Albert, R. and A.L. Barabási (2002). "Statistical mechanics of complex networks". In: *Reviews of Modern Physics* 74.1, pp. 47–97. DOI: 10.1103/RevModPhys.74.47.

Alligood, K.T., T.D. Sauer, and J.A. Yorke (2000). *Chaos: An introduction to dynamical systems*. Springer, New York.

Anderssen, R.S., R.P. Brent, D.J. Daley, and P.A.P. Moran (1976). "Concerning $\int_0^1 \cdots \int_0^1 \sqrt{x_1^2 + \cdots + x_k^2} dx_1 \cdots dx_k$ and a Taylor series method". In: *SIAM Journal on Applied Mathematics* 30.1, pp. 22–30. DOI: 10.1137/0130003.

Andrews, D.G., J.R. Holton, and C.B. Leovy (1987). *Middle atmosphere dynamics*. Academic Press, San Diego.

Andrzejak, R.G., K. Lehnertz, F. Mormann, C. Rieke, P. David, and C.E. Elger (2001). "Indications of nonlinear deterministic and finite-dimensional structures in time series of brain electrical activity: Dependence on recording region and brain state". In: *Physical Review E* 64.6, 061907.

Antón, S.C. and C.C. Swisher (2004). "Early dispersals of Homo from Africa". In: *Annual Review of Anthropology* 33, pp. 271–296. DOI: 10.1146/annurev.anthro.33.070203.144024.

Arenas, A., A. Cabrales, A. Díaz-Guilera, R. Guimerà, and F. Vega-Redondo (2003). "Search and Congestion in Complex Networks". In: *Statistical Mechanics of Complex Networks*. Ed. by R. Pastor-Satorras, M. Rubi, and A. Díaz-Guilera. Vol. 625. Lecture Notes in Physics. Springer, Berlin, pp. 175–194.

Arenas, A., A. Díaz-Guilera, J. Kurths, Y. Moreno, and C.S. Zhou (2008). "Synchronization in complex networks". In: *Physics Reports* 469.3, pp. 93–153. DOI: 10.1016/j.physrep.2008.09.002.

Babu, P. and P. Stoica (2010). "Spectral analysis of nonuniformly sampled data – a review". In: *Digital Signal Processing* 20.2, pp. 359–378. DOI: 10.1016/j.dsp.2009.06.019.

Bailey, D.H., J.M. Borwein, and R.E. Crandall (2007). "Box integrals". In: *Journal of Computational and Applied Mathematics* 206.1, pp. 196–208. DOI: `10.1016/j.cam.2006.06.010`.

– (2010). "Advances in the theory of box integrals". In: *Mathematics of Computation* 79.271, pp. 1839–1866. DOI: `10.1090/S0025-5718-10-02338-0`.

Bailey, D.H., J.M. Borwein, V. Kapoor, and E.W. Weisstein (2006). "Ten problems in experimental mathematics". In: *American Mathematical Monthly* 113.6, pp. 481–509. DOI: `10.2307/27641975`.

Banerjee, A. (2011). "Probabilistic graphical models for climate data analysis". In: *Proceedings of the 2011 Workshop on Climate Knowledge Discovery (CKD '11)*. ACM, New York. DOI: `10.1145/2110230.2110235`.

Bang-Jensen, J. and G.Z. Gutin (2009). *Digraphs: Theory, algorithms and applications.* 2nd ed. Springer Monographs in Mathematics. Springer, London.

Barabási, A.L. and R. Albert (1999). "Emergence of scaling in random networks". In: *Science* 286.5439, pp. 509–512. DOI: `10.1126/science.286.5439.509`.

Barnett, L., E. Di Paolo, and S. Bullock (2007). "Spatially embedded random networks". In: *Physical Review E* 76.5, 056115. DOI: `10.1103/PhysRevE.76.056115`.

Barreiro, M., A. C. Marti, and C. Masoller (2011). "Inferring long memory processes in the climate network via ordinal pattern analysis." In: *Chaos* 21.1, 13101. DOI: `10.1063/1.3545273`.

Barreto, E., B. Hunt, E. Ott, and P. So (2008). "Synchronization in networks of networks: The onset of coherent collective behavior in systems of interacting populations of heterogeneous oscillators". In: *Physical Review E* 77.3, 036107. DOI: `10.1103/PhysRevE.77.036107`.

Barrio, R. and S. Serrano (2007). "A three-parametric study of the Lorenz model". In: *Physica D* 229.1, pp. 43–51. DOI: `10.1016/j.physd.2007.03.013`.

Barthélemy, M. (2011). "Spatial networks". In: *Physics Reports* 499.1-3, pp. 1–101. DOI: `10.1016/j.physrep.2010.11.002`.

Bartoli, G., M. Sarnthein, M. Weinelt, H. Erlenkeuser, D. Garbe-Schönberg, and D.W. Lea (2005). "Final closure of Panama and the onset of northern hemisphere glaciation". In: *Earth and Planetary Science Letters* 237.1-2, pp. 33–44. DOI: `10.1016/j.epsl.2005.06.020`.

Bashan, A., R. Parshani, and S. Havlin (2011). "Percolation in networks composed of connectivity and dependency links". In: *Physical Review E* 83.5, 051127. DOI: `10.1103/PhysRevE.83.051127`.

Bastian, M., S. Heymann, and M. Jacomy (2009). "Gephi: An open source software for exploring and manipulating networks". In: *International AAAI Conference on Weblogs and Social Media*.

Battista, G., P. Eades, R. Tamassia, and I.G. Tollis (1994). "Algorithms for drawing graphs: An annotated bibliography". In: *Computational Geometry: Theory and Applications* 4.5, pp. 235–282. DOI: `10.1016/0925-7721(94)00014-X`.

Becker, J. (2009). *Aus der Kölner Bucht: Gedichte.* Suhrkamp, Frankfurt am Main.

Berezin, Y., A. Gozolchiani, O. Guez, and S. Havlin (2012). "Stability of climate networks with time". In: *Nature Scientific Reports* 2, p. 666. DOI: `10.1038/srep00 666`.

Berger, W.H. and E. Jansen (1994). "Mid-Pleistocene climate shift – the Nansen connection". In: *The polar oceans and their role in shaping the global environment*. Ed. by O.M. Johannessen, R.D. Muench, and J.E. Overland. Vol. 85. Geophysical Monograph. American Geophysical Union, Washington, D.C., pp. 295–311.

Berkowitz, B. (1995). "Analysis of fracture network connectivity using percolation theory". In: *Mathematical Geology* 27.4, pp. 467–483. DOI: `10.1007/BF02084422`.

Bialonski, S., M.T. Horstmann, and K. Lehnertz (2010). "From brain to earth and climate systems: Small-world interaction networks or not?" In: *Chaos* 20.1, 013134. DOI: `10.1063/1.3360561`.

Bialonski, S., M. Wendler, and K. Lehnertz (2011). "Unraveling spurious properties of interaction networks with tailored random networks". In: *PLoS ONE* 6.8, e22826. DOI: `10.1371/journal.pone.0022826`.

Bloemendal, J. and P. deMenocal (1989). "Evidence for a change in the periodicity of tropical climate cycles at 2.4 Myr from whole-core magnetic susceptibility measurements". In: *Nature* 342.6252, pp. 897–900. DOI: `10.1038/342897a0`.

Boccaletti, S., J. Kurths, G. Osipov, D. L. Valladares, and C. S. Zhou (2002). "The synchronization of chaotic systems". In: *Physics Reports* 366.1-2, pp. 1–101. DOI: `10.1016/S0370-1573(02)00137-0`.

Boccaletti, S., V. Latora, Y. Moreno, M. Chavez, and D.U. Hwang (2006). "Complex networks: Structure and dynamics". In: *Physics Reports* 424.4-5, pp. 175–308. DOI: `10.1016/j.physrep.2005.10.009`.

Bonacich, P. (1972). "Factoring and weighing approaches to status scores and clique identification". In: *Journal of Mathematical Sociology* 2.1, pp. 113–120. DOI: `10.10 80/0022250X.1972.9989806`.

Bonanno, G., G. Caldarelli, F. Lillo, and R.N. Mantegna (2003). "Topology of correlation-based minimal spanning trees in real and model markets". In: *Physical Review E* 68.4, 046130. DOI: `10.1103/PhysRevE.68.046130`.

Bradley, R.S. (1999). *Paleoclimatology: Reconstructing climates of the Quaternary*. 2nd ed. Vol. 64. International Geophysics Series. Academic Press, San Diego.

Brandes, U. (2008). "On variants of shortest-path betweenness centrality and their generic computation". In: *Social Networks* 30.2, pp. 136–145. DOI: `10.1016/j.soc net.2007.11.001`.

Breitenbach, S.F.M., T. Kohn, and J.F. Donges (2009). "INSPEMO 2009: 6. bis 19. April 2009". In: *Speläoclub Berlin Newsletter* 62, pp. 1–3. ISSN: 1618-4785.

Breitenbach, S.F.M., J.F. Donges, B. Kharpran Daly, T. Kohn, and T. Kohn (2010). "Two sandstone caves on the southern edge of the Meghalaya Plateau, India". In: *Cave and Karst Science* 37.2, pp. 49–52.

Bretherton, C.S., C. Smith, and J.M. Wallace (1992). "An intercomparison of methods for finding coupled patterns in climate data". In: *Journal of Climate* 5.6, pp. 541–560. DOI: `10.1175/1520-0442(1992)005<0541:AIOMFF>2.0.CO;2`.

Bibliography

Brockwell, P.J. and R.A. Davies (1991). *Introduction to time series and forecasting.* 2nd ed. Springer, New York.

– (2002). *Time series: Theory and methods.* 2nd ed. Springer, New York.

Bröker, O., O. Chinellato, and R. Geus (2005). "Using Python for large scale linear algebra applications". In: *Future Generation Computer Systems* 21.6, pp. 969–979. DOI: 10.1016/j.future.2005.02.001.

Bromage, T.G., F. Schrenk, and F.W. Zonneveld (1995). "Paleoanthropology of the Malawi Rift: An early hominid mandible from the Chiwondo Beds, northern Malawi". In: *Journal of Human Evolution* 28.1, pp. 71–108. DOI: 10.1006/jhev.1995.1007.

Brown, D., M. Haley, F. Clare, D. Shea, and D. Middleton (2008). "Frameworks for geoscience data analysis and visualization". In: *Geophysical Research Abstracts* 10, EGU2008–A–06018.

Buldyrev, S.V., N.W. Shere, and G.A. Cwilich (2011). "Interdependent networks with identical degrees of mutually dependent nodes". In: *Physical Review E* 83.1, 016112. DOI: 10.1103/PhysRevE.83.016112.

Buldyrev, S.V., R. Parshani, G. Paul, H.E. Stanley, and S. Havlin (2010). "Catastrophic cascade of failures in interdependent networks". In: *Nature* 464.7291, pp. 1025–1028. DOI: 10.1038/nature08932.

Bullmore, E. and O. Sporns (2009). "Complex brain networks: Graph theoretical analysis of structural and functional systems". In: *Nature Reviews Neuroscience* 10, pp. 186–198. DOI: 10.1038/nrn2575.

Bullock, S., L. Barnett, and E.A. Di Paolo (2010). "Spatial embedding and the structure of complex networks". In: *Complexity* 16.2, pp. 20–28. DOI: 10.1002/cplx.20338.

Campisano, C.J. and C.S. Feibel (2007). "Connecting local environmental sequences to global climate patterns: Evidence from the hominin-bearing Hadar Formation, Ethiopia". In: *Journal of Human Evolution* 53.5, pp. 515–527. DOI: 10.1016/j.jhevol.2007.05.015.

Cane, M.A. and P. Molnar (2001). "Closing of the Indonesian seaway as a precursor to east African aridification around 3-4 million years ago". In: *Nature* 411.6834, pp. 157–162. DOI: 10.1038/35075500.

Capocci, A., V.D.P. Servedio, F. Colaiori, L.S. Buriol, D. Donato, S. Leonardi, and G. Caldarelli (2006). "Preferential attachment in the growth of social networks: The internet encyclopedia Wikipedia". In: *Physical Review E* 74.3, 036116. DOI: 10.1103/PhysRevE.74.036116.

Carpi, L.C., O.A. Rosso, P.M. Saco, and M.G. Ravetti (2011). "Analyzing complex networks evolution through information theory quantifiers". In: *Physics Letters A* 375.4, pp. 801–804. DOI: 10.1016/j.physleta.2010.12.038.

Chan, S.H.Y, R.V. Donner, and S. Lämmer (2011). "Urban road networks – spatial networks with universal geometric features? A case study on Germany's largest cities". In: *European Physical Journal B* 84.4, pp. 563–577. DOI: 10.1140/epjb/e2011-10889-3.

Chlouverakis, K.E. and J.C. Sprott (2005). "A comparison of correlation and Lyapunov dimensions". In: *Physica D* 200.1-2, pp. 156–164. DOI: `10.1016/j.physd.2004.10.006`.

Clark, P.U., D. Archer, D. Pollard, J.D. Blum, J.A. Rial, V. Brovkin, A.C. Mix, N.G. Pisias, and M. Roy (2006). "The middle Pleistocene transition: Characteristics, mechanisms, and implications for long-term changes in atmospheric pCO$_2$". In: *Quaternary Science Reviews* 25.23-24, pp. 3150 –3184. DOI: `10.1016/j.quascirev.2006.07.008`.

Clemens, S., W. Prell, D. Murray, G. Shimmield, and G. Weedon (1991). "Forcing mechanisms of the Indian Ocean monsoon". In: *Nature* 353.6346, pp. 720–725. DOI: `10.1038/353720a0`.

Clemens, S.C., D.W. Murray, and W.L. Prell (1996). "Nonstationary phase of the Plio-Pleistocene Asian monsoon". In: *Science* 274.5289, pp. 943–948. DOI: `10.1126/science.274.5289.943`.

Cohen, R. and S. Havlin (2010). *Complex networks: Structure, robustness and function*. Cambridge University Press, Cambridge.

Costa, L. da F., F.A. Rodrigues, G. Travieso, and P.R. Villas Boas (2007). "Characterization of complex networks: A survey of measurements". In: *Advances in Physics* 56.1, pp. 167–242. DOI: `10.1080/00018732.2011.572452`.

Csárdi, G. and T. Nepusz (2006). "The igraph software package for complex network research". In: *InterJournal* CX.18, 1695.

Dakos, V., M. Scheffer, E.H. van Nes, V. Brovkin, V. Petoukhov, and H. Held (2008). "Slowing down as an early warning signal for abrupt climate change". In: *Proceedings of the National Academy of Sciences of the United States of America* 105.38, pp. 14308–14312. DOI: `10.1073/pnas.0802430105`.

Dalcín, L.D., R.R. Paz, P.A. Kler, and A. Cosimo (2011). "Parallel distributed computing using Python". In: *Advances in Water Resources* 34.9, pp. 1124–1139. DOI: `10.1016/j.advwatres.2011.04.013`.

Dall, J. and M. Christensen (2002). "Random geometric graphs". In: *Physical Review E* 66.1, 016121. DOI: `10.1103/PhysRevE.66.016121`.

Darwin, C. (1859). *On the origin of species by means of natural selection*. John Murray, London. Chap. 3.

Das, K. and A.N. Srivastava (2011). "Sparse inverse gaussian process regression with application to climate network discovery". In: *NASA Conference on Intelligent Data Understanding (CIDU), Mountain View, California*, pp. 233–247.

Davidsen, J., P. Grassberger, and M. Paczuski (2008). "Networks of recurrent events, a theory of records, and an application to finding causal signatures in seismicity". In: *Physical Review E* 77.6, 066104. DOI: `10.1103/PhysRevE.77.066104`.

Davis, D., R. Lichtenwalter, and N. V. Chawla (2011). "Multi-relational link prediction in heterogeneous information networks". In: *International Conference on Advances in Social Networks Analysis and Mining (ASONAM)*. IEEE, pp. 281–288. DOI: `10.1109/ASONAM.2011.107`.

Bibliography

de Schepper, S., M.J. Head, and J. Groeneveld (2009). "North Atlantic Current variability through marine isotope stage M2 (circa 3.3 Ma) during the mid-Pliocene". In: *Paleoceanography* 24, PA4206. DOI: 10.1029/2008PA001725.

deMenocal, P.B. (1995). "Plio-Pleistocene African climate". In: *Science* 270.5233, pp. 53–59. DOI: 10.1126/science.270.5233.53.

– (2004). "African climate change and faunal evolution during the Pliocene-Pleistocene". In: *Earth and Planetary Science Letters* 220.1-2, pp. 3–24. DOI: 10.1016/S0012-821X(04)00003-2.

– (2011). "Climate and human evolution". In: *Science* 331.6017, pp. 540–542. DOI: 10.1126/science.1190683.

Diaconis, P. and F. Mosteller (1989). "Methods for studying coincidences". In: *Journal of the American Statistical Association* 84.408, pp. 853–861.

Dijkstra, E.W. (1959). "A note on two problems in connexion with graphs". In: *Numerische Mathematik* 1.1, pp. 269–271. DOI: 10.1007/BF01386390.

Diks, C., J.C. van Houwelingen, F. Takens, and J. DeGoede (1995). "Reversibility as a criterion for discriminating time series". In: *Physics Letters A* 201.2–3, pp. 221–228.

Dixon, P.M. (2006). "Ripley's K function". In: *Encyclopedia of environmetrics*. Wiley Online Library. DOI: 10.1002/9780470057339.var046.

Donges, J.F. (2009). "Complex networks in the climate system". Diploma thesis, urn:nbn:de:kobv:517-opus-49775. University of Potsdam.

Donges, J.F., R.V. Donner, and J. Kurths (2012). "Testing time series reversibility using complex network methods". In: *ArXiv preprint* arXiv:1211.1162 [physics.data-an].

Donges, J.F., J. Heitzig, J. Runge, H.C.H. Schultz, M. Wiedermann, A. Radebach, A. Zech, A. Rheinwalt, and H. Kutza (2008-2012). *pyunicorn – A Python package for inferring and analyzing complex networks*.

Donges, J.F., Y. Zou, N. Marwan, and J. Kurths (2009a, P22). "Complex networks in climate dynamics". In: *European Physical Journal Special Topics* 174.1, pp. 157–179. DOI: 10.1140/epjst/e2009-01098-2.

– (2009b, P21). "The backbone of the climate network". In: *Europhysics Letters* 87.4, 48007. DOI: 10.1209/0295-5075/87/48007.

Donges, J.F., R.V. Donner, K. Rehfeld, N. Marwan, M.H. Trauth, and J. Kurths (2011a, P11). "Identification of dynamical transitions in marine palaeoclimate records by recurrence network analysis". In: *Nonlinear Processes in Geophysics* 18.5, pp. 545–562. DOI: 10.5194/npg-18-545-2011.

Donges, J.F., H.C.H. Schultz, N. Marwan, Y. Zou, and J. Kurths (2011b, P14). "Investigating the topology of interacting networks – Theory and application to coupled climate subnetworks". In: *European Physical Journal B* 84.4, pp. 635–652. DOI: 10.1140/epjb/e2011-10795-8.

Donges, J.F., R.V. Donner, M.H. Trauth, N. Marwan, H.-J. Schellnhuber, and J. Kurths (2011c, P10). "Nonlinear detection of paleoclimate-variability transitions possibly related to human evolution". In: *Proceedings of the National Academy of Sciences of the United States of America* 108.51, pp. 20422–20427. DOI: 10.1073/pnas.1117052108.

Donges, J.F., J. Heitzig, R.V. Donner, and J. Kurths (2012). "Analytical framework for recurrence network analysis of time series". In: *Physical Review E* 85.4, 046105. DOI: `10.1103/PhysRevE.85.046105`.

Donner, R.V. and J.F Donges (2012a, C3). "Identifying nonlinearities by time-reversal asymmetry of vertex properties in visibility graphs". In: *Proceedings of the International Symposium on Nonlinear Theory and its Applications (NOLTA2012), Palma de Majorca, Spain*. IEICE, Tokyo, pp. 435–438.

Donner, R.V. and J.F. Donges (2012b, P7). "Visibility graph analysis of geophysical time series: Potentials and possible pitfalls". In: *Acta Geophysica* 60.3, pp. 589–623. DOI: `10.2478/s11600-012-0032-x`.

Donner, R.V., T. Sakamoto, and N. Tanizuka (2008). "Complexity of spatio-temporal correlations in Japanese air temperature records". In: *Nonlinear time series analysis in the geosciences: Applications in climatology, geodynamics and solar-terrestrial physics*. Ed. by R.V. Donner and S.M. Barbosa. Vol. 112. Lecture Notes in Earth Science. Springer, Berlin, pp. 125–154.

Donner, R.V. and A. Witt (2006). "Characterisation of long-term climate change by dimension estimates of multivariate palaeoclimatic proxy data". In: *Nonlinear Processes in Geophysics* 13.5, pp. 485–497. DOI: `10.5194/npg-13-485-2006`.

Donner, R.V., S. Barbosa, J. Kurths, and N. Marwan (2009). "Understanding the Earth as a complex system – Recent advances in data analysis and modelling in Earth sciences". In: *European Physical Journal Special Topics* 174.1, pp. 1–9. DOI: `10.1140/epjst/e2009-01086-6`.

Donner, R.V., Y. Zou, J.F. Donges, N. Marwan, and J. Kurths (2010a, P18). "Ambiguities in recurrence-based complex network representations of time series". In: *Physical Review E* 81.1, 015101(R). DOI: `10.1103/PhysRevE.81.015101`.

Donner, R.V., J.F. Donges, Y. Zou, N. Marwan, and J. Kurths (2010b, C5). "Recurrence-based evolving networks for time series analysis of complex systems". In: *Proceedings of the International Symposium on Nonlinear Theory and its Applications (NOLTA2010), Krakow, Poland*. IEICE, Tokyo, pp. 87–90.

Donner, R.V., Y. Zou, J.F. Donges, N. Marwan, and J. Kurths (2010c, P19). "Recurrence networks – A novel paradigm for nonlinear time series analysis". In: *New Journal of Physics* 12.3, 033205. DOI: `10.1088/1367-2630/12/3/033025`.

Donner, R.V., M. Small, J.F. Donges, N. Marwan, Y. Zou, R. Xiang, and J. Kurths (2011a, P13). "Recurrence-based time series analysis by means of complex network methods". In: *International Journal of Bifurcation and Chaos* 21.4, pp. 1019–1046. DOI: `10.1142/S0218127411029021`.

Donner, R.V., J. Heitzig, J.F. Donges, Y. Zou, and J. Kurths (2011b, P15). "The geometry of chaotic dynamics – A complex network perspective". In: *European Physical Journal B* 84.4, pp. 653–672. DOI: `10.1140/epjb/e2011-10899-1`.

Donner, R.V., J.H. Feldhoff, J.F Donges, N. Marwan, and J. Kurths (2013). "Multivariate extensions of recurrence networks: Geometric signatures of coupled nonlinear systems". In: *Proceedings of the IEEE International Symposium on Circuits and Systems (ISCAS 2013), Beijing, China*. IEEE Xplore.

Bibliography

Dowsett, H.J., M.M. Robinson, and K.M. Foley (2009). "Pliocene three-dimensional global ocean temperature reconstruction". In: *Climate of the Past* 5.4, pp. 769–783. DOI: 10.5194/cp-5-769-2009.

Dunsworth, H. and A. Walker (2002). "Early genus *Homo*". In: *The primate fossil record*. Ed. by W.C. Hartwig. Cambridge University Press, Cambridge, pp. 419–436.

Dwyer, G.S. and M.A. Chandler (2009). "Mid-Pliocene sea level and continental ice volume based on coupled benthic Mg/Ca palaeotemperatures and oxygen isotopes". In: *Philosophical Transactions of the Royal Society of London A* 367.1886, pp. 157–168. DOI: 10.1098/rsta.2008.0222.

Dykoski, C.A., R.L. Edwards, H. Cheng, D. Yuan, Y. Cai, M. Zhang, Y. Lin, J. Qing, Z. An, and J. Revenaugh (2005). "A high-resolution, absolute-dated Holocene and deglacial Asian monsoon record from Dongge Cave, China". In: *Earth and Planetary Science Letters* 233.1, pp. 71–86. DOI: 10.1016/j.epsl.2005.01.036.

Ebert-Uphoff, I. and Y. Deng (2012a). "A new type of climate network based on probabilistic graphical models: Results of boreal winter versus summer". In: *Geophysical Research Letters* 39, p. L19701. DOI: 10.1029/2012GL053269.

– (2012b). "Causal discovery for climate research using graphical models". In: *Journal of Climate* 25.17, pp. 5648–5665. DOI: 10.1175/JCLI-D-11-00387.1.

Eckmann, J.-P., S.O. Kamphorst, and D. Ruelle (1987). "Recurrence plots of dynamic systems". In: *Europhysics Letters* 4.9, pp. 973–977. DOI: 10.1209/0295-5075/4/9/004.

Eckmann, J.-P. and D. Ruelle (1992). "Fundamental limitations for estimating dimensions and Lyapunov exponents in dynamic systems". In: *Physica D* 56.2-3, pp. 185–187. DOI: 10.1016/0167-2789(92)90023-G.

Elsner, J.B., T.H. Jagger, and E.A. Fogarty (2009). "Visibility network of United States hurricanes". In: *Geophysical Research Letters* 36, L16702. DOI: 10.1029/2009GL039129.

Erdős, P. and A. Rényi (1959). "On random graphs I." In: *Publicationes Mathematicae Debrecen* 6, pp. 290–297.

– (1960). "On the evolution of random graphs". In: *Publications of the Mathematical Institute of the Hungarian Academy of Sciences* 5, pp. 17–60.

Fagiolo, G. (2007). "Clustering in complex directed networks". In: *Physical Review E* 76.2, 026107. DOI: 10.1103/PhysRevE.76.026107.

Farmer, J.D., E. Ott, and J.A. Yorke (1983). "The dimension of chaotic attractors". In: *Physica D* 7.1-3, pp. 153–180. DOI: 10.1016/0167-2789(83)90125-2.

Fekete, S.P., J.S.B. Mitchell, and K. Beurer (2005). "On the continuous Fermat-Weber problem". In: *Operations Research* 53.1, pp. 61–76. DOI: 10.1287/opre.1040.0137.

Feldhoff, J.H. (2011). "Multivariate extensions to recurrence network analysis". Diploma thesis. Humboldt University, Berlin.

Feldhoff, J.H., R.V. Donner, J.F. Donges, N. Marwan, and J. Kurths (2012). "Geometric detection of coupling directions by means of inter-system recurrence networks". In: *Physics Letters A* 376.46, pp. 3504–3513. DOI: 10.1016/j.physleta.2012.10.008.

– (2013). "Geometric signature of complex synchronisation scenarios". In: *ArXiv preprint* arxiv:1301.0806 [nlin.CD].

Feng, A., Z. Gong, Q. Wang, and G. Feng (2012). "Three-dimensional air–sea interactions investigated with bilayer networks". In: *Theoretical and Applied Climatology* 109.3-4, pp. 635–643. DOI: `10.1007/s00704-012-0600-7`.

Fischer, R. A. (1937). *The design of experiments.* 2nd ed. Oliver & Boyd, London.

Flammarion, C. (1888). *L'Atmosphère: Météorologie populaire.* Librairie Hachette et Cie., Paris.

Fleitmann, D., S.J. Burns, A. Mangini, M. Mudelsee, J. Kramers, I. Villa, U. Neff, A.A. Al-Subbary, A. Buettner, D. Hippler, and A. Matter (2007). "Holocene ITCZ and Indian monsoon dynamics recorded in stalagmites from Oman and Yemen (Socotra)". In: *Quaternary Science Reviews* 26.1, pp. 170–188. DOI: `10.1016/j.quascirev.2006.04.012`.

Flom, P.L., S.R. Friedman, S. Strauss, and A. Neaigus (2004). "A new measure of linkage between two sub-networks". In: *Connections* 26.1, pp. 62–70.

Fortunato, S. (2010). "Community detection in graphs". In: *Physics Reports* 486.3-5, pp. 75–174. DOI: `10.1016/j.physrep.2009.11.002`.

Foster, G. (1996a). "Time series analysis by projection. I. Statistical properties of Fourier analysis". In: *Astronomical Journal* 111.1, pp. 541–554. DOI: `10.1086/117805`.

– (1996b). "Time series analysis by projection. II. Tensor methods for time series analysis". In: *Astronomical Journal* 111.1, pp. 555–566. DOI: `10.1086/117806`.

Fraser, A.M. and H.L. Swinney (1986). "Independent coordinates for strange attractors from mutual information". In: *Physical Review A* 33.2, pp. 1134–1140. DOI: `10.1103/PhysRevA.33.1134`.

Freeman, L.C. (1979). "Centrality in social networks: Conceptual clarification". In: *Social Networks* 1.3, pp. 215–239. DOI: `10.1016/0378-8733(78)90021-7`.

Frenzel, S. and B. Pompe (2007). "Partial mutual information for coupling analysis of multivariate time series". In: *Physical Review Letters* 99.20, 204101. DOI: `10.1103/PhysRevLett.99.204101`.

Gámez, A.J., C.S. Zhou, A. Timmermann, and J. Kurths (2004). "Nonlinear dimensionality reduction in climate data". In: *Nonlinear Processes in Geophysics* 11.3, pp. 393–398. DOI: `10.5194/npg-11-393-2004`.

Gao, J., S.V. Buldyrev, H.E. Stanley, and S. Havlin (2011a). "Networks formed from interdependent networks". In: *Nature Physics* 8.1, pp. 40–48. DOI: `10.1038/NPHYS2180`.

Gao, J., S.V. Buldyrev, S. Havlin, and H.E. Stanley (2011b). "Robustness of a network of networks". In: *Physical Review Letters* 107.19, 195701. DOI: `10.1103/PhysRevLett.107.195701`.

Gao, Z.-K. and N.-D. Jin (2009a). "Complex network from time series based on phase space reconstruction". In: *Chaos* 19.3, 033137. DOI: `10.1063/1.3227736`.

– (2009b). "Flow-pattern identification and nonlinear dynamics of gas-liquid two-phase flow in complex networks". In: *Physical Review E* 79.6, 066303. DOI: `10.1103/PhysRevE.79.066303`.

Bibliography

Gao, Z.-K., N.-D. Jin, W.-X. Wang, and Y.-C. Lai (2010). "Motif distributions in phase-space networks for characterizing experimental two-phase flow patterns with chaotic features". In: *Physical Review E* 82.1, 016210. DOI: 10.1103/PhysRevE.82.016210.

Gastner, M.T. and M.E.J. Newman (2006). "The spatial structure of networks". In: *European Physical Journal B* 49.2, pp. 247–252. DOI: 10.1140/epjb/e2006-00046-8.

Geus, R. and P. Arbenz (2003). "PySparse and PyFemax: A Python framework for large scale sparse linear algebra". In: *Proceedings of PyCon'03, Washington D.C.*

Gibson, J.F., J.D. Farmer, M. Casdagli, and S. Eubank (1992). "An analytic approach to practical state space reconstruction". In: *Physica D* 57.1-2, pp. 1–30. DOI: 10.1016/0167-2789(92)90085-2.

Gong, Z.-Q., L. Zhou, R. Zhi, and G.-L. Feng (2008). "Analysis of dynamical statistical characteristics of temperature correlation networks of 1-30 d scales". In: *Acta Physica Sinica* 57.8, pp. 5351–5360.

Gozolchiani, A., S. Havlin, and K. Yamasaki (2011). "Emergence of El Niño as an autonomous component in the climate network". In: *Physical Review Letters* 107.14, 148501. DOI: 10.1103/PhysRevLett.107.148501.

Gozolchiani, A., K. Yamasaki, O. Gazit, and S. Havlin (2008). "Pattern of climate network blinking links follows El Niño events". In: *Europhysics Letters* 83.2, 28005. DOI: 10.1209/0295-5075/83/28005.

Granger, C. W. J. (1969). "Investigating causal relations by econometric models and cross-spectral methods". In: *Econometrica* 37.3, pp. 424–438.

Grassberger, P. and I. Procaccia (1983). "Measuring the strangeness of strange attractors". In: *Physica D* 9.1-2, pp. 189–208. DOI: 10.1016/0167-2789(83)90298-1.

Grootes, P.M. and M. Stuiver (1997). "Oxygen 18/16 variability in Greenland snow and ice with 10^{-3}- to 10^5-year time resolution". In: *Journal of Geophysical Research* 102.C12, pp. 26455–26. DOI: 10.1029/97JC00880.

Guez, O., A. Gozolchiani, Y. Berezin, S. Brenner, and S. Havlin (2012). "Climate network structure evolves with North Atlantic Oscillation phases". In: *Europhysics Letters* 98, p. 38006. DOI: 10.1209/0295-5075/98/38006.

Hailemichael, M., J.L. Aronson, S. Savin, M.J.S. Tevesz, and J.G. Carter (2002). "δ^{18}O in mollusk shells from Pliocene Lake Hadar and modern Ethiopian lakes: Implications for history of the Ethiopian monsoon". In: *Palaeogeography Palaeoclimatology Palaeoecology* 186.1-2, pp. 81–99. DOI: 10.1016/S0031-0182(02)00445-5.

Hamilton, J.D. (1994). *Time series analysis.* Princeton University Press, Princeton.

Hammersley, J.M. (1950). "The distribution of distance in a hypersphere". In: *Annals of Mathematical Statistics* 21.3, pp. 447–452. DOI: 10.1214/aoms/1177729805.

Hartmann, D.L. (2007). "The atmospheric general circulation and its variability". In: *Journal of the Meteorological Society of Japan* 85B, pp. 123–143. DOI: 10.2151/jmsj.85B.123.

Haug, G.H. and R. Tiedemann (1998). "Effect of the formation of the Isthmus of Panama on Atlantic Ocean thermohaline circulation". In: *Nature* 393.6686, pp. 673–676. DOI: 10.1038/31447.

Haykin, S. (2008). *Neural networks and learning machines.* 3rd ed. Prentice Hall, Upper Saddle River, New Jersey.

Haywood, A.M., P. Dekens, A.C. Ravelo, and M. Williams (2005). "Warmer tropics during the mid-Pliocene? Evidence from alkenone paleothermometry and a fully coupled ocean-atmosphere GCM". In: *Geochemistry Geophysics Geosystems* 6, Q03010. DOI: `10.1029/2004GC000799`.

Heikes, R. and D.A. Randall (1995). "Numerical integration of the shallow-water equations on a twisted icosahedral grid. I: Basic design and results of tests". In: *Monthly Weather Review* 123.6, pp. 1862–1880. DOI: `10.1175/1520-0493(1995)1 23<1862:NIOTSW>2.0.CO;2`.

Heitzig, J. (2012). "Moving Taylor Bayesian Regression for nonparametric multidimensional function estimation with possibly correlated errors". In: *ArXiv preprint* arXiv:1204.2841 [physics.data-an].

Heitzig, J., J.F. Donges, Y. Zou, N. Marwan, and J. Kurths (2012). "Node-weighted measures for complex networks with spatially embedded, sampled, or differently sized nodes". In: *European Physical Journal B* 85.1, 38. DOI: `10.1140/epjb/e201 1-20678-7`.

Held, H. and T. Kleinen (2004). "Detection of climate system bifurcations by degenerate fingerprinting". In: *Geophysical Research Letters* 31.23, L23207. DOI: `10.1029/2004GL020972`.

Hempel, S., A. Koseska, J. Kurths, and Z. Nikoloski (2011). "Inner composition alignment for inferring directed networks from short time series". In: *Physical Review Letters* 107.5, 54101. DOI: `10.1103/PhysRevLett.107.054101`.

Hentschel, H.G.E. and I. Procaccia (1983). "The infinite number of generalized dimensions of fractals and strange attractors". In: *Physica D* 8.3, pp. 435–444. DOI: `10.1016/0167-2789(83)90235-X`.

Herbert, T.D., L.C. Peterson, K.T. Lawrence, and Z. Liu (2010). "Tropical ocean temperatures over the past 3.5 million years". In: *Science* 328.5985, pp. 1530–1534. DOI: `10.1126/science.1185435`.

Herrmann, C., M. Barthélemy, and P. Provero (2003). "Connectivity distribution of spatial networks". In: *Physical Review E* 68.2, 026128. DOI: `10.1103/PhysRevE.6 8.026128`.

Hirata, Y., Y. Shimo, H.L. Tanaka, and K. Aihara (2011). "Chaotic properties of the Arctic Oscillation Index". In: *SOLA* 7, pp. 33–36. DOI: `10.2151/sola.2011-009`.

Holton, J.R. (2004). *An introduction to dynamic meteorology.* 4th ed. Elsevier, Burlington.

Hsieh, W.W. (2004). "Nonlinear multivariate and time series analysis by neural network methods". In: *Reviews of Geophysics* 42.1, RG1003. DOI: `10.1029/2002RG000112`.

Huang, X., J. Gao, S.V. Buldyrev, S. Havlin, and H.E. Stanley (2011). "Robustness of interdependent networks under targeted attack". In: *Physical Review E* 83.6, 065101. DOI: `10.1103/PhysRevE.83.065101`.

Hunter, J.D. (2007). "Matplotlib: A 2D graphics environment". In: *Computing In Science & Engineering* 9.3, pp. 90–95. DOI: `10.1109/MCSE.2007.55`.

Bibliography

Inman, D.L. (2003). "Scripps in the 1940s: The Sverdrup era". In: *Oceanography* 16.3, pp. 20–28.

Itzkovitz, S. and U. Alon (2005). "Subgraphs and network motifs in geometric networks". In: *Physical Review E* 71.2, 026117. DOI: 10.1103/PhysRevE.71.026117.

Jaynes, E.T. and G.L. Bretthorst (2003). *Probability theory: The logic of science.* Cambridge University Press, Cambridge.

Jiménez, A., K. F. Tiampo, A. M. Posadas, F. Luzón, and R. Donner (2009). "Analysis of complex networks associated to seismic clusters near the Itoiz reservoir dam". In: *European Physical Journal Special Topics* 174.1, pp. 181–195. DOI: 10.1140/epjst/e2009-01099-1.

Jones, E., T.E. Oliphant, P. Petersen, et al. (2011). *SciPy: Open source scientific tools for Python.*

Jones, P.W. (1998). *A user's guide for SCRIP: A spherical coordinate remapping and interpolation package.* Tech. rep. Los Alamos National Laboratory, Los Alamos, New Mexico.

Jung, W.S., D.I. Lee, Y.-J. Choi, K.-H. Chang, J.-W. Jung, S.-K. Seo, M. Yi, and K. Kim (2012). "Analysis of the network mechanism for sea surface temperatures around the Korean Peninsula". In: *Journal of the Korean Physical Society* 60.4, pp. 566–569. DOI: 10.3938/jkps.60.566.

Kaiser, M. and C.C. Hilgetag (2004). "Spatial growth of real-world networks". In: *Physical Review E* 69.3, 036103. DOI: 10.1103/PhysRevE.69.036103.

Kantz, H. and T. Schreiber (2004). *Nonlinear time series analysis.* 2nd ed. Cambridge University Press, Cambridge.

Karas, C., D. Nürnberg, A.K. Gupta, R. Tiedemann, K. Mohan, and T. Bickert (2009). "Mid-Pliocene climate change amplified by a switch in Indonesian subsurface throughflow". In: *Nature Geoscience* 2.6, pp. 434–438. DOI: 10.1038/ngeo520.

Katz, R.W. (2002). "Sir Gilbert Walker and a connection between El Niño and statistics". In: *Statistical Science* 17.1, pp. 97–112. DOI: 10.1214/ss/1023799000.

Kawale, J., S. Liess, A. Kumar, M. Steinbach, A. R. Ganguly, N. F. Samatova, F. Semazzi, P. Snyder, and V. Kumar (2011). "Data guided discovery of dynamic climate dipoles". In: *Proceedings of the NASA Conference on Intelligent Data Understanding.*

Kennel, M.B., R. Brown, and H.D.I. Abarbanel (1992). "Determining embedding dimension for phase-space reconstruction using a geometrical construction". In: *Physical Review A* 45.6, pp. 3403–3411. DOI: 10.1103/PhysRevA.45.3403.

Kimbel, W.H., R.C. Walter, D.C. Johanson, K.E. Reed, J.L. Aronson, Z. Assefa, C.W. Marean, G.G. Eck, R. Robe, E. Hovers, Y. Rak, C. Vondra, T. Yemane, D. York, Y. Chen, N.M. Evensen, and P.E. Smith (1996). "Late Pliocene Homo and Oldowan tools from the Hadar Formation (Kada Hadar Member), Ethiopia". In: *Journal of Human Evolution* 31.6, pp. 549–561. DOI: 10.1006/jhev.1996.0079.

Kistler, R., E. Kalnay, W. Collins, S. Saha, G. White, J. Woollen, M. Chelliah, W. Ebisuzaki, M. Kanamitsu, V. Kousky, H.V.D. Dool, R. Jenne, and M. Fiorino (2001). "The NCEP–NCAR 50–year reanalysis: Monthly means CD–ROM and

documentation". In: *Bulletin of the American Meteorological Society* 82.2, pp. 247–268. DOI: `10.1175/1520-0477(2001)082<0247:TNNYRM>2.3.CO;2`.

Kolaczyk, E.D. (2009). *Statistical analysis of network data: Methods and models.* Springer Series in Statistics. Springer, New York.

Kolaczyk, E.D., D.B. Chua, and M. Barthélemy (2009). "Group betweenness and co-betweenness: Inter-related notions of coalition centrality". In: *Social Networks* 31.3, pp. 190–203. DOI: `10.1016/j.socnet.2009.02.003`.

Koller, D. and N. Friedman (2009). *Probabilistic graphical models: Principles and techniques.* Adaptive Computation and Machine Learning series. MIT Press, Cambridge, Massachusetts.

Kong, Z.N and E.M. Yeh (2007). "Characterization of the critical density for percolation in random geometric graphs". In: *Proceedings of the IEEE International Symposium on Information Theory (ISIT).* IEEE, pp. 151–155. DOI: `10.1109/ISIT.2007.4557082`.

Kramer, M.A., U.T. Eden, S.S. Cash, and E.D. Kolaczyk (2009). "Network inference with confidence from multivariate time series". In: *Physical Review E* 79.6, 061916. DOI: `10.1103/PhysRevE.79.061916`.

Kreuz, T., F. Mormann, R.G. Andrzejak, A. Kraskov, K. Lehnertz, and P. Grassberger (2007). "Measuring synchronization in coupled model systems: A comparison of different approaches". In: *Physica D* 225, pp. 29–42. DOI: `10.1016/j.physd.2006.09.039`.

Krishna Kumar, K., B. Rajagopalan, M. Hoerling, G. Bates, and M. Cane (2006). "Unraveling the mystery of Indian monsoon failure during El Niño". In: *Science* 314.5796, pp. 115–119. DOI: `10.1126/science.1131152`.

Kuehn, C. (2011). "A mathematical framework for critical transitions: Bifurcations, fast-slow systems and stochastic dynamics". In: *Physica D* 240.12, pp. 1020–1035. DOI: `10.1016/j.physd.2011.02.012`.

Kurant, M. and P. Thiran (2006a). "Extraction and analysis of traffic and topologies of transportation networks". In: *Physical Review E* 74.3, 036114. DOI: `10.1103/PhysRevE.74.036114`.

– (2006b). "Layered complex networks". In: *Physical Review Letters* 96.13, 138701. DOI: `10.1103/PhysRevLett.93.138701`.

Kurant, M., P. Thiran, and P. Hagmann (2007). "Error and attack tolerance of layered complex networks". In: *Physical Review E* 76.2, 026103. DOI: `10.1103/PhysRevE.76.026103`.

Kutza, H. (2012). "Pattern recognition in complex networks based on spatially embedded time series". Master's thesis. Humboldt University, Berlin.

Kutzbach, J.E. (1967). "Empirical eigenvectors of sea-level pressure, surface temperature and precipitation complexes over North America". In: *Journal of Applied Meteorology* 6.5, pp. 791–802. DOI: `10.1175/1520-0450(1967)006<0791:EEOSLP>2.0.CO;2`.

Kutzbach, J.E. and Z. Liu (1997). "Response of the African monsoon to orbital forcing and ocean feedbacks in the middle Holocene". In: *Science* 278.5337, pp. 440–443. DOI: `10.1126/science.278.5337.440`.

Bibliography

Kutzbach, J.E. and F.A. Streetperrott (1985). "Milankovitch forcing of fluctuations in the level of tropical lakes from 18 to 0 kyr BP". In: *Nature* 317.6033, pp. 130–134. DOI: `10.1038/317130a0`.

Lacasa, L., B. Luque, F. Ballesteros, J. Luque, and J.C. Nuno (2008). "From time series to complex networks: The visibility graph". In: *Proceedings of the National Academy of Sciences of the United States of America* 105.13, pp. 4972–4975. DOI: `10.1073/pnas.0709247105`.

Lacasa, L., B. Luque, J. Luque, and J.C. Nuno (2009). "The visibility graph: A new method for estimating the Hurst exponent of fractional Brownian motion". In: *Europhysics Letters* 86.3, 30001. DOI: `10.1209/0295-5075/86/30001`.

Lacasa, L., Á.M. Núñez, É. Roldán, J.M.R. Parrondo, and B. Luque (2012). "Time series irreversibility: A visibility graph approach". In: *European Physical Journal B* 85, p. 217. DOI: `10.1140/epjb/e2012-20809-8`.

Langford, E., N. Schwertman, and M. Owens (2001). "Is the property of being positively correlated transitive?" In: *American Statistician* 55.4, pp. 322–325. DOI: `10.1198/000313001753272286`.

Larrasoaña, J.C., A.P. Roberts, E.J. Rohling, M. Winklhofer, and R. Wehausen (2003). "Three million years of monsoon variability over the northern Sahara". In: *Climate Dynamics* 21.7, pp. 689–698. DOI: `10.1007/s00382-003-0355-z`.

Lenton, T.M. (2011). "Early warning of climate tipping points". In: *Nature Climate Change* 1.4, pp. 201–209. DOI: `10.1038/nclimate1143`.

Lenton, T.M., H.-J. Schellnhuber, and E. Szathmáry (2004). "Climbing the co-evolution ladder". In: *Nature* 431.7011, pp. 913–913. DOI: `10.1038/431913a`.

Lenton, T.M., H. Held, J.W. Hall, E. Kriegler, W. Lucht, S. Rahmstorf, and H.-J. Schellnhuber (2008). "Tipping elements in the Earth's climate system". In: *Proceedings of the National Academy of Sciences of the United States of America* 105.6, pp. 1786–1793. DOI: `10.1073/pnas.0705414105`.

Levermann, A., J.L. Bamber, S. Drijfhout, A. Ganopolski, W. Haeberli, N.R.P. Harris, M. Huss, K. Krüger, T.M. Lenton, R.W. Lindsay, D. Notz, P. Wadhams, and S. Weber (2012). "Potential climatic transitions with profound impact on Europe - Review of the current state of six 'tipping elements of the climate system'". In: *Climatic Change* 110.3-4, pp. 845–878. DOI: `10.1007/s10584-011-0126-5`.

Lew, J.S., J.C. Frauenthal, and N. Keyfitz (1978). "On the average distances in a circular disc". In: *SIAM Review* 20.3, pp. 584–592. DOI: `10.1137/1020073`.

Li, Y., H. Cao, and Y. Tan (2011). "A comparison of two methods for modeling large-scale data from time series as complex networks". In: *AIP Advances* 1, 012103. DOI: `10.1063/1.3556121`.

Lisiecki, L.E. and M.E. Raymo (2005). "A Pliocene-Pleistocene stack of 57 globally distributed benthic δ^{18}O records". In: *Paleoceanography* 20.1, PA1003. DOI: `10.1029/2004PA001071`.

Livina, V.N., F. Kwasniok, and T.M. Lenton (2010). "Potential analysis reveals changing number of climate states during the last 60 kyr". In: *Climate of the Past* 6.1, pp. 77–82. DOI: `10.5194/cp-6-77-2010`.

Livina, V.N. and T.M. Lenton (2007). "A modified method for detecting incipient bifurcations in a dynamical system". In: *Geophysical Research Letters* 34.3, L03712. DOI: 10.1029/2006GL028672.

Lomb, N.R. (1976). "Least-squares frequency analysis of unequally spaced data". In: *Astrophysics and Space Science* 39.2, pp. 447–462. DOI: 10.1007/BF00648343.

Lourens, L.J., A. Antonarakou, F.J. Hilgen, A.A.M. VanHoof, C. Vergnaud Grazzini, and W.J. Zachariasse (1996). "Evaluation of the Plio-Pleistocene astronomical timescale". In: *Paleoceanography* 11.4, pp. 391–413. DOI: 10.1029/96PA01125.

Lovelock, J.E. (1979). *Gaia: A new look at life on earth.* Oxford University Press, Oxford.

– (2000). *The ages of Gaia: A biography of our living earth.* 2nd ed. Oxford University Press, Oxford.

Luque, B., L. Lacasa, F. Ballesteros, and J. Luque (2009). "Horizontal visibility graphs: Exact results for random time series". In: *Physical Review E* 80.4, 046103. DOI: 10.1103/PhysRevE.80.046103.

Majewski, D., D. Liermann, P. Prohl, B. Ritter, M. Buchhold, T. Hanisch, G. Paul, W. Wergen, and J. Baumgardner (2002). "The operational global icosahedral–hexagonal gridpoint model GME: Description and high-resolution tests". In: *Monthly Weather Review* 130.2, pp. 319–338. DOI: 10.1175/1520-0493(2002)130<0319:TOGIHG>2.0.CO;2.

Malik, N., B. Bookhagen, N. Marwan, and J. Kurths (2012). "Analysis of spatial and temporal extreme monsoonal rainfall over South Asia using complex networks". In: *Climate Dynamics* 39.3-4, pp. 971–987. DOI: 10.1007/s00382-011-1156-4.

Maraun, D. and J. Kurths (2005). "Epochs of phase coherence between El Niño/Southern Oscillation and Indian monsoon". In: *Geophysical Research Letters* 32.15, L15709. DOI: 10.1029/2005GL023225.

Maraun, D., J. Kurths, and M. Holschneider (2007). "Nonstationary Gaussian processes in wavelet domain: Synthesis, estimation, and significance testing". In: *Physical Review E* 75.1, 016707. DOI: 10.1103/PhysRevE.75.016707.

Marwan, N. and J. Kurths (2002). "Nonlinear analysis of bivariate data with cross recurrence plots". In: *Physics Letters A* 302.5-6, pp. 299–307. DOI: 10.1016/S0375-9601(02)01170-2.

Marwan, N., M. Thiel, and N.R. Nowaczyk (2002). "Cross recurrence plot based synchronization of time series". In: *Nonlinear Processes in Geophysics* 9.3-4, pp. 325–331. DOI: 10.5194/npg-9-325-2002.

Marwan, N., M.H. Trauth, M. Vuille, and J. Kurths (2003). "Comparing modern and Pleistocene ENSO-like influences in NW Argentina using nonlinear time series analysis methods". In: *Climate Dynamics* 21.3-4, pp. 317–326. DOI: 10.1007/s00382-003-0335-3.

Marwan, N., M. C. Romano, M. Thiel, and J. Kurths (2007). "Recurrence plots for the analysis of complex systems". In: *Physics Reports* 438.5–6, pp. 237–329. DOI: 10.1016/j.physrep.2006.11.001.

Marwan, N., J.F. Donges, Y. Zou, R.V. Donner, and J. Kurths (2009). "Complex network approach for recurrence analysis of time series". In: *Physics Letters A* 373.46, pp. 4246–4254. DOI: 10.1016/j.physleta.2009.09.042.

Marwan, N., J.F. Donges, A. Radebach, J.G.B. Runge, and J. Kurths (2010a, C4). "Evolving climate networks". In: *Proceedings of the International Symposium on Nonlinear Theory and its Applications (NOLTA2010), Krakow, Poland*. IEICE, Tokyo, pp. 3–6.

Marwan, N., N. Wessel, H. Stepan, and J. Kurths (2010b). "Recurrence based complex network analysis of cardiovascular variability data to predict pre-eclampsia". In: *Proceedings of the International Symposium on Nonlinear Theory and its Applications (NOLTA2010), Krakow, Poland*. IEICE, Tokyo, pp. 585–588.

Marwan, N., J.H. Feldhoff, R.V. Donner, J.F Donges, and J. Kurths (2012). "Detection of coupling directions with intersystem recurrence networks". In: *Proceedings of the International Symposium on Nonlinear Theory and its Applications (NOLTA2012), Palma de Majorca, Spain*. IEICE, Tokyo, pp. 231–234.

Maslin, M.A. and M.H. Trauth (2009). "Plio-Pleistocene East African pulsed climate variability and its influence on early human evolution". In: *The first humans: Origin and early evolution of the genus Homo*. Ed. by F.E. Grine, R.E. Leakey, and J.G. Fleagle. Vertebrate Paleobiology and Paleoanthropology Series. Springer, New York, pp. 151–158.

McHenry, H.M. (2002). "Introduction to the fossil record of human ancestry". In: *The primate fossil record*. Ed. by W.C. Hartwig. Cambridge University Press, Cambridge, pp. 401–406.

McKechnie, J. S. (2010). "Complex network analysis of tipping elements of the climate system". Bachelor's thesis. Trinity College, University of Dublin.

Milo, R., S. Shen-Orr, S. Itzkovitz, N. Kashtan, D. Chklovskii, and U. Alon (2002). "Network motifs: Simple building blocks of complex networks". In: *Science* 298.5594, pp. 824–827. DOI: 10.1126/science.298.5594.824.

Molkenthin, N., N. Marwan, and J. Kurths (2012). "Networks in a bucket, from dynamics to topology". In: *Verhandlungen der Deutschen Physikalischen Gesellschaft* SOE 15.11.

Mudelsee, M. (2010). *Climate time series analysis: Classical statistical and bootstrap methods*. Vol. 42. Atmospheric and Oceanographic Sciences Library. Springer, Dordrecht. DOI: 10.1007/978-90-481-9482-7.

Mudelsee, M. and M. Schulz (1997). "The Mid-Pleistocene climate transition: Onset of 100 ka cycle lags ice volume build-up by 280 ka". In: *Earth and Planetary Science Letters* 151.1-2, pp. 117–123. DOI: 10.1016/S0012-821X(97)00114-3.

Mudelsee, M., D. Scholz, R. Röthlisberger, D. Fleitmann, A. Mangini, and E.W. Wolff (2009). "Climate spectrum estimation in the presence of timescale errors". In: *Nonlinear Processes in Geophysics* 16.1, pp. 43–56. DOI: 10.5194/npg-16-43-2009.

Newman, M.E.J. (2002). "Assortative mixing in networks". In: *Physical Review Letters* 89.20, 208701. DOI: 10.1103/PhysRevLett.89.208701.

– (2003). "The structure and function of complex networks". In: *SIAM Review* 45.2, pp. 167–256. DOI: 10.1137/S003614450342480.

– (2005). "A measure of betweenness centrality based on random walks". In: *Social Networks* 27.1, pp. 39–54. DOI: `10.1016/j.socnet.2004.11.009`.

– (2010). *Networks: An Introduction*. Oxford University Press, Oxford.

Newman, M.E.J. and M. Girvan (2004). "Finding and evaluating community structure in networks". In: *Physical Review E* 69.2, 026113. DOI: `10.1103/PhysRevE.69.026113`.

Nicholls, K.W., S. Østerhus, K. Makinson, T. Gammelsrød, and E. Fahrbach (2009). "Ice-ocean processes over the continental shelf of the southern Weddell Sea, Antarctica: A review". In: *Reviews of Geophysics* 47.3, RG3003. DOI: `10.1029/2007RG000250`.

Nicolis, G., A. Garciá Cantú, and C. Nicolis (2005). "Dynamical aspects of interaction networks". In: *International Journal of Bifurcation and Chaos* 15.11, pp. 3467–3480. DOI: `10.1142/S0218127405014167`.

Nunnari, G., G. Puglisi, A. Bonforte, and A. Spata (2009). "Small world behavior of the planetary active volcanoes network: Preliminary results". In: *Complex Networks: Results of the 1st International Workshop on Complex Networks (CompleNet 2009)*. Ed. by S. Fortunato, G. Mangioni, R. Menezes, and V. Nicosia. Vol. 207. Studies in Computational Intelligence. Berlin: Springer, pp. 15–21. DOI: `10.1007/978-3-642-01206-8_2`.

Øksendal, B.K. (2003). *Stochastic differential equations: An introduction with applications*. 6th ed. Springer, Heidelberg. DOI: `10.1007/978-3-642-14394-6`.

Oliphant, T.E. (2006). *Guide to NumPy*. Brigham Young University, Provo. URL: `http://www.tramy.us/`.

O'Neill, B. (2006). *Elementary differential geometry*. 2nd ed. Academic Press, Burlington.

Ott, E. (2002). *Chaos in dynamical systems*. 2nd ed. Cambridge University Press, Cambridge.

Packard, N.H., J.P. Crutchfield, J.D. Farmer, and R.S. Shaw (1980). "Geometry from a time series". In: *Physical Review Letters* 45.9, pp. 712–716. DOI: `10.1103/PhysRevLett.45.712`.

Paluš, M., D. Hartman, J. Hlinka, and M. Vejmelka (2011). "Discerning connectivity from dynamics in climate networks". In: *Nonlinear Processes in Geophysics* 18.5, pp. 751–763. DOI: `10.5194/npg-18-751-2011`.

Parshani, R., S. Buldyrev, and S. Havlin (2010). "Interdependent networks: Reducing the coupling strength leads to a change from a first to second order percolation transition". In: *Physical Review Letters* 105.4, 048701. DOI: `10.1103/PhysRevLett.105.048701`.

Parshani, R., S.V. Buldyrev, and S. Havlin (2011). "Critical effect of dependency groups on the function of networks". In: *Proceedings of the National Academy of Sciences of the United States of America* 108.3, pp. 1007–1010. DOI: `10.1073/pnas.1008404108`.

Parshani, R., C. Rozenblat, D. Ietri, C. Ducruet, and S. Havlin (2010). "Intersimilarity between coupled networks". In: *Europhysics Letters* 92, 68002. DOI: `10.1209/0295-5075/92/68002`.

Pedlosky, J. (1979). *Geophysical fluid dynamics.* Springer, New York.

Pelan, A., K. Steinhaeuser, N. V. Chawla, D. A. de Alwis Pitts, and A. R. Ganguly (2011). "Empirical comparison of correlation measures and pruning levels in complex networks representing the global climate system". In: *IEEE Symposium on Computational Intelligence and Data Mining (CIDM).* IEEE, pp. 239–245. DOI: `10.1109/CIDM.2011.5949305`.

Penrose, M. (2003). *Random geometric graphs.* Oxford University Press, Oxford.

Pikovsky, A. S., M. G. Rosenblum, and J. Kurths (2001). *Synchronization: A universal concept in nonlinear sciences.* Cambridge University Press, Cambridge.

Poincaré, H. (1890). "Sur la problème des trois corps et les équations de la dynamique". In: *Acta Mathematica* 13, A3–A270.

Potts, R. (1996). "Evolution and climate variability". In: *Science* 273.5277, pp. 922–923. DOI: `10.1126/science.273.5277.922`.

– (1998). "Environmental hypotheses of hominin evolution". In: *Yearbook of Physical Anthropology* 41, pp. 93–136. DOI: `10.1002/(SICI)1096-8644(1998)107:27+ <93::AID-AJPA5>3.0.CO;2-X`.

Prospero, J.M., P. Ginoux, O. Torres, S.E. Nicholson, and T.E. Gill (2002). "Environmental characterization of global sources of atmospheric soil dust identified with the Nimbus 7 Total Ozone Mapping Spectrometer (TOMS) absorbing aerosol product". In: *Reviews of Geophysics* 40.1, 1002. DOI: `10.1029/2000RG000095`.

Radebach, A. (2010). "Evolving climate networks: Investigating the evolution of correlation structure of the Earth's climate system". Diploma thesis. Humboldt University, Berlin.

Radebach, A., R. V. Donner, J. Runge, J. F. Donges, and J. Kurths (subm.). "Disentangling different types of El Niño episodes by evolving climate network analysis". In: *Physical Review E.*

Raustiala, K. (2001). "Nonstate actors in the global climate regime". In: *International relations and global climate change.* Ed. by U. Luterbacher and D. F. Sprinz. MIT Press, Cambridge, Massachusetts, pp. 95–117.

Ravelo, A.C., D.H. Andreasen, M. Lyle, A.O. Lyle, and M.W. Wara (2004). "Regional climate shifts caused by gradual global cooling in the Pliocene epoch". In: *Nature* 429.6989, pp. 263–267. DOI: `10.1038/nature02567`.

Reed, K.E. (1997). "Early hominid evolution and ecological change through the African Plio-Pleistocene". In: *Journal of Human Evolution* 32.2-3, pp. 289–322. DOI: `10.1006/jhev.1996.0106`.

Rehfeld, K., N. Marwan, J. Heitzig, and J. Kurths (2011). "Comparison of correlation analysis techniques for irregularly sampled time series". In: *Nonlinear Processes in Geophysics* 18.3, pp. 389–404. DOI: `10.5194/npg-18-389-2011`.

Rehfeld, K., N. Marwan, S.F.M. Breitenbach, and J. Kurths (in press). "Late Holocene Asian summer monsoon dynamics from small but complex networks of paleoclimate data". In: *Climate Dynamics.* DOI: `10.1007/s00382-012-1448-3`.

Rényi, A. (1961). "On Measures of Entropy and Information". In: *Proceedings of the Fourth Berkeley Symposium on Mathematical Statistics and Probability.* Vol. 1. University of California Press, pp. 547–561.

Reynolds, S.C., G.N. Bailey, and G.C.P. King (2011). "Landscapes and their relation to hominin habitats: Case studies from Australopithecus sites in eastern and southern Africa". In: *Journal of Human Evolution* 60.3, pp. 281–298. DOI: 10.101 6/j.jhevol.2010.10.001.

Rheinwalt, A. (2011). "Rainfall networks: Precipitation analysis for the region of Germany using complex networks". Diploma thesis. Humboldt University, Berlin.

Rheinwalt, A., N. Marwan, J. Kurths, P. Werner, and F.-W. Gerstengarbe (2012). "Boundary effects in network measures of spatially embedded networks". In: *Europhysics Letters* 100.2, p. 28002. DOI: 10.1209/0295-5075/100/28002.

Riehl, H. and J.S. Malkus (1958). "On the heat balance of the equatorial trough zone". In: *Geophysica* 6.3-4, pp. 503–538.

Rignot, E., M. Koppes, and I. Velicogna (2010). "Rapid submarine melting of the calving faces of West Greenland glaciers". In: *Nature Geoscience* 3.3, pp. 187–191. DOI: 10.1038/ngeo765.

Robinson, M.M. (2009). "New quantitative evidence of extreme warmth in the Pliocene Arctic". In: *Stratigraphy* 6.4, pp. 265–275.

Rockström, J., W. Steffen, K. Noone, A. Persson, F.S. Chapin, E.F. Lambin, T.M. Lenton, M. Scheffer, C. Folke, H.-J. Schellnhuber, B. Nykvist, C.A. de Wit, T. Hughes, S. van der Leeuw, H. Rodhe, S. Sörlin, P.K. Snyder, R. Costanza, U. Svedin, M. Falkenmark, L. Karlberg, R.W. Corell, V.J. Fabry, J. Hansen, B. Walker, D. Liverman, K. Richardson, P. Crutzen, and J.A. Foley (2009). "A safe operating space for humanity". In: *Nature* 461.7263, pp. 472–475. DOI: 10.1038/461472a.

Romano, M.C., M. Thiel, J. Kurths, and W. von Bloh (2004). "Multivariate recurrence plots". In: *Physics Letters A* 330.3, pp. 214–223. DOI: 10.1016/j.physleta.2004. 07.066.

Rossum, G. van and F.L. Drake, eds. (2006). *Python reference manual*. Python Software Foundation. URL: http://docs.python.org/ref/ref.html.

Ruddiman, W.F. (2007). "The early anthropogenic hypothesis: Challenges and responses". In: *Reviews of Geophysics* 45.3, RG4001. DOI: 10.1029/2006RG000207.

– (2008). "Book review: Human environments in the East African Pliocene: An assessment of the faunal evidence". In: *EOS Transactions AGU* 89.15, p. 145. DOI: 10.1029/2008EO150006.

Runge, J., J. Heitzig, V. Petoukhov, and J. Kurths (2012). "Escaping the curse of dimensionality in estimating multivariate transfer entropy". In: *Physical Review Letters* 108.25, p. 258701. DOI: 10.1103/PhysRevLett.108.258701.

Salby, M.L. (1996). *Fundamentals of atmospheric physics*. Academic Press, San Diego.

Santiago, A., J. P. Cárdenas, J. C. Losada, R. M. Benito, A. M Tarquis, and F. Borondo (2008). "Multiscaling of porous soils as heterogeneous complex networks". In: *Nonlinear Processes in Geophysics* 15.6, pp. 893–902. DOI: 10.5194/npg-15-8 93-2008.

Sarnthein, M., G. Bartoli, M. Prange, A. Schmittner, B. Schneider, M. Weinelt, N. Andersen, and D. Garbe-Schönberg (2009). "Mid-Pliocene shifts in ocean overturning circulation and the onset of Quaternary-style climates". In: *Climate of the Past* 5.2, pp. 269–283. DOI: 10.5194/cp-5-269-2009.

Bibliography

Scargle, J.D. (1982). "Studies in astronomical time series analysis II. Statistical aspects of spectral analysis of unevenly spaced data". In: *Astrophysical Journal* 263.2, pp. 835–853. DOI: 10.1086/160554.

Schank, T. and D. Wagner (2005). "Approximating clustering coefficient and transitivity". In: *Journal of Graph Algorithms and Applications* 9.2, pp. 265–275.

Scheffer, M. (2009). *Critical transitions in nature and society*. Princeton University Press, Princeton.

Scheffer, M., J. Bascompte, W.A. Brock, V. Brovkin, S.R. Carpenter, V. Dakos, H. Held, E.H. van Nes, M. Rietkerk, and G. Sugihara (2009). "Early-warning signals for critical transitions". In: *Nature* 461.7260, pp. 53–59. DOI: 10.1038/nature08227.

Schellnhuber, H.-J., P.J. Crutzen, W.C. Clark, M. Claussen, and H. Held, eds. (2004). *Earth system analysis for sustainability*. Vol. 91. Dahlem Workshop Reports. MIT Press, Cambridge, Massachusetts.

Schellnhuber, H.-J. (1998). "Discourse: Earth system analysis – The scope of the challenge". In: *Earth system analysis: Integrating science for sustainability*. Ed. by H.-J. Schellnhuber and V. Wenzel. Springer, Berlin, pp. 3–195.

– (1999). "'Earth system' analysis and the second Copernican revolution". In: *Nature* 402.6761, pp. C19–C23. DOI: 10.1038/35011515.

– (2009). "Tipping elements in the Earth System". In: *Proceedings of the National Academy of Sciences of the United States of America* 106.49, pp. 20561–20563. DOI: 10.1073/pnas.0911106106.

Schellnhuber, H.-J. and V. Wenzel, eds. (1998). *Earth system analysis: Integrating science for sustainability*. Springer, Berlin.

Schils, T. and E. Coppejans (2003). "Phytogeography of upwelling areas in the Arabian Sea". In: *Journal of Biogeography* 30.9, pp. 1339–1356. DOI: 10.1046/j.1365-269 9.2003.00933.x.

Schinkel, S., N. Marwan, O. Dimigen, and J. Kurths (2009). "Confidence bounds of recurrence-based complexity measures". In: *Physics Letters A* 373.26, pp. 2245–2250. DOI: 10.1016/j.physleta.2009.04.045.

Schmidli, J., J. Whitaker, and L. Wicker (2011). *PyNGL and PyNIO: Python packages for scientific visualization, file input/output and data analysis*. URL: http://www.pyngl.ucar.edu/.

Schneider, T. (2006). "The general circulation of the atmosphere". In: *Annual Review of Earth and Planetary Sciences* 34.1, pp. 655–688. DOI: 10.1146/annurev.earth.34.031405.125144.

Schreiber, T. (2000). "Measuring information transfer". In: *Physical Review Letters* 85.2, pp. 461–464. DOI: 10.1103/PhysRevLett.85.461.

Schreiber, T. and A. Schmitz (2000). "Surrogate time series". In: *Physica D* 142.3-4, pp. 346–382. DOI: 10.1016/S0167-2789(00)00043-9.

Schultz, H.C.H. (2010). "Coupled climate networks: Investigating the terrestrial atmosphere's dynamical structure". Diploma thesis. Free University, Berlin.

Schulz, M. and M. Mudelsee (2002). "REDFIT: Estimating red-noise spectra directly from unevenly spaced paleoclimatic time series". In: *Computers & Geosciences* 28.3, pp. 421–426. DOI: 10.1016/S0098-3004(01)00044-9.

Schulz, M. and K. Stattegger (1997). "SPECTRUM: Spectral analysis of unevenly spaced paleoclimatic time series". In: *Computers & Geosciences* 23.9, pp. 929–945. DOI: `10.1016/S0098-3004(97)00087-3`.

Scott, D.W. (1982). *Multivariate density estimation: Theory, practice, and visualization*. Wiley, New York.

Senthilkumar, D.V., N. Marwan, and J. Kurths (2010). "Recurrence network approach to a phase space of a time-delay system". In: *Proceedings of the International Symposium on Nonlinear Theory and its Applications (NOLTA2010), Krakow, Poland*. IEICE, Tokyo, pp. 83–86.

Sexton, M. (2009). "The spatial resolution dependence of complex climate networks". Bachelor's thesis. Trinity College, University of Dublin.

Shackleton, N.J., M.A. Hall, and D. Pate (1995). "Pliocene stable isotope stratigraphy of site 846". In: *Proceedings of the Ocean Drilling Program: Scientific results*. Ed. by N.G. Pisias, L.A. Mayer, T.R. Janecek, A. Palmer-Julson, and T.H. van Andel. Vol. 138. Ocean Drilling Program, College Station, pp. 337–355. DOI: `10.2973/odp.proc.sr.138.117.1995`.

Shao, J., S.V. Buldyrev, S. Havlin, and H.E. Stanley (2011). "Cascade of failures in coupled network systems with multiple support-dependence relations". In: *Physical Review E* 83.3, 036116. DOI: `10.1103/PhysRevE.83.036116`.

Shimada, Y., T. Kimura, and T. Ikeguchi (2008). "Analysis of chaotic dynamics using measures of the complex network theory". In: *Artificial neural networks: ICANN 2008, Pt. I*. Ed. by V. Kurkova, R. Neruda, and J. Koutnik. Vol. 5163. Lecture Notes in Computer Science. Springer, New York, pp. 61–70.

Smith, L.A. (1988). "Intrinsic limits on dimension calculations". In: *Physics Letters A* 133.6, pp. 283–288. DOI: `10.1016/0375-9601(88)90445-8`.

So, P., B.C. Cotton, and E. Barreto (2008). "Synchronization in interacting populations of heterogeneous oscillators with time-varying coupling". In: *Chaos* 18.3, 037114. DOI: `10.1063/1.2979693`.

Solomon, S., D. Qin, M. Manning, Z. Chen, M. Marquis, K.B. Averyt, M. Tignor, and H.L. Miller, eds. (2007). *Contribution of Working Group I to the Fourth Assessment Report of the Intergovernmental Panel on Climate Change*. Cambridge University Press, Cambridge.

Sprott, J.C. (2003). *Chaos and time series analysis*. Oxford University Press, Oxford.

Steffen, K. and J. Box (2001). "Surface climatology of the Greenland ice sheet: Greenland climate network 1995-1999". In: *Journal of Geophysical Research* 106.D24, pp. 33,951–33,964. DOI: `10.1029/2001JD900161`.

Steinhaeuser, K. (2011). "Knowledge discovery with networks for climate science: Questions and answers from CKD Hamburg". In: *Proceedings of the 2011 Workshop on Climate Knowledge Discovery (CKD '11)*. ACM, New York. DOI: `10.1145/2110230.2110232`.

Steinhaeuser, K., N. V. Chawla, and A. R. Ganguly (2010a). "An exploration of climate data using complex networks". In: *ACM SIGKDD Explorations* 12.1, pp. 25–32. DOI: `10.1145/1882471.1882476`.

Steinhaeuser, K., N. V. Chawla, and A. R. Ganguly (2010b). "Complex networks in climate science: Progress, opportunities and challenges". In: *Proceedings of the NASA Conference on Intelligent Data Understanding (CIDU), Mountain View, California*, pp. 16–26.

– (2011a). "Comparing predictive power in climate data: Clustering matters". In: *Advances in Spatial and Temporal Databases*. Ed. by D. Pfoser, Y. Tao, K. Mouratidis, M. Nascimento, M. Mokbel, S. Shekhar, and Y. Huang. Vol. 6849. Lecture Notes in Computer Science. Springer, Berlin/Heidelberg, pp. 39–55. DOI: `10.1007/978-3-642-22922-0_4`.

– (2011b). "Complex networks as a unified framework for descriptive analysis and predictive modeling in climate science". In: *Statistical Analysis and Data Mining* 4.5, pp. 497–511. DOI: `10.1002/sam.10100`.

Steinhaeuser, K., A. R. Ganguly, and N. V. Chawla (2012). "Multivariate and multi-scale dependence in the global climate system revealed through complex networks". In: *Climate Dynamics* 39.3-4, pp. 889–895. DOI: `10.1007/s00382-011-1135-9`.

Steph, S., R. Tiedemann, M. Prange, J. Groeneveld, D. Nuernberg, L. Reuning, M. Schulz, and G.H. Haug (2006). "Changes in Caribbean surface hydrography during the Pliocene shoaling of the Central American Seaway". In: *Paleoceanography* 21.4, PA4221. DOI: `10.1029/2004PA001092`.

Storch, H. von and F.W. Zwiers (2003). *Statistical analysis in climate research*. Cambridge University Press, Cambridge.

Stouffer, R.J., J. Yin, J.M. Gregory, K.W. Dixon, M.J. Spelman, W. Hurlin, A.J. Weaver, M. Eby, G.M. Flato, H. Hasumi, A. Hu, J.H. Jungclaus, I.V. Kamenkovich, A. Levermann, M. Montoya, S. Murakami, S. Nawrath, A. Oka, W.R. Peltier, D.Y. Robitaille, A. Sokolov, G. Vettoretti, and S.L. Weber (2006). "Investigating the causes of the response of the thermohaline circulation to past and future climate changes". In: *Journal of Climate* 19.8, pp. 1365–1387. DOI: `10.1175/JCLI3689.1`.

Strait, D.S. and B.A. Wood (1999). "Early hominid biogeography". In: *Proceedings of the National Academy of Sciences of the United States of America* 96.16, pp. 9196–9200. DOI: `10.1073/pnas.96.16.9196`.

Straneo, F., G.S. Hamilton, D.A. Sutherland, L.A. Stearns, F. Davidson, M.O. Hammill, G.B. Stenson, and A. Rosing-Asvid (2010). "Rapid circulation of warm subtropical waters in a major glacial fjord in East Greenland". In: *Nature Geoscience* 3.3, pp. 182–186. DOI: `10.1038/ngeo764`.

Strozzi, F., K. Poljansek, F. Bono, E. Gutiérrez, and J.M. Zaldívar (2011). "Recurrence networks: Evolution and robustness". In: *International Journal of Bifurcation and Chaos* 21.4, pp. 1047–1063. DOI: `10.1142/S0218127411028891`.

Stumpf, M.P.H. and M.A. Porter (2012). "Critical truths about power laws". In: *Science* 335.6069, pp. 665–666. DOI: `10.1126/science.1216142`.

Takens, F. (1981). "Detecting strange attractors in turbulence". In: *Dynamical systems and turbulence, Warwick 1980: Proceedings of a symposium held at the University of Warwick 1979-80*. Ed. by D.A. Rand and L.-S. Young. Vol. 898. Lecture Notes in Mathematics. Springer, New York, pp. 366–381. DOI: `10.1007/BFb0091924`.

Telesca, L. and M. Lovallo (2012). "Analysis of seismic sequences by using the method of visibility graph". In: *Europhysics Letters* 97.5, 50002. DOI: `10.1209/0295-5075/97/50002`.

Telford, R.J., E. Heegaard, and H.J.B. Birks (2004). "All age-depth models are wrong: But how badly?" In: *Quaternary Science Reviews* 23.1-2, pp. 1–5. DOI: `10.1016/j.quascirev.2003.11.003`.

Theiler, J., S. Eubank, A. Longtin, B. Galdrikian, and J.D. Farmer (1992). "Testing for nonlinearity in time series: The method of surrogate data". In: *Physica D* 58.1, pp. 77–94. DOI: `10.1016/0167-2789(92)90102-S`.

Thiel, M., M.C. Romano, and J. Kurths (2004). "How much information is contained in a recurrence plot?" In: *Physics Letters A* 330.5, pp. 343–349. DOI: `10.1016/j.physleta.2004.07.050`.

– (2006). "Spurious structures in recurrence plots induced by embedding". In: *Nonlinear Dynamics* 44.1-4, pp. 299–305. DOI: `10.1007/s11071-006-2010-9`.

Thiel, M., M.C. Romano, P.L. Read, and J. Kurths (2004). "Estimation of dynamical invariants without embedding by recurrence plots". In: *Chaos* 14.2, pp. 234–243. DOI: `10.1063/1.1667633`.

Thompson, J.M.T. and J. Sieber (2011[a]). "Climate tipping as a noisy bifurcation: A predictive technique". In: *IMA Journal of Applied Mathematics* 76.1, pp. 27–46. DOI: `10.1093/imamat/hxq060`.

– (2011[b]). "Predicting climate tipping as a noisy bifurcation: A review". In: *International Journal of Bifurcation and Chaos* 21.2, pp. 399–423. DOI: `10.1142/S021812741028519`.

Tiedemann, R., M. Sarnthein, and N.J. Shackleton (1994). "Astronomic timescale for the Pliocene Atlantic δ^{18}O and dust flux records of Ocean Drilling Program Site 659". In: *Paleoceanography* 9.4, pp. 619–638. DOI: `10.1029/94PA00208`.

Timmer, J., C. Gantert, G. Deuschl, and J. Honerkamp (1993). "Characteristics of hand tremor time series". In: *Biological Cybernetics* 70.1, pp. 75–80. DOI: `10.1007/BF00202568`.

Tominski, C., J. Abello, and H. Schumann (2009). "CGV – An interactive graph visualization system". In: *Computers & Graphics* 33.6, pp. 660–678. DOI: `10.1016/j.cag.2009.06.002`.

Tominski, C., J.F. Donges, and T. Nocke (2011). "Information visualization in climate research". In: *Proceedings of the International Conference Information Visualisation (IV), London*. IEEE Computer Society, pp. 298–305.

Trauth, M.H., J.C. Larrasoaña, and M. Mudelsee (2009). "Trends, rhythms and events in Plio-Pleistocene African climate". In: *Quaternary Science Reviews* 28.5-6, pp. 399–411. DOI: `10.1016/j.quascirev.2008.11.003`.

Trauth, M.H., A.L. Deino, A.G.N. Bergner, and M.R. Strecker (2003). "East African climate change and orbital forcing during the last 175 kyr BP". In: *Earth and Planetary Science Letters* 206.3-4, pp. 297–313. DOI: `10.1016/S0012-821X(02)01105-6`.

Bibliography

Trauth, M.H., M.A. Maslin, A. Deino, and M.R. Strecker (2005). "Late Cenozoic moisture history of East Africa". In: *Science* 309.5743, pp. 2051–2053. DOI: 10.1126/science.1112964.

Trauth, M.H., M.A. Maslin, A.L. Deino, M.R. Strecker, A.G.N. Bergner, and M. Dühnforth (2007). "High- and low-latitude forcing of Plio-Pleistocene East African climate and human evolution". In: *Journal of Human Evolution* 53.5, pp. 475 –486. DOI: 10.1016/j.jhevol.2006.12.009.

Trauth, M.H., M.A. Maslin, A.L. Deino, A. Junginger, M. Lesoloyia, E.O. Odada, D.O. Olago, L.A. Olaka, M.R. Strecker, and R. Tiedemann (2010). "Human evolution in a variable environment: The amplifier lakes of Eastern Africa". In: *Quaternary Science Reviews* 29.23-24, pp. 2981–2988. DOI: 10.1016/j.quascirev.2010.07.007.

Trulla, L.L., A. Giuliani, J.P. Zbilut, and C.L. Webber Jr. (1996). "Recurrence quantification analysis of the logistic equation with transients". In: *Physics Letters A* 223.4, pp. 255–260. DOI: 10.1016/S0375-9601(96)00741-4.

Tsonis, A. A., K. L. Swanson, and G. Wang (2008a). "Estimating the clustering coefficient in scale-free networks on lattices with local spatial correlation structure". In: *Physica A* 387.21, pp. 5287–5294. DOI: 10.1016/j.physa.2008.05.048.

Tsonis, A.A. (2007). "Introducing networks in climate studies". In: *Nonlinear Dynamics in Geosciences*. Ed. by A.A. Tsonis and J.B. Elsner. Springer, New York, pp. 1–15. DOI: 10.1007/978-0-387-34918-3_1.

Tsonis, A.A. and P.J. Roebber (2004). "The architecture of the climate network". In: *Physica A* 333, pp. 497–504. DOI: 10.1016/j.physa.2003.10.045.

Tsonis, A.A. and K.L. Swanson (2008). "Topology and predictability of El Niño and La Niña networks". In: *Physical Review Letters* 100.22, 228502. DOI: 10.1103/PhysRevLett.100.228502.

Tsonis, A.A., K.L. Swanson, and S. Kravtsov (2007). "A new dynamical mechanism for major climate shifts". In: *Geophysical Research Letters* 34.13, L13705. DOI: 10.1029/2007GL030288.

Tsonis, A.A., K.L. Swanson, and P.J. Roebber (2006). "What do networks have to do with climate?" In: *Bulletin of the American Meteorological Society* 87.5, pp. 585–595. DOI: 10.1175/BAMS-87-5-585.

Tsonis, A.A., K.L. Swanson, and G. Wang (2008b). "On the role of atmospheric teleconnections in climate". In: *Journal of Climate* 21.12, 2990. DOI: 10.1175/2007JCLI1907.1.

Tsonis, A.A., G. Wang, K.L. Swanson, F.A. Rodrigues, and L. da F. Costa (2011). "Community structure and dynamics in climate networks". In: *Climate Dynamics* 37.5-6, pp. 933–940. DOI: 10.1007/s00382-010-0874-3.

Vastano, J.A. and H.L. Swinney (1988). "Information transport in spatiotemporal systems". In: *Physical Review Letters* 60.18, pp. 1773–1776. DOI: 10.1103/PhysRevLett.60.1773.

Vautard, R. and M. Ghil (1989). "Singular spectrum analysis in nonlinear dynamics, with applications to paleoclimatic time series". In: *Physica D* 35.3, pp. 395–424. DOI: 10.1016/0167-2789(89)90077-8.

Vespignani, A. (2010). "The fragility of interdependency". In: *Nature* 464.7291, pp. 984–985. DOI: 10.1038/464984a.

Volpato, N. (2011). *Python-progressbar: Text progressbar library for Python.* URL: http://code.google.com/p/python-progressbar/.

Vrba, E.S. (1985). "Environment and evolution: Alternative causes of the temporal distribution of evolutionary events". In: *South African Journal of Science* 81.5, pp. 229–236.

– (1993). "The pulse that produced us: Two major global coolings may have prodded antelopes and humans to evolve: How did humans get that way?" In: *Natural History* 102.5, pp. 47–51.

Wackerbauer, R., A. Witt, H. Atmanspacher, J. Kurths, and H. Scheingraber (1994). "A comparative classification of complexity measures". In: *Chaos, Solitons & Fractals* 4.1, pp. 133–173. DOI: 10.1016/0960-0779(94)90023-X.

Walker, G. T. (1910). "Correlation in seasonal variations of weather. II." In: *Memoirs of the Indian Meteorological Department* 21.2, pp. 22–45.

Wallace, J.M. and D.S. Gutzler (1981). "Teleconnections in the geopotential height field during the Northern Hemisphere winter". In: *Monthly Weather Review* 109.4, pp. 784–812. DOI: 10.1175/1520-0493(1981)109<0784:TITGHF>2.0.CO;2.

Wang, G. and A. A. Tsonis (2009). "A preliminary investigation on the topology of Chinese climate networks". In: *Chinese Physics B* 18.11, pp. 5091–5096. DOI: 10.1088/1674-1056/18/11/080.

Wang, X.-J., Z.-Q. Gong, L. Zhou, and R. Zhi (2009). "Analysis of the stability of temperature networks part I: The influence of extreme events". In: *Acta Physica Sinica* 58.9, pp. 6651–6658.

Watts, D.J. and S.H. Strogatz (1998). "Collective dynamics of "small-world" networks". In: *Nature* 393.6684, pp. 440–442. DOI: 10.1038/30918.

Werner, P.C. and F.-W. Gerstengarbe (2011). *Spatial-temporal changes of meteorological parameters in selected circulation patterns.* PIK-Report 123. Potsdam Institute for Climate Impact Research, Potsdam, Germany.

Wernicke, S. and F. Rasche (2006). "FANMOD: A tool for fast network motif detection". In: *Bioinformatics* 22.9, pp. 1152–1153. DOI: 10.1093/bioinformatics/btl038.

Whitaker, J. (2012). *netcdf4-python: Python/numpy interface to NetCDF.* URL: http://code.google.com/p/netcdf4-python/.

White, T. (2002). "Earliest hominids". In: *The primate fossil record.* Ed. by W.C. Hartwig. Cambridge University Press, Cambridge, pp. 407–417.

White, T.D., G. WoldeGabriel, B. Asfaw, S. Ambrose, Y. Beyene, R.L. Bernor, J.-R. Boisserie, B. Currie, H. Gilbert, Y. Haile-Selassie, W.H. Hart, L.J. Hlusko, F.C. Howell, R.T. Kono, T. Lehmann, A. Louchart, C.O. Lovejoy, P.R. Renne, H. Saegusa, E.S. Vrba, H. Wesselman, and G. Suwa (2006). "Asa Issie, Aramis and the origin of *Australopithecus*". In: *Nature* 440.7086, pp. 883–889. DOI: 10.1038/nature04629.

Wiedermann, M. (2011). "Coupled climate network analysis of multidecadal dynamics in the Arctic". Bachelor's thesis. Humboldt University, Berlin.

Bibliography

Wiedermann, M., J.F. Donges, J. Heitzig, and J. Kurths (2013). "Node-weighted interacting network measures improve the representation of real-world complex systems". In: *ArXiv preprint* arxiv:1301.0805 [physics.soc-ph].

Winter, C. and M. Damron (2009). "A non-Markovian model of rill erosion". In: *Networks and Heterogeneous Media* 4.4, pp. 731–753. DOI: 10.3934/nhm.2009.4.731.

Wunsch, C. (2007). "Extremes, patterns, and other structures in oceanographic and climate records". In: *Proceedings of the 15th 'Aha Huliko'a Hawaiian Winter Workshop on Extreme Events*. University of Hawaii, Honolulu, pp. 141–148.

Xiang, R., J. Zhang, X.K. Xu, and M. Small (2012). "Multiscale characterization of recurrence-based phase space networks constructed from time series". In: *Chaos* 22.1, 013107. DOI: 10.1063/1.3673789.

Xu, X., J. Zhang, and M. Small (2008). "Superfamily phenomena and motifs of networks induced from time series". In: *Proceedings of the National Academy of Sciences of the United States of America* 105.50, pp. 19601–19605. DOI: 10.1073/pnas.0806082105.

Yamasaki, K., A. Gozolchiani, and S. Havlin (2008). "Climate networks around the globe are significantly affected by El Niño". In: *Physical Review Letters* 100.22, 228501. DOI: 10.1103/PhysRevLett.100.228501.

– (2009). "Climate networks based on phase synchronization analysis track El-Niño". In: *Progress of Theoretical Physics Supplement* 179, pp. 178–188. DOI: 10.1143/PTPS.179.178.

Yang, X.-S. (2001). "Small-world networks in geophysics". In: *Geophysical Research Letters* 28.13, pp. 2549–2552. DOI: 10.1029/2000GL011898.

Yang, Y. and H. Yang (2008). "Complex network-based time series analysis". In: *Physica A* 387.5–6, pp. 1381–1386. DOI: 10.1016/j.physa.2007.10.055.

Zaliapin, I., E. Foufoula-Georgiou, and M. Ghil (2010). "Transport on river networks: A dynamic tree approach". In: *Journal of Geophysical Research* 115, F00A15. DOI: 10.1029/2009JF001281.

Zamora-López, G. (2009). "Linking structure and function of complex cortical networks". PhD thesis, urn:nbn:de:kobv:517-opus-52257. University of Potsdam.

Zamora-López, G., C.S. Zhou, and J. Kurths (2009). "Graph analysis of cortical networks reveals complex anatomical communication substrate". In: *Chaos* 19.1, 015117. DOI: 10.1063/1.3089559.

– (2010). "Cortical hubs form a module for multisensory integration on top of the hierarchy of cortical networks." In: *Frontiers in Neuroinformatics* 4, 1. DOI: 10.3389/neuro.11.001.2010.

Zhang, J. and M. Small (2006). "Complex network from pseudoperiodic time series: Topology versus dynamics". In: *Physical Review Letters* 96.23, 238701. DOI: 10.1103/PhysRevLett.96.238701.

Zhou, C.S., L. Zemanová, G. Zamora-Lopéz, C.C. Hilgetag, and J. Kurths (2006). "Hierarchical organization unveiled by functional connectivity in complex brain networks". In: *Physical Review Letters* 97.23, 238103. DOI: 10.1103/PhysRevLett.97.238103.

Zhou, C.S., L. Zemanová, G. Zamora-López, C.C. Hilgetag, and J. Kurths (2007). "Structure–function relationship in complex brain networks expressed by hierarchical synchronization". In: *New Journal of Physics* 9.6, 178. DOI: 10.1088/1367-2630/9/6/178.

Zou, Y., J.F. Donges, and J. Kurths (2011). "Recent advances in complex climate network analysis". In: *Complex Systems and Complexity Science* 8.1, pp. 27–38.

Zou, Y., R.V. Donner, and J. Kurths (2012). "Geometric and dynamic perspectives on phase-coherent and noncoherent chaos". In: *Chaos* 22.1, 013115. DOI: 10.1063/1.3677367.

Zou, Y., R.V. Donner, J.F. Donges, N. Marwan, and J. Kurths (2010). "Identifying complex periodic windows in continuous-time dynamical systems using recurrence-based methods". In: *Chaos* 20.4, 043130. DOI: 10.1063/1.3523304.

Zou, Y., J. Heitzig, R.V. Donner, J.F. Donges, J.D. Farmer, R. Meucci, S. Euzzor, N. Marwan, and J. Kurths (2012). "Power-laws in recurrence networks from dynamical systems". In: *Europhysics Letters* 98.4, p. 48001. DOI: 10.1209/0295-5075/98/48001.

Selbständigkeitserklärung

Ich erkläre, dass ich die vorliegende Arbeit selbständig und nur unter Verwendung der angegebenen Literatur und Hilfsmittel angefertigt habe.

Potsdam, den 11. Januar 2013   Jonathan Friedemann Donges